Structural Characterisation of Biominerals and Biomimetic Crystallisation of Calcium Carbonate

Dissertation

zur Erlangung der Doktorwürde (Dr. rer. nat.)

vorgelegt von

Alexander Becker

aus Hattingen

Institut für Anorganische Chemie

der

Universität Duisburg-Essen

Gutachter: Prof. Dr. M. Epple
Prof. Dr. R. Boese
Vorsitzender: Prof. Dr. P. Rademacher

Tag der mündlichen Prüfung: 14.07.2005

“Where did you get that piece of wisdom from?”
Prof. Dr. Steve Weiner, Weizmann Institute of Science, Rehovot, Israel, during a discussion

List of contents

1. Introduction

During the process of writing this thesis, two objects were inevitably in my view, because they had found a place directly below the computer screen. Both are made of the same material - calcium carbonate to be exact - and are nevertheless so different from each other that it is hardly believable. The first object is a calcite crystal of nearly perfect morphology and absolutely clear. The other object is a brownish shell of the fresh-water snail *Biomphalaria glabrata* (Pulmonata, Basommatophora) in usual spindle design consisting of aragonite. Despite these two objects being made of the same compound $CaCO_3$, their physical and chemical properties differ considerably. This is due to their origin, rather than the comparison of two polymorphs of a compound. The calcite crystal was formed millions of years ago under high temperature and pressure in the depths of the earth. The shell was formed by an animal four years ago under ambient conditions (room temperature and usual pressure).

Crystallisation is the formation of crystals in a former homogeneous system. Crystals are the thermodynamically stable state of solids. In crystals, atoms are arranged in a characteristic form, repetitive in all three dimensions which is described as the crystal lattice. Crystallisation usually occurs in the liquid phase but is also possible from the gas phase. The process of crystallisation can be divided into three general groups. The most common type is geological crystallisation which usually occurs under high pressure and/or temperature over a long period of time. It results in highly ordered crystals of great size. The small sample mentioned above is a piece of a rhombohedron of about 4 x 3 x 3 cm. Geologically formed crystals usually contain a lot of added atoms which often result in beautiful or even expensive coloured forms e.g. rubies. The second group is chemical crystallisation which happens under ambient conditions. The crystals precipitated from mother liquor are usually very small and rather unordered. The powder-like product is formed quickly (a matter of seconds, usually) and shows a quite high amount of lattice defects. The third

group is biological crystallisation which is also known as biomineralisation. Under controlled conditions, usually very small, but highly ordered crystals are formed by biological systems. The products are precipitates with often astonishing mechanical properties resulting from organic macromolecules which form a composite material with the crystalline phase e.g. the snail shell mentioned above shows the hardness of steel.

Over 60 minerals are precipitated by organisms and more are still being discovered.[1-3] Biomineralisation is a process of planet-wide importance, as the atmosphere's carbon dioxide is in equilibrium with the oceans where huge quantities of calcium carbonate are precipitated by organisms.[4] Usually, organisms employ mineral precipitates for protection (shells, spikes), mechanical work (teeth) or structural integrity (skeleton). A rather unusual approach to the employment of biominerals is found in land snails. They use "love darts" (gypsobelia) during mating which are exchanged by partners and trigger conformational changes in the female reproductive organs.[5] However, biomineralisation does not only cover desired precipitation. Pathologic biomineralisation processes are responsible for major diseases i.e. atherosclerosis. This calcification of arteries is the most important cause of death in industrialised nations.

Organisms show an astonishing degree of control of mineralisation processes. They can precipitate crystalline phases which would not be accessible under the physical conditions of the environment in which these organisms dwell. Good examples are the gravity sensors of certain jellyfish which consist of a water-deficient calcium sulphate phase despite the organism consisting almost exclusively of water (99 %) and living in the deep sea (4°C, high pressure). Mineralisation control is so developed that certain organisms can precipitate non-crystalline material, thus combining the advantages of an amorphous phase (high solubility) with the advantages of a mineralised tissue (protection). This

can be found in crustaceans (woodlice, crabs etc.) possessing a mineralised cuticle which has to be shed regularly to accommodate animal growth.

Analysing biominerals gives an impression of the ability of nature to adapt and develop. Today, it is not possible to rebuild any biomineral *in vitro*. However, basic ideas have been developed as to how organisms exercise control over mineralisation processes.[6] A water-insoluble organic framework acts as nucleation site or template for crystallisation. Crystal growth is regulated by the control of ion flow into the precipitation zone. Water soluble organic macromolecules regulate the crystal morphology by adsorption on specific faces of the growing crystal. Therefore, it is of great interest how organic macromolecules can be combined with inorganic minerals in a way which generates materials similar to biominerals in properties. The behaviour of extracted soluble organic components present during precipitations is tested in many different crystallisation essays. A constant improvement of the control of conditions during crystallisation is necessary to understand these interactions.

2. Theoretical background

2.1 Crystals and crystallisation

2.1.1 The ordered form of the solid state: crystals

The term “crystal” (Greek *krystallos*) is derived from *kryos*, meaning ice-cold or frost. Crystals are the thermodynamically stable solid state with a structure built of repetitive units of their constituent atoms, ions or molecules. These repetitive units form a characteristic, three-dimensional arrangement, resulting in typical crystal anisotropy. The anisotropy results in distinctive properties such as fracturing or splitting, as well as conductivity (graphite), refraction index (calcite) or colour (turmalin, a complex silicate).[7]

Fig. 2.1-1: Geological quartz crystal (SiO_2).

The ideal crystal consists of structural units, repeated regularly in all three dimensions, forming a crystal lattice. In reality, a strongly regular arrangement is never achieved. Real crystals exhibit lattice defects.[8] One class of defects are zero-dimensional defects, describing unoccupied (vacancies, Schottky-Defect) or additional occupied (interstitials, Frenkel-Defect) positions. These flaws are very common in minerals composed of elements with more than one stable oxidation state e.g. FeO (Fe^{2+} and Fe^{3+}). However, vacancies and interstitials are in thermodynamical equilibrium with the ideal lattice and cannot be avoided in any crystal. The concentration of defects can be estimated according to

$$\frac{N_D}{N} = \exp\left(-\frac{E_D}{k_B T}\right) \qquad \text{(eq. 2.1-1)}$$

where N_D represents the number of defects, N the number of atoms of the crystal (hence N_D/N equals the defect concentration), E_D the energy necessary to form the defect [J], $k_B=1.381\cdot10^{-23}$ J K^{-1} (Boltzmann's constant) and T the temperature [K]. Substitution defects occur by replacement of a lattice atom or ion by another element. This occurs frequently when the substituted atoms or ions show a relatively similar radius or chemical behaviour e.g. magnesium replaces calcium in calcium carbonate (and vice versa). As substituted atoms or ions change the electronic structure of the material, aimed substitution is used in the construction of modern semiconductors and is called doping. Special zero-dimensional defects are possible in crystals composed of ions. An anti-site defect occurs when the positions of anions and cations are interchanged. The replacement of an anion by an electron gives rise to a colour centre.

One-dimensional defects include step-disclosures or screw-disclosures. Both occur frequently in real crystals and can be imagined as the addition of a "half-lattice" plane. Depending on the exact manner in which this "half-plane" is added, the defect can be either a step-disclosure or a screw-disclosure. Polycrystalline materials show two-dimensional defects at the interface of two individuals of crystals (particle boundaries). A special form of this defect is the twin-crystal occurring if the interfaces of two individuals follow certain crystal faces. Three-dimensional defects are macroscopic defects resulting from the incorporation of solvent or air/gas (occlusion) during fast growth of a crystal. A real crystal with few lattice defects is called a single crystal. Crystal analysis is very effectively possible with X-ray diffraction (see chapter 5.1).

The formation of crystals (crystallisation) is one of the least understood processes of phase transition. The basic theories addressing the growth of crystals from supersaturated solutions were developed in the 1920s[9] and expanded in the 1950s.[10] The current theory is summarised by Nyvlt and Ulrich.[11] Despite the theoretical progress, the first steps of crystallisation, when the ions find each other and combine, are processes occurring on an atomic

scale, and thus are not yet accessible experimentally except for atomic force microscopy.

The coalescing of ions from clear solutions into crystal nuclei – a process called primary nucleation – is thought to occur in one of two ways. Heterogeneous primary nucleation occurs when an added solid phase e.g. the container wall or a dust particle catalytically induces the formation of crystal nuclei. In the case of homogeneous primary nucleation, the nuclei are spontaneously formed from the solution. Secondary nucleation occurs in the presence of crystallites of the substance which induce the formation of new crystal nuclei. Shear stress may transfer parts of these crystallites into the solution. Then if certain conditions are met, those nuclei form new crystallites and finally grow to crystals.

The driving force of crystallisation is the difference between the chemical potential of the supersaturated liquid phase and the chemical potential of the solid phase. The thermodynamic expression of this driving force is given by the change of the Gibbs-enthalpy from supersaturated to saturated solution (ΔG_{cryst})[12]:

$$\Delta G_{Cryst} = -\mathrm{R} \cdot T \cdot \ln\left(\frac{IP}{K_L}\right)^{\frac{1}{\nu}} \qquad \text{(eq. 2.1-2)}$$

with R=8.31451 J mol^{-1} K^{-1} (gas constant), T the temperature [K], IP the product of the ion activities in solution, ν the sum of the stoichiometric coefficients, and K_L the solubility product of the solid mater. Because the formation of the new solid phase induces the formation of a surface, the system must overcome the energy necessary for the formation of the new surface. Finally, the difference of the change of the Gibbs-enthalpy from supersaturated to saturated solution ΔG_{cryst} and the work necessary for the surface formation ΔG_{Nuc} determines the effective driving force of nucleation. The pre-existing surfaces of added phases

during heterogeneous primary nucleation reduce the work necessary for surface creation, and thus make crystallisation easier.

The growth of a crystal nucleus is in equilibrium with its dissolution. Only if a critical size is reached the probability of dissolution decreases. Crystal growth is described with the *terrace-edge-kink*-model. The model states that a crystal grows by the adsorption of ions transported to the crystallite by convection and diffusion. The adsorbed ions diffuse on the surface (*terrace*) until they are either desorbed or until they meet an atomic *edge*. Diffusion continues along the edge until they reach an incomplete layer (*kink*). There, the probability for incorporation of the ion into the lattice is highest. At this point, the hydrate shell of the ion detaches and the ion is installed. It was proposed that the dehydratation of the ions is the rate determining step of crystal growth.[13] Depending on the conditions during crystal growth, the polymorphic phase (crystal phase) of the crystalline material is determined as well as the occurrence of crystal defects. Sufficiently slow growth allows thermodynamic control on the formation of the new crystal. A characteristic polyhedron develops which possesses the least surface energy for the given crystal structure. The surfaces of the crystal correspond to certain preferred lattice planes (see Figure 2.1-2).

Three crystallisation processes with very different resulting crystals can be distinguished. There is geological crystallisation, which occurs over long periods of time at high temperatures and pressures. Geological crystals are large and usually highly ordered. The second important crystallisation is chemical precipitation in the laboratory or in industry. Usually, small and relatively

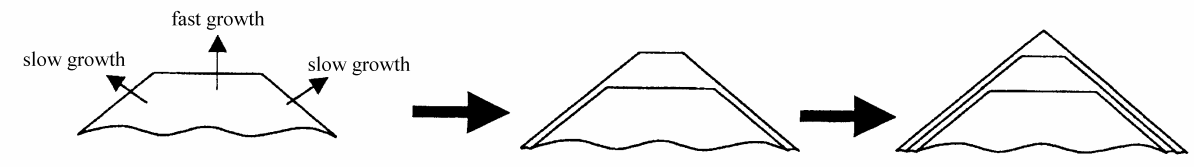

Fig. 2.1-2: The growth rate of certain crystal faces determines the final morphology (shape) of a crystal. The final shape corresponds to a structure of least surface energy. The scheme was taken from F. Peters.[14]

disordered crystals result from chemical crystallisation. The high formation rate results in a high number of defects. However, the crystallisation from smelts results in highly ordered crystals of enormous size e.g. silicon single-crystals for wafer production. Biological crystallisation, also called biomineralisation, is the third crystallisation process. Slow precipitation under the influence of biological macromolecules and controlled conditions results in small crystals embedded in an organic matrix. Biological crystals are mostly structurally defective and contain added atoms. Biomineralisation is presented in chapter 2.1.4 in more detail.

If an added phase is present during crystallisation (heterogeneous nucleation), the new crystals can also precipitate on the surface of the added phase. In the case when the added phase offers a suitable surface for the growth of the solid material, this surface can act as a template for crystallisation. Such a template can induce the formation of crystals, which grow oriented on the template surface. Templates are known to induce the growth of another polymorphic phase than the thermodynamically most favoured under the conditions of the precipitation. The oriented growth of a crystal on a specific heterogeneous surface is called epitaxy.[15]

Whether a specific polymorphic phase is formed during precipitation depends not on the thermodynamic stability of the formed phase. The activation energy necessary to form a specific polymorphic phase and the precipitation kinetics control the crystallisation process. Figure 2.1-3 schematically explains the connections. Although the formation of the most stable crystalline phase of a compound is thermodynamically favoured, the activation barrier for this precipitation is rather high. As the activation energy necessary to form the amorphous precipitate is much lower and faster, this polymorph is formed first, and only then slowly recrystallises into that phase which is thermodynamically most stable under the conditions of the performed precipitation. The finding that

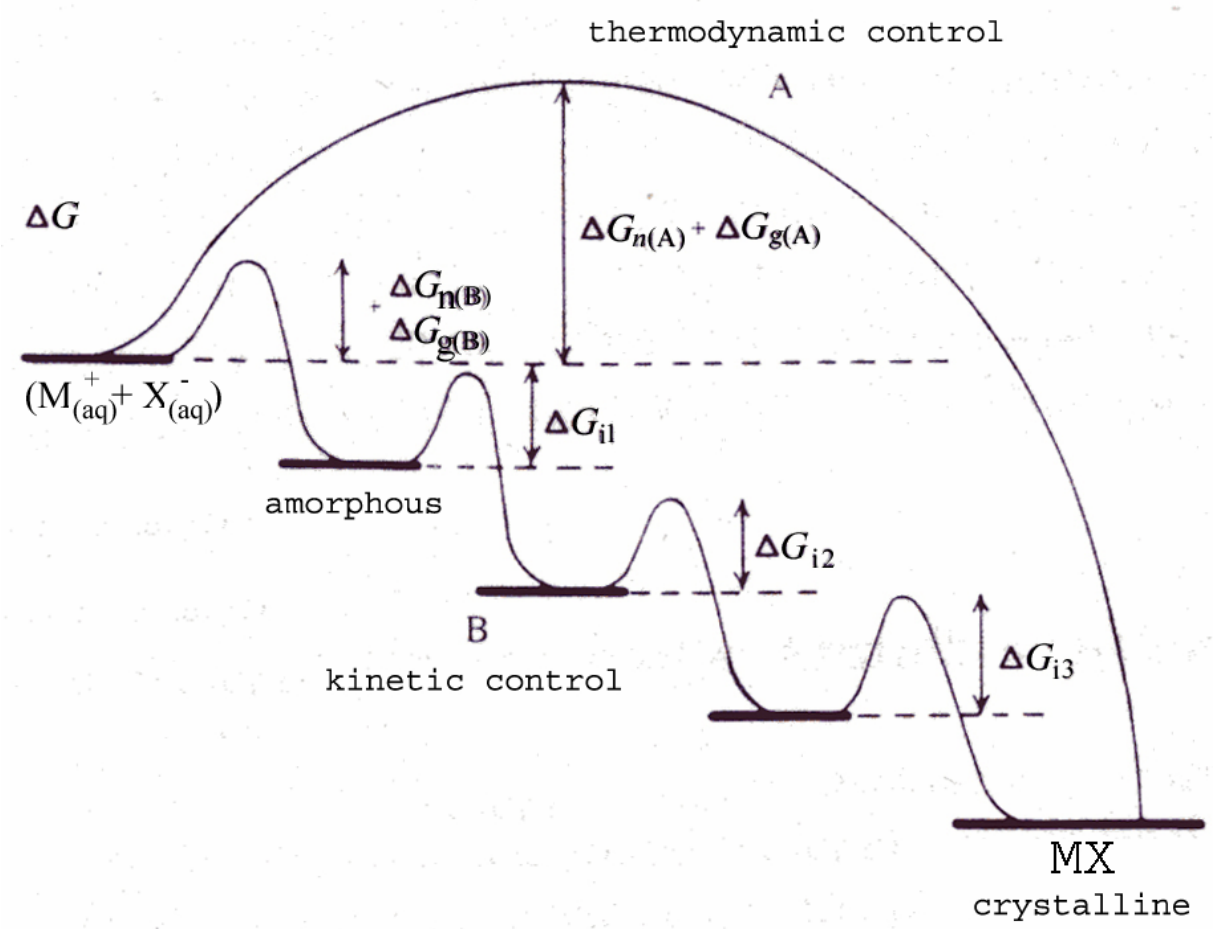

Fig. 2.1-3: Schematic explanation of the Ostwald rule. The activation energy to form a less stable polymorph is lower than to from a more stable polymorph. Thermodynamic rules predict the formation of the most stable phase, kinetic controlled precipitations lead to less stable polymorphs.

a system does not change from highest state of energy (ions in solution) directly to the lowest state of energy (the thermodynamically most stable crystal polymorph) but undergoes states of intermediate energy is referred to as Ostwald's step rule.[16]

2.1.2 The influence of additives during crystallisation

The influence of additives such as other ions or organic components on a developing crystal is manifold. All kinds of added substances can adsorb to the crystal surface. The creation of a layer of adsorbed material or its adsorption on certain crystal surfaces or on certain positions can alter crystal growth.[17] Adsorption on specific surfaces changes the outer appearance (morphology) of

the crystal by inhibiting the growth of an otherwise growing surface. If added substances are adsorbed on *kink*-sites, crystal growth can even be completely inhibited. Aside from their adsorption and the resulting modification of crystal morphology, added ions can be incorporated into the lattice, thus forming a kind of mixed crystal with properties different from those of the pure crystal.

Different substances in the mother liquor can affect crystal growth in different ways. An additive that negatively influences crystal growth rate is called an inhibitor. Three classes of inhibitors can be distinguished[11]:

1. acids and bases: The pH value of the mother liquor influences the ion activity and the ion concentrations, e.g. the carbonate/hydrogencarbonate ratio. The pH influences growth the rates and thus the morphology and the size of the developing crystals.[18]
2. inorganic additives: Small concentrations of inorganic ions like Fe^{3+}, Cr^{3+}, Al^{3+}, or WO_4^{2-}, MoO_4^{2-}, PO_4^{2-}, are known to influence the size and the form of the crystals as well as its polymorph.[19] These ions also influence the ion activities and the ion concentrations.
3. organic additives: Many organic components are surface active and influence the morphology and the crystal growth rate even in low concentrations. However, substances of different kinds can create similar morphologies, indicating a non-specific surface adsorption. These additives have only little effect on the ion concentrations.

Usually, a change in morphology goes hand in hand with a reduction of the crystal growth rates. As adsorption of added substances to the crystal surface is

responsible for these effects, processes of inhibition are often described by the Langmuir-Adsorption-isotherm model, assuming the energetic equivalence of all surface adsorption sites – an assumption which is not accurate. Currently, quantitative relations in inhibition processes or organic components are rarely possible, as experiments are hardly reproducible.

Another factor influencing crystal growth with additives is the addition of complexing (coordinating) agents to the mother liquor. The formation of soluble complexes effectively reduces the effective ion concentration. A prominent example is the real concentration of calcium ions and phosphate ions in blood. These exceed the solubility product of calcium phosphate, but as these ions are present as complexes, effectively reducing the concentration of calcium and phosphate below the solubility product, no pathologic crystallisation occurs in healthy animals. Complete inhibition may also arise from the coordination of crystal nuclei by organic macromolecules.

2.1.3 Biological macromolecules: proteins

The term "protein" is derived from the Greek word *proteuein* which means "to be first". It is a collective noun for biologically produced polymers of the 20 different natural α-amino acids (see Figure 2.1-4). Amino acids are molecules consisting of a carboxylic acid group, an α-amino group and an organic residue R, attached to the same α-carbon atom. Amino acids are classified depending on the properties of the side group R into polar, apolar, acidic and basic molecules. The reaction of an acid group of one amino acid with the α-amino group of another amino acid leads to a condensation reaction and the formation of a peptide bond:

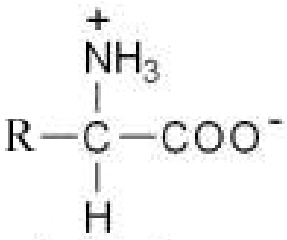

Fig. 2.1-4: General formula of an α-amino acid.

$$R_1\text{-}C(NH_2)COOH + H_2N(HOOC)C\text{-}R_2 \rightarrow R_1\text{-}C(NH_2)O\text{-}HN(HOOC)C\text{-}R_2 + H_2O$$

Polypeptides are also polymers of these amino acids, but much shorter than proteins. Up to about 100 monomers, amino acid polymers are called proteins, below that number, they are called polypeptides; however, there is no exact definition. Molar masses of about ten thousand to several hundred thousand Dalton are usual for proteins. Molecules with masses larger than a million Dalton are known, but they are rare.

Proteins are roughly divided into groups according to their behaviour in (salt) water as globular proteins and fibrilous proteins. Concerning their composition they are divided into simple proteins which consist entirely of amino acids, and conjugated proteins which also incorporate non-protein components, such as sugars (glycoproteins), fatty acids (lipoproteins) or metals (metalloproteins). Furthermore, proteins are classified according to their biological task e.g. enzymes, hormones or receptors. Most proteins are water soluble. Other proteins, including those used for construction of structural elements like fibrils or those incorporated into membranes are not.

The primary structure of a protein is given by the linear sequence of amino acids, as laid down by the genetic code. Parts of the polypeptide chain assume a specific spatial arrangement, called secondary structure. The secondary structure is determined by the bond angles and possible rotation around C-C or C-N bonds. The exact conformation under physiological conditions depends on the type and number of groups present in the chain, which determine the possible local interactions of the chain elements among themselves largely through H-bond bridges. The overall spatial arrangement of the whole protein is called tertiary structure. This structure describes the three-dimensional form of the molecule and may also result from covalent bonds between chain elements. For example, the amino acid cysteine allows the formation of disulfide bridges; other amino acids offer additional amino or acid functions which can form isopeptide bonds. Figure 2.1-5 shows the crystal structure of human serum albumin, one of the most prominent proteins in human blood.[20] The complex

three-dimensional structure can be easily seen. Very large proteins may consist of complexes of several polypeptide chains. The arrangement of these single chains in the whole complex is the quarternary structure. One example of this is haemoglobin, which consists of four different polypeptide chains.

Fig. 2.1-5: Sturcture of human serum albumin as determined by X-ray diffractometry. The protein consists of four different polypeptide chaines. The image was taken from the protein database.

The function of proteins depends especially on their tertiary structure. A change of environmental conditions, especially changes of pH, strongly influences this structure and thus affects the function of the protein. The most devastating influence is the destruction of the tertiary structure which is usually irreversible. This process is called denaturation and is visible if protein solutions form foam. The primary structure is also of special importance to proteins found in biomineralisation. As they adsorb on polar crystal phases, they are often rich in the amino acids aspartic acid and glutamic acid.[21]

2.1.4 Biomineralisation

The mineralisation of inorganic crystals by living organisms is called biomineralisation. Aside from geological crystallisation and chemical crystallisation, living organisms produce over 60 different biominerals.[1, 22] Addadi and Weiner give a detailed introduction into biomineralisation in German[6] and English[23]. Table 2.1-1 lists some of the most prominent examples of biominerals; Figure 2.1-6 shows the complex structure of a radiolarian “glasshouse”, a structure made of amorphous silica.

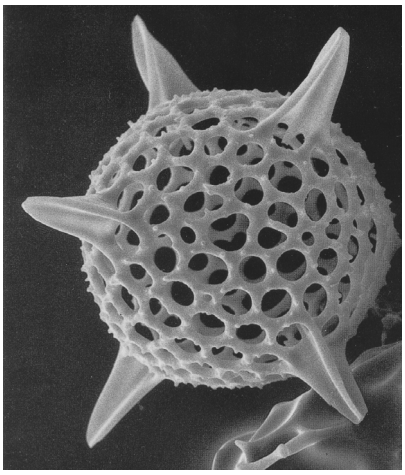

Fig. 2.1-6: A Radiolarian "glasshouse", a structure made of amorphous silica. Image by courtesy of M. Epple.

Biologically produced minerals often possess astonishing mechanical properties and are used for many purposes, including protection (shells of snails or mussels), body stabilisation (skeleton) or as teeth. The iron oxide mineral magnetite is used for navigation in the earth's magnetic field by several bacteria, algae and even higher animals (birds).[24] Magnetite is also found in the outer layer of the teeth of chiton.[25] A rather exotic biomineral is atacamite $Ca_2(OH)_3Cl$ which is found in the jaw of the marine bloodworm *Glycera dibranchiate*.[3] But about half of all biologically precipitated minerals consist only of poorly water-soluble calcium compounds. Most prominent are the calcium carbonate phases calcite, aragonite, vaterite, and monohydrocalcite as well as several calcium phosphates in the form of different apatite derivates or octacalcium phosphate. This is supposed to be due to the fact that biomineralisation evolved in the oceans and calcium is very abundant in sea water of all ages. However, organisms have developed specialised precipitation mechanisms to overcome the thermodynamic boundaries.

The earliest use of minerals by organisms can be traced to over 3500 million years ago. Fossils of colonies of prokaryotic organisms (stematoliths) incorporating minerals, show that these organisms have somehow induced mineral growth. Since then, organisms have improved their mechanisms of controlling mineralisation. In the Cambrian period about 570 million years ago, the first mineralised skeletal structures appeared. In this period, the basic principles for the formation of skeletal structures evolved, possibly based on the mineralisation principles obtained from earlier organisms.[1] Species from many different phyla began the formation of mineralised exoskeletons.[26] This process

was possibly induced by a major extinction, as most of the new biomineralising phylogenetic groups newly evolved.[27]

During evolution, the precipitation of minerals played a very important ecological role, especially in the oceans. The mineralisation of enormous quantities of calcium carbonate by marine protozoa reduced the content of carbon dioxide in the atmosphere. Even today, it continues to be a major factor influencing the carbon dioxide equilibrium in the atmosphere.[4] The mineralised shells and skeletons of mineralised organisms sink to ocean floor after their death and are either redissolved or incorporated into the sediment. Similar processes occur for silicon dioxide which is precipitated in huge quantities by diatoms and radiolarians. Many present-day geological formations on land are actually sediments from ancient oceans.

Tab. 2.1-1: List of common biominerals as given in literature.[1]

Calcite	$CaCO_3$
Aragonite	$CaCO_3$
Vaterite	$CaCO_3$
Monohydrocalcite	$CaCO_3 \cdot H_2O$
Protodolomite	$CaMg(CO_3)_2$
Hydrocerussite	$Pb_3(CO_3)_2(OH)_2$
Hydroxyapatite	$Ca_5(PO_4)_3(OH)$
Octacalciumphosphate	$Ca_8H_2(PO_4)_6 \cdot SH_2O$
Fluorapatite (Francolite)	$Ca_5(PO_4)_3F$
Carbonated-hydroxyapatite	$Ca_5(PO_4,CO_3)_3(OH)$
Whitlockite	$Ca_{18}H_2(Mg, Fe)_2^{2+}(PO_4)_{14}$
Struvite	$Mg(NH_4)(PO_4) \cdot 6\ H_2O$
Brusite	$Ca(HPO_4) \cdot 8\ H_2O$
Vivianite	$Fe_3(PO_4)_2 \cdot 8\ H_2O$
Fluorite	CaF_2
Hieratite	K_2SiF_6
Gypsum	$CaSO_4 \cdot 2\ H_2O$
Celestine	$SrSO_4$
Barite	$BaSO_4$
Jarosite	$KFe_3^{3+}(SO_4)_2(OH)_6$
Opal	$SiO_2 \cdot n\ H_2O$
Magnetite	$Fe^{2+}Fe^{3+}O_4$
Goethite	α-FeO(OH)
Lepidocrokite	γ-FeO(OH)
Ferrihydrite	$5\ Fe_2O_3 \cdot 9\ H_2O$
Todorokite	$(Mn^{2+}CaMg)Mn_3^{4+}O_7 \cdot\ H_2O$
Birnessite	$Na_4\ Mn_{14}O_{27} \cdot 9\ H_2O$
Pyrite	FeS_2
Hydrotroilite	$FeS \cdot n\ H_2O$
Sphalerite	ZnS
Wurtzite	ZnS
Galenite	PbS
Greigite	$Fe^{2+}Fe_2^{3+}S_4$
Mackinawite	$(Fe, Ni)_9S_8$
Earlandite	$Ca_3(C_6H_5O_2)_2 \cdot 4\ H_2O$
Whewellite	$CaC_2O_4 \cdot H_2O$
Weddelite	$CaC_2O_4 \cdot (2+x)\ H_2O,\ (x < 0,5)$
Glushinskite	$MgC_2O_4 \cdot 4\ H_2O$

By aimed synthesis, organisms control the phase and the morphology of precipitated crystals.[22, 28-31] Biological macromolecules (proteins) are often found within crystals or at the interface between cells and crystals.[32] Proteins are known for their ability to adsorb on certain crystal faces, e.g. the 001-faces

of calcite, and therefore to decrease the growth rate of these crystal faces while increasing the growth rate of others.[33] Current theory states that organisms form specialised, intracellular crystallisation compartments (vesicles) where ions of the nascent biomineral are precipitated under the influence of a crystallisation matrix consisting of biological macromolecules.[34, 35] The inorganic compounds are transferred by complex mechanisms into specialised cells which accumulate cations and anions in storage vesicles, while at the same time the insoluble matrix in the crystallisation vesicles is biosynthesised. Thus, precipitation localisation and crystal size are determined.

The insoluble matrix consists mainly of hydrophobic proteins, lipids, and polysaccharides. Current theory states that structure directing soluble proteins adsorb on this insoluble matrix, thus creating adsorption sites for cations. Therefore, a network with a specific surface is created that provides a good basis for epitaxial growth of the inorganic mineral. The adsorption sites direct the ion distance in the forming mineral, and therefore determine the polymorphic phase of the precipitated mineral even if it is not the thermodynamically most stable phase that is mineralised.[36] Proteins extracted from aragonitic mollusc shells show calcium active groups of aspartic acid (Asp) whose geometry resembles the positions of calcium in the 001-faces of aragonite.[37] Similar effects are visible *in vitro* during the crystallisation of calcium carbonate on self-assembling monolayers (SAMs): monolayers of organic substances attached to a substrate surface. The terminal groups of the layer are variable and can be used as surfaces for epitaxial overgrowth of minerals used in biomineralisation. Thus, morphology and phase of the growing crystals are directed. Calcite has been shown to orient itself specifically according to amide-containing phospholipids[38] or calixarenes[39]. The crystal phase can be altered under crystallisation conditions to thermodynamically unfavourable phases, depending on the template on which the crystals are deposited.[40] By choosing deposition sites accordingly, elaborate films of calcium carbonate can be grown on

SAMs.[41] Different models discuss the effects of surfaces on calcite growth and on the stability of the various possible interfaces.[42, 43] The more closely an organic surface imitates the structure of the inorganic precipitate stereochemically, the more a crystallisation is preferred. But the crystal phase does not only depend on the template; inorganic additives also influence the crystal phase. Magnesium is known to trigger the formation of aragonite instead of calcite. The presence of soluble matrix proteins is also responsible for phase direction. This effect has been proven in many experiments.[44-48] Phase direction is also thought to be directed by regulation of the flow of ions into the mineralisation vesicle.[49]

However, this model considers almost exclusively extracellular activities. Mount *et al.* found a hemocyte-mediated mineralisation of the shell of eastern oyster.[50] These cells are able to initiate mineral growth on secreted organic sheets. Therefore Mount *et al*. postulate an intracellular nucleation mechanism. Apparently, biological crystal formation involves complex interactions between organic compounds, ions, and cells.

Once a crystallite has reached its critical size, its growth can theoretically continue provided that the solubility product of the mineral is exceeded. Growth control in biomineralisation is exercised by the soluble matrix proteins through adsorption and through regulation of the flow of ions into the mineralisation vesicle. Furthermore, crystal morphology is directed as needed by the organism.[51] Specific adsorption on special crystal faces has been shown for antibodies adsorbing on cholesterol.[52] A model for the adsorption of organic substituents on calcite has been developed and allows a prediction of necessary structural elements for specific adsorption.[53] Morphology control can also be achieved by *in vitro* experiments. Synthetic polymers give rise to special morphologies like spheres or chains of interlinked calcite chains.[54, 55] Sugarawa and co-workers were able to mimic calcium carbonate biomineral morphology

by precipitation on a modified hydrophobic polysaccharide in the presence of poly-acrylic acid.[56]

Kato *et al.* give a brief overview of the effects of soluble and insoluble compounds on calcium carbonate crystallisation, both natural and artificial.[57] Recently, Söllner *et al*. reported on the control of crystal size and formation by proteins encoded by a gene identified as Starmaker.[58] They showed that the genetic modification of Starmaker changed the expression of otoliths in the ears of teleost fishes, thus proving the genetic control an organism possesses on mineralisation processes. In gastropod nacre, the effect of an insoluble organic matrix present during precipitation results in flat and polygonal crystals of aragonite.[59] In addition, it should not be forgotten that the variations of the pH value and the ion concentration also play an important role in biomineral formation.

Soluble and insoluble proteins direct not only the phase and shape of precipitated minerals, but also determine their mechanical properties by their incorporation into the biomineral.[60] The composite materials formed are more flexible than the pure mineral, yet much more mechanically stable than the organic framework alone. Naka *et al.* illustrate schematically in Figure 2.1-7 the structure of nacre, an aragonite composite.[61] Nacre is about 1000 times harder than aragonite and about 40 times harder than concrete.[62] The organic matrix of mollusc shells is composed of β-chitin, silk-like proteins, and acidic glycoproteins rich in aspartic acid.[63, 64] The shell of the fresh-water snail *Biomphalaria glabrata* contains up to 1 wt% of organic material (water soluble and insoluble matrix) and shows the hardness of steel.[65] Aizenberg *et al.* conducted a comparative study of the effect of biological macromolecules in sea urchin spines consisting of calcite and synthetic calcite crystals, visualizing the changes in the material by the incorporation of proteins in the biomineral.[66]

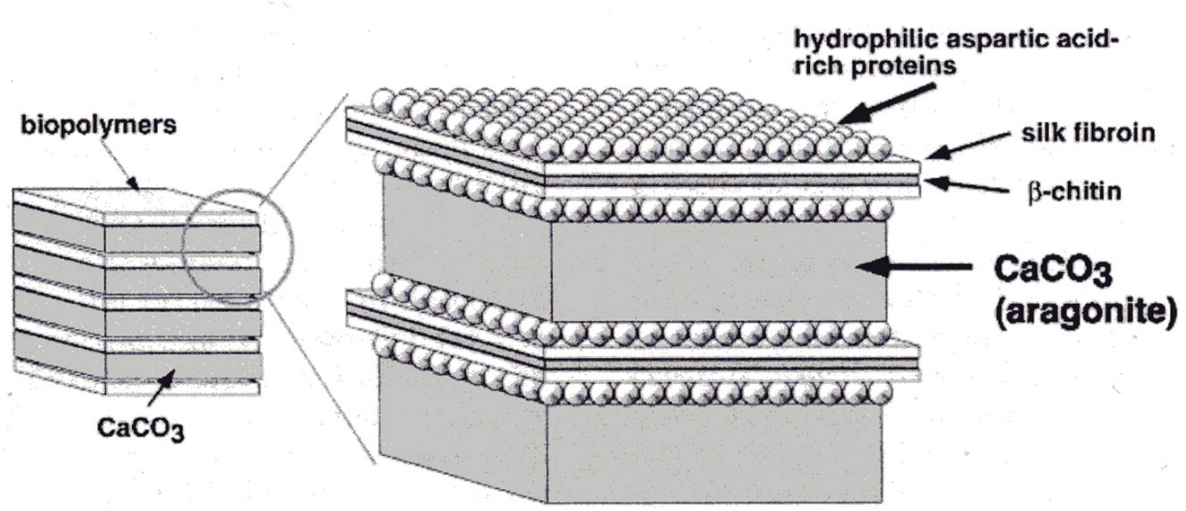

Fig. 2.1-7: A schematic representation of the structure of nacre as given by Naka *et al.*[61] Between layers of insoluble matrix consisting of β-chitin and silk fibroin on which hydrophilic acididc proteins are adsorbed, the mineral is deposited.

Biominerals can be roughly divided into three types, based on the organisation of the mineral constituent.[23] The first type comprises materials like teeth, bone, and various shells which are composed of multicrystalline arrays. Individual crystals in these arrays are generally all aligned in one direction, and often in all three dimensions. Biominerals consisting of single crystals or a limited array of relatively large crystals, make up the second type. This is true for the sea urchin spicules, which consist of single crystals of calcite as do the gravity sensor statoliths in medusae (see chapter 3.1). The third type of biominerals contains amorphous material. The most prominent example is silica structures found in animals and plants. Nowadays, much research focuses on amorphous calcium carbonate.

2.2 Calcium carbonate

2.2.1 The ions involved

Calcium is an earth-alkaline element with the atomic number 20. It is one of the five most abundant elements and the third most frequent metal after aluminium and iron. The name calcium is derived from the Latin word *calx* which means limestone. Its chemical properties are similar to those of barium and strontium. Calcium forms two-valence ions with a radius of 0.99 Å, yet it lacks both redox capability and flexible coordination geometry. In water, calcium forms hydrate complexes of the form $[Ca(H_2O)_6]^{2+}$. Many biominerals consist of calcium minerals. Calcium compounds play an important role in many cellular processes such as in nerve signal propagation and in muscle contraction. In plants, calcium serves an important function as a growth factor. Too low or too high concentrations of calcium can be toxic to living organisms, therefore, its concentration in biological systems is closely monitored and regulated. Examples of geological compounds containing calcium include carbonates (calcspar, dolomite), sulphates (gypsum) and phosphates (apatite). It is also found in many silicates.

Carbonates are the esters and salts of carbonic acid, usually appearing in the form of poorly water-soluble carbonates $M^{II}CO_3$ and the more soluble hydrogen carbonates $M^{I}HCO_3$. The most common of these are the calcium carbonates, such as calcite (calcspar, $CaCO_3$) and dolomite, $CaMg(CO_3)_2$. Under the influence of heat, they decompose into the corresponding metal oxide and carbon dioxide at about 600°C. Carbonates are basic salts and are decomposed by acids at pH<4 while forming carbon dioxide. The carbonate ion is planar and shows a O-C-O bond angle of 120°. The average C-O bond distance is 1.3 Å, but the maximum diameter of the ion is greater than 2.6 Å. Carbonic acid H_2CO_3 is a two-proton acid first isolated by Loerting *at al.*[67] In aqueous solution, carbonic acid is in equilibrium with hydrated carbon dioxide[68]:

$CO_2 + H_2O \rightarrow H_2CO_3$ $pK_S=3.2$

$H_2CO_3 + H_2O \rightarrow H_3O^+ + HCO_3^-$ $pK_S=3.3$

$CO_2 + 2\ H_2O \rightarrow H_3O^+ + HCO_3^-$ $pK_S=6.35$

$HCO_3^- + H_2O \rightarrow H_3O^+ + CO_3^{2-}$ $pK_S=10.33$

Mixtures of carbon dioxide and hydrogen carbonate form buffers in the range of pH 7-7.5. In solutions of carbonates, a pH-dependent concentration ratio of carbonate ions to hydrogen carbonate ions evolves.

2.2.2 The polymorph phases of calcium carbonate

Calcium carbonate is a poorly water-soluble salt which can be found in five crystalline polymorphic phases and in one amorphous phase in biominerals. Polymorphs or modifications of a mineral result when a substance can form different crystal structures. Calcium carbonate appears in three water-free modifications: calcite, aragonite, and vaterite, with calcite being the most thermodynamically stable, and vaterite the most unstable. Two water-containing phases are also known, namely, monohydrocalcite and ikaite. Table 2.2-1 summarizes crystallographic and physical data of the different crystalline phases.

The precipitation of calcium carbonate from aqueous solution was monitored by Sawada.[69] First, amorphous calcium carbonate forms which gradually transforms into calcite and vaterite. The latter then recrystallises into calcite. Both transformations constitute recrystallisation processes, while the formation of calcite is the rate-determining step. With increasing temperature, the formation of calcite is reduced, in favour of the precipitation of vaterite and aragonite. However, all phases are finally transformed into calcite. The transformation of aragonite to calcite results from the dissolution of aragonite and the re-precipitation of calcite. The presence of inhibitors may prevent calcite formation at any step.

Tab. 2.2-1: Crystallographic and physical data of the different calcium carbonate phases. These data were taken for reference throughout this work if a calcium carbonate phase is concerned.

Property	Calcite	Aragonite	Vaterite	Monohydro-calcite	Ikaite
formula	$CaCO_3$	$CaCO_3$	$CaCO_3$	$CaCO_3 \cdot H_2O$	$CaCO_3 \cdot 6\ H_2O$
space group	$R\ \bar{3}\ c$[70] (167)	$P\ mcn$[71] (62)	$P\ 6_3/mmc$[72] (194)	$P\ 3_1$[73] (144)	$C\ 2/c$[74] (15)
crystal system	trigonal	orthorhombic	hexagonal	hexagonal	monoclinic
lattice constants / Å	a=b=4.991 c=17.062 γ=120°	a=4.959 b=7.964 c=5.738 α=β=γ=90°	a=b=4.130 c=8.490 γ=120°	a=b=10.5536 c=7.5446 γ=120°	a=8.792 b=8.312 c=11.021 β=110.53°
density / g·cm^3	2.71	2.93	2.65	2.43	1.83
abundance	very common	common	rare	rare	very rare
ICDD-Reference	81-2027	76-0606	72-0506	83-1923	75-1733

Calcium carbonate precipitation is important for many natural and synthetic processes. As mentioned in chapter 2.1.4, this biomineral is the base material for sediments of either modern or ancient oceans. The precipitation of calcium carbonate in the oceans largely determines the carbon dioxide equilibrium of the atmosphere. Additionally, calcium carbonate, together with magnesium carbonate, contributes to the hard water phenomenon in heating installations. This phenomenon is based on the relatively low solubility of calcium carbonate in comparison to calcium hydrogen carbonate. In water containing carbon dioxide, calcium carbonate forms the more soluble calcium hydrogen carbonate according to:

$$CaCO_3 + CO_2 + H_2O \rightarrow Ca(HCO_3)_2$$

Heating this solution leads to the removal of carbon dioxide from water and the formation of the less soluble calcium carbonate which precipitates inside heating installations. Furthermore, the calcium carbonate-induced hardness of water also reduces the effectiveness of detergents. It causes the formation of calcium salts

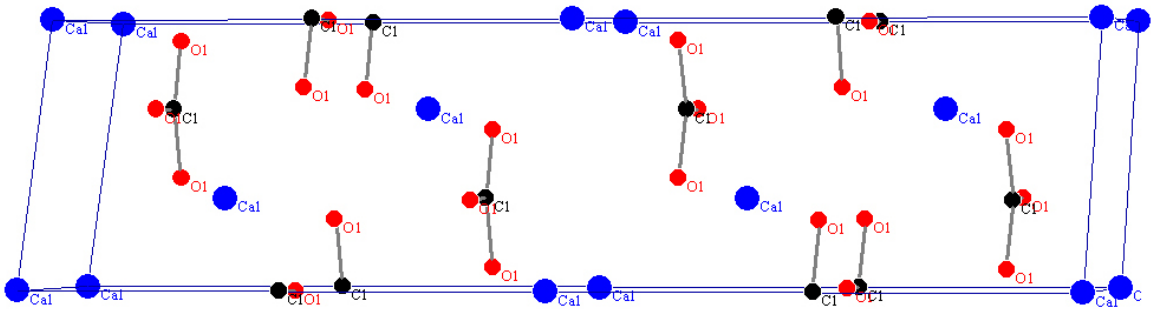

Fig. 2.2-1: The unit cell of calcite in the *bc*-plane.

of weak fatty acids from the detergent's compounds, thus reducing the concentration of active detergents.

The precipitation of calcium carbonate at temperatures below 29°C results in the formation of calcite, the most stable and abundant phase.[68] It usually forms small rhombohedral crystals. Calcite shows an anisotropic refraction index and is famous for its ability to divide an incoming beam of light into two polarised beams. These two beams are refracted differentially, resulting in the display of two separate images through a single calcite crystal. However, this is only one of many different varieties in which calcite can be found. It is known to be the most variable mineral.[7] Geological formations of calcite can be found on Iceland, in the US and in Germany. Figure 2.2-1 shows the unit cell of calcite in (100) projection. This view does not permit the identification of the threefold symmetry, but does show the packing of the ions more clearly. Kinetics and mechanisms of calcite growth are discussed in detail by Gutjahr.[17] It decomposes at about 600°C while releasing of carbon dioxide and calcium oxide. The exact decomposition temperature depends on the prevailing carbon dioxide partial pressure.

Calcite may also appear as a mixed crystal containing magnesium. However, the incorporation of magnesium ions into the calcite crystal lattice is not favoured, because the magnesium ion has a smaller diameter than the calcium ion.[68] Therefore, crystal mixtures with only a maximum of 30 mol% magnesium can be obtained from aqueous solutions with high *Mg:Ca* ratios under ambient

conditions.[75, 76] These high concentrations of magnesium also induce the formation of aragonite in which magnesium is not incorporated.[77] The Mg^{2+} ion is more hydrated than the Ca^{2+} ion and is easily adsorbed on the surface of a growing calcite crystal, thus poisoning active growth sites. Magnesium calcite with an amount of magnesium greater than about 10 mol% is more soluble than aragonite and is therefore thermodynamically unstable with respect to this phase.[78] Therefore, magnesium calcites are most commonly found as geological minerals or as biominerals. The most important of these geological minerals is dolomite, a *50:50* solid solution of calcite and magnesite ($MgCO_3$).

The disturbance resulting from the incorporation of magnesium into the calcite lattice also affects the infrared absorption behaviour of magnesium calcite.[79] The υ_4 band (713 cm^{-1} in calcite) undergoes a frequency shift up to 730 cm^{-1} in dolomite. In contrast to the XRD case, there is no quantification of this shifting-effect possible, because mass and size effects are antagonizing forces whose strengths depend on magnesium content.[79] Substitution of calcium by magnesium results in a smaller unit cell. In order to determine the magnesium content of calcite, Goldsmith *et al*. have quantified this effect by correlating cell parameters and magnesium content (see appendix).[80]

The next important calcium carbonate phase is aragonite which can be precipitated from aqueous solution at temperatures above 29°C, usually forming needle-like crystals. Aragonite is a common biomineral and is found often as the material of which pearls are made. Its unit cell is shown in Figure 2.2-2. This phase is found in geological formations and often forms outside its experimentally determined thermodynamic boundaries. Aside from a lower activation energy necessary for aragonite formation, this might be explained crystallographically. Carbonates of two valence cations with radii between 0.78 and 1.00 Å usually crystallise in hexagonal space groups (calcite, trigonal) whereas carbonates of two valence ions with radii between 1.00 and 1.43 Å

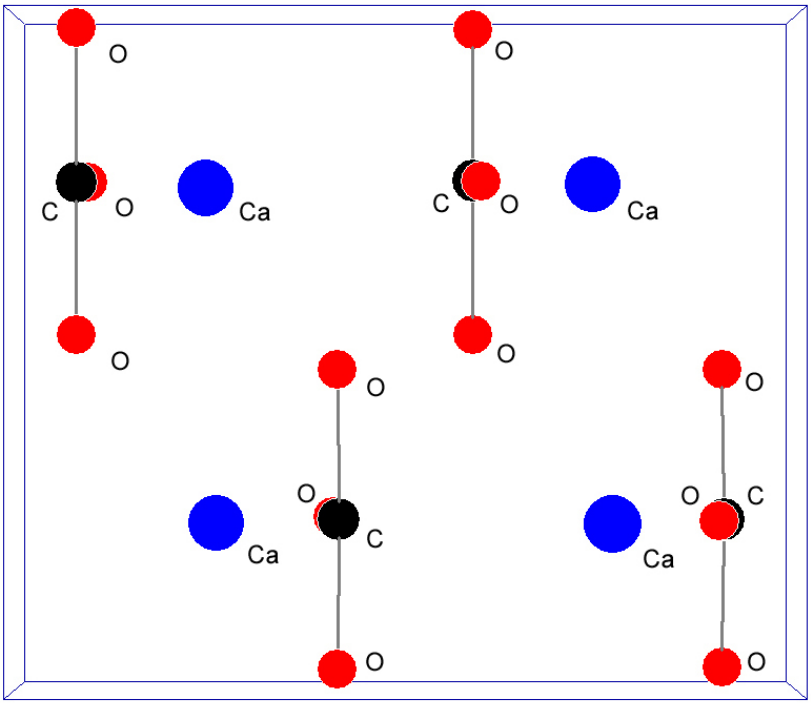

Fig. 2.2-2: The unit cell of aragonite in the *ab*-plane.

usually crystallise in orthorhombic space groups (aragonite).[68] Calcium which has an ion radius of 0.99 Å is at the boundary of the estimations above, allowing energetically favourable formation of both crystal structures. Aragonite transforms endothermically into calcite at 455°C.[81] Like biologically formed calcite, biologically formed aragonite may contain magnesium which affects the υ_2 doublet position.[82]

The least stable water-free calcium carbonate modification is vaterite. In the presence of ammonium or rare-earth element ions, it is formed in rather high quantities. However, structural data of vaterite is rather poor, as it forms very disordered crystals, and therefore no single crystal structure of vaterite has been determined. Vaterite transforms rapidly into calcite by an exothermic process, and thus it is not easily precipitated from aqueous solution. Exact thermodynamic data of this phase is still under debate.[83, 84] Geological formations of vaterite are unknown. Likewise, vaterite is not found as a distinctive biomineral, but is present in differing quantities in sponges of marine organisms[1] and mollusc shells[85] such as *Biomphalaria glabrata* (Pulmonata)[65].

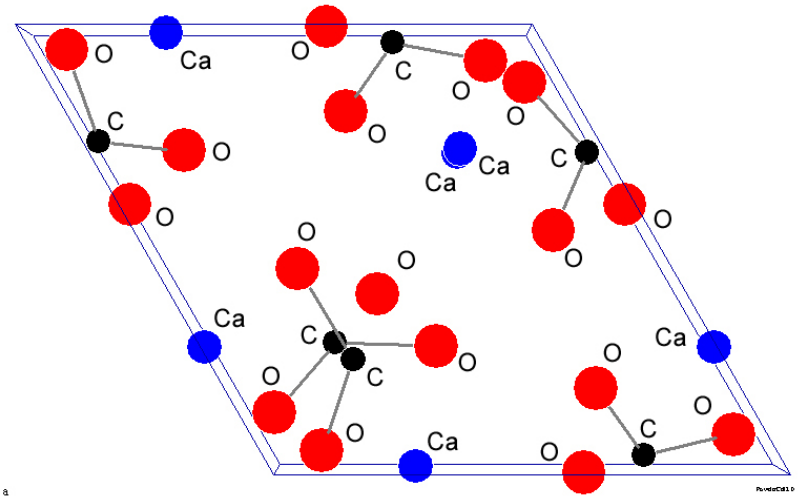

Fig. 2.2-3: The unit cell of monohydrocalcite in the *ab*-plane.

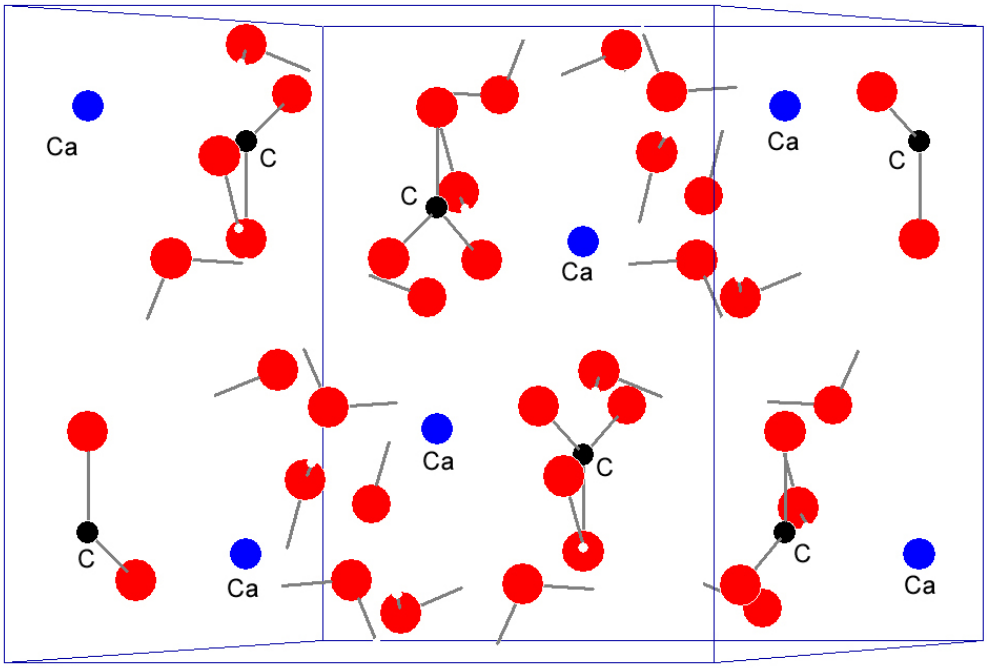

Fig. 2.2-4: The unit cell of ikaite in the *ab*-plane. The oxygene atoms are not indicated.

Two hydrated calcium carbonate phases are known: monohydrocalcite, and the extremely rare ikaite. Monohydrocalcite $CaCO_3 \cdot H_2O$ can be found in geological formations in the Australian desert. In contact with water, it rapidly transforms into calcite. However, it was found as a biomineral in fish[86] and in bladder stones of guinea pigs[87]. In the presence of magnesium, it can be synthesised at room temperature.[88] It is also formed on crystallisation of amorphous calcium carbonate in a magnesium containing solution.[89] Figure 2.2-3 shows its

elementary cell. The much rarer ikaite $CaCO_3 \cdot 6\ H_2O$ may form if submarine basic phosphate-rich fresh-water mixes with sea water.[90] However, it can be synthesised without any additives from aqueous solution and is stabilised by polyphosphate and magnesium.[89] Nevertheless, it easily transforms into calcite. No reports of ikaite as a biomineral are known. Figure 2.2-4 shows the unit cell of ikaite.

2.2.3 Amorphous calcium carbonate

Amorphous calcium carbonate (ACC) was first synthesised by Johnston *et al*. by mixing concentrated solutions of calcium chloride and sodium carbonate, and was described as non-crystalline, similar to an under-cooled liquid.[91] ACC solubility was first determined by Brecevic[92] and later verified by Clarkson *et al.*[93] Specifically, they found that it is much more soluble than vaterite, aragonite, and calcite (see Table 2.2-2).[94] Precipitated ACC is more stable at lower temperatures, whereas increasing the precipitation temperature results in rapidly crystallising material.[69] Dorfmüller found an increasing alkalinity of the mother liquor to stabilise the amorphous material.[95] Koga *et al.* quantified this observation by determining transformation enthalpies for calcite as a function of mother liquor pH value.[96] Several methods for the precipitation of amorphous calcium carbonate are known, including bubbling carbon dioxide through a calcium salt solution[95, 97], mixing of saturated solutions of calcium salts and carbonate salts,[69, 91, 92, 96] or by hydrolysis of dimethylcarbonate in calcium salt solution.[98] A biomimetic approach of ACC synthesis was described by Loste *et al*. who precipitated ACC in a membrane by diffusion of calcium ions from one side and carbonate ions from the other

Table 2.2-2: Solubility and calcium saturation concentration of ACC[92] and the water-free modifications of calcium carbonate[94].

phase	solubility $\cdot 10^{-9}$ (mol l^{-1})^2	concentration mmol l^{-1}
ACC	400	0.632
vaterite	12	0.109
aragonite	4,6	0.068
calcite	3,3	0.057

side.[99] However, the physical properties of this state depend on the size of the particles and thus depend on the method of preparation, the material age and stabilisation.

The amorphous state can be stabilised by several methods. One of these includes increasing the magnesium content of ACC, which consequently reduces its solubility.[99-102] The magnesium content also directly affects the crystalline phase formed during aging and the morphology of this phase. The synthesis of high-Mg calcites was enabled first by precipitating Mg-containing ACC. Additionally, the presence of triphosphate ions stabilises the amorphous state.[93] The crystallisation of ACC can be prevented by synthetic organic additives. Precipitation of ACC in the presence of functionalised poly(propylenimin)-dendrimeres[103-105], hydrophilic blockcopolymers[106], or diphosphate-substituted poly(ethylene glycol)[107] results in material stable over longer time periods, even in aqueous solution. Gal *et al.* examined the solubility of calcium carbonate polymorphs and the order of appearance of the different phases during transition to calcite with respect to the ion pair formation $CaCO_3 \cdot H_2O$.[108] The interaction of the uncharged hydrated ion pairs with an inhibitor determines the polymorphic phase to form.

Biologically, ACC is a more common material than would be expected, considering its instability. It fulfils two roles in biomineralisation. First, it serves as a precursor phase during the formation of other biomineral phases. This has been shown for the growth of spicules in sea urchin larvae of different species[109, 110], as well as in the first stages of precipitation of the later aragonitic shell of snail embryos.[65, 111] Specifically, these structures are first precipitated in the form of ACC, which then crystallises. The second role of ACC in biomineralisation is a storage phase for calcium carbonate, as it is often found in crustaceans[112] (see chapters 3.2 and 3.3 for more information), and, to a lesser degree, in plants. Intracellular calcified bodies (cystoliths) are found in great

numbers in the leaves of higher plants of the genus *Ficus*[113, 114] although their function in plants is still controversial.

In order to understand biological ACC precipitation, several experiments have been executed. Inspired by the observed role as transient phase, Xu *et al*[115] used polyacrylate to stabilise a thin film of ACC on a monolayer of amphipathic carboxylated diphorphyrin templates. They succeeded in transforming it into a polycrystalline film of calcite. Aizenberg *et al*. obtained a single crystal of calcite by incorporating a calcite nucleation site on the substrate on which ACC was precipitated.[116] Additionally, transient phases of ACC were stabilised by the precipitation of calcium carbonate in the presence of biological macromolecules extracted from ACC biominerals. Raz *et al.* showed that proteins extracted from amorphous phase of sea urchin spicules, in the presence of magnesium, induced the precipitation of ACC, while proteins extracted from calcitic phase of spicules lead to the formation of calcite.[110] In the same artificial, insoluble matrix consisting of β-chitin and silk fibroin, ACC crystallisation is either directed towards aragonite or calcite, depending on the source from which the proteins were extracted. The exact control exercised by organisms during mineralisation is clearly seen in ascidian skeletons which consist of distinctive layers of calcite and amorphous calcium carbonate, separated by membranes.[117-119] Thus one can appreciate the importance of the organic matrix in biomineralisation.[120, 121]

However, the amorphous state of calcium carbonate is defined only by the absence of crystallinity - a rather inadequate definition. In the solid state of calcium carbonate, many arrangements of close range order are possible, in contrast to crystalline behaviour, which exhibits ordered, long-range three-dimensional order. This variability of ACC short-range structure results in differences between biogenic amorphous calcium carbonate phases in different organisms.[114] While stable biominerals of ACC in lobster (Crustacea), ascidian spicules, and plant cystoliths show the same composition of $CaCO_3 \cdot H_2O$ (similar

but not identical to monohydrocalcite), all ACC samples show different short-range environments around calcium atoms as determined by extended X-ray absorption fine structure (EXAFS) spectroscopy. Moreover, the transient ACC phase observed in the freshwater snail *Biomphalaria glabrata* shows an entirely different behaviour.[65] Raman and infrared spectroscopy studies indicate a difference in structure between transient and stable ACC phases.[122] Transient phases seem to be more ordered than in stable phases, as though in preparation for the phase into which they will transform. The former are stabilised by a higher amount of incorporated magnesium and phosphate ions than in transient phases. Both types of ACC are stabilised by organic matrix. It is assumed that stable forms of ACC contain water molecules whereas the transient phases do not.

2.3 Calcium phosphate

2.3.1 The phosphate ion

Phosphates are the esters and salts of the medium-strength phosphoric acid H_3PO_4. This group includes many different kinds of acids: ortho acids H_3PO_n n=2-6, meta acids HPO_{n-1} n=3,4, and diacids: $H_4P_2O_n$ n=4-8.[68] The phosphate ion exhibits tetrahedral symmetry, with phosphorous in the centre and oxygen at the corners. The primary phosphates ($M^IH_2PO_4$; dihydrogen phosphates) are all soluble in water, while secondary ($M_2^IHPO_4$; hydrogen phosphates) and tertiary phosphates ($M_3^IPO_4$) are water soluble only if M is an alkali metal. Phosphate ions are only found in very basic solutions. Under biological conditions dihydrogen phosphate and monohydrogen phosphate ions are present:

$$H_3PO_4 + H_2O \rightarrow H_3O^+ + H_2PO_4^- \qquad pK_{S1}=2.161$$
$$H_2PO_4^- + H_2O \rightarrow H_3O^+ + HPO_4^{2-} \qquad pK_{S2}=7.207$$
$$HPO_4^{2-} + H_2O \rightarrow H_3O^+ + PO_4^{3-} \qquad pK_{S2}=12.325$$

The phosphate ion concentration depends on the pH and serves as a very effective buffer at physiological pH of 7.4 (~pK_{S2}).

Hydrogen phosphates are rarely found in geological formations, although they are common for industrial and biological purposes. Industrially, calcium dihydrogen phosphate $Ca(H_2PO_4)_2$ and hydroxyapatite $Ca_5(PO_4)_3(OH)$ are used as additives to salt, sugar, baking powder, and fertilizers. Likewise, calcium hydrogen phosphate $CaHPO_4$ is also a very important component of fertilisers. Triscalcium phosphate $Ca_3(PO_4)_2$ is insoluble and transforms slowly into the more soluble hydroxyapatite. Hydroxyapatite is the most prominent calcium phosphate biomineral, forming vertebrate bones and teeth. Phosphate esters are very important in biology, e.g. in form of adenosine triphosphate (ATP), whose exothermic dephosphorylation reaction serves as energy source, or in nucleic

acids, which contain monophopshate diesters as bonding bridges between nucleoside subunits.

2.3.2 Calcium phosphates

Thermodynamically, hydroxyapatite (HAP) is the most stable calcium phosphate phase even at pH values as acidic as 4.5. Still, both pH and kinetic factors are very important during calcium phosphate precipitation. Table 2.3-1 lists the most common calcium phosphates of which hydroxyapatite is the most important here. The two HAP polymorphs listed have no distinct names.[123] Of these, the more stable form under ambient conditions crystallises in space group $P\,6_3/m$ (No. 176), whilst the other is very rare, and crystallises in space group $P\,2_1/b$ (No. 14, setting 8). Note also that the monoclinic polymorph has not been precipitated from aqueous solution and is only accessible under high temperature conditions.[124] The elementary cell of the hexagonal apatite structure is given in Figure 2.3-1; Table 2.3-2 lists the crystallographic data of both phases.

Chemically, the hydroxy group of hydroxyapatite is easily substituted, because it is positioned in the crystal lattice in a channel formed by a structure determined by calcium and phosphate ions. This feature allows a rather easy exchange of

Table 2.3-1: Names and identification of the most prominent calcium phosphates.[123] The phases are given in order of their solubility in water.

Name	Abbreviation	Formula	Mineral	*Ca:P* ratio
Amorphous calcium phosphate	ACP	?	-	?
Dicalcium phosphate anhydrite	DCPA	$CaHPO_4$	Monetite	1.0
Dicalcium phosphate dihydrate	DCPD	$CaHPO_4{\cdot}2\,H_2O$	Brushite	1.0
α-Tricalcium phosphate	α-TCP	$\alpha\text{-}Ca_3(PO_4)_2$	-	1.5
β-Tricalcium phosphate	β-TCP	$\beta\text{-}Ca_3(PO_4)_2$	Whitlockite	1.5
Octacalcium phosphate	OCP	$Ca_8H_2(PO_4)_6{\cdot}5\,H_2O$	-	1.33
Pentacalcium hydroxyl apatite	HAP	$Ca_{10}(PO_4)_6(OH)_2$	Hydroxyapatite	1.67

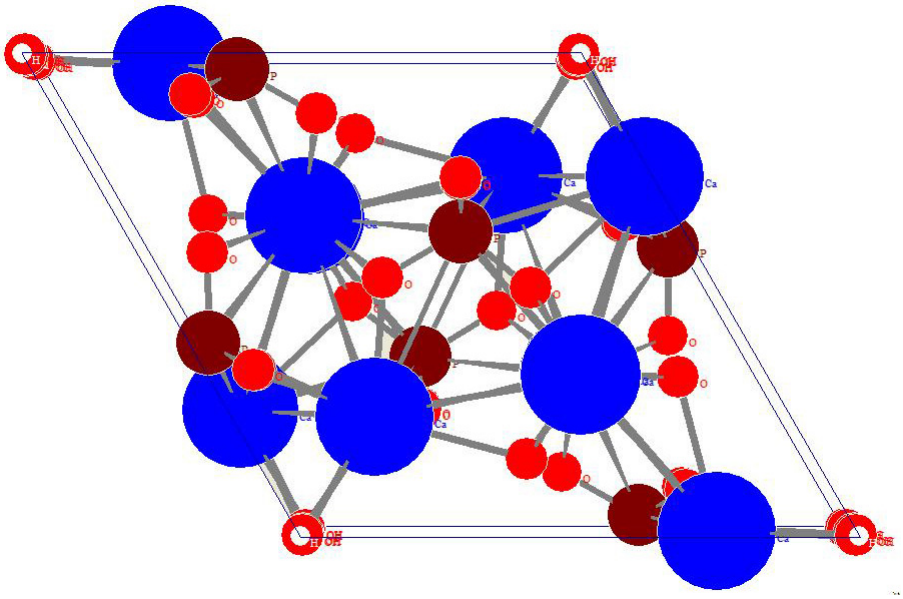

Fig. 2.3-1: The unit cell of the hexagonal and common form of hydroxyapatite in the *ab*-plane. The big atoms represent calcium, the medium atoms represent phosphorous, and the smallest atoms represent oxygene.

ions, especially of fluorine and chlorine. However, this substitution is not easily detected, because the XRD patterns of all three substances are nearly identical, showing only differences in peak intensity which could also be related to measurement conditions. In IR spectra, hydroxyapatite can be identified by a characteristic O-H absorption peak at about 3500 cm^{-1} and in the fingerprint area of the spectrum at about 630 cm^{-1}.

Another important exchange ion is carbonate CO_3^{2-} which leads to the formation of one of two kinds of carbonate apatites. It can replace either the OH^--groups (A-type) or PO_4^{3-}-groups (B-type) of HAP. The A-type carbonate apatite forms

Tab. 2.3-2: Crystallographic and physical data of hydroxyapatite. The data of the hexagonal phase was taken for reference throughout this work if hydroxyapatite is concerned.

Property	Hydroxyapatite	Hydroxyapatite
formula	$Ca_{10}(PO_4)_6(OH)_2$	$Ca_{10}(PO_4)_6(OH)_2$
space group	$P\,6_3/m$	$P\,2_1/b$[123]
	(176)	(14, setting 3)
crystal system	hexagonal	monoclinic
lattice constants [Å]	a=b=9.418	a=9.4214 b=18.8428
	c=6.884	c=6.8814
	γ=120°	γ=120°
density [g·cm^3]	3.16	3.16
abundance	very common	very rare
ICDD-Reference	09-0432	76-0694

under dry conditions at high temperatures in the presence of carbon dioxide. The B-type, on the other hand, is a precipitation product, but shows a much lower carbonate content compared to A-type carbonate apatites. Carbonate apatite can be identified in the IR spectrum by C-O vibration bands. The A-type shows bands at 1410-1450 cm^{-1}, whereas the B-type shows bands at 871 cm^{-1}, 1423 cm^{-1}, and 1493 cm^{-1}. Carbonate apatite is found in considerable quantities in apatite biominerals, especially bone. Under the influence of heat, the carbonate group decomposes, leaving hydroxyapatite as residue.

While less supersaturated solutions will directly lead to the formation of HAP,[125] the crystallisation of hydroxyapatite from highly supersaturated solution proceeds through an amorphous calcium phosphate (ACP) phase. ACP shows *Ca:P* ratios smaller than 1.3 or higher than 1.7, depending on the extent of mother liquor supersaturation. Defect apatites are more common precipitation products and are characterised by *Ca:P* ratios of 1.5 to 1.66, in contrast to the ratio 1.67 seen in HAP. These ratios demonstrate the difficulty in formation of stoichiometric apatites.

As there are many calcium phosphates, there may also be many amorphous calcium phosphates with different coordination environments of calcium. Therefore, IR spectra of ACP show broad, diffuse, absorption bands. The precipitation of ACP occurs in pH ranges of 6.6 to 10.6, but is inhibited to crystallise by Mg^{2+}, $P_2O_7^{4-}$ or CO_3^{2-}.[126] It was found as a part of the mineral phase in crustaceans[1, 127] and as a transient phase in the teeth of the chiton *Acanthopleura*.[128] The conversion from ACP to HAP in aqueous solution is fast and also possible in dry state[129] as well as under the influence of heat. However, it can be stabilised by proteins.[130]

2.4 Calcium sulphate

2.4.1 The sulphate ion

As with carbonates and phosphates, sulphates are the esters and salts of the corresponding sulphuric acid H_2SO_4. Like its counterpart phosphate, the sulphate ion has tetrahedral symmetry with sulphur in the centre and oxygen at the corners. Sulphur offers a variety of oxidation states, as phosphorous does, enabling the existence of a wide variety of sulphur (H_2SO_n n=1-4) and many disulphur ($H_2S_2O_n$ n=1-8) acids.[68] Sulphuric acid (H_2SO_4) is very strong, and hence readily releases protons in aqueous solution forming primary and secondary sulphates as follows:

$$H_2SO_4 + H_2O \rightarrow H_3O^+ + HSO_4^- \qquad pK_{S1}=-3$$
$$HSO_4^- + H_2O \rightarrow H_3O^+ + SO_4^{2-} \qquad pK_{S2}=1.87$$

Primary sulphates appear in the form of M^IHSO_4, are acidic salts and generally dissolve well in water. Likewise, secondary sulphates ($M_2^ISO_4$) are neutral salts and are also usually soluble in water. Some exceptions include sulphates of the elements calcium, barium, and strontium which are nearly insoluble. Secondary sulphates tend to form salts incorporating crystal water. One such example appears in minerals where sulphates often form double-salts called alums of the form $M^IM^{III}(SO_4)_2 \cdot 12\ H_2O$. In biology, sulphates serve several important functions. The protein chondroitin sulphate is a glycosaminoglycan (negatively charged polysaccharide) and a major component of cartilage. Additionally, biological waste molecules are often transferred into sulphuric acid esters in order to increase solubility.[7]

2.4.2 Calcium sulphates

Calcium sulphate is a very important geological mineral. It is found in three stable geological polymorphs defined by the content of water incorporated into

their crystal structures: $CaSO_4 \cdot 2\ H_2O$ (gypsum), $CaSO_4 \cdot 0.5\ H_2O$ (bassanite) and $CaSO_4$ (anhydrite). All three are used in the construction industry. An amorphous phase has also been proposed, but not yet confirmed as a biomineral. Table 2.4-1 lists the crystallographic data available for the calcium sulphate phases.

Gypsum is a common mineral found either in discrete deposits or together with other minerals. It is the thermodynamically stable product precipitated from aqueous solution under ambient conditions, or at temperatures up to 50°C. Industrially, it is produced by desulphuration of smoke gases. Both industrial and mined geological gypsum can undergo dehydratation by heating according to the following equation:

$$CaSO_4 \cdot 2\ H_2O \rightarrow CaSO_4 \cdot n\ H_2O + (2\text{-}n)\ H_2O\uparrow$$

The main products of this reaction are bassanite (n=0.48-0.67) and anhydrite (n=0) which are then used for construction, as "gypsum", mortar, and cement. The hardening process of this "gypsum" is often referred to as drying, but actually, it is the reincorporation of water into the dehydrated material. The

Tab. 2.4-1: Crystallographic and physical data of the different calcium sulphate phases. The data listed here are taken for reference if calcium sulphate phases are concerned.

Property	Gypsum	Bassanite	Anhydrite -III	Anhydrite -II	Anhydrite -I
formula	$CaSO_4 \cdot 2\ H_2O$	$CaSO_4 \cdot 0.5\ H_2O$	γ-$CaSO_4$	β-$CaSO_4$	α-$CaSO_4$
space group	*I* 2/*c*[131]	*I* 121[132]	*C* 222[133]	*A mma*[134]	*P* 31*c*[135]
	(15, setting 14)	(5, setting 13)	(21)	(63)	(159)
crystal system	monoclinic	monoclinic	orthorhombic	orthorhombic	trigonal
lattice constants / Å	a=5.679 b=15.202 c=6.522 β=118.4°	a=12.028 b=6.931 c=12.692 β=90.2°	a=12.078 b=6.972 c=6.304 α=β=γ=90°	a=7.006 b=6.998 c=6.245 α=β=γ=90°	a=b=5.064 c=7.978 γ=120°
density /g·cm^3	2.31	2.73	2.56	2.95	-
abundance	very common	rare	rare	artificial	artificial
ICDD-Reference	74-1433	81-1849	83-0437	72-0916	-

formed gypsum crystallites hold the cement together, hence its use in the construction industry. This process and its derivates cover a whole branch of literature which exceeds the scope of this thesis. For review, see the theses of Freyer[136] and Oetzel[137] who investigated the connections of the different calcium sulphate phases and water. Gypsum shows a structure composed of double layers of CaO_8-polyhedra whose terminal oxygen atoms belong either to irregular SO_4-tetrahedra or to water molecules.[131] Between the CaO_8-polyhedra is a layer of water molecules. The chains of CaO_8-polyhedra are held together by relatively weak H-bond bridges, allowing easy splitting of gypsum crystals along the (010) plane. Figure 2.4-1 shows the unit cell of gypsum along the 010-axis, illustrating the planes of polyhedra and water. Gypsum is thermally stable up to about 80°C, when water begins to leave the crystal structure. Depending on the exact temperature, bassanite or anhydrite forms.

Bassanite is a natural mineral found in dry regions of earth. The exact structure of bassanite was long in debate and even today, no single crystal data from untwined crystals exist. Figure 2.4-2 shows the unit cell structure, as determined by Abriel and Nesper.[132] Under the influence of air humidity, it incorporates water and transforms into gypsum exothermically. This reaction is known, for example, in the setting of plaster. The loss or addition of water, from or to the crystal, induces a major change in structure. Unlike in gypsum, the water molecules in bassanite are not arranged in layers, but are found in channels formed by the CaO_8-polyhedra and SO_4-tetrahedra. This filling of the channels with water molecules reduces symmetry. These channels form the base structure for all structures of $CaSO_4 \cdot n\ H_2O$ with n=0-0.67 and show an overall hexagonal (trigonal) structure. This trigonal super-symmetry is described by the space group $P\ 3_121$, and is caused by the backbone of the structure.[132] The structure of bassanite is monoclinic, but the monocline angle of β=90.2° shows only slight divergence from orthorhombic symmetry.

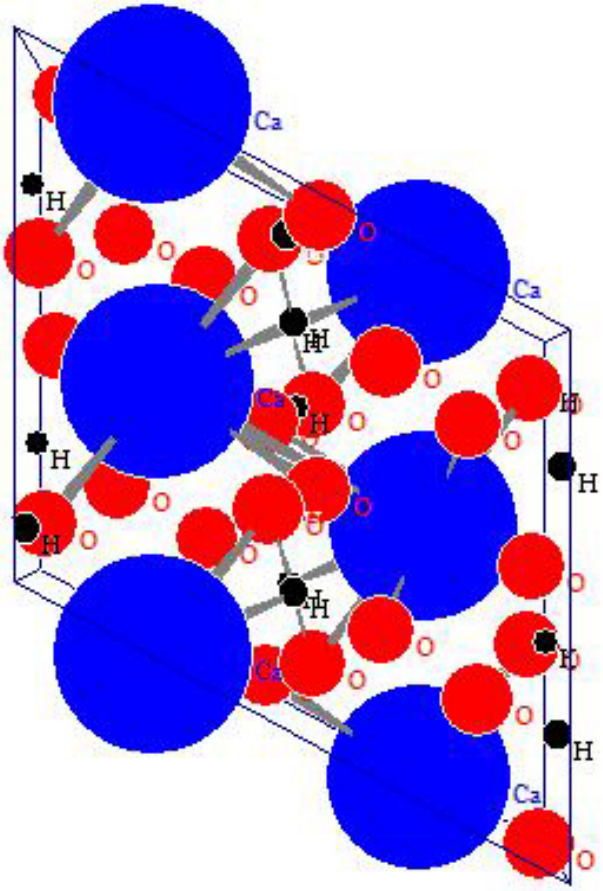

Fig. 2.4-1: The unit cell of gypsum in the *ab*-plane.

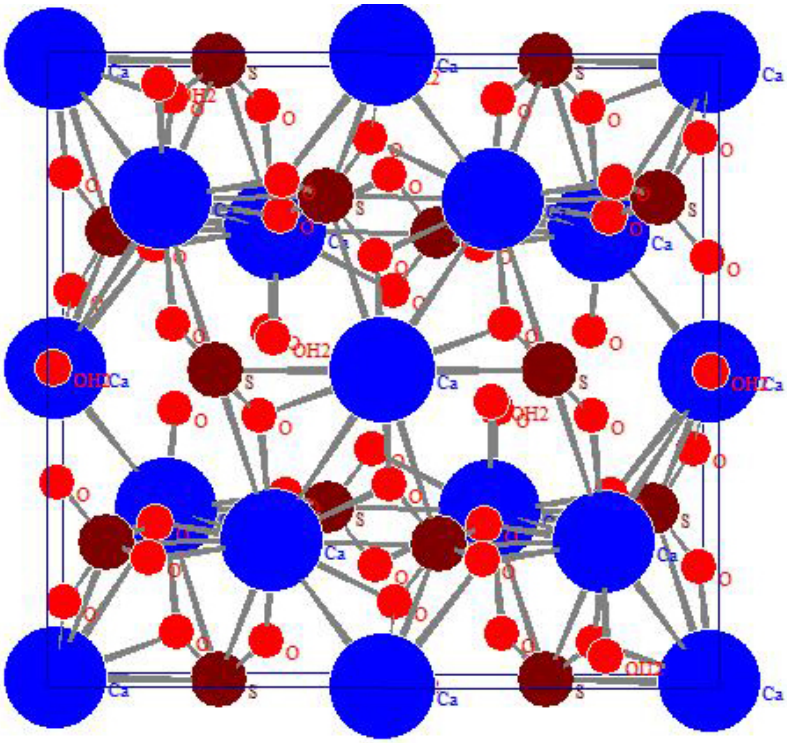

Fig. 2.4-2: The unit cell of bassanite in the *ab*-plane.

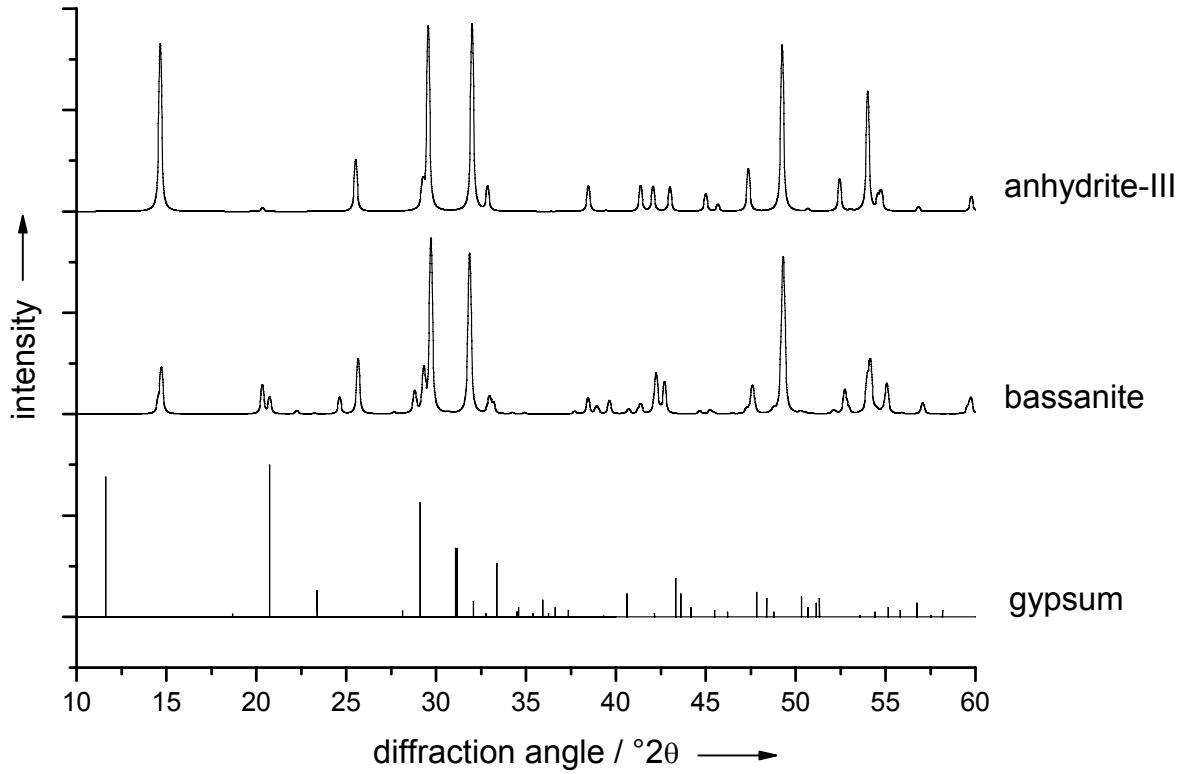

Fig. 2.4-3: Powder X-ray diffraction patterns of the three most important polymorphs of calcium sulphate. The water-deficient bassanite and the water-free anhydrite-III show very similar patterns, not easily distinguished.

Anhydrite exists in three distinct forms. Natural anhydrite-III is a low temperature phase and can be found in mineral deposits along with gypsum. It is water soluble and used in the construction industry. Solubility is possible due to rapid rehydratation and solvation of gypsum. Anhydrite-III is formed by the heating of bassanite to about 90°C. The content of anhydrite in bassanite determines some of the properties of construction "gypsum". As stated above, the crystal structures of bassanite and anhydrite-III are very similar. This leads to very similar powder diffractograms; only in some low intensity peaks do the diffractograms of bassanite and anhydrite-III differ. Figure 2.4-3 shows X-.ray diffractograms of gypsum, bassanite, and anhydrite-III. The data have been created with PowderCell V 2.3 simulating a Cu-Kα_1-radiation source in Bragg-Brentano geometry using a monochromator (d=3.343) in the range of 10-60°2Θ in steps of 0.01°2Θ using the structure references given in Table 2.4-1.[138] Figure 2.4-4 shows the elementary cell of anhydrite-III.

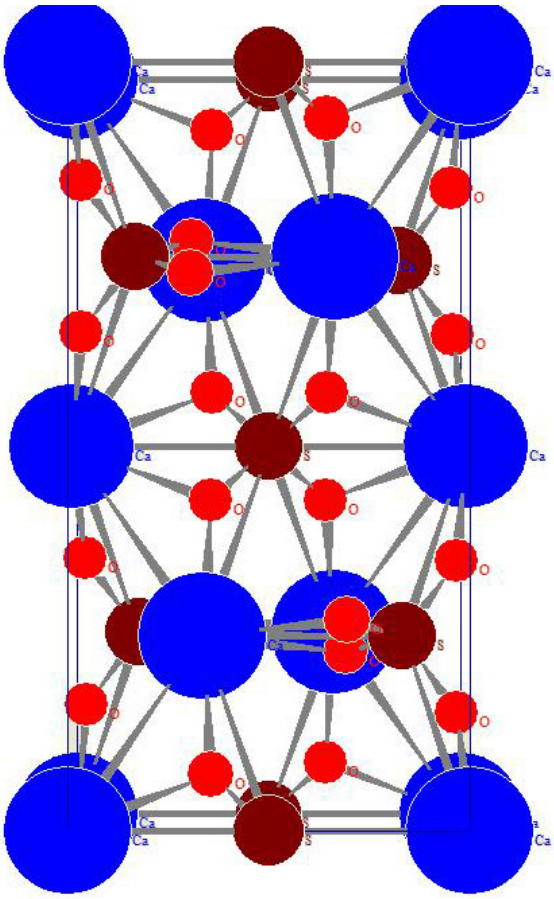

Fig. 2.4-4: The unit cell of anhydrite-III in the *ab*-plane.

The continued heating of anhydrite-III leads to the formation anhydrite-II. This is an irreversible reaction and a real phase transition because no water leaves the structure. The chains of polyhedrons of the anhydrite-II ions are connected over the edges and form a tight net. Anhydrite-II is a purely artificial product which occurs industrially by the overheating of gypsum – a process which is also referred to as "dead-burned gypsum". Anhydrite-I is the high-temperature modification of calcium sulphate and is formed at 1230°C. At about 1300°C, calcium sulphate decomposes into calcium oxide, sulphur dioxide, and molecular oxygen according to:

$$\alpha\text{-}CaSO_4 \rightarrow CaO + SO_2\uparrow + 0.5\ O_2\uparrow$$

3. Structural determination of biominerals

3.1 Gravity sensing organs of medusae (jellyfish)

3.1.1 Jellyfish in biology

Jellyfish are marine animals that belong to the phylum Cnidaria. This name is derived from the Greek word *cnidos* which means stinging nettle, referring to the stinging cells called nematocysts that are found on the tentacles of all members of this phylum. These nematocysts are common to all cnidarians, and are presumed to have originated from a single common ancestor. When jellyfish are touched, most species eject barbed threads tipped with poison. Cnidarians are radially symmetric with one end of the animal bearing a mouth and tentacles. Some live attached to a surface with the mouth directed upwards (i.e. corals). Others, such as jellyfish, are free-swimming with the mouth directed downwards. Several thousand cnidarian species dwell in the oceans of the world, dispersed between the surface to the ocean floor. A smaller number of species are found in rivers and freshwater lakes.

The life cycle of the jellyfish consists of several stages. The first of these stages is the polyp, a stationary form in which the animal is attached to a surface. Polyps produce ephyra larvae by a mechanism of asexual reproduction called strobilation. The ephyrae then develop into adult free-swimming medusae. Finally, the medusae produce planula larvae that metamorphose into new polyps, starting the life cycle anew.

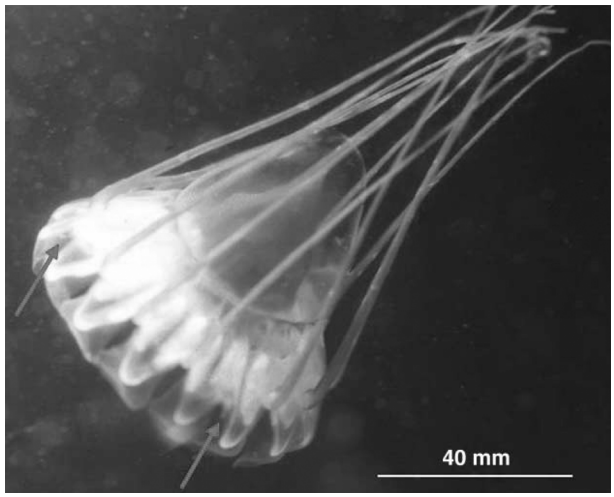

Fig. 3.1-1: The medusa *Peryphylla periphylla*. The arrows mark the positions of some rhophalia in the coronar ring. Medusae swim with the head pointing downwards. The picture is by courtesy of H. Tiemann.[2]

For orientation and navigation in the deep-sea, the free-swimming medusae use inorganic crystals in

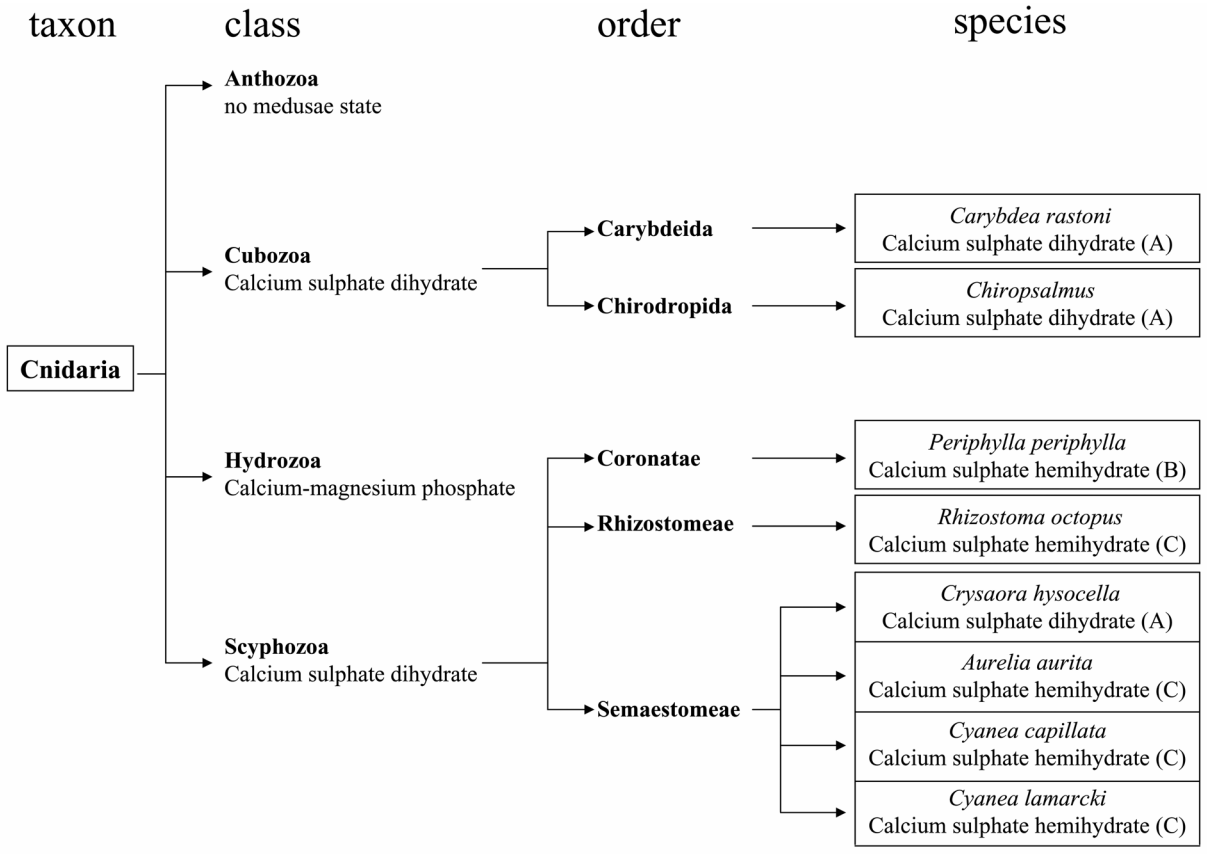

Fig. 3.1-2: Schematic overview of the phylogenetic relationships of the Cnidaria. The material of the statoliths in the rhopalia of species marked with (A) is given in literature. The statoliths of the species marked with (B) consists of calcium sulphate dihydrate (gypsum) according to literature. Our observations indicate calcium sulphate hemihydrate (bassanite) instead. The material of the species marked with (C) was examined in this study for the first time and identified as bassanite.

the form of statoliths. These probably serve as sensors for gravity and inertia, like otoliths in the ears of fish and mammals.[139] Agglomerates of statoliths are found in the responsible organs, called the rhopalia. The statoliths occur first in the youngest ephyra stage. Medusae possess fully grown statoliths. Figure 3.1-1 shows the location of the rhopalia in the ring of the scyphozoa medusa *Periphylla periphylla*.

The Cnidaria are divided into four classes: the Anthozoa, the Cubozoa, the Hydrozoa and the Scyphozoa. Figure 3.1-2 outlines the phylogenetic relations of species, orders, and classes in the taxon Cnidaria. Anthozoa include corals, anemones, and sea pens. These animals do not undergo a medusa stage; the polyp is their only generation.[140] Hydrozoa is the most diverse class and

includes siphonophores, hydroids and fire corals. This class differs from the other classes with medusa stage by a different medusa formation process as well as by different construction of their gravity sense organs.[139] The Cubozoa ("box jellies") and the Scyphozoa ("true" jellyfish) share many features, and thus are also referred to collectively as Rhopaliophora. However, they are divided into two classes because of their different life cycle.[141, 142] The class Scyphozoa includes many species and is divided further into four orders, three of them with free-swimming medusae: the Semaestomeae, the Coronatae, and the Rhizostomeae. The class Cubozoa, on the other hand, consists of only a few species. Animals from the class Scyphozoa are the subject of this work.

3.1.2 Calcium sulphate as inorganic material in statoliths

Calcium sulphate, regardless of the amount of water it contains, is rarely found as a product of biomineralisation processes.[1, 143] Besides the statoliths in medusae, it is known only in green algae of the family Desmidiaceae. In this family too, some species were reported to use calcium sulphate as a biomineral, possibly also as statoliths.[144] In addition, there were early reports of calcium sulphate in the genus *Closterium* of the Desmidiaceae family.[145] However, these crystals were later identified as barium sulphate with traces of strontium sulphate by Brook *et al.*[146]

So far, the biological literature has focused mostly on the life cycles and biology of jellyfish.[147] Literature on the statoliths in rhopalia and the material of which they consist is rather sparse. It is known that in contrast to those of the other classes, the statoliths of hydrozoa medusae (of the genera *Obelia*, *Lovenella*, *Phialidium*, *Phialella* and *Mitrocomella*; Hydroida; and the species *Aglantha digitale*; Trachylida) consist of calcium magnesium phosphate.[148, 149] Structural studies showed that statoliths of the scyphozoa medusae *Aurelia aurita* and *Chrysaora hysoscella* (Semaeostomeae) consist of calcium sulphate dihydrate ($CaSO_4 \cdot 2\ H_2O$; i.e. gypsum).[149-151] The statoliths of the species *Carybdea*

rastoni (Carybdeida) and *Chiropsalmus* (Chirodropida) of the class Cubozoa were also reported to be made of calcium sulphate dihydrate.[149, 152, 153] Surprisingly, however, our group and cooperation partners have recently identified calcium sulphate hemihydrate ($CaSO_4 \cdot 1/2\ H_2O$, i.e. bassanite) as the inorganic mineral of the statoliths of the scyphozoa medusa *Periphylla periphylla* (Coronatae).[2] Considering that after buoyancy correction, bassanite is about a third denser than gypsum, this could presumably support the theory of rhopalia functioning as gravity sensing organs. This should logically make a difference if used for gravity sensing.[83] This unexpected finding - a water-deficient phase as a biomineral of a deep-sea animal consisting mostly of water – promoted further investigation of the statoliths of medusae.

3.1.3 Calcium sulphate hemihydrate is the inorganic mineral in statoliths of scyphozoan medusae (Cnidaria)[154]

The presence of bassanite and the absence of gypsum in *Periphylla periphylla* led us to study whether calcium sulphate hemihydrate is also present in the statoliths of other scyphomedusae. Statoliths of animals of the three orders of the Scyphozoa comprising species with free-swimming medusae were investigated in order to enable more general statements about the phylogenetic status of the entire Scyphozoa class. Specifically, the scyphomedusae *Aurelia aurita, Cyanea capillata*, *Cyanea lamarcki* (order Semaestomeae), *Periphylla periphylla* (order Coronatae), and *Rhizostoma octopus* (order Rhizostomeae) were examined. The small size (typically of the order of 10-60 μm) and quantity (despite pooling the rhopalia) of the statoliths required the application of high-end structure sensitive tools such as scanning electron microscopy (SEM), energy-dispersive X-ray spectrometry (EDX), synchrotron powder diffraction (XRD), synchrotron single-crystal diffraction, and synchrotron computer micro-tomography (μ-CT).

Morphological results of the crystals after explantation were obtained by SEM analysis, carried out by my cooperation partners Dr. I. Sötje and Dr. H. Tiemann. Additionally, the examined crystals were analysed with EDX-spectroscopy. The results are comprised in Figure 3.1-3. Morphologically, the statoliths of all species can be described as trigonal needles of about 50 µm in length and about 20 µm in diameter. The crystals from each rhopalium were of different sizes. However, it was clear that the crystals of different species were generally of the same order of magnitude. The elemental analysis performed by EDX showed mainly the presence of calcium, sulphur and oxygen, indicating the presence of calcium sulphate. Additionally, traces of sodium, potassium and phosphorous (all less than 1 mol%) were also found, although these traces may have also originated from the surrounding tissue which could not be removed completely from the surface of the crystals. The presence of carbon and aluminium is due to the sample preparation (sputtering and the sample holder).

Synchrotron X-ray powder diffraction (XRD) was applied to crystals extracted from rhopalia of all species. The statoliths remained in the statocysts (cell arrangements containing the statoliths) and were not ground. Figure 3.1-4 shows the diffractograms obtained. All data were converted to Cu-Kα_1-radiation wavelength (λ=1.54056 Å) and compared to the given diffractograms of bassanite[132] and gypsum[131]. The examined species *Aurelia aurita*, C*yanea capillata*, *Cyanea lamarcki* (Semaeostomeae), *Periphylla periphylla* (Coronatae), and *Rhizostoma octopus* (Rhizostomeae) showed diffraction peaks at 14.5, 25.4, 29.1, 29.5, and 31.7°2Θ, respectively, consistent with bassanite peaks. The peak intensities, however, were not comparable to those of synthetic hemihydrate. This may be due to preferred orientation of the sample or due to the fact that the sample did not consist of a true powder, but rather of aggregates of unordered single crystals (see below).

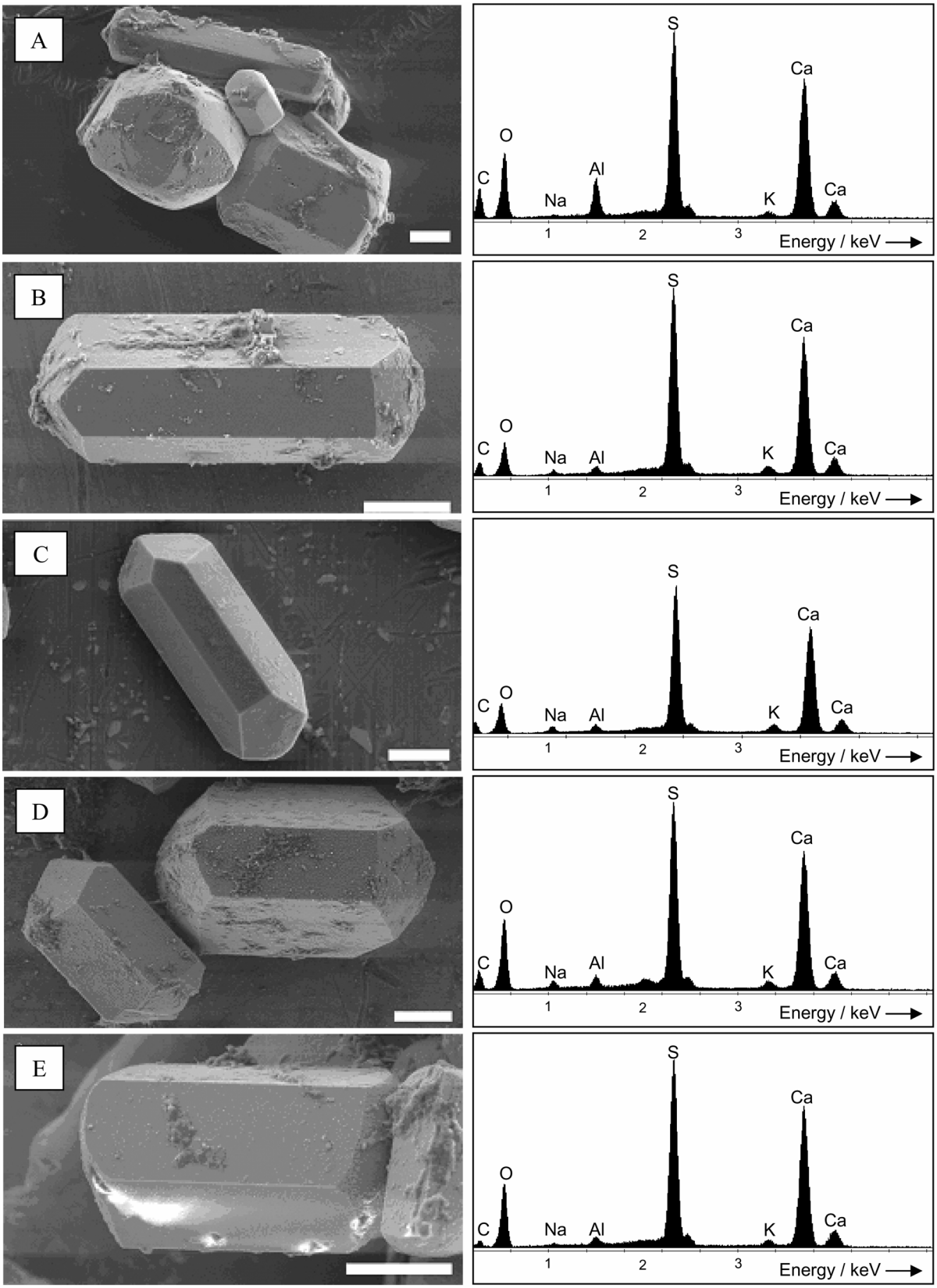

Fig. 3.1-3: Results of the SEM (left) and EDX (right) analysis of statoliths of the species *Aurelia aurita* (A), *Cyanea capillata* (B), *Cyanea lamarcki* (C), *Periphylla periphylla* (D), and *Rhizostoma octopus* (E). Results are discussed in the text. Images by courtesy of H. Tiemann.

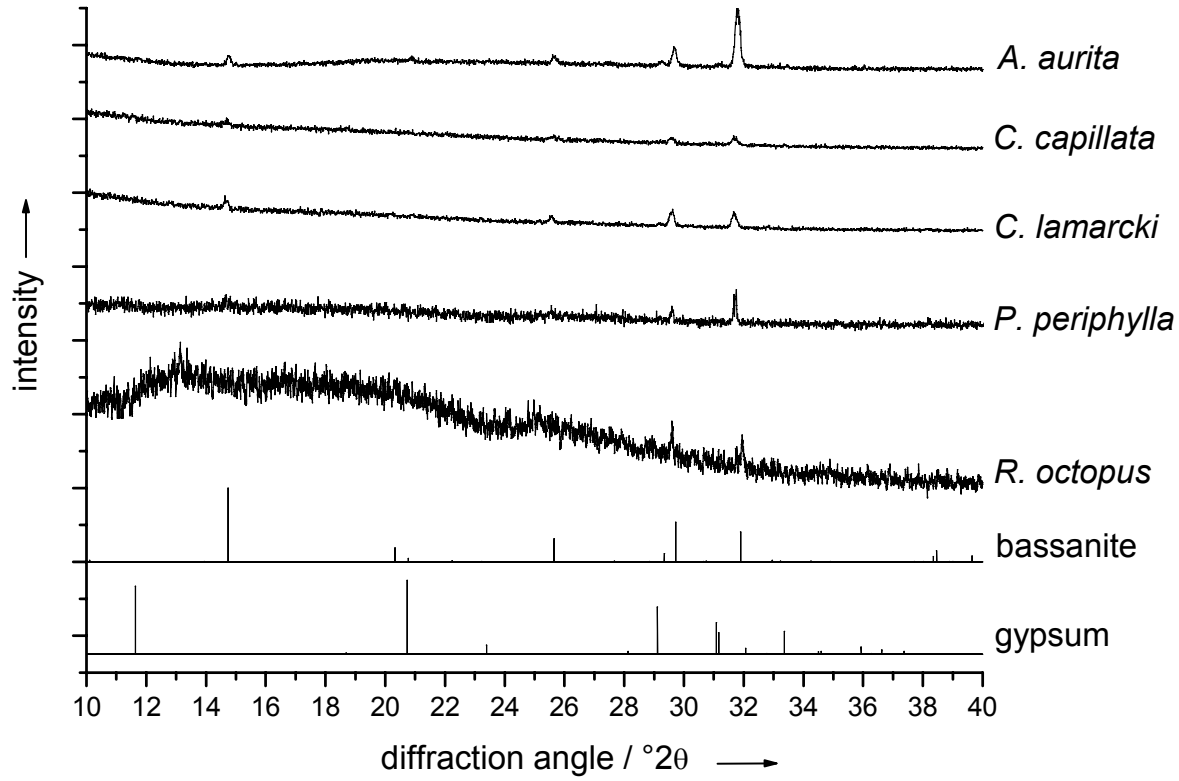

Fig. 3.1-4: High intensity synchrotron powder X-ray diffraction patterns of statoliths of the examined species. No trace of gypsum was found. All diffraction peaks observed correspond to bassanite. All data were converted to Cu $K\alpha_1$-radiation wavelength (λ=1.54056 Å). For comparison, patterns of bassanite and gypsum from ICDD reference are shown.

Although Spangenberg *et al.*[151] and Chapman[149], using XRD, have reported gypsum as the biomineral of the statoliths of both Scyphozoa *Aurelia aurita* and *Chrysaora hysoscella* (Semaestomeae), the presence of bassanite in all species examined here (including *Aurelia* aurita) was observed with no trace of gypsum. This discrepancy might be explained by uptake of moisture by the samples: a phenomenon well known in the construction industry as "hardening of gypsum" (see chapter 2.3). While Spangenberg *et al.* stored their samples in absolute ethanol, further preparation involved drying the hygroscopic samples on microscope slides in air. It can be assumed that the material of the crystals "hardened" from bassanite (construction industry's "gypsum") into the more stable mineral gypsum because of the contact with humidity or, in the case of Chapman, distilled water during preparation. The samples used in our work

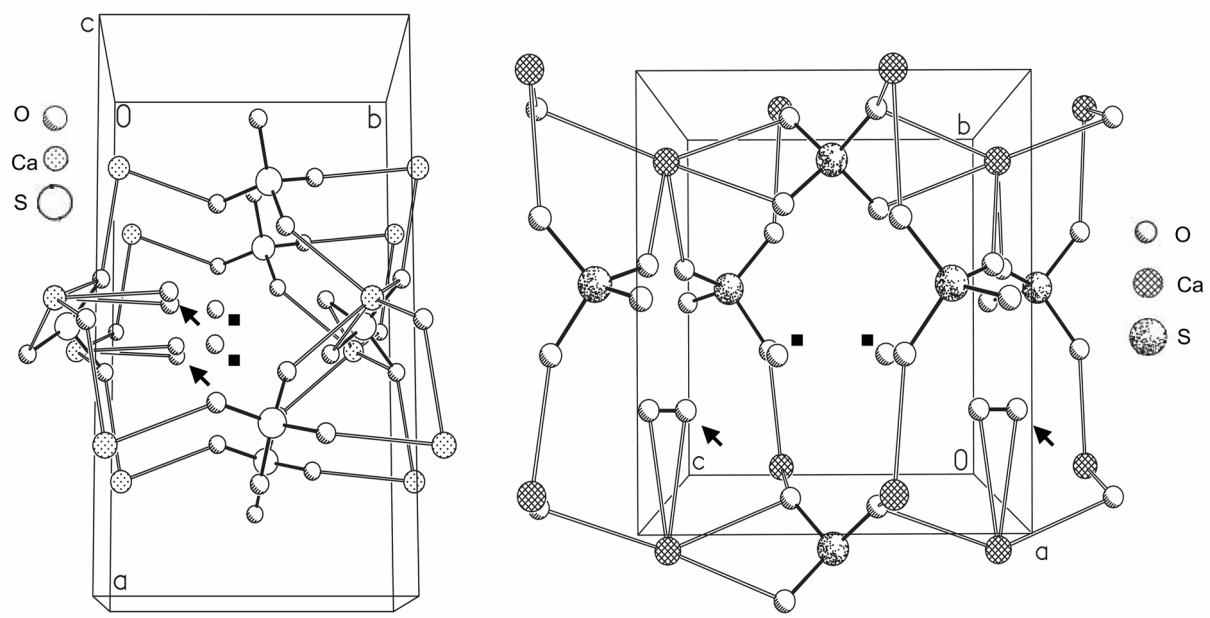

Fig. 3.1-5: The structure of the bassanite mineral of *Aurelia aurita* as determined by single crystal diffractometry is shown along the c-axis (left) and along the a-axis (right). Lines indicate topological coordinations and not bonds. Channels formed by alternating sulphate group anions and calcium cations can be identified. The oxygen atoms indicated by arrows are disordered with smeared positions. The oxygen atoms indicated with a little black square are water molecules located in the channels.

were stored in a mixture of 80% ethanol and 20% water after extraction. This mixture was shown not to dehydrate gypsum or hydrate bassanite.[83] Thus the observed presence of bassanite in all samples was not due to a preparation artefact, and hence gives rise to the hypothesis that bassanite might be the material of which all scyphozoa medusae produce their statoliths.

In addition to powder diffraction, synchrotron X-ray single crystal diffraction was performed with statoliths from the species *Aurelia aurita*. Structure determination with this method had already been successfully carried out with statoliths of *Periphylla periphylla*.[2] In the case of *Aurelia aurita*, contrary to the earlier results of Spangenberg *et* al., single crystal diffraction confirmed that the statolith consisted of single crystalline calcium sulphate hemihydrate (bassanite). The structure of the mineral could be confirmed as bassanite in accordance with the crystallographic literature,[132] although the crystal was twinned. The determined structure is shown in Figure 3.1-5. As expected for bassanite, this sample exhibited chains of alternating sulphate group anions and

calcium cations forming channels in which water is incorporated (for details see chapter 2.3). Additionally, the monoclinic space group *C* 2 (No. 5, setting 1) describes the symmetry well. Bassanite generally shows a superstructure described by the monoclinic space group *I* 121 (No. 5, setting 13) and a substructure described by the trigonal space group $P\,3_1 21$ (No. 152). The determined monoclinic space group *C* 2 is between those two in group-subgroup-relations (see Figure 3.1-6). The structural data for *Aurelia aurita* statoliths are summarised in Table 3.1-1; all data from structure refinement are listed in the appendix. Experiments with statoliths from *Cyanea lamarcki* did not give a meaningful data set despite the applied high intensity method. Statoliths from the other species are yet to be investigated.

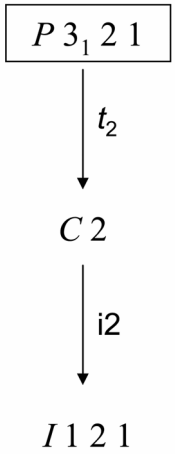

Fig. 3.1-6: Group-subgroup relations of the monoclinic space groups describing the symmetry of bassanite.

Synchrotron micro-computer tomography (μ-CT) is a non-destructive method used to visualise the location of the crystals in a rhopalium. Figure 3.1-7 shows the distribution of the statoliths within a rhopalium. The organic tissue of the organ was invisible in the high-energy beam. The largest crystals were located in the subumbrellar (mouthwards) part of the rhopalium (Figure 3.1-7a) whereas the smaller crystals were located on the exumbrellar (bellwards) side (Figure 3.1-7b). The crystals became bigger centrifugally from the base of the statolith to the subumbrellar and distal area of the statolith (Figure 3.1-7d). The largest crystals were mostly oriented with their longitudinal axis to the centre of the rhopalium.

Species of the other class of the Rhopaliophora, the Cubozoa, were also reported to use gypsum as the material forming statoliths.[149] As already stated, Chapman also applied XRD as a method of identification, but he did not avoid the contact

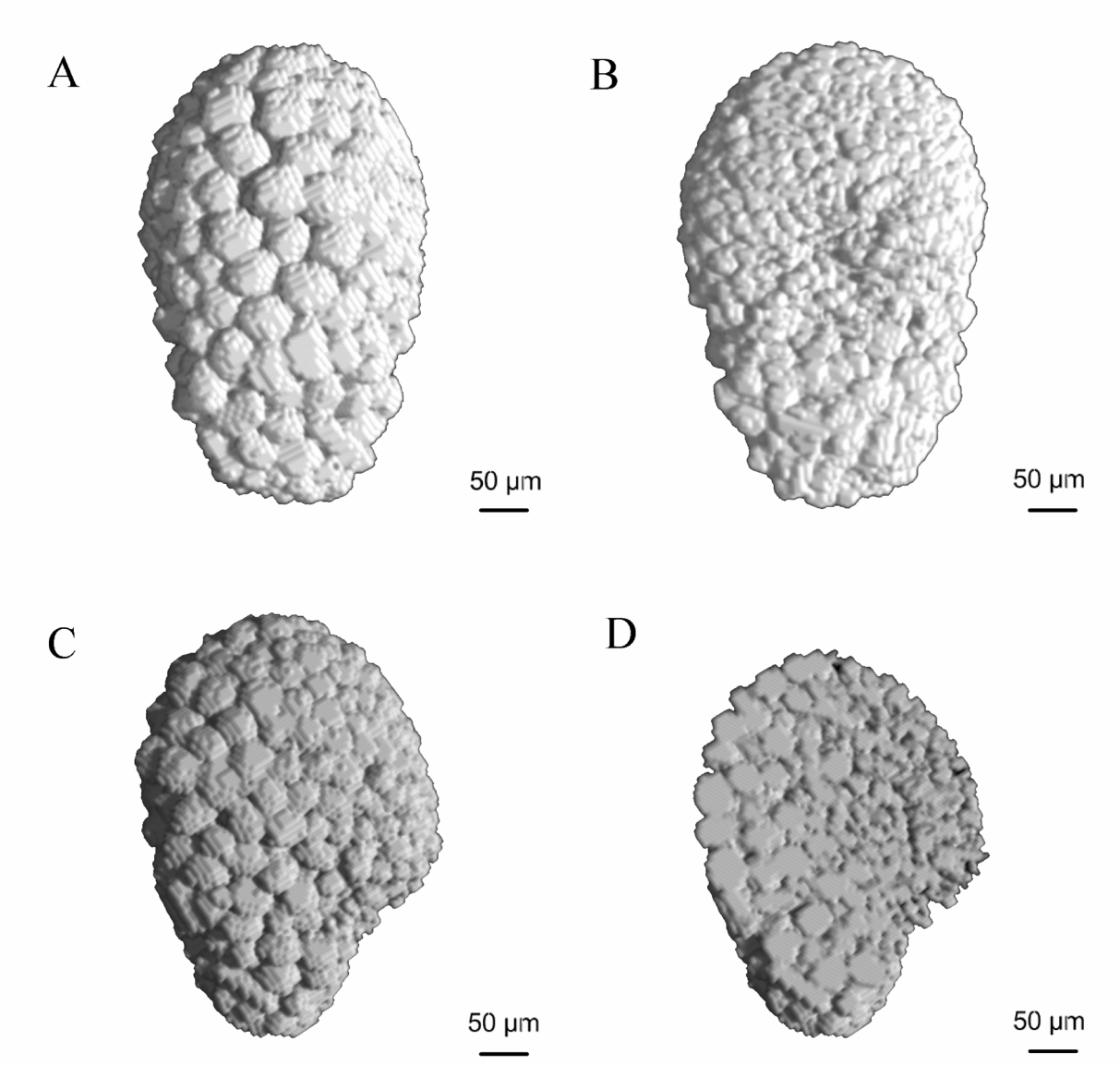

Fig. 3.1-7: Microtomographic images of intact rhopalia of the medusa *Aurelia aurita*. Picture A shows an integral rhopalium from the front (subumbrellar side view), whereas picture B shows it from the back (exumbrellar side view). Picture C shows a side view and picture D a cut through the rophalium from the sub- to the exumbrellar side. Domains of larger crystals can be distinguished from those with smaller crystals at the base of the organ.

with water during sample preparation. Therefore, a transformation of bassanite into gypsum seems possible also for the Cubozoa specimens. In addition, it will be necessary to use these methods to study the statolith material of the cubozoa medusae.

Nowadays it is possible, using new preparation and detection methods, to determine the statolith composition with a much higher degree of accuracy than in the past. The results obtained here show new evidence that the statoliths of

several species in the three orders Semastomeae, Coronatae and Rhizostomeae of the class Scyphozoa consist of calcium sulphate hemihydrate (bassanite). Therefore, it may be proposed that bassanite is the material of which all scyphomedusae produce their statoliths despite contradicting literature. The existence of bassanite in all studied groups of Scyphozoans showed that the use of this biomineral in animals is a very ancient development, considering that Scyphozoans already existed in the Praecambrian Ediacara-fauna, over 750 million years ago. The Scyphozoans are among the earliest metazoans and must have had free-swimming medusae at the time of their evolution. The rhopalia are a necessary organ for the free-swimming state and can be assumed to contain a biomineral since the development of these classes. Although, the Cnidaria are very primitive organisms, they have apparently developed sophisticated cellular processes to produce this hygroscopic biomineral which would not be stable as a mineral under deep-sea conditions (T=4-6°C, p=50-100 bar) and would transform into gypsum.

3.2 Amorphous calcium carbonate in terrestrial isopods

3.2.1 Isopods in biology[155, 156]

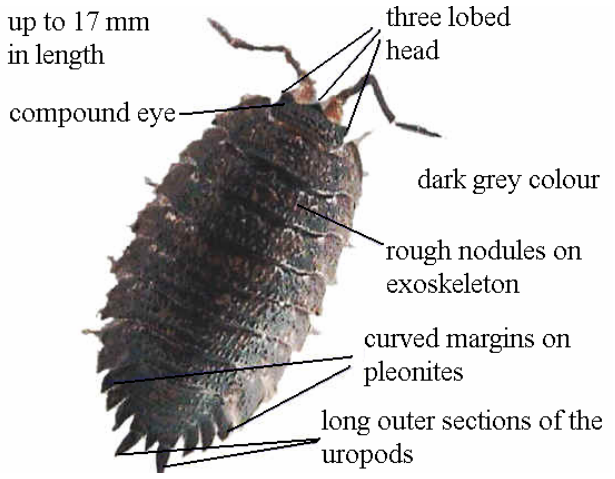

Fig. 3.2-1: The body plan of the terrestrial isopod *Porcellio scaber*. These animals are also known as "woodlice".

Most of earth's animals belong to the phylum Arthropoda. The name was created from the Greek words *arthron* which means joint and *pous* which means foot. Animals of this phylum possess a hard jointed exoskeleton, and jointed limbs, so crabs and prawns, woodlice, spiders, scorpions, insects, millipedes and centipedes are all arthropods. The phylum Arthropoda is huge in terms of numbers of species and in terms of numbers of animals. Arthropods are supposed to cover about 80% of animal life on earth and possibly half of all living organisms. Animals from this phylum live in every habitat imaginable: at the poles, the tropical zones (very abundant), the deep ocean, the tops of mountains, even underground and inside other animals. The arthropods evolved in the warm seas of the Cambrian period about 500 million years ago. Several major and minor lineages are now extinct, the most well known of these are the Trilobites. Fossils indicate that about 540 million years ago, an arthropod lineage known as the Euthycarcinoids were possibly the first animals to colonise the terrestrial environment.

Today's arthropods can be divided into three subphyla, 16 classes and numerous orders and families. Figure 3.2-2 gives a brief description of the phylogenetic relationships within this phylum. These three subphylae are the Chelicerata, the Crustacea and the Uniramia. The Chelicerata consists of animals whose body can be divided into two parts and who do not posses antennae. Its three classes

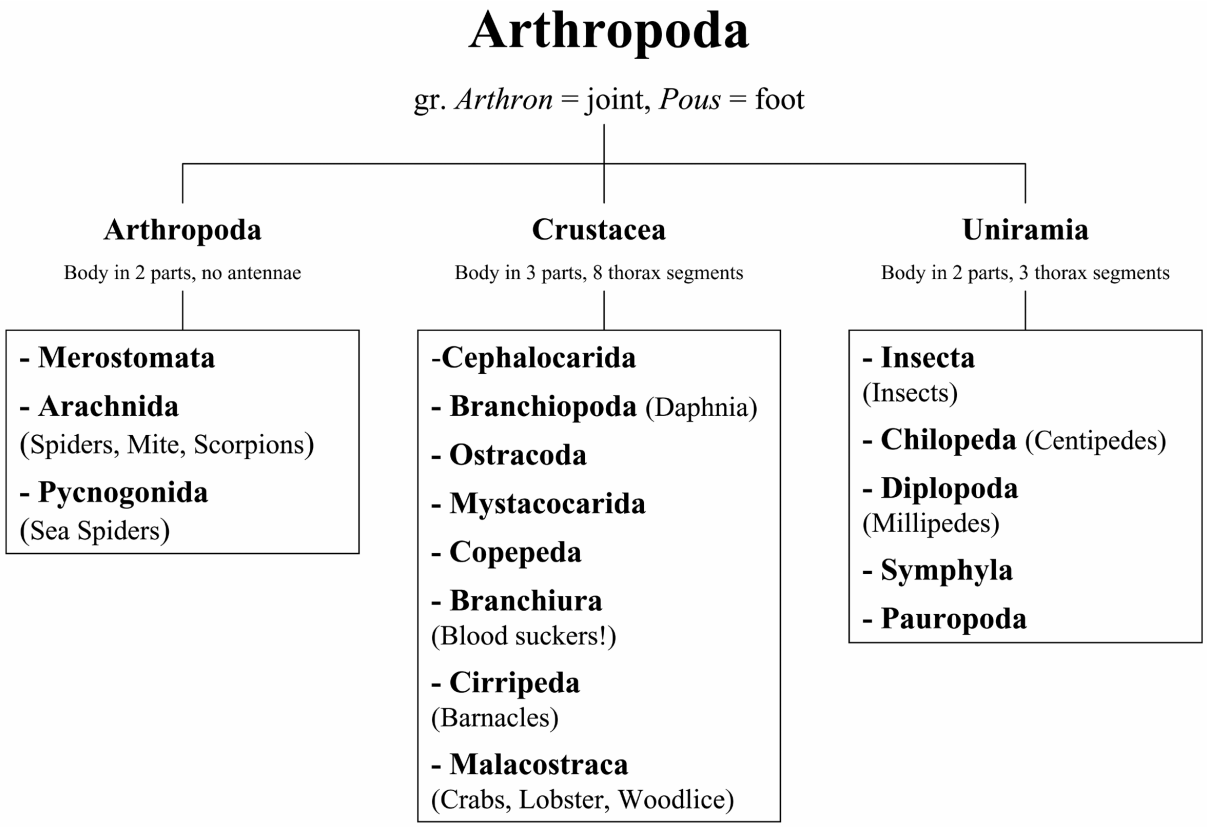

Fig. 3.2-2: The phylogenetic relationships in the phylum Arthropoda which comprises most of earth's animal life.

are the Merostomata (Horseshoe Crabs), the Arachnida (spiders, mite, scorpions etc.) and the Pycnogonida (sea spiders). The Crustacea show an incredible variability and cover mostly aquatic animals. In many cases, fundamental characteristics of the phylum Arthropoda have been lost during evolution or are only visible in embryonic form. Crustacean bodies can be divided into three parts and their thorax in eight segments. Its eight classes are the Branchiura (small blood sucking ectoparasites), the Branchiopoda (small primitive animals with gills on their feet, i.e. daphnia), the Cephalocarida (small primitive shrimps), the Cirripedia (barnacles), the Copepoda (cyclops), the Malacostraca (crabs, lobsters, shrimps, prawns, woodlice), the Mystacocarida (small crustaceans living interstitial on intertidal and subtidal beaches) and the Ostracoda (seed shrimps). Among these classes, the Malacostraca cover 75% of all crustaceans. The subphylum Uniramia comprises animals with a three-part body and a thorax that can be divided into three parts. Its five classes are the

Chilopoda (centipedes), the Diplopoda (millipedes), the Insecta (insects), the Pauropoda (wikipedia) and the Symphyla (garden centipedes). Of all arthropods, the insects are the most numerous.

One of the most prominent characteristics of arthropods is their strong external skeleton, the cuticle.[156] It provides support, lines tracheal tubes, sense organs and serves as effective barrier between the interior of the animal and the environment. This feature is believed to be the main reason for the ability of the arthropods to make a successful transformation from aquatic to terrestrial existence. The cuticle can be rigid, nearly armour-like as in many crustaceans or soft as in many insects. The outermost layer of the cuticle is the epicuticle which is rich in lipids (wax layer) and seems to be the primary barrier for water loss. It does not contribute to the mechanical properties of the exoskeleton. The next inward layer is the procuticle which can be divided into exocuticle (outward) and endocuticle (inward). This layer consists primarily of the polysaccharide chitin embedded in a protein matrix. These two components make up for nearly 90% of the organic substance of the cuticle. Depending on the species, layer shell hardening minerals, mostly calcium carbonate, are deposited in the procuticle. The last layer connects to the body through a layer of epithelial cells and is called the epidermis. The described setup of the cuticle has a major disadvantage; it is not flexible or expandable. During animal growth the exoskeleton is moulted periodically to accommodate size increase.

The term “Isopoda” comprises Arthropoda animals from the subphylum Crustracea and the class Malacostraca. The suborder Oniscidea comprises all land dwelling Isopoda. In fact, the latter are the only true terrestrial Crustacea and are fully independent from life in water. Figure 3.2-3 shows the phylogentic relationships of the different terrestrial isopod species investigated in this work. Largest of the four sister groups Ligiidae, Tylidae, Synochaeta, and Crinochaeta are the Crinochaeta with 27 families. Of those, species from the families

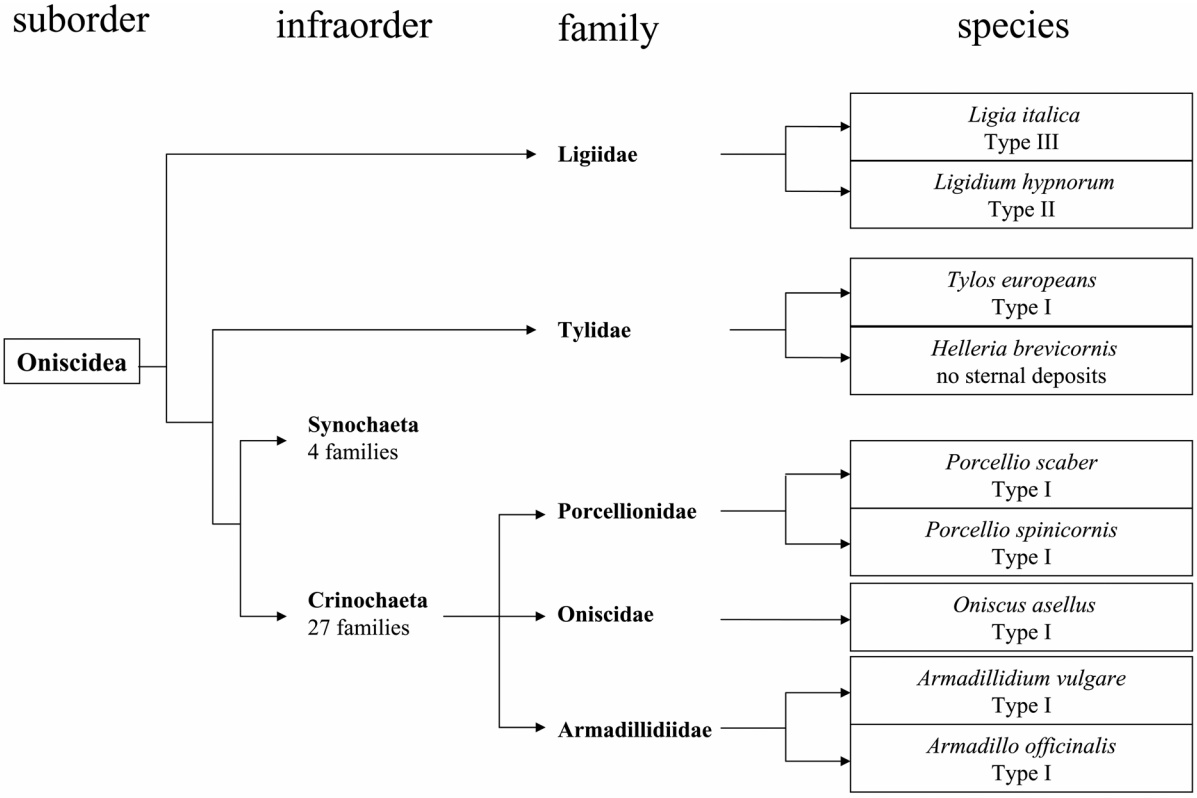

Fig. 3.1-3: Schematic explanation of the phylogenetic relationships among the terrestrial isopods. The exact definitions of orders and families are under constant debate in biology. Most disturbing for non-biologists are the Latin name endings. The ending –ae relates to a family classification, whereas the ending –ea refers to a suborder. The type classification of the different species refers to the morphology of calcium carbonate deposits during moulting and is explained in the text.

Armadillidiidae, Oniscidae, and Porcellionidae were sampled. The infraorder Crinochaeta is a sister group to the families Ligiidia and Tylidea. Often, the Ligiidea and the Tylidea are comprised in the non-phylogenetic infraorder Diplochaeta. Even today, the exact phylogenetic relationships remain still under debate.

3.2.2 Moulting in isopods

The growing animal has to shed its exoskeleton and to generate a new one to accommodate its increase in size. The moulting process (ecdysis) begins with the formation of a new epicuticle by the epidermis cells.[156] Then, enzymes pass the new epicuticle layer and begin to digest the old cuticle. When the old cuticle is partially digested, the epidermis cells begin the production of a new

procuticle. Once the old endocuticle is fully digested, the animal emerges from the old outer shell and swells by the uptake of water to stretch the new still soft cuticle. The composition and volume of the hemolymph ("blood") of the supralittoral isopod *Ligia pallasii* was monitored by Ziegler *et al.*[157] The shedding process in terrestrial isopods is biphasic.[158] First, the animal loses the posterior half (tailside) of the cuticle, then the anterior half (frontside).

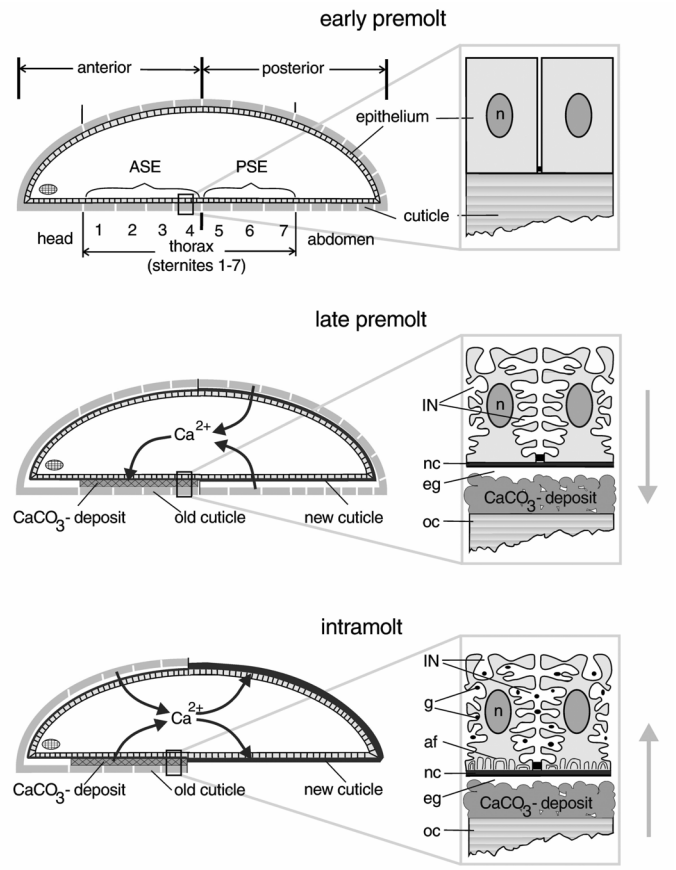

Fig. 3.2-4: Schematic representation of the flow of calcium during the different moult stages. The ispod is divided into an anterior and a posterior half. The sternal epidermis of the anterior part bordering on the calcium carbonate storage sites has been found to be specialised for calcium transport. For details see text. Scheme by courtesy of A. Ziegler.

As stated in the above paragraph, some species are true terrestrial isopods which are fully independent from aquatic habitats. During moult, calcium in the shed cuticle would normally be lost for the animal. This is no problem for aquatic crustaceans which can easily replace the lost calcium by taking up Ca^{2+} from the seawater across their gills.[159] Calcium is abundant in seawater, but not in the diet of terrestrial isopods (plants). Therefore, storage or recycling of calcium is of high significance for terrestrial isopods. Before moult, the calcium carbonate of the old cuticle is resorbed.[160] During this process, cuticular calcium is transported across the preexuvial (non-shed) cuticle and the epithelium. The resulting increase of the Ca^{2+} concentration in the ionic hemolymph composition could be shown in the terrestrial isopod *Porcellio scaber*.[161] The pathway for cuticular calcium during

the moult cycle is well described for *Porcellio scaber* and *Oniscus asellus*.[158, 162-164] Figure 3.2-4 summarises the calcium movements in a schematic representation. About a week (premoult phase) before the posterior moult, the animal dissolves calcium carbonate from the posterior cuticle. The ions are transported across the anterior sternal epithelium (ASE) into the ecdysial space between the cuticle secreting epithelium and the old cuticle of the first four sternites. Most terrestrial isopods store calcium carbonate there.[158, 165-167] The cells of the anterior sternal epithelium have been shown to be differentiated especially for epithelial ion transport.[163, 164] During calcium ion transport, either resorption or deposition, an elaborate system of channels is formed by the membranes of the ASE cells, known as the interstitial network (IN). The surface of the basolateral plasma membrane increases drastically. In epithelial cells, specialised cell junctions separate the plasma membrane in an apical (storage deposit side) and a basolateral (hemolymph side) compartment to allow vectorial ion transport across the epithelium. The role of the membranes and their surfaces is discussed in detail by Ziegler *et al.*[164, 168-170] The calcium ion transport process from and to the hemolymph through the membranes is supposed to be regulated by Ca^{2+} channels and/or Ca^{2+}/H^{+} exchange as passive influx mechanism and a Ca^{2+}-ATPase and/or Na^{+}/Ca^{2+} exchanger as an active extrusion mechanism.[171-175] Ziegler proposed an ATP and Na^{+} depending mechanism for transcellular Ca^{2+} transport.[172] After shedding the old posterior cuticle, but before shedding the anterior cuticle (intramoult phase), the animal dissolves the sternal storage deposits and the calcium carbonate in the old anterior cuticle in the relatively short period of less than one day and transports calcium across the ASE and the epithelium of the anterior integument into the hemolymph in order to mineralise the new posterior cuticle. The shed cuticle parts (exuviae) are eaten by the animal, possibly to regenerate non-dissolved calcium carbonate in order to mineralise the new anterior cuticle. Moulting occurs frequently, e.g. every six weeks in *Porcellio scaber*.[176]

3.2.3 The sternal deposits as calcium carbonate storage sites

The storage site for cuticular calcium carbonate varies among woodlouse species.[177] Many decapods store it in gastroliths, consisting of calcite and organic matrix. These objects are located between epithelium and stomach and shed with the cuticle. By uptake across the epithelium and the interstine, the calcium carbonate is regained. The freshwater crab *Holthuisana transversa* stores more than half of its total body calcium in microspherules located in the hemolymph.[178] Terrestrial amphipods are known to store calcium in the posterior midgut caeca.[179, 180] Terrestrial isopods like woodlice store calcium carbonate in the ecdysial space in the first four sternites. Figure 3.2-5 shows the exact location of these storage sites.

Ziegler *et al.* performed an extensive study of sternal calcium carbonate deposits.[181] Depending on species and family (see Fig. 3.2-3), differences in the structure of the storage sites were found. In the family Ligiidae, the deposits of the species *Ligia italica* and *Ligia oceania* consist exclusively of individual

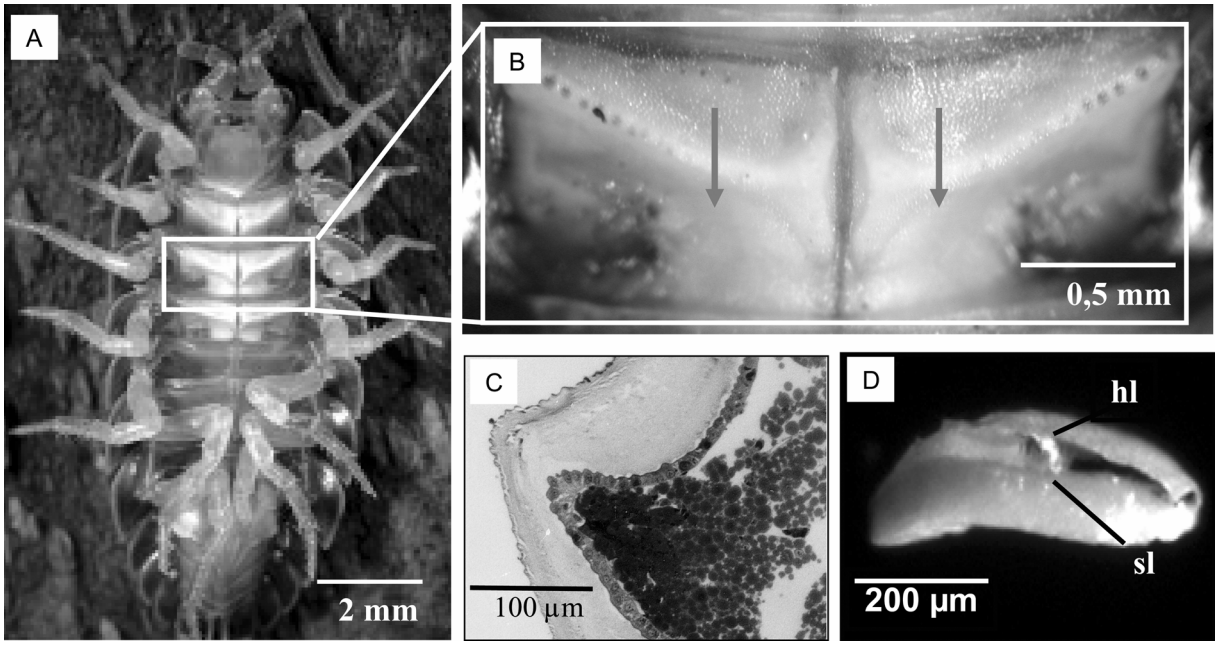

Fig. 3.2-5: A specimen of *Porcellio scaber* is shown in image A. In magnification, image B shows the sternal calcium carbonate storage deposits. Image C shows a cross-section of these sites (roughly along the arrow in image B) with the cuticle visible and the mineral seen as mini spheres. An explanted sternal storage site is seen in image D. It can be divided into a homogeneous layer (hl) and a spherular layer (sl). The image is by courtesy of A. Ziegler.

spherules without any distinct material between the spherules which resemble a close-packed structure (see Figure 3.2-6). However, the family Ligiidae species *Ligidium hypnorum* showed a two-layer storage site with a proximal spherular layer (psl, towards the body centre) consisting of individual spherules as in the Ligia species, and a distal spherular layer (dsl, towards the body surface) in which "the spherules appear to be fused with each other". Species of the infraorder Crinochaeta (*Porcellio scaber, Armadillidium vulgare,* and *Oniscus asellus* among them) resemble the storage setup of *Ligidium hypnorum*.

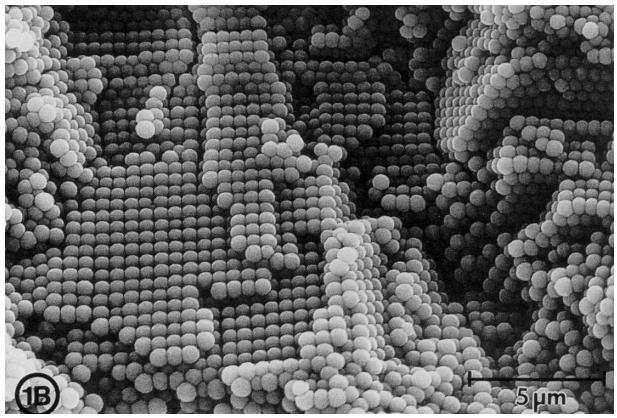

Fig. 3.2-6: Spherules of calcium carbonate in closed packed structure in the sternal storage deposits of *Ligia italica*. Picture by courtesy of A. Ziegler.

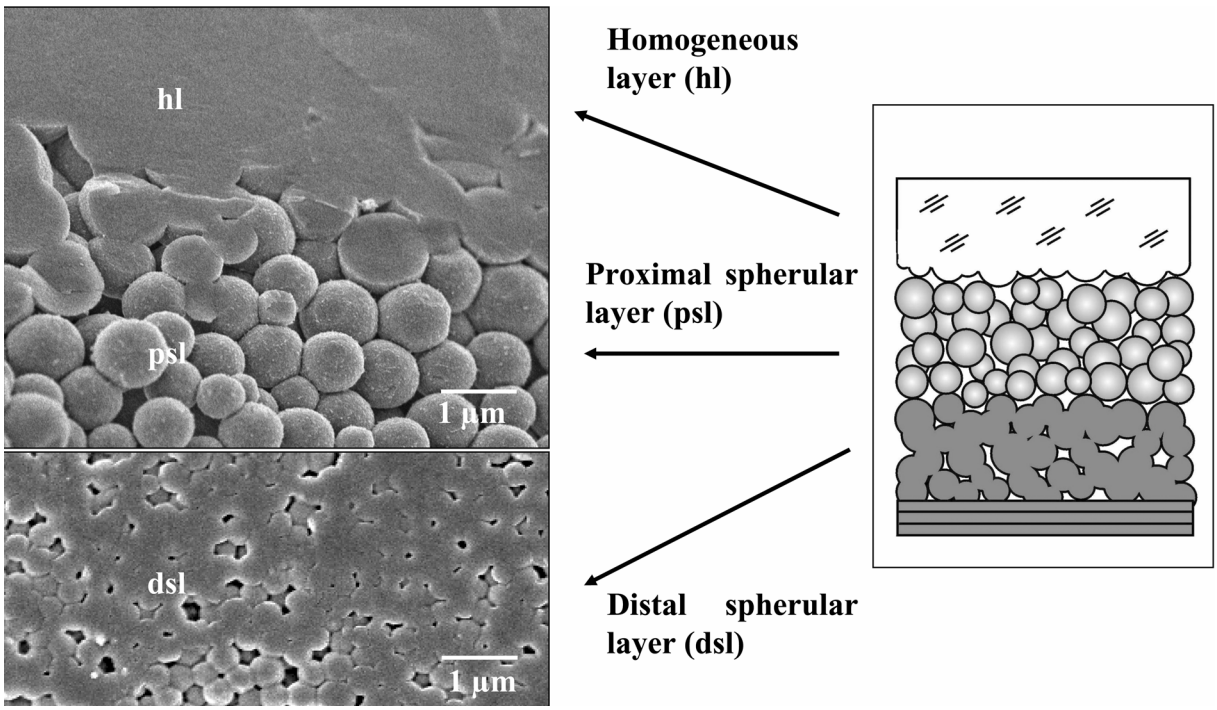

Fig. 3.2-7: SEM images of the three morphological layers found in sternal calcium carbonate deposits in terrestrial isopods and the resulting schematic representation. Pictures by courtesy of A. Ziegler.

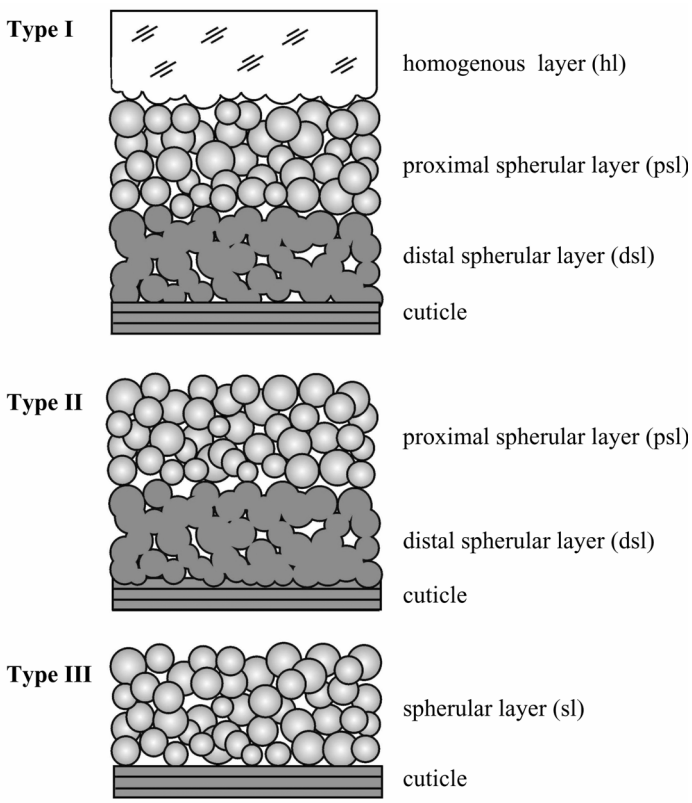

Fig. 3.2-8: The different types of sternal deposits depending on the form of calcium carbonate deposition. Image courtesy of A. Ziegler.

However, in addition to distal and proximal spherule layer, a homogenous layer (hl) of glassy appearance of calcium carbonate can be identified. Figure 3.2-7 shows SEM images of the three layers in the calcium carbonate storage deposits for *Porcellio scaber* and a schematic representation. For *Porecellio scaber*, deposit formation and degradation was extensively studied and is still in focus of Ziegler *et al.*[182] So far, three types of storage deposits can be distinguished. Type I, found in the Diplochaeta family Tylidae, the Synochaeta family Trichoniscidae, and the Crinochaeta families, shows three layers of deposition: hl, dsl and psl. Type II, found in genus Ligidium of Diplochaeta family Ligiidae, consists of dsl and psl. Type I, found in genus Ligia of Diplochaeta family Ligidiiae, shows only one layer of spherules (sl). Figure 3.2-8 shows a scheme of layers and types. In the homogenous layer and the distal spherular layer with fused spherules, more calcium per volume can be stored than in distinct close-packed spherules structures. This leads to the suggestion that the multilayered deposits are an adaptation to terrestrial life, as a consequence of the need for increased resorption of cuticular calcium.

3.2.4 Structural characterisation of calcium carbonate in the sternal deposits of the crustacean *Porcellio scaber*[112]

The mineral phase of the sternal storage deposits of terrestrial isopod *Porcellio scaber* is X-ray amorphous.[183] As described in chapter 2.2, amorphous calcium carbonate (ACC) is about 10 times more soluble than calcite, aragonite or vaterite, the known water-free crystal phases of calcium carbonate.[92] This predestines the use of ACC as temporary storage phase for calcium ions. The occurrence of amorphous calcium carbonate in biomineralisation was discussed in chapter 3.1. In order to further characterise the structure of the mineral in the deposits, samples of mineralised sternal storage deposits of *Porcellio scaber* in the late premoult stage were analysed by high-resolution X-ray diffraction (XRD), reflection infrared spectroscopy (IR), and X-ray absorption spectroscopy (EXAFS).

High-resolution synchrotron X-ray powder diffraction showed clearly that the material is fully X-ray amorphous (see Fig. 3.2-9). The diffractogram showed no distinct diffraction peaks. For comparison, the positions of the main reflection peaks (I>2.5%) of calcite are shown.[73] The high background count of the sample is due to the amorphous organic components of the samples.

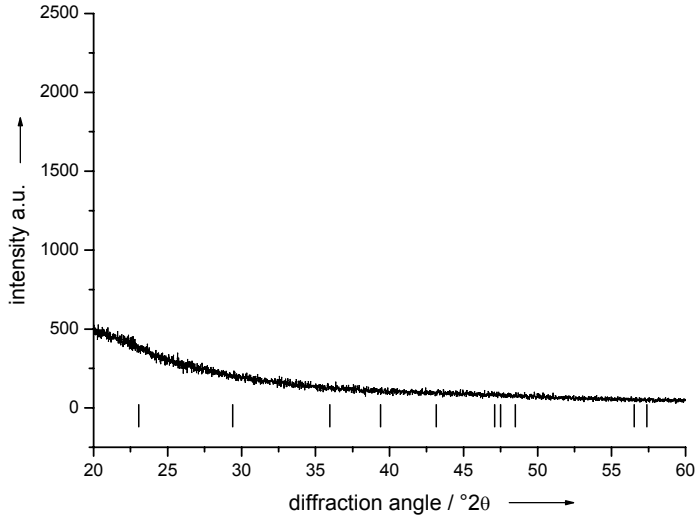

Fig. 3.2-9: High resolution synchrotron powder X-ray diffractogram of the explanted sternal deposits of *Porcellio scaber*. The bars indicate the Bragg reflex positions of calcite (*I*>2.5%). The material is fully X-ray amorphous.

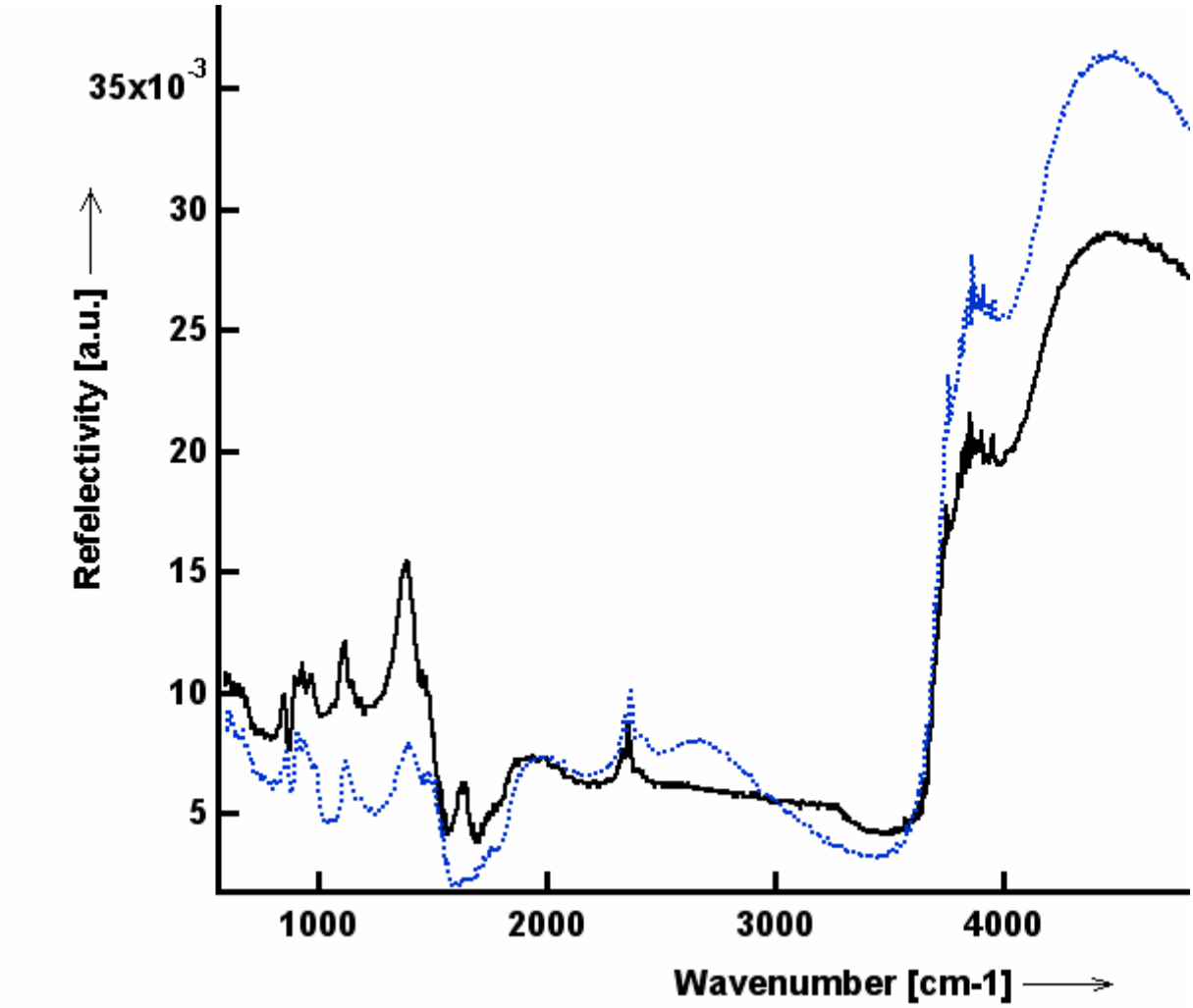

Fig. 3.2-10: Infrared spectra of the mineral phase in the homogeneous layer (solid line) and the proximal spherular layer (dotted line) of the sternal deposists of *Porcellio scaber*. Image by courtesy of U. Bismayer.

Reflection infrared spectroscopy was done by J. Shi, M.Sc. and Prof. Dr. U. Bismayer (Hamburg). They measured spectra of the glassy homogenous layer (hl) and the proximal spherular layer (psl, see Fig. 3.2-10). Both spectra (hl: solid line, psl: dotted line) reveal the presence of nanocrystalline calcium carbonate. In the area of 600-1500 cm^{-1} the signals caused by the mineral can clearly be identified. At 1400 and 1480 cm^{-1}, the ν_3 asymmetric stretch of the carbonate ion (E_u) can be seen. In stable biogenic ACC, these two reflections occur as a doublet indicating the lack of symmetry in the environment of the carbonate ions.[122] It is noteworthy that the ν_3 doublet in the spectrum of the psl resembles a true doublet whereas in the spectrum of the hl, the 1480 cm^{-1} peak,

it is only visible as a shoulder. The strong intensity of the 1400 cm^{-1} peak may be due to the small particle size of the crystallites. The lack of symmetry is also visible in a broad peak at 1080 cm^{-1} which is visible in both spectra.[122] However, at 1070 cm^{-1} the phosphate group shows an absorption peak, too. The ν_2 carbonate out-of-plane bending absorption (A_{2u}) at 860 cm^{-1} and the ν_4 in-plane bending (E_u) at 710 cm^{-1} are broadened as expected for biogenic amorphous calcium carbonate.[122] The hl and the psl show similar spectra except for an additional peak at 1630 cm^{-1} in the hl absorption spectrum. This signal is not related to calcium carbonate and thus supposed to arise from absorption of the organic material of the sample as the other signals gained in the region above 2000 cm^{-1}.[184] The excellent IR light scattering signals obtained of the X-ray amorphous material allow a suggestion of the particle size of the corresponding coherent lattice. Particle size must be smaller than 100 Å but larger than a few interatomic distances. Corresponding signals were observed in the case of small clusters of ferrioic materials which were of the order of 30 Å.[185]

The method of choice to learn about the coordination sphere of calcium in the amorphous material is extended X-ray absorption fine structure spectroscopy of at the calcium K-edge at 4038.5 eV. Because EXAFS is a very accurate method to determine the distances of the first coordination shell, the values obtained are characteristic for the short-range order of the material observed. Figure 3.2-11a shows the primary EXAFS oscillations of a sample of the sternal deposits of *Porcellio scaber*. Figure 3.2-11b shows the Fourier transform magnitude of the obtained spectrum together with a fit to a suitable model. For comparison, the results for the crystalline phase vaterite are also shown. Because the “structure” of ACC is unknown, a suitable model was derived from crystalline calcium carbonate phases and used for calculation. Samples of calcite, aragonite and vaterite were also measured. The latter was generously provided by Prof. Dr. G. Wolf and Dr. C. Günther (Freiberg/Sachsen). An EXAFS fit for monohydrocalcite $CaCO_3 \cdot H_2O$ is available from the literature.[186]

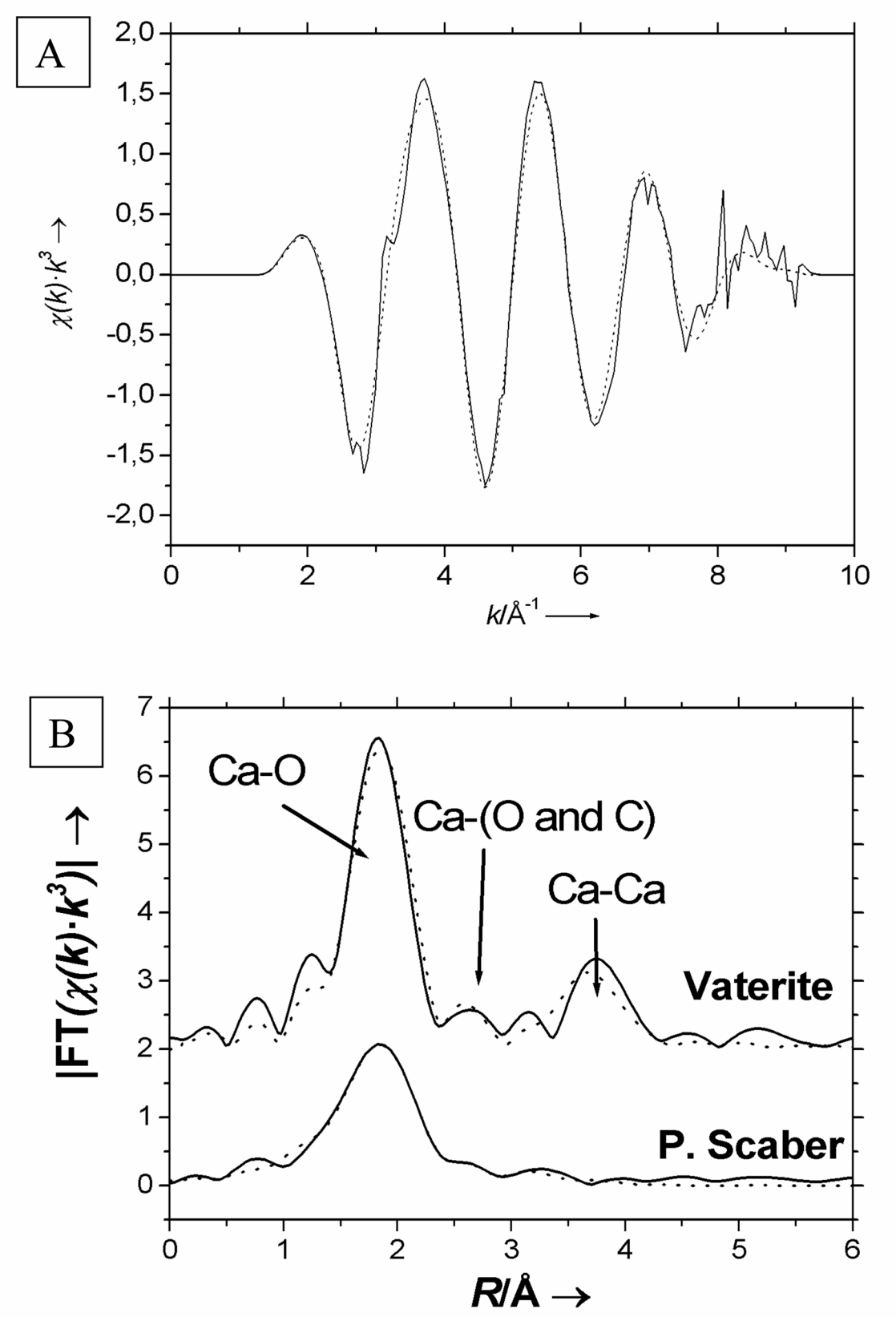

Fig. 3.2-11: Image A shows primary EXAFS oscillations of a sample of the sternal deposists of *Porcellio scaber*. The Fourier transform magnitude of the obtained spectrum and the model substance vaterite are shown in image B.

Tab. 3.2-1: Ca K-edge EXAFS data of ACC deposits in *Porcellio scaber*, together with EXAFS data for the three water-free crystalline calcium carbonate polymorphs and for monohydrocalcite. (a) fit result, (b) number fixed to crystallographic value.

Sample	E_o / eV	**First shell: oxygen**			**Second shell**			**Third shell**			**Fourth shell: 6 Ca**	
		N	R / Å	$\sigma^2 \cdot 10^3$ / Å^2	N	R / Å	$\sigma^2 \cdot 10^3$ / Å^2	N	R / Å	$\sigma^2 \cdot 10^3$ / Å^2	R / Å	$\sigma^2 \cdot 10^3$ / Å^2
Porcellio Scaber deposit	+0.33	3.8[a]	2.38 [a]	14	1.4 C[a]	3.00	7	0.4 C[a]	3.72	1	3.89	109
Aragonite	-1.04	9[b]	2.47	33	3 C[b]	2.98	3	3 C[b]	3.26	10	3.94	28
Calcite	-0.29	6[b]	2.33	9	6 C[b]	3.27	35	6 O[b]	3.65	16	4.05	9
Vaterite	+1.62	6[b]	2.37	7	2 O, 2 C[b]	3.09	21	——	——	——	4.24	15
Monohydro-calcite[186]	+1.3..1.5	7.4[a]	2.37	9	1.5 C[a]	3.03	7	3 C[a]	3.36	0	——	——

The data obtained by calculation is comprised in Table 3.2-1. Up to four coordination shells can be distinguished. The fourth shell at about 4 Å distance is the same in all three water-free crystalline phases of calcium carbonate calcite, aragonite, and vaterite and consists always of six calcium atoms. The two coordination shells in between vary in coordination number and type of coordinating atom, depending on the polymorph observed. From the fit results, it can be concluded that the calcium-oxygen distance in the first coordination sphere of the ACC sample resembles either vaterite or monohydrocalcite. The coordination number N of this shell of 3.8 with an estimated error of ±30 % (see chapter 5.6) is low but closer to calcite and/or vaterite (6) or monohydrocalcite (7.4) than to aragonite (9). Statements concerning the other shells are not possible as the data on them is rather weak. This is also true for the calcium coordination shell (fourth shell), indicated by a very high Debye-Waller factor. These observations indicate a high degree of disorder in the ACC of the sternal deposits beyond the first coordination shell. In the first shell, the calcium atoms are coordinated by carbonate groups via the oxygen atoms.

Levi-Kalisman *et al* already noted that the name amorphous calcium carbonate does not correspond to a single structure but to a number of structurally different materials.[114] The material analysed here has a particularly low long-range-order

Tab. 3.2-2: Results reported in the literature for EXAFS spectra of X-ray amorphous calcium carbonates found in biology, together with crystalline phases. The entries are sorted with ascending distance of the first coordination shell of oxygen. The second, third and fourth shells in the sternal deposits of *Porcellio scaber* are weak and of poor significance. (a) shell was not included in fit.

Sample	**Shell distance by EXAFS / Å**			
	1st Shell: Ca-O	2nd Shell: Ca-C or Ca-O	3rd Shell: Ca-C or Ca-O	4th Shell: Ca-6 Ca
ACC in carapaces of *Homarus american*[187]	2.27	——[a]	3.47	3.79
ACC in plant cystoliths of *Ficus microcarpa* [187]	2.31	——[a]	3.48	3.79
calcite	2.34	3.30	3.64	4.05
calcite[188]	2.35	3.23	3.48	3.98
ACC in plant cystoliths of *Ficus retusa* [188]	2.36	3.22	3.39	4.06
calcite[189]	2.37	3.21	3.52	4.11
monohydrocalcite[189]	2.37	3.03	3.36	——[a]
vaterite	2.37	3.09	——[a]	4.24
ACC in spicules of *Pyura Pachydermatina*[189]	2.37	3.03	3.36	——[a]
ACC in sternal deposits of *Porcellio scaber*	2.38	3.00	3.72	(3.89)
ACC in larval shells of *Biomphalaria glabrata*[190, 191]	2.44	——[a]	——[a]	3.92
aragonite	2.47	2.98	3.26	3.94

which leads to the assumption that the thermodynamic stability is low, resulting in a high solubility. This makes sense, because the material is only temporarily stored in the ecdysial space and dissolved within less than a day in order to remineralise the new anterior cuticle. Table 3.2-2 shows the available EXAFS data on ACC materials from the literature. The ACC described there is not only deposited for temporal storage. It serves a precursor phase for crystallisation into a stable polymorph[65], it is found in plant cystoliths[113], or serves as a stabilised biomineral[114, 186].

It could be shown that the amorphous calcium carbonate in the sternal deposits of *Porcellio scaber* is of high disorder but not without structure. The coordination spheres determined by EXAFS correspond well to those described in literature. The particle size can be estimated to be of the order of a few nanometres. The organic matrix protecting the material from crystallisation is now in the focus of Ziegler *et al*.

3.2.5 The mineral phase in the cuticles of terrestrial isopods[127]

We have shown that the sternal ecdysial deposits in *Porcellio scaber* consist of disordered amorphous calcium carbonate. However, ACC was also reported in the cuticle of *Oniscus asellus*.[192] It was identified by infrared spectroscopy and by X-ray powder diffraction which yielded only minimal or non-detectable calcite reflections. But so far, quantitative data on mineral and organic components of the cuticle of isopods which are not in moult (intermoult phase) are still missing. We have analysed the fully mineralised cuticles of *Armadillidium vulgare* (Armadillidiidae), *Armadillo officinalis* (Armadillidae), *Oniscus asellus* (Oniscidae), *Porcellio scaber, Porcellio spinicornis* (Porcellionidae), *Tylos europaeus, Helleria brevicornis* (Tylidae), and *Ligidium hypnorum* (Ligiidae) with quantitative X-ray powder diffractometry (XRD), X-ray absorption spectroscopy (EXAFS), infrared spectroscopy (IR),

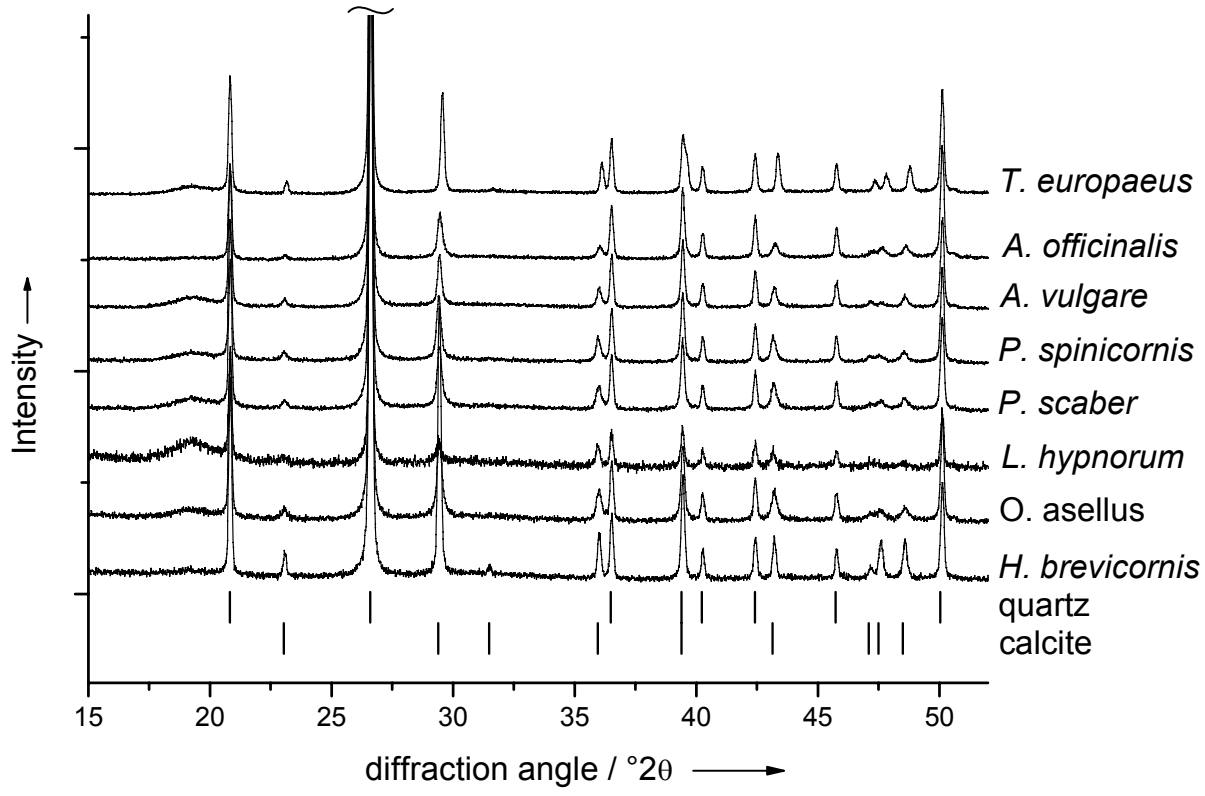

Fig. 3.2-12: Synchrotron powder X-ray diffraction patterns of 1:1=*w:w*-mixtures of cuticle sample and quartz standard. The bars indicate the Bragg reflex positions of calcite (I>2.5%) and of quartz.

thermogravimetric analysis (TGA), and elemental analysis by atomic absorption spectroscopy (AAS) in order to identify and quantify mineral phases in the cuticle.

Quantitative powder X-ray diffraction was applied on 1:1=*w*:*w*-mixtures of cuticle sample and quartz. The resulting diffractograms are shown in Figure 3.2-12. All data shown were converted to Cu Kα_1-radiation (λ=1.54056 Å) and weighed in intensity to the same intensity of the main quartz peaks. Differences in calcite content can be seen. No other phases could be detected despite the high-intensity method applied. Quantitative phase analysis on the mixtures was done by Rietveld refinement (see chapter 5.1) on the unweighted and unconverted raw data. Table 3.2-3a comprises the results; Figure 3.2-13 shows the Rietveld refinement for *Porcellio scaber*. To a given mass of cuticle sample about the same mass of quartz was added to act as internal standard material. Quantitative phase analysis yields the ratio of diffracting material (quartz and calcite) in weight percent of crystalline material [cry-wt%]. The overall goodness of fit is expressed in the weighed R^2-factor. The closer the value is to one, the better is the fit. All calculations can be considered reasonably accurate. The replacement of calcium by magnesium and the biological origin of the sample resulted in intensity shifts compared to a mixture of pure calcite and quartz. In Rietveld refinement, this results in a relative overestimation of the amorphous phase.[193] The mass of the crystalline material in the mixture is accessible through

$$m(\text{cryst}) = \frac{m(\text{quartz}) \cdot 100}{w(\text{quartz, RV})} \qquad \text{(eq. 3.2.5-1)}$$

with m(cryst) being the mass of diffracting material in the mixture [mg], m(quartz) the mass of quartz in the mixture [mg] and w(quartz, RV) the weight

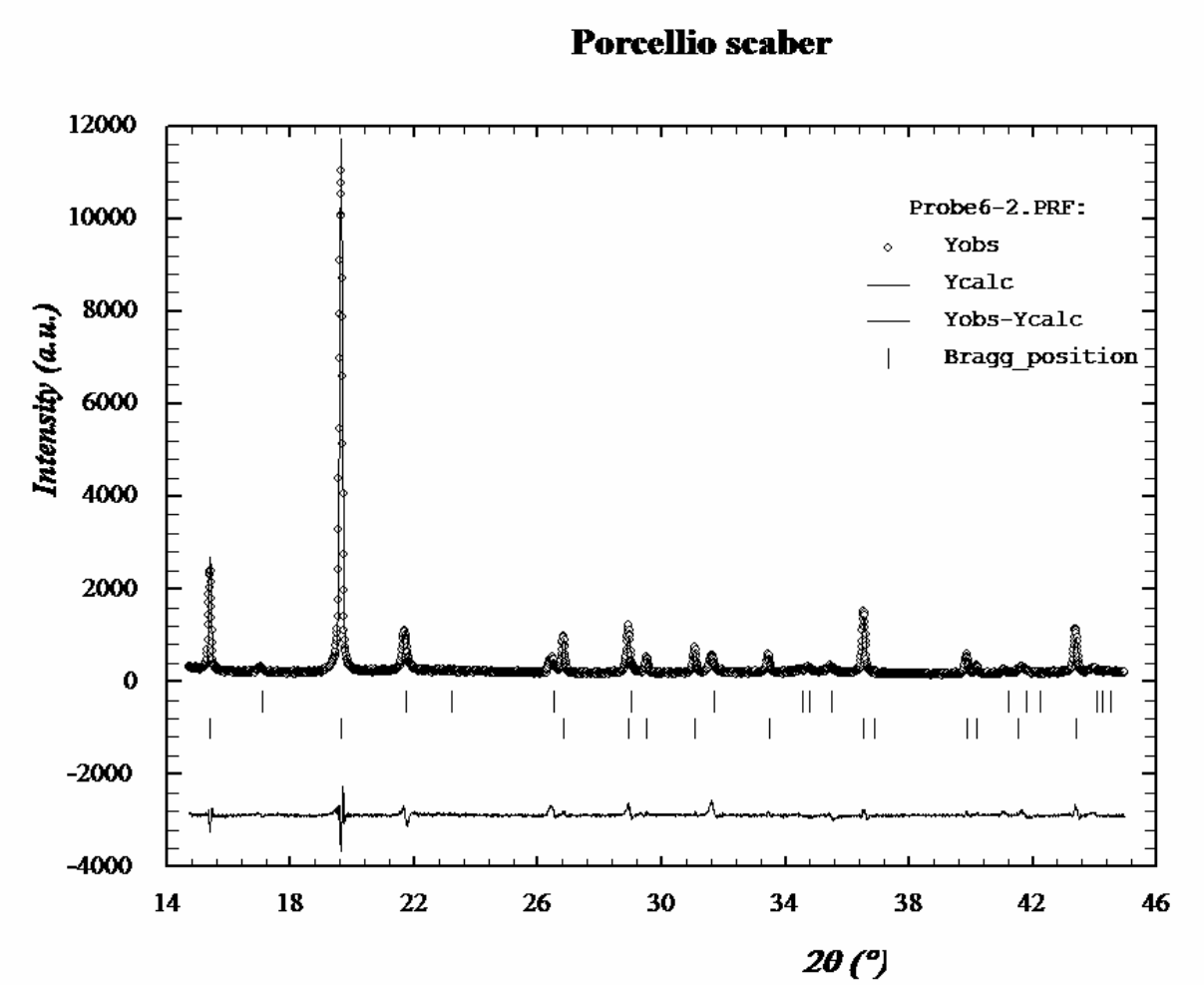

Fig. 3.2-13: Image of a Rietveld refinement fit plot. The dots indicate the observed pattern. The solid line is the calculated pattern. The difference between observed and calculated pattern is shown in the curve below.

proportion of quartz in crystalline material obtained by quantitative phase analysis [cry-wt%]. By subtracting the known mass of quartz from the mass of the diffracting material of the mixture, the mass of calcite can be determined by

$$m(\text{calcite}) = m(\text{cryst}) - m(\text{quartz}) \qquad \text{(eq. 3.2.5-2)}$$

with m(calcite) being the mass of calcite in the mixture and thus in the cuticle [mg], m(cryst) the overall mass of diffracting material in the mixture [mg] and m(quartz) the mass of quartz [mg]. With this value and the mass of the sample known, the weight ratio [wt%] of crystalline material (calcite) and amorphous material in the cuticle sample can be calculated according to

Table 3.2-3 Results of the quantitative phase analysis of the diffractograms of 1:1=*w*:*w*-mixtures of cuticle and quartz standard (A) and the magnesium content determination after the Goldsmith method (see Appendix) with cell constants obtained during Rietveld refinement (B). Values are explained in the text.

A	**masses used**				**Rietveld refinement**			**calculated values**			
Sample	**sample m [mg]**	**quartz m [mg]**	**mass m [mg]**	**quartz mix-wt%**	**RV calcit cry-wt%**	**RV quartz cry-wt%**	**R^2**	**cryst. m [mg]**	**calcite m [mg]**	**cryst. material wt%**	**amor. material wt%**
A. officinalis	4.46	4.63	9.09	50.94	10.98	89.02	5.24	5.20	0.57	13	87
A. vulgare	3.95	3.80	7.75	49.03	10.10	89.90	2.88	4.23	0.43	11	89
O. asellus	1.97	1.85	3.82	48.43	15.45	84.55	2.77	2.19	0.34	17	83
P. scaber	3.51	3.57	7.08	50.42	12.51	87.49	2.81	4.08	0.51	15	85
P. spinicornis	2.56	2.58	5.14	50.19	14.66	85.34	3.03	3.02	0.44	17	83
L. hypnorum	2.20	2.09	4.29	48.72	9.26	90.74	1.95	2.30	0.21	10	90
H. brevicornis	2.39	2.52	4.91	51.32	27.49	72.51	2.18	3.48	0.96	40	60
T. europeans	5.46	5.44	10.90	49.91	19.51	80.49	6.32	6.76	1.32	24	76

B	**Rietveld refinement**		**Goldsmith method**			**calculated values**		
Sample	***a*-axis [Å]**	***c*-axis [Å]**	**Mg content *a*-axis mol% Calcite**	**Mg content *c*-axis mol% Calcite**	**average Mg content mol% Calcite**	**M (Mg-calcite) g mol^{-1}**	**Mg content of calcite wt% calcite**	**Mg content of calcite wt%**
A. officinalis	4.966	17.000	5.3	2.8	4.1	99.36	0.99	0.13
A. vulgare	4.971	17.010	4.2	2.4	3.3	99.49	0.80	0.09
O. asellus	4.985	17.009	1.0	2.4	1.7	99.73	0.42	0.07
P. scaber	4.967	17.012	5.1	2.3	3.7	99.42	0.89	0.13
P. spinicornis	4.981	17.030	1.9	1.4	1.7	99.73	0.41	0.07
L. hypnorum	4.990	17.034	-0.1	1.3	0.6	99.91	0.14	0.01
H. brevicornis	4.975	17.017	3.3	2.0	2.7	99.58	0.65	0.26
T. europeans	4.971	16.924	4.2	6.3	5.2	99.17	1.29	0.31

$$w(\text{calcite}) = \frac{m(\text{calcite}) \cdot 100}{m(\text{sample})} \qquad \text{(eq. 3.2.5-3)}$$

with w(calcite) being the mass proportion of calcite in the cuticle sample [wt%], m(calcite) the mass of calcite determined [mg] and m(sample) the overall mass of the sample [mg]. Except for *Helleria brevicornis* with 40 wt% and *Tylos eurpopeans* with 24 wt%, all samples show about 13 wt% of calcite in the cuticle.

By applying the Rietveld method during quantitative phase analysis of the diffractograms, the values for the cell parameters (axes and angles) of calcite are also obtained. These correspond to the peak positions of the material in 2Θ space. During calculation, the cell parameters of the model (calcite) had to be refined because the calcite peak positions did not match with the peak positions observed. This observation corresponds to the content of magnesium incorporated in calcite on calcium positions. The more calcium is replaced by magnesium, the smaller the elementary cell becomes (Vegard's rule). Goldsmith *et al*. quantified the relation of magnesium incorporated in calcite [mol%] to the cell axis length.[80] Their values and the calculated linear correlations can be found in the appendix. Table 3.2-3b comprises the results obtained. From the cell axis values, the content of magnesium is calculated. The values vary considerably, depending on whether *a*-axis or *c*-axis values were taken for calculation. This is due to the biogenic origin of the samples. Goldsmith *et al*. used mineral magnesium calcite for their calculations and the Rietveld method covers simple models of preferred orientation only (see chapters 9.2 and 5.1, respectively). As a result, the average of both values was used for further estimations, not giving exact values but close estimates of the proportion of magnesium incorporated in the biogenic calcite. With the content of magnesium carbonate in calcite known, the molar mass of the individual magnesium calcite can be calculated by

$$M(\text{MgCalcite}) = \frac{(100 - x) \cdot 100.0872 + x \cdot 84.3412}{100} \quad \text{(eq. 3.2.5-4)}$$

with M(MgCalcite) being the molar mass of the magnesium calcite [g mol^{-1}] and x the proportion of magnesium carbonate [mol%]. This value is used to determine the weight proportion of magnesium in calcite by

$$w(\text{Mg, calcite}) = \frac{x \cdot 24.305}{\text{M}(\text{MgCalcite})} \quad \text{(eq. 3.2.5-5)}$$

with w(Mg, calcite) being the mass proportion of magnesium in calcite [wt% calcite], x the proportion of magnesium carbonate [mol%] and M(MgCalcite) the molar mass of the magnesium calcite calculated above [g mol^{-1}]. Finally, the mass proportion of magnesium in calcite in the sample can be determined by

$$w(\text{Mg}) = \frac{w(\text{calcite}) \cdot w(\text{Mg, calcite})}{100} \quad \text{(eq. 3.2.5-6)}$$

with w(Mg) being the mass proportion of magnesium in calcite in the sample [wt%], w(calcite) being the mass proportion of calcite in the sample [wt%] and w(Mg, calcite) being the mass proportion of magnesium in calcite [wt% calcite]. Unfortunately, for an application of the rest of the methods (TGA and AAS), there was insufficient material remaining in some samples. For *Armadillidium vulgare, Porcellio scaber, Ligidium hypnorum* and *Tylos europeans*, elementary analysis was possible. The samples consist of about 24 to 30 wt% of calcium and about 0.6 to 1.2 wt% of magnesium. There is no correlation between overall calcium and magnesium content. Table 3.2-4a comprises the results.

Table 3.2-4: Results of the elementary analysis and of the thermogravimetric analysis of the cuticle samples (A) and calculations on the base of the values obtained (B). Unfortunately, only for *A. vulgare* and *P. scaber* enough material for all methods was available. Values are explained in the text.

A	**From table 3.3-3**		**AAS**		**TGA**			**calculated values**		
Sample	**calcite wt%**	**Mg content of calcite wt%**	**Ca wt%**	**Mg wt%**	**water wt%**	**organic wt%**	**CO_2 wt%**	**TGA residue wt%**	**$CaCO_3$ from CO_2 wt%**	**ACC wt%**
A. officinalis	13	0.13	-	-	-	-	-	-	-	-
A. vulgare	11	0.09	29.8	0.72	9.7	11.7	28.5	50.1	64.8	54.0
O. asellus	17	0.07	-	-	-	-	-	-	-	-
P. scaber	15	0.13	24.3	0.71	8.0	24.8	21.8	45.4	49.5	35.0
P. spinicornis	17	0.07	-	-	-	-	-	-	-	-
L. hypnorum	10	0.01	30.2	0.59	-	-	-	-	-	-
H. brevicornis	40	0.26	-	-	10.6	6.6	29.4	53.4	66.8	26.8
T. europeans	24	0.31	26.8	1.25	-	-	-	-	-	-

B	**calculated values**			
Sample	**Ca in $CaCO_3$ wt%**	**Ca not in $CaCO_3$ wt%**	**amorphous Ca-phosphate wt%**	**Mg not in calcite wt%**
A. officinalis	-	-	-	-
A. vulgare	26.0	3.8	9.7	0.63
O. asellus	-	-	-	-
P. scaber	19.9	4.4	11.2	0.58
P. spinicornis	-	-	-	-
L. hypnorum	-	-	-	0.58
H. brevicornis	26.8	-	-	-
T. europeans	-	-	-	0.94

The samples *Armadillidium vulgare, Porcellio scaber* and *Helleria brevicornis* had sufficient material left for thermogravimetric analysis. Samples were heated to 1000°C under oxygen atmosphere. This led first to the release of incorporated water. The samples contained about 8 to 10 wt% of water, which left the samples up to 200°C in an endothermic process as determined by dynamic scanning calorimetry (DSC, data not shown). From about 200 to 600°C, organic material fused and left the sample in an exothermic process. Between 7 and 25 wt% of organic material were found. Above 600°C, carbonate decarboxylates and carbon dioxide leaves the sample. About 22 to 30 wt% of carbon dioxide were detected. Figure 3.2-14 shows the TGA diagrams of the three samples and Table 3.2-4 summarises the values. About 50 wt% of the sample remain as residue. From the mass of carbon dioxide leaving the sample, the mass of calcium carbonate can be calculated, assuming all carbonate is contained in calcium carbonate mineral:

$$w(\mathrm{CaCO_3}) = \frac{w(\mathrm{CO_2}) \cdot 100.0872}{44.0098} \qquad \text{(eq. 3.2.5-7)}$$

with $w(CaCO_3)$ being the mass proportion of calcium carbonate [wt%] and $w(CO_2)$ the mass proportion of carbon dioxide from TGA [wt%]. With about 50 to 67 wt% the overall amount of calcium carbonate is far greater than the amount of calcite determined, therefore the excess of calcium carbonate must be present in the amorphous state:

$$w(\mathrm{ACC}) = w(\mathrm{CaCO_3}) - w(\mathrm{calcite}) \qquad \text{(eq. 3.2.5-8)}$$

This calculation reveals that about 27 to 54 wt% of the cuticle consist of amorphous calcium carbonate. However, elementary analysis showed a lot more calcium residing in the samples than bound in calcium carbonate (see Table 3.2-

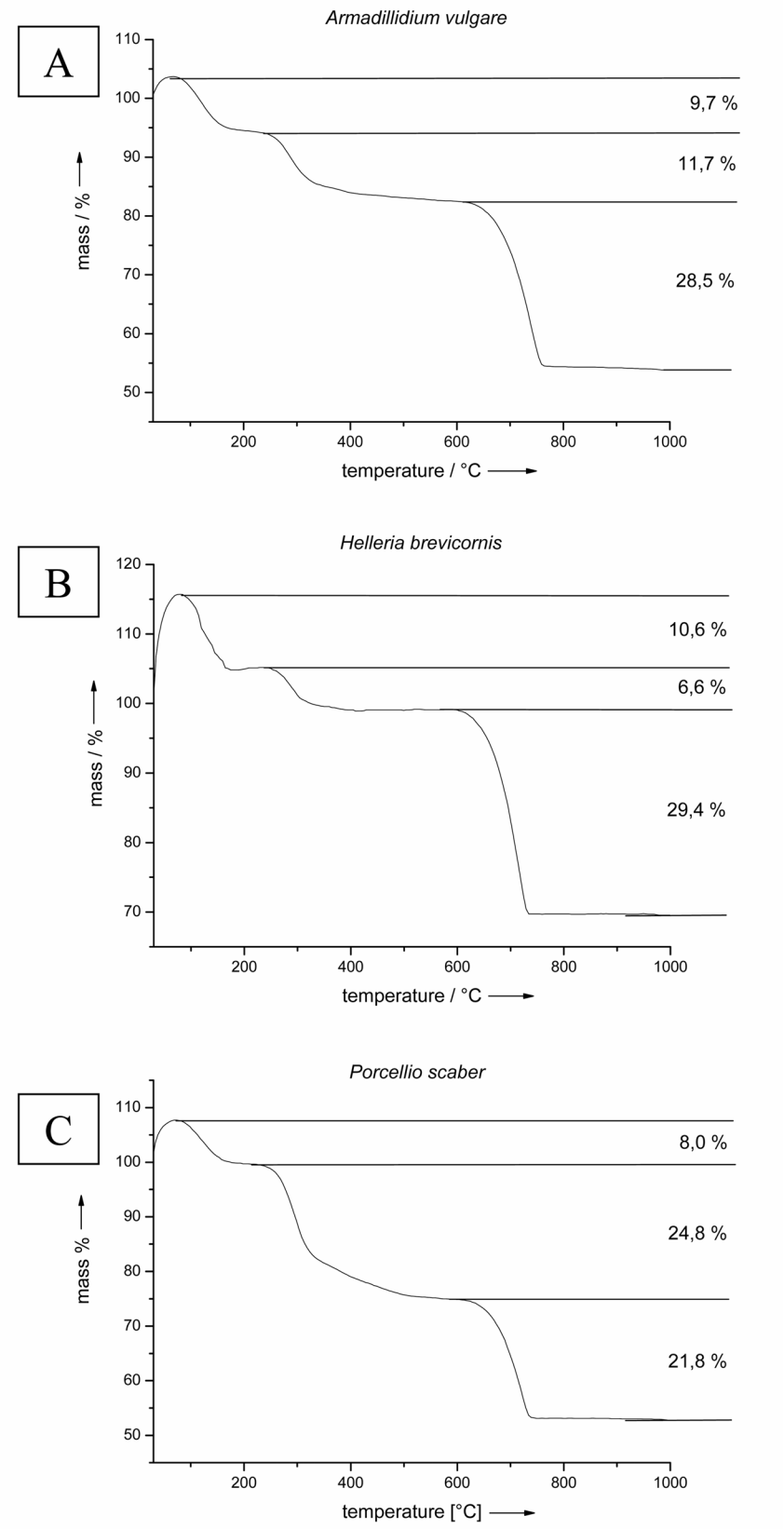

Fig. 3.2-14: TGA curves of cuticula samples of *Armadillidium vulgare* (A), *Helleria brevicornis* (B), and *Porcellio scaber* (C). In all cases, a three-step mass loss is observed. In the first step, water leaves the sample. In the second step, the organic components are combusted. In the final step, calcium carbonate decarboxylates.

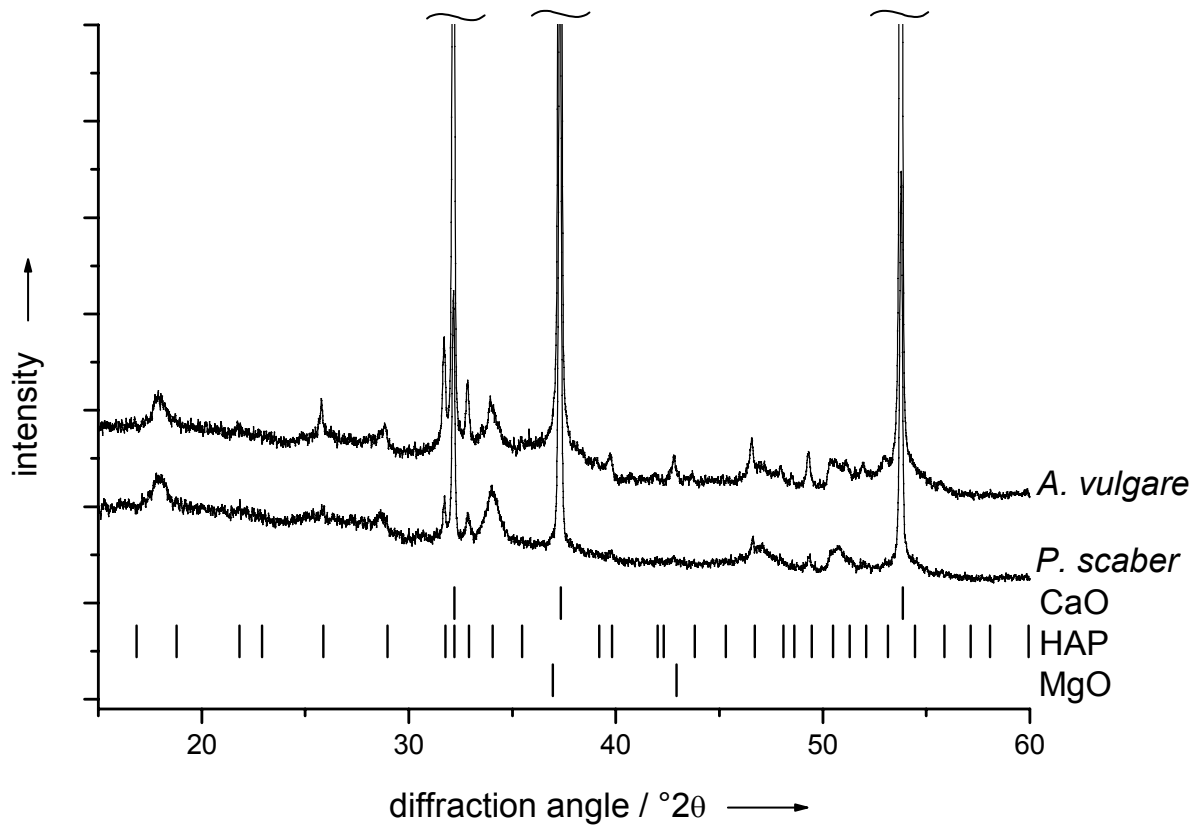

Fig. 3.2-15: Powder X-ray diffraction patterns of the thermal analysis residues. The bars indicate the Bragg reflex positions of the mentioned minerals (HAP=hydroxyapatite).

4b). From the biological point of view, the remaining about 4 wt% of calcium cannot arise from possible dried body fluids during sample preparation. X-ray diffractograms of the TGA residues are shown in Figure 3.2-15 and allow the identification of calcium oxide, magnesium oxide and hydroxyapatite (HAP). While the presence of magnesium oxide can be ascribed to the decomposition of magnesium calcite, the presence of HAP indicates either that amorphous calcium phosphate (ACP) constitutes a considerable proportion of the cuticle or that a reaction took place during heating between organic phosphorous-containing components i.e. phosphorylated proteins. However, it is known that both magnesium as well as carbonate can be incorporated as ionic substituents in crystalline and amorphous calcium phosphate.[194] The amount of calcium in the demineralised cuticle of *Porcellio scaber* was determined earlier to be 136 mmol (kg dry mass)$^{-1}$, equivalent to 0.55 wt% in the dry mass.[172] The calcium excess of 4.4 wt% in the wet mass is far too high to be explained as residue of

hemolymph or tissue ("organic calcium"). Therefore, it can be concluded that the excess calcium must be associated to a mineral phase which cannot be calcium carbonate based on the thermogravimetric results. The content of phosphorous in the fully mineralised cuticle was determined to 619 mmol (kg dry mass)$^{-1}$,[172] yielding 10.4 wt% of hydroxyapatite if it is assumed that all phosphorous is of inorganic origin. In the demineralised cuticle, the phosphorous content was 10.4 mmol (kg dry mass)$^{-1}$, equivalent to 0.17 wt% of HAP (given for comparison). Consequently, almost all phosphorous belongs to the mineral phase and does not originate from organic components of the cuticle which are still all present after demineralisation. Assuming that phosphorous in the mineral phase is present as phosphate, this compound would make up 5.9 wt% of the dry, fully mineralised cuticle. Furthermore assuming that all phosphate is present in a mineral phase with HAP stoichiometry, the calcium phosphate mineral phase is present in the dry cuticle with 10.4 wt%.

The detection of crystalline hydroxyapatite in the residues from thermogravimetry, the absence of a phosphate mineral in the X-ray diffractograms of the mineralised cuticles, and the difference between the content of phosphorous in the mineralised and the demineralised cuticle support the assumption that the excesss calcium is present as amorphous calcium phosphate. Tentatively assuming the stoichiometry of hydroxyapatite, $Ca_5(PO_4)_3OH$, for ACP, the content of ACP can be computed by

$$w(\mathrm{ACP}) = \frac{w(\mathrm{Ca, excess})}{40.078} \cdot \frac{502.3103}{5} \qquad \text{(eq. 3.2.5-9)}$$

with w(ACP) being the mass proportion of amorphous calcium phosphate [wt%] and w(Ca, excess) being the mass proportion of calcium not bound in calcium carbonate [wt%].

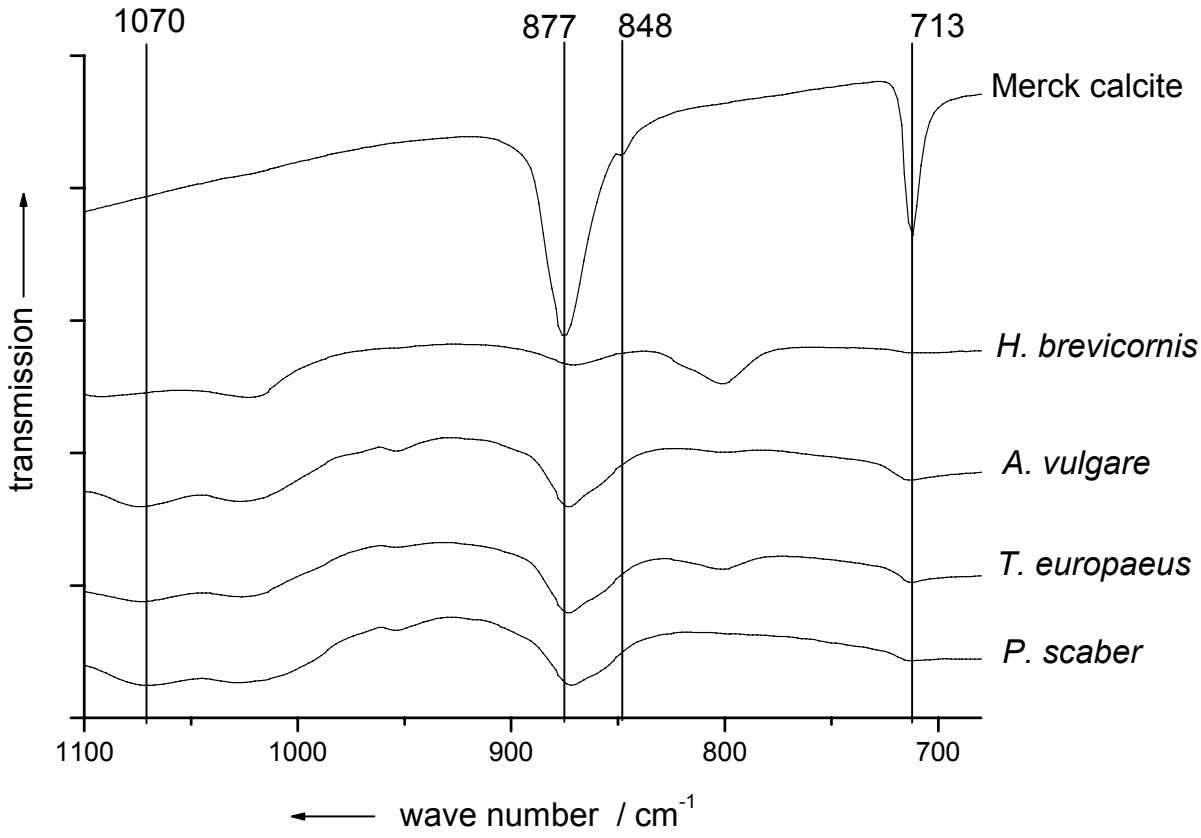

Fig. 3.2-16: Infrared spectra of cuticle samples. For comparison, the spectrum of calcite is shown. The relativly high ratio of the 877 cm^{-1} to 713 cm^{-1} peak in the cuticle spectra gives a hint to the presence of amorphous calcium carbonate. See the text for details.

Elementary analysis showed furthermore that most magnesium is present in the amorphous components of the cuticle, not in the calcite. This finding is in accordance with the literature. Magnesium is known to stabilise amorphous calcium carbonate.[100, 110]

The presence of ACC is also indicated by infrared spectroscopy (IR). The IR bands at 877 and 848 cm^{-1} correspond to the ν_2 out-of-plane bending and that at about 713 cm^{-1} to the ν_4 planar bending of the carbonate group in calcitic minerals.[195, 196] The ν_4 band position depends on the amount of magnesium present in the sample. In the infrared spectra of the biological samples no significant shift of this band could be detected (Figure 3.2-16). This is in accordance with the literature for the amounts of magnesium determined in the samples.[197] In comparison to pure calcite, the sample spectra show a high ratio between the ν_2 and the ν_4 band intensities. While at high magnesium contents in

calcite the ν_2/ν_4 ratio also increases, this effect is negligible for the amount of magnesium present here.[198] In stable biogenic ACC, the ν_2 band is found at about 866 cm^{-1} and considerably broadened compared to crystalline material.[122] The cuticle spectra show asymmetric broad peaks with maxima at 877 cm^{-1} and long tails up to 850 cm^{-1}, indicating the presence of the ACC peak at 866 cm^{-1} below the calcite band at 877 cm^{-1}. Furthermore, stable biogenic ACC infrared spectra show a high ν_2/ν_4 intensity ratio as it can be found here, indicating the presence of ACC in the samples. At 1070 cm^{-1}, a broad peak of phosphate is visible, indicating the presence of a calcium phosphate phase. Unfortunately, in the region of 950 to 1200 cm^{-1} the organic matrix of the cuticula also gives rise to infrared absorption.

X-ray absorption spectroscopy (EXAFS) has turned out to be a powerful tool for the analysis of amorphous calcium carbonate phases as seen above. However, if two calcium-containing phases are present in a sample, the weighed overlap of both calcium environments is observed. In the case of the cuticles, EXAFS spectra of calcite together with those of ACC and ACP are expected. However, because calcium carbonate (=calcite+ACC) is always the major component, it can be expected that the spectrum will be dominated by this compound. The EXAFS results, also for reference compounds, are comprised in Table 3.2-5. The results for the first shell (Ca-O) suggest that the mineral phase in the cuticles consists of a calcitic or a monohydrocalcitic phase. The fourth shell (Ca-Ca) also suggests that the mineral phase in the cuticles consists of a calcitic phase. Taking into account the high content of ACC compared to calcite (2.5:1 for *Porcellio scaber* and 5:1 for *Armadillidium vulgare*), it may therefore be assumed that the ACC also has a calcite-like short-range order. The amount of calcium phosphate is probably too small to be visible in the EXAFS spectrum.

As stated above, there was not sufficient material from all species to apply all methods to all samples. Only for *Armadillidium vulgare* and *Porcellio scaber*

Tab. 3.2-5: Results of the EXAFS analysis of amorphous calcium carbonate phase in the cuticles of *Porcellio scaber* and *Armadillidium vulgare* in comparison with ACC phases from literature.

Sample	1st shell: Ca-O			2nd shell: Ca-C			3rd shell: Ca-O			4th shell: Ca-Ca		
	R [Å]	N	$\sigma^2 \cdot 10^3$ [Å^2]	*R* [Å]	N	$\sigma^2 \cdot 10^3$ [Å^2]	*R* [Å]	N	$\sigma^2 \cdot 10^3$ [Å^2]	*R* [Å]	N	$\sigma^2 \cdot 10^3$ [Å^2]
calcite[199]	2.34	6	9	3.30	6C	35	3.64	6O	16	4.05	6	9
aragonite[199]	2.47	9	33	2.98	3C	3	3.26	3C	10	3.94	6	28
vaterite[199]	2.37	6	7	3.09	2O, 2C	21	-	-	-	4.24	6	15
monohydrocalcite[189]	2.37	7.4	9	3.03	1.5C	7	3.36	3C	0	-	-	-
ACC in larval shells of *Biomphalaria glabrata*[190, 200]	2.44			-			-			3.92		
ACC in carapaces of *Homarus american*[187]	2.27			-			3.47			3.79		
ACC in plant cystoliths of *Ficus micro-carpa*[187]	2.31			-			3.48			3.79		
ACC in plant cystoliths of *Ficus retusa*[188]	2.36			3.22			3.39			4.06		
ACC in spicules of *Pyura Pachyderma-tina*[189]	2.37			3.03			3.36			-		
ACC in sternal deposits of *Porcellio scaber*[199]	2.38			3.00			3.72			(3.89)		
cuticula of *P. scaber*	2.37	5.1	10	2.99	2.2	48	3.64	1.0	0	4.05	6	38
cuticula of *A. vulgare*	2.37	6.6	12	3.00	2.4	-23	3.64	0.8	0	4.02	6	35

enough material allowed a full analysis. All calculations have been done with respect to the sample mass including water. Because the content of magnesium in calcite is much smaller than the content of pure calcite, the influence of magnesium on the above gravimetric results was intentionally neglected. Of course, these calculations contain a number of simplifications, but taking into account the limits of the methods applied, the results still give a good impression of the relative fractions of all components in the cuticle of terrestrial isopods. For *Armadillidium vulgare* and *Porcellio scaber*, the results have been converted to the samples' dry masses. These results are comprised in Table 3.2-6. Figure 3.2-17 shows the determined composition of the cuticles in the dry state. The difference between the sum of the components determined by calculation and 100 % is either unknown or due to errors made by simplifications during calculation.

The presence of magnesium calcite, amorphous calcium carbonate and amorphous calcium phosphate within the cuticles of at least two species of terrestrial isopods has considerable functional implications. Interestingly, the

amount of ACC considerably exceeds the amount of calcite (5.1:1 for *Armadillidium vulgare* and 2.5:1 for *Porcellio scaber*). As described above, considerable amounts of calcium carbonate are resorbed from the cuticle (anterior as well as posterior half) during each moult cycle. The high solubility of ACC allows a quick mobilisation of calcium and hydrogen ions. It seems likely that most of the amorphous fraction of $CaCO_3$ is resorbed and recycled during moult, while most of the crystalline part is shed with the old cuticle (see next chapter), explaining the large amounts of ACC in the cuticles. This hypothesis is supported by the difference in the relative amount of ACC between the analysed species. According to Schmalfuß,[201] terrestrial isopods can be grouped by their skeletal construction into a number of categories which are correlated to ecological strategies and behavioural patterns. *Armadillidium vulgare* walks very slowly and its cuticle is very thick and well mineralised as shown. To avoid predation,

Table 3.2-6: Overall composition of the cuticles of the terrestrial isopods *Armadillidium vulgare* and *Porcellio scaber* related to the samples' dry mass.

Species	org. matrix wt%	Mg-calcite wt%	ACC wt%	ACP wt%	Sum wt%
A. vulgare	13.0	12.0	59.8	10.7	95.4
P. scaber	27.0	15.8	38.1	12.2	93.0

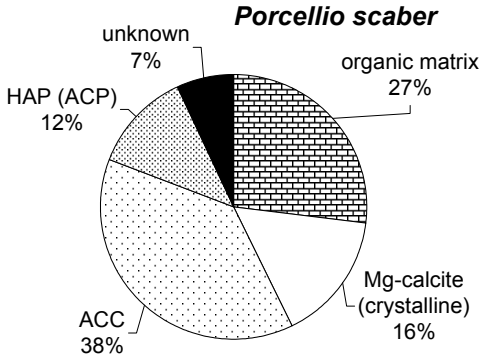

Fig. 3.2-17a: Visualisation of the relative proportions of the contents of the cuticle of *Porcellio scaber.*

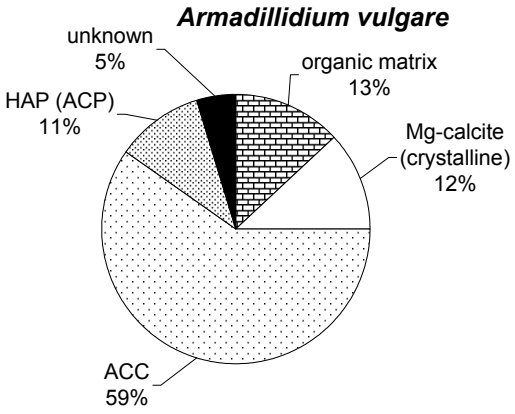

Fig. 3.2-17b: Visualisation of the relative proportions of the contents of the cuticle of *Armadillidium vulgare.*

it rolls itself into a perfectly smooth ball to protect its soft ventral side. The ball often slides out of the gripping mechanism of a predator and rolls into some inaccessible crevice. *Porcellio scaber* cannot roll itself into a ball, however it can run quite fast compared to *Armadillidium vulgare*. In order to avoid predation, *Porcellio scaber* either clings its ventral side to some solid substrate or simply runs away. Therefore, the cuticle of *Porcellio scaber* is thinner, less mineralised and more flexible than that of *Armadilldium vulgare*. In this context, a higher proportion of ACC in the cuticle of *Armadillidium vulgare* compared to the amount of ACC in the cuticle of *Porcellio scaber* makes perfect sense, since a larger amount of $CaCO_3$ must be stored and recycled during moult.

Significant amounts of magnesium and phosphorus in addition to calcium are found in the cuticle of virtually all crustaceans including terrestrial isopods.[172, 202-204] The relative concentration of these elements, however, varies considerably between species. Our data indicate that in the intermoult phase cuticles of terrestrial isopods, a proportion of cuticular magnesium occurs within the lattice of crystalline calcite. This may affect the mechanical properties of the cuticle because Mg-calcite is harder than calcite without magnesium, suggesting that it is formed for functional reasons. However, at the present stage of investigation it cannot be excluded that Mg-calcite is formed as a side effect of calcite crystal "poisoning" during ACC formation.

It is believed that much of the phosphorous in crustacean cuticles occurs in organic form such as phospholipids. Phospholipids are a major component of cellular plasma membranes and the crustacean cuticle contains numerous cellular extensions that account for part of the phosphorous content.[205] The results presented here indicate that most phosphorous within the cuticle of terrestrial isopods occurs as amorphous calcium phosphate. This is in accordance with previous studies on the elemental composition in the cuticle and the sternal deposits of *Porcellio scaber* that suggest that up to 14 % of cuticular calcium and 9 % of the calcium deposits occur as an amorphous

calcium phosphate compound.[172] Amorphous calcium phosphate is more soluble than its crystalline phases.[206] The use of calcium phosphate in its amorphous form, therefore, suggests that it is subject to resorption and recycling during the frequent moulting cycles of terrestrial isopods, as proposed above for amorphous $CaCO_3$.

3.2.6 The mineral phases in the cuticle of *Porcellio scaber* during the moult cycle

As shown in the previous chapter, the main mineral components of the cuticle of *Porcellio scaber* in intermoult stage are calcite, amorphous calcium carbonate, and amorphous calcium phosphate. In order to verify the hypothesis that ACC from the cuticle is resolved during moult and most crystalline material is shed with the cuticle, samples from *Porcellio scaber* in different stages of moult were examined with synchrotron X-ray powder diffraction (XRD) and atomic absorption spectroscopy (AAS) for elementary analysis. The moult cycle was empirically divided into seven stages by A. Ziegler. For each stage, the cuticles of several animals were pooled, separated by anterior cuticle and posterior cuticle. Two sets of pools of seven stages for each body half were sampled. Stage one corresponds to the phase with moderately developed deposits (premoult). Stage two is in late pre-moult with fully developed deposits, shortly before the shed of the posterior cuticle. Therefore, calcium carbonate from the posterior cuticle is in resolving process. Stage three is directly after shed of the posterior cuticle, when calcium carbonate from the anterior cuticle and from the storage deposits is fully dissolved to mineralise the new posterior cuticle. Stage four is after shed of the anterior cuticle. The fifth stage is one day after anterior moult when the cuticle is not yet fully mineralised. Stage six is 6-7 days after anterior moult, and stage seven is 12-14 days after anterior moult. These two

Tab. 3.2-7a: Results of the quantitative phase and the elementary analysis of the cuticle samples of *Porcellio scaber* in seven different moult stages of set I. Calculations are made on the base of the values obtained. Values are explained in the text.

	masses used		Rietveld		calculcated		AAS	calculated		Rietveld	AAS	calculated	
stage	sample m [mg]	quartz m [mg]	RV calcit cry-wt%	RV SiO_2 cry-wt%	calcite m [mg]	calcite wt%	Ca wt%	ACC wt%	ACC/cal. ratio	Mg in calcite cry-wt%	Mg wt%	Mg in ACC am-wt%	Mg ratio cry/am.
I 1 A	7.22	7.19	6.89	93.11	0.53	7	22.2	48.1	6.5	0.332	0.55	1.09	0.304
I 1 P	7.73	7.92	5.28	94.72	0.44	6	23.6	53.3	9.3	0.431	0.54	0.97	0.446
I 2 A	8.81	8.88	4.39	95.61	0.41	5	23.0	52.8	11.4	0.416	0.64	1.17	0.354
I 2 P	6.02	6.95	6.33	93.67	0.47	8	23.8	51.7	6.6	0.190	0.66	1.25	0.152
I 3 A	8.04	8.42	3.26	96.74	0.28	4	20.0	46.4	13.1	0.269	0.52	1.09	0.247
I 3 EP	4.69	4.36	26.81	73.19	1.60	34	28.1	36.0	1.1	0.547	0.71	1.45	0.376
I 4 EA	3.88	3.12	14.15	85.85	0.51	13	27.0	54.1	4.1	0.317	0.56	0.96	0.331
I 4 P	7.82	7.38	3.21	96.79	0.24	3	25.1	59.6	19.1	0.267	0.64	1.05	0.254
I 5 A	3.97	3.43	8.45	91.55	0.32	8	24.6	53.4	6.7	0.289	0.65	1.18	0.246
I 5 P	6.56	6.32	29.83	70.17	2.69	41	21.4	12.5	0.3	0.233	0.58	3.83	0.061
I 6 A	9.46	10.89	4.29	95.71	0.49	5	19.4	43.2	8.4	0.296	0.71	1.61	0.184
I 6 P	11.35	11.56	6.55	93.45	0.81	7	23.8	52.3	7.3	0.236	0.65	1.21	0.195
I 7 A	5.64	6.10	8.39	91.61	0.56	10	23.6	49.0	4.9	0.433	0.66	1.26	0.344
I 7 P	5.68	5.13	6.98	93.02	0.38	7	24.4	54.1	8.0	0.337	0.66	1.18	0.286

Tab. 3.2-7b: Results of the quantitative phase and the elementary analysis of the cuticle samples of *Porcellio scaber* in seven different moult stages of set II. Calculations are made on the base of the values obtained. Values are explained in the text.

	masses used		Rietveld		calculcated		AAS	calculated		Rietveld	AAS	calculated	
stage	sample m [mg]	quartz m [mg]	RV calcit cry-wt%	RV SiO_2 cry-wt%	calcite m [mg]	calcite wt%	Ca wt%	ACC wt%	ACC/cal. ratio	Mg in calcite cry-wt%	Mg wt%	Mg in ACC am-wt%	Mg ratio cry/am.
II 1 A	5.45	5.91	3.58	96.42	0.22	4	22.6	52.4	13.0	0.240	0.62	1.17	0.206
II 1 P	4.40	3.92	11.75	88.25	0.52	12	23.2	46.0	3.9	0.231	0.62	1.29	0.179
II 2 A	8.69	9.32	7.96	92.04	0.81	9	24.1	50.9	5.5	0.494	0.58	1.05	0.470
II 2 P	6.61	5.78	12.74	87.26	0.84	13	26.1	52.3	4.1	0.450	0.61	1.05	0.430
II 3 A	4.94	3.91	5.86	94.14	0.24	5	23.9	54.8	11.1	0.034	0.57	1.03	0.033
II 3 EP	4.36	3.56	14.54	85.46	0.61	14	26.0	50.9	3.7	0.267	0.61	1.13	0.237
II 4 EA	4.05	3.95	7.50	92.50	0.32	8	26.0	57.0	7.2	0.337	0.48	0.79	0.424
II 4 P	6.82	5.57	20.86	79.14	1.47	22	23.5	37.1	1.7	0.226	0.49	1.17	0.192
II 5 A	4.14	4.65	1.57	98.43	0.07	2	23.5	56.8	31.7	0.409	0.57	0.99	0.413
II 5 P	4.54	4.60	9.60	90.40	0.49	11	23.6	48.2	4.5	0.260	0.52	1.02	0.255
II 6 A	8.62	7.46	8.18	91.82	0.66	8	21.6	46.2	6.0	0.086	0.59	1.26	0.069
II 6 P	7.23	7.26	8.86	91.14	0.71	10	22.8	47.2	4.8	0.159	0.58	1.20	0.133
II 7 A	5.13	5.04	10.49	89.51	0.59	12	22.3	44.1	3.8	0.260	0.59	1.27	0.205
II 7 P	4.42	3.16	19.02	80.98	0.74	17	23.7	42.4	2.5	0.593	0.61	1.20	0.493

stages are defined as the intermoult phase. In stage three the shed posterior cuticle and in stage four the shed anterior cuticle (exuvia) were examined.

As described in the previous chapter, 1:1=*w*:*w*-mixtures of cuticle sample and quartz were examined with XRD and the resulting diffractograms calculated with the Rietveld method for quantitative phase analysis. Table 3.2-7a comprises the results for set I and Table 3.2-7b for set II. The computation of the calcite and magnesium in calcite content followed the procedure described in the preceeding chapter. From elementary analysis, the overall content of calcium is known. Assuming that all calcium is bound as calcium carbonate (without TGA, it is not possible to determine the content of ACP), the content of calcium carbonate can be calculated [wt%]. Subtracting the content of calcite, the content of amorphous calcium carbonate is computed [wt%], allowing to calculate the ratio of ACC to calcite in each stage. From the amount of magnesium determined by AAS, the amount of magnesium in calcite is subtracted and the content of magnesium in the amorphous fraction of the sample can be calculated. Both values can be used to determine the ratio of magnesium in ACC to calcite, thus making any possible magnesium flows during moult visible.

Figure 3.2-18 shows the weight ratios of ACC to calcite and of magnesium in ACC to magnesium in calcite for both sets. In set I, a biologically interpretable change in the weight ratio of ACC to calcite during moult can be seen. From stage 1 to 3, the ratio in the posterior cuticle decreases, pointing to the mobilisation of ACC in preparation for moult which occurred in stage 3. In the anterior cuticle, the ratio increases, pointing either to a deposition of new ACC, which is unlikely, or to a dissolution of magnesium calcite which may be possibly deposited again in the form of ACC.[207] In stage 4, the new posterior cuticle is mineralised and ACC deposited which crystallises to magnesium calcite thus reducing the ratio (stage 5). The anterior cuticle shows an increasing

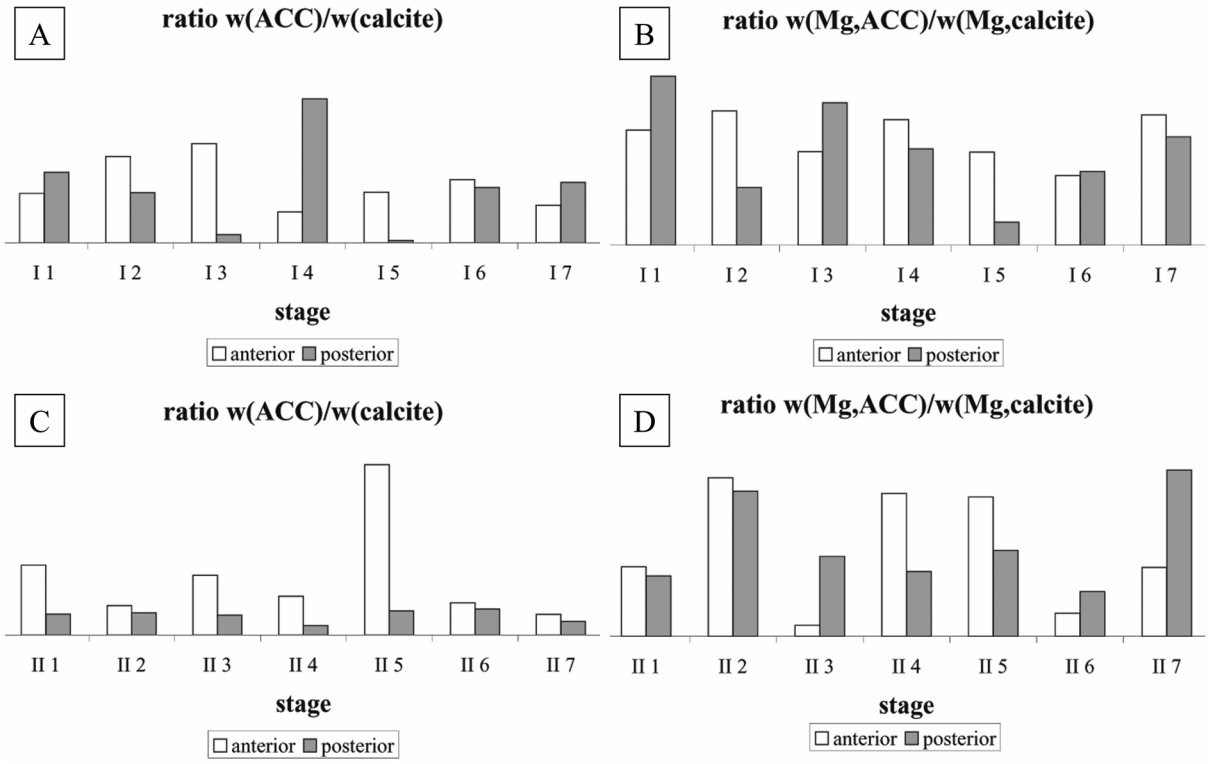

Fig. 3.2-18: Weight ratio of ACC to calcite (A) and the weight ratio of magnesium in ACC to magnesium in calcite (B) for set I. Image C shows the weight ratio of ACC to calcite for set II. Image D shows the magnesium weight ratio for both phases in set II. Whereas in set I a correlation between moult stage and ACC content can be identified, this result was not verified in set II.

ratio, pointing to ACC reduction (Mg-calcite formation). In the last stages with further calcium carbonate deposition, the ratio stabilises in both parts of the animal. Unfortunately, set II does not confirm these findings. However, in both sets, no correlation of magnesium in amorphous or crystalline fraction in anterior or posterior cuticle could be determined.

A flow of calcium carbonate during moult could be seen but not verified. No visible correlation in magnesium content to moult stage could be detected. Further investigations to prove the findings are necessary.

3.3 Amorphous calcium carbonate in crabs

3.3.1 The crab *Pachygrapsus marmoratus* in biology[208-212]

The phylogenetic relationships of the phylum Arthropoda were explained in chapter 3.2 in detail. Crabs belong to the class Malacostraca of the subphylum Crustacea. In crabs, the protective properties of the arthropod cuticle are easily recognised because the cuticle is strongly mineralised and forms strong armour. The first pair of the decapods' legs has changed during evolution to a pair of strong claws (chelipeds). During animal growth, the crab's exoskeleton is moulted periodically to accommodate size increase as described for woodlice. Different from the woodlice species examined, crabs are marine animals whose need for calcium carbonate storage is limited. They are able to equilibrate the loss of calcium and carbonate by taking these ions up from sea water.

Fig. 3.3-1: The crab *Pachygrapsus marmoratus*.

The crab species examined here was *Pachygrapsus marmoratus* (Brachyura, Grapsidae), living in the rocky midlittoral zone among rocks near the coast. It is common in the Mediterranean Sea, the Atlantic Ocean, and the Black Sea and becomes about 4 cm in length and diameter (excluding the legs). Figure 3.3-1 shows a *Pachygrapsus marmoratus* crab.

3.3.2 Structural characterisation of calcium carbonate in the cuticle of the crustacea *Pachygrapsus marmoratus*

The mineral phase of the cuticle of crabs consists of calcium carbonate.[1] In addition to calcite which can be detected by X-ray diffraction, the presence of amorphous calcium carbonate (ACC) can be seen in the infrared spectra of the mineralised cuticle. In cooperation with Lia Addadi and Steve Weiner (Weizmann Institute of Science, Rehovot, Israel), the carapace of the marbled

crab *Pachygrapsus marmoratus* in different moult stages was investigated with powder and single crystal X-ray diffraction (XRD), thermogravimetric analysis (TGA) and infrared spectroscopy (IR). Furthermore, the soluble organic matrix of the biomineral was extracted and the amino acid composition of the proteins was examined. The behaviour of the soluble organic matrix was investigated in crystallisation experiments. The overall structure of the cuticle before and after protein extraction was investigated by scanning electron microscopy (SEM). Specimens were sacrificed by immersion into liquid nitrogen. The carapace was cleaned from organic material and ground to a powder.

As described in chapter 2.2.3, amorphous calcium carbonate (ACC) can be found as a stable biogenic compound, forming a biomineral of its own. ACC is further found as a precursor phase for the precipitation of crystalline phases. In the X-ray diffractograms of carapace powder, calcite is present in different quantities. Figure 3.3-2 shows diffractograms of the same amount (about 200 mg) of two samples of the dorsal plate from different specimens and of geological calcite for reference. In comparison to the same amount of calcite, the carapace powders contain less calcite because their peaks are much weaker. Differences in the calcite content in the two specimens can also be seen. The peak positions of the mineral phases of the two specimens differ from those of calcite because of their content of magnesium in calcite.[80] The infrared spectra (Figure 3.3-3) taken from these carapace powders, show the presence of amorphous calcium carbonate. By comparing the relative intensities of the ν_2 out-of-plane bending IR absorption band at 873 cm^{-1} and the ν_4 planar bending of the carbonate group at 716 cm^{-1},[122] a high ν_2:ν_4 peak intensity ratios of 7.3 for animal A and 10.6 for animal B was determined. In geological calcite, this ratio is 2.5 and the peaks are sharp.[184] Furthermore, the ν_4 peak position in the biogenic samples is shifted to higher wave numbers in comparison to calcite due

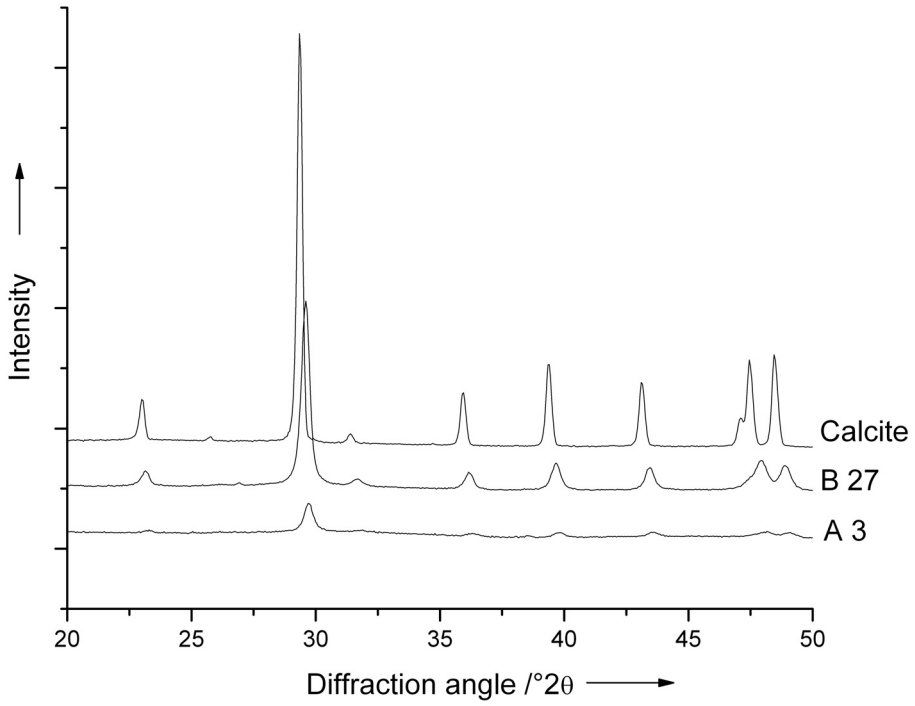

Fig. 3.3-2: X-ray diffraction patterns of samples of about the same weight from the dorsal plate of two different specimens. The calcite pattern is shown for comparison. The peaks of the samples are shifted due to their content of magnesium. Despite the same amount of sample exposed to X-rays, the intensity, and therefore the content of magnesium calcite in the samples, is different.

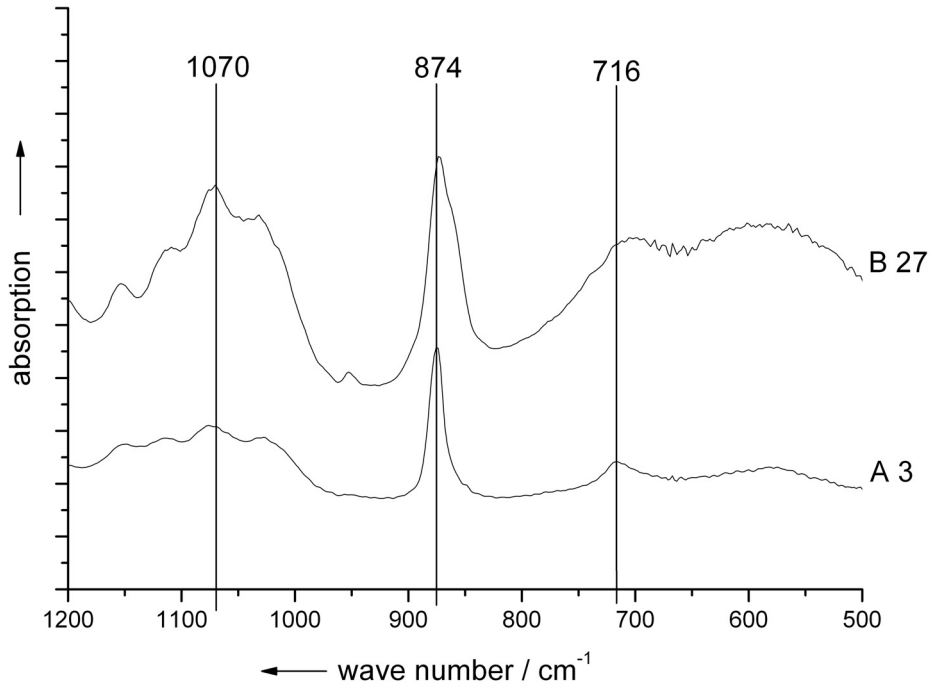

Fig. 3.3-3: Infrared spectra of carapace samples. Relativly high ratios of the 874 cm^{-1} and the 716 cm^{-1} peaks indicate the presence of amorphous calcium carbonate.

to the high magnesium content of the mineral.[79] The high magnesium content also increases the ν_2:ν_4 peak ratio so that the high ratios are caused by mineral lattice distortion (disordered = amorphous phase) as well as the magnesium content. A quantification of each effect is not possible.[79] It should be noted that in stable biogenic ACC, the υ_2 absorption band is red-shifted to about 866 cm^{-1}.[122] This shift is not observed in the ACC phase present here.

Table 3.3-1: Infrared absorption peak positions and magnesium content of two animals and calcite for comparison.[184] Due to magnesium content, the υ_4 band position is blue-shifted in comparison to calcite. In the biogenic samples, the υ_3 band could not be determined due to co-absorption of the organic material in the samples. The υ_2-2 absorption band was covered by the broad υ_2-1 peak.

	unit	Calcite	Animal A	Animal B
υ_3	cm^{-1}	1429	-	-
υ_2-1	cm^{-1}	877	873	872
υ_2-2	cm^{-1}	848	-	-
υ_4	cm^{-1}	713	716	716
υ_2-1: υ_4 ratio		2.5	7.3	10.6
Mg-content	mol%	0	5.98	9.66

The high amount of ACC found in infrared spectroscopy leads to the question whether the calcite found in XRD is either a sample preparation artefact (crystallisation of ACC during storage or preparation) or whether it is present in the animal as a phase of its own. In order to solve this question, fresh specimens were sacrificed by immersion into liquid nitrogen. Samples from the main dorsal plate were taken immediately and examined as a piece in a single crystal diffractometer with image plate detector. This method was chosen to avoid possible artefacts by grinding in preparation for X-ray powder diffraction. The presence of calcite diffraction rings could be determined (see Figure 3.3-4); therefore, the observation of calcite in the cuticle is not a preparation artefact.

During moult, differences in the mineral content of the carapace can be determined. The results are comprised in Table 3.3-2. All specimens investigated were in the intermoult stage (hard cuticle) and in pre- or postmoult stage (soft cuticle). Animals A and L possessed a soft cuticle, whereas animals H and M had a hard cuticle. For the animals with soft cuticle, the exact stage

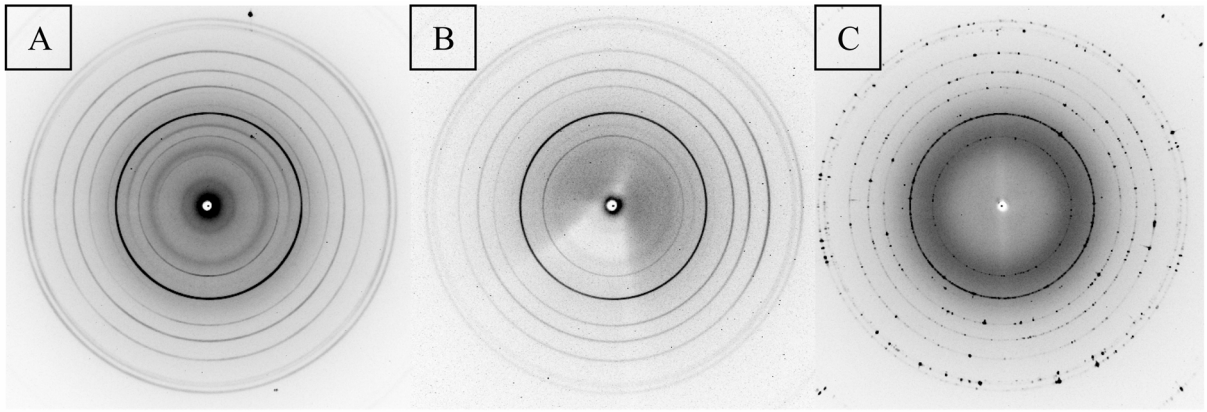

Fig. 3.3-4: Diffraction rings of two different carapace samples of freshly prepared specimens (A, B) and of crystalline geological calcite (C). Therefore, calcite is present in freshly prepared specimens and is not a preparation artefact.

could not be determined correctly due to my lack of biological knowledge. Thermogravimetric analysis was possible for one soft and two hard cuticles. The diagrams are shown in Figure 3.3-5. The water content of the soft cuticle was determined to be 13.0 wt%. A soft cuticle consists of 27.1 wt% organic material and 25.3 wt% carbon dioxide, corresponding to 57.5 wt% of calcium carbonate. On average, hard cuticles consist of 6.5 wt% water, 20.0 wt% organic material, and 29.5 wt% carbon dioxide, corresponding to 67 wt% of calcium carbonate. Thus, the soft cuticle contains less mineral than the hard cuticles.

With X-ray powder diffraction (XRD), the content of magnesium in calcite was determined. Mixtures of 10 wt% sodium chloride and 90 wt% carapace powder were examined. The addition of sodium chloride was necessary to determine the

Table 3.3-2: Composition of the carapaces as determined by thermogravimetry. The calcium carbonate content was calculated from the loss of carbon dioxide. The magnesium content of calcite was determined by Rietveld refinement after Goldsmith *et al.*[80] IR peak ratios estimate the presence of amorphous calcium carbonate.

Sample	Shell	H_2O wt%	matrix wt%	CO_2 wt%	$CaCO_3$ wt%	Mg in calcite mol-%	IR υ_2/υ_4 peak ratio
A3	soft	-	-	-	-	5,98	7.2
L60	soft	13,0	27,1	25,3	57,5	6,40	6.8
H56	hard	7,1	19,0	30,2	68,7	9,00	6.1
M61	hard	5,9	21,3	28,8	65,5	8,92	5.0

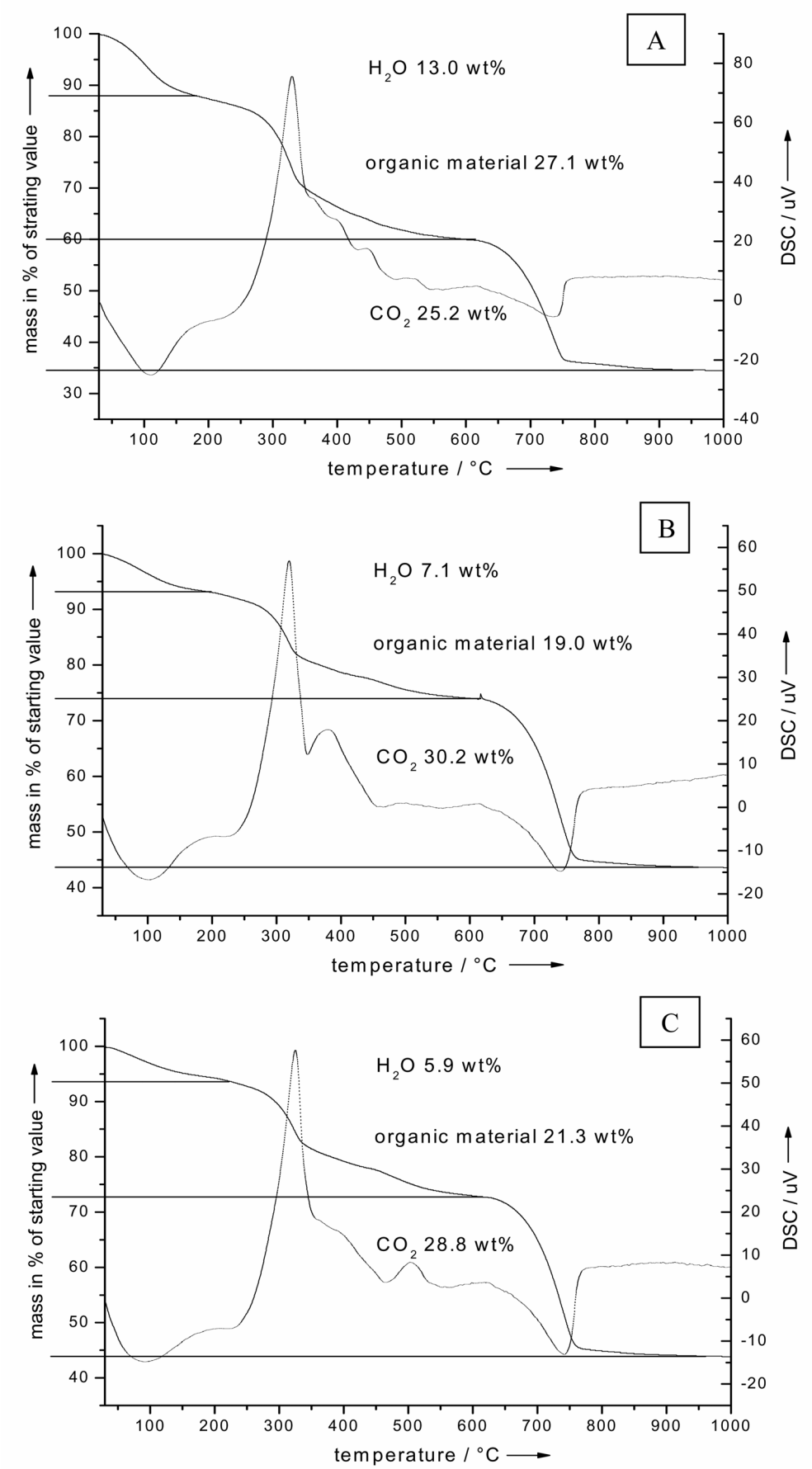

Fig. 3.3-5: Thermograms (solid lines) and DSC curves (dotted lines) for a hard shell (A) and two soft shells (B and C). In all cases, a three-step mass loss is observed. For details, see text.

exact zero point shift. Figure 3.3-6 shows the diffractograms of animals L, H, and M. Rietveld refinement yielded the cell parameters which allowed the determination of the magnesium content in calcite according to Goldsmith *et al.* (see appendix).[80] The animals with soft cuticles showed 5.9 and 6.4 mol% magnesium in calcite (A and L, respectively), whereas the animals with hard cuticles contained 9.0 and 8.9 mol% of magnesium in calcite (H and M, respectively). These values are rather high and correspond to the overall hardness of the cuticles.[79]

Infrared spectroscopy (IR) was possible for two specimens with hard and soft cuticle, respectively. The spectra are shown in Figure 3.3-7. The determined ν_2:ν_4 peak ratios are 7.2 for animal A (soft), 6.8 for animal L (soft), 6.1 for animal H (hard), and 5.0 for animal M (hard). In soft cuticle animals, the peak ratios are higher than in animals with hard cuticles. Therefore, the amorphous phase predominates in soft cuticles. The high magnesium content of the samples also increases the IR peak ratio and blue-shifts the peak positions in all cases.[79]

The observation of smaller amounts of a mineral phase which is more disordered in soft cuticles is in contrast to a higher amount of mineral phase which is more ordered in hard cuticles and corresponds to crustaceans in moult phase as described in the preceeding chapter. The soft cuticle is either in the process of being demineralised or remineralised. Furthermore, in the smaller amount of magnesium calcite in the soft cuticles, there is less magnesium incorporated than in the higher amount of magnesium calcite in the hard cuticles. The formation of magnesium calcite in order to achieve a harder carapace can be part of the crab's predation defence strategy.

The structure of the cuticle was examined by scanning electron microscopy (SEM). Figure 3.3-8 shows a cross-section of a piece of carapace broken out of the main dorsal plate. The structure of the cuticle can be divided into epicuticle, exocuticle and endocuticle as described in the preceeding chapter.[213] The

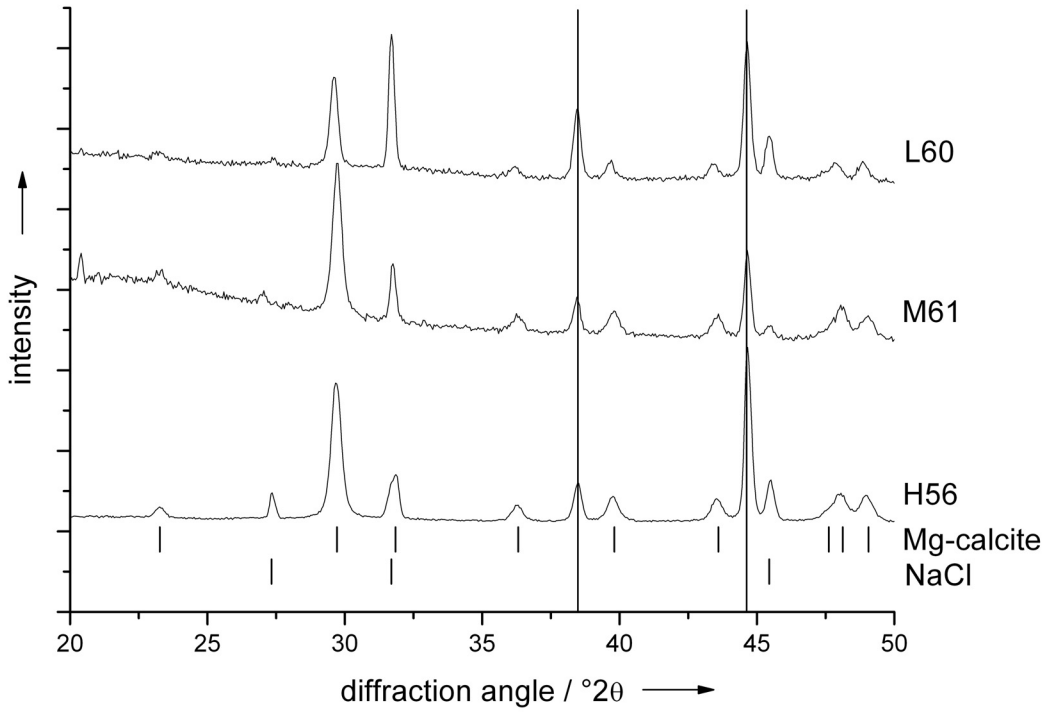

Fig. 3.3-6: X-ray diffractograms of samples of a soft carapace (L60) and two hard carapaces (M61 and H56) in mixture with sodium chloride. The latter was added for zero point correction. The big bars indicate the diffraction peaks of aluminium, the material of the sample holder.

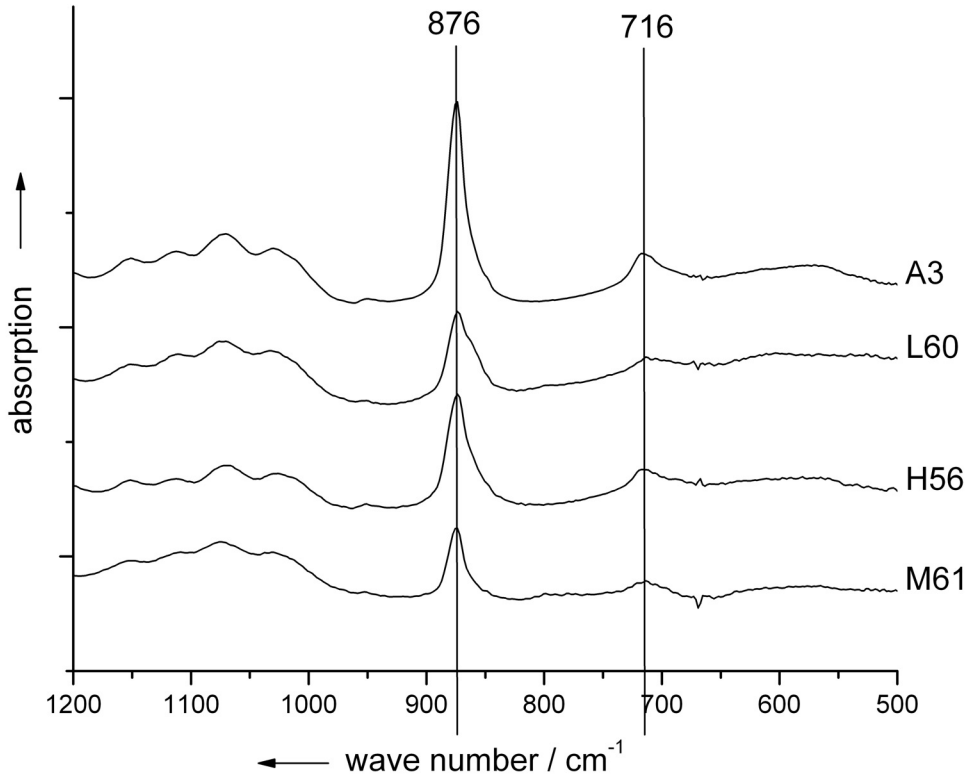

Fig. 3.3-7: Infrared spectra of two soft carapaces (A3, L60) and two hard carapaces (M61 and H56). For details see text.

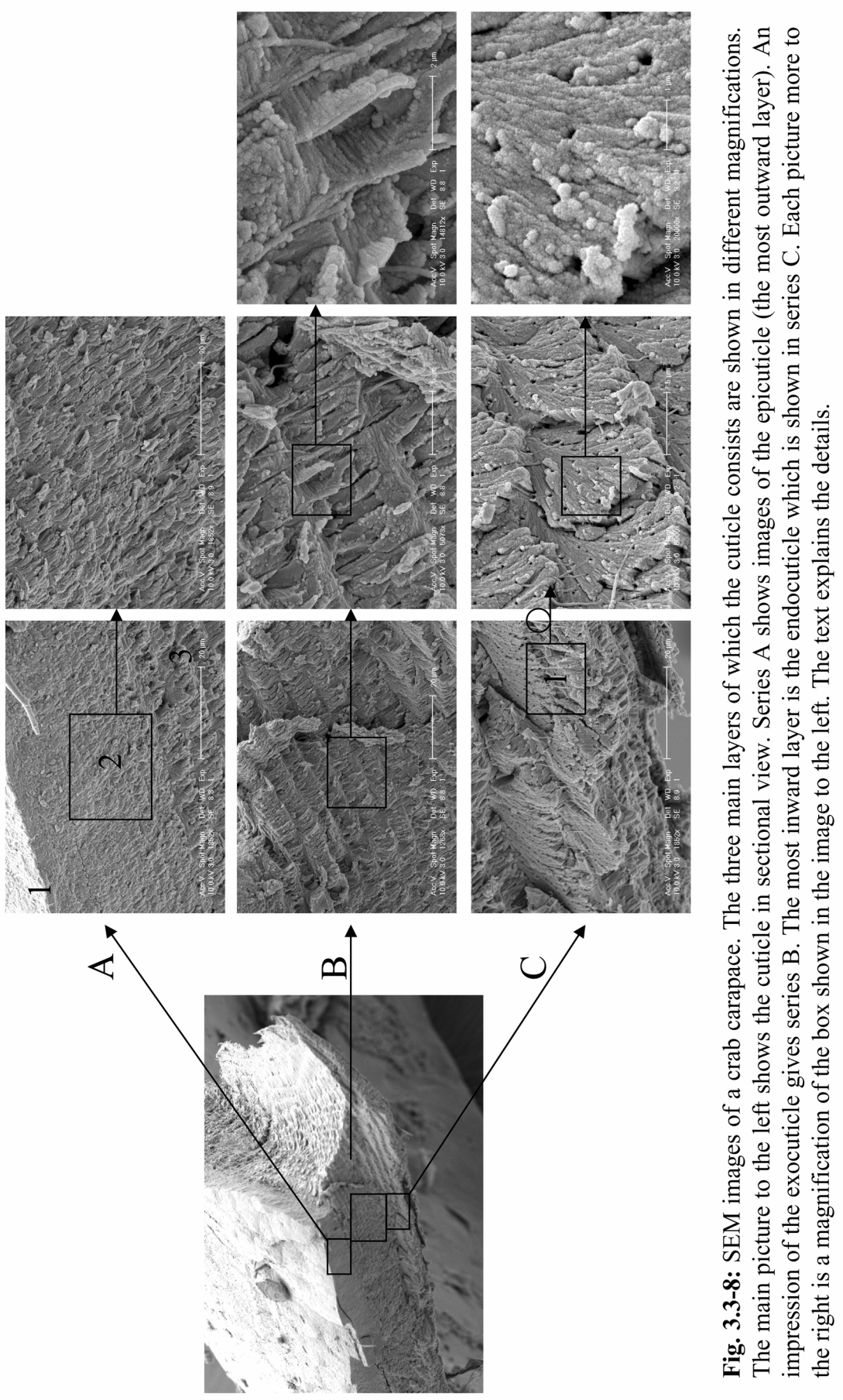

Fig. 3.3-8: SEM images of a crab carapace. The three main layers of which the cuticle consists are shown in different magnifications. The main picture to the left shows the cuticle in sectional view. Series A shows images of the epicuticle (the most outward layer). An impression of the exocuticle gives series B. The most inward layer is the endocuticle which is shown in series C. Each picture more to the right is a magnification of the box shown in the image to the left. The text explains the details.

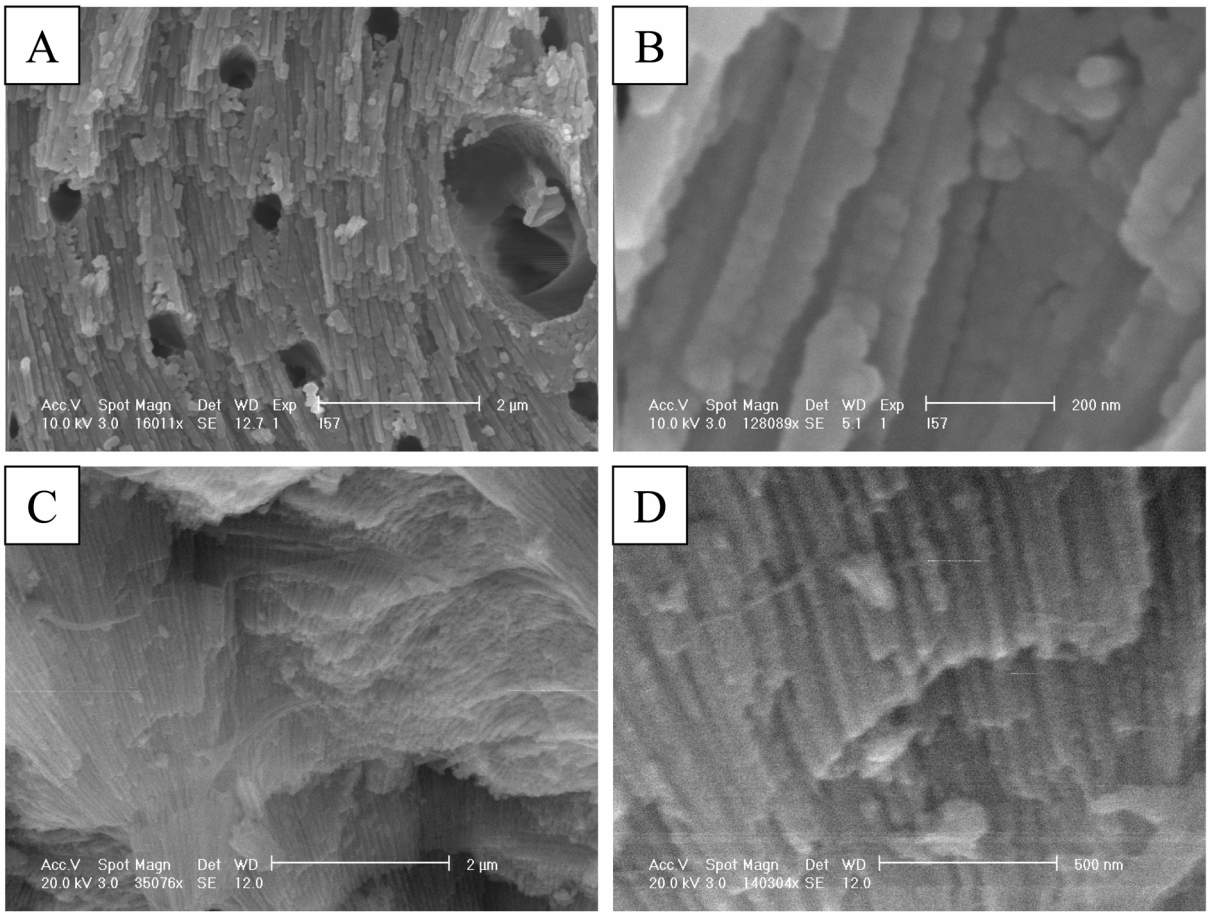

Fig. 3.3-9: Mineralised chitin fibres in the exocuticle layer of the carapace (A, magnification B). Image C shows the same sample after demineralisation (magnification D).

epicuticle (A, 1) as outermost layer is rich in lipids, does not contain chitin and is the primary barrier against water loss. It is very small compared to the rest of the cuticle and barely seen at this magnification. The exocuticle (A, 2) is different in structure from the endocuticle (B and C). More channels lead to the outside; the layers of chitin are thinner compared to the endocuticle. The endocuticle was magnified to reveal the packing of the mineralised chitin fibres (B series). Due to sample preparation, the breaking of the sample also allows a view of one layer of mineralised chitin fibres (C series). The sample was rotated by 90 degrees to allow a better view (C, 1). The channels seen from the side in series before are now seen from above and can be seen as black dots. The chitin fibres are clearly mineralised. The differences between mineralised and demineralised fibres are shown in Figure 3.3-9. Image A shows a mineralised chitin fibre layer; B its magnification. Image C shows a demineralised chitin

fibre layer and image D the magnified view. The demineralised fibres are smooth in contrast to the mineralised ones.

3.3.3 The soluble organic matrix in the cuticle

The soluble organic matrix of thoroughly ground cuticle parts was extracted with an ion-exchange resin.[214] This method allows the dissolution of the mineral phase at ambient pH values and without the aid of chelating agents such as EDTA. Thus, the extracted proteins are obtained in a well preserved state and do not contain unwanted additives. The sample was brought into a dialysis bag (MWCO < 7500 g mol^{-1}) with 3 ml double distilled water (DDW). The dialysis bag was placed in a receptacle filled with about 10 ml DDW and ion-exchange-resin. The cylindrical receptacle was rotated at room temperature, allowing the sample pieces and the resin to be shaken. Water in the receptacle was changed very twelve hours. After extraction, the content of the dialysis bag was centrifuged to remove the insoluble residue (4500 rpm, 10 min at 4°C). The protein solution obtained was lyophilised and the dried proteins dissolved in 1 ml of DDW. Samples for amino acid analysis and crystallisation experiments were taken from this solution. Analysis was done by a central facility in the Weizmann Institute of Science.

In the case of ACC being in a transport situation stabilised by special proteins in animals with a soft cuticle (pre- or postmoult stage), differences in the amino acid composition should be visible between extracted soluble matrix from hard and from soft cuticles. The soluble organic matrix from hard (H56) and soft (F53) cuticle was extracted by double-distilled water (DDW) without the aid of ion-exchange resin. After one day of extraction, much of the mineral phase (ACC only) has been dissolved as shown by experience.[215] Three other samples of the hard shell (H56) were extracted with ion-exchange resin for five days. Infrared spectra confirmed that all mineral was dissolved. Table 3.3-3

Table 3.3-3: Composition of the extracted soluble matrix of hard cuticle (H56) and soft cuticle (F53) after one day of extraction with double distilled water and the composition of hard shell matrix after 5 day extraction with ion-exchange resin. Values are given in mol%. The amino acids cysteine and tryptophane were not determined because of analysis complexity. The contents of asparagine and glycine are included in the values of aspartic and glutamic acid. (abr.=abbreviation)

extraction time			**1 day**		**5 days**			
amino acid	**abr.**	**type**	**H56**	**F53**	**H56-1**	**H56-2**	**H56-3**	**average**
aspartic acid	Asp	acidic	9.3	9.5	7.6	7.8	8.1	7.8
glutamic acid	Glu	acidic	10.3	9.9	8.4	8.5	8.8	8.6
			19.6	*19.4*				*16.4*
arginine	Arg	basic	3.0	2.6	3.8	3.9	3.7	3.8
histidine	His	basic	2.9	2.8	2.4	2.4	2.4	2.4
lysine	Lys	basic	1.8	3.1	3.3	3.3	3.3	3.3
			7.7	*8.5*				*9.5*
alanine	Ala	apolar	10.0	8.6	14.4	13.9	12.9	13.7
leucine	Leu	apolar	6.5	8.1	6.6	6.6	7.2	6.8
isoleucine	Ile	apolar	4.8	5.4	3.6	3.6	4.2	3.8
methonine	Met	apolar	1.3	2.1	1.0	0.8	1.2	1.0
proline	Pro	apolar	7.7	7.8	10.9	11.1	10.0	10.7
valine	Val	apolar	10.2	8.7	8.9	9.0	8.8	8.9
			40.5	*40.7*				*44.9*
phenylalanine	Phe	aromatic, apolar	3.9	4.1	3.7	3.7	3.9	3.8
tryptophane	Trp	aromatic, apolar	-	-	-	-	-	-
tyrosine	Tyr	aromatic, polar	2.9	2.2	2.3	2.4	2.3	2.3
			6.8	*6.3*				*6.1*
asparagine	Asn	polar	Asp	Asp	Asp	Asp	Asp	Asp
cysteine	Cys	polar	-	-	-	-	-	-
glutamine	Gln	polar	Glu	Glu	Glu	Glu	Glu	Glu
glycine	Gly	polar	14.6	13.7	10.9	10.9	11.5	11.1
serine	Ser	polar	6.1	6.0	6.3	6.1	6.0	6.2
threonine	Thr	polar	4.7	5.6	6.0	5.9	5.9	5.9
			25.4	*25.3*				*23.2*

summarises the amino acid composition of the samples. The soluble organic matrix extracted during one day from hard and soft shell shows minor variations in composition for each individual amino acid. However, the overall composition of acid, basic, aromatic and apolar amino acids is comparable and roughly identical. The backbone of the proteins is made up of apolar amino acids with about 40 mol%. About 15 mol% consist of basic and aromatic amino acids. The rest of 45 mol% consists of acidic or polar amino acids. The extracted soluble matrix consists of acidic proteins, but not as highly charged as those

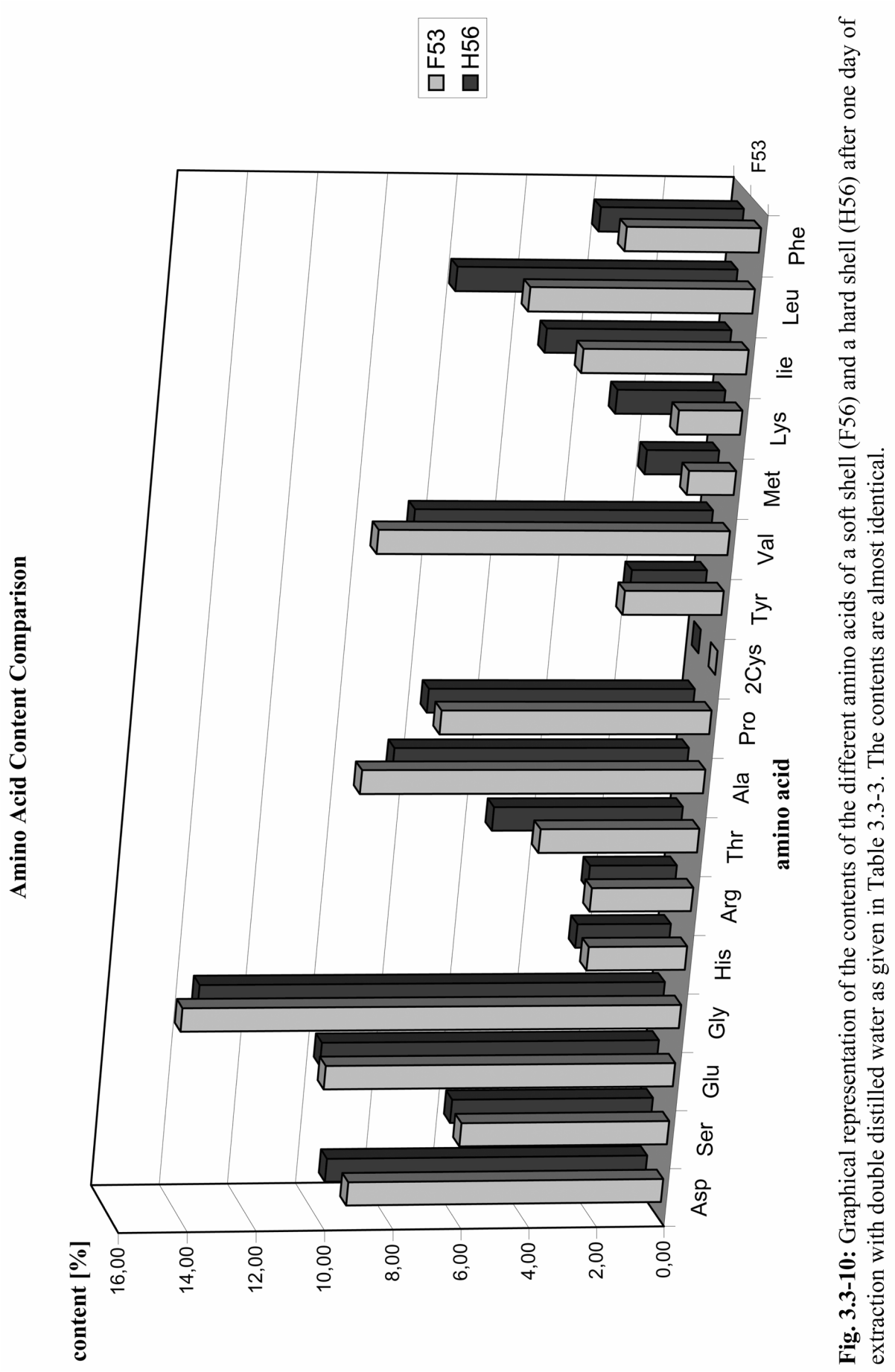

Fig. 3.3-10: Graphical representation of the contents of the different amino acids of a soft shell (F56) and a hard shell (H56) after one day of extraction with double distilled water as given in Table 3.3-3. The contents are almost identical.

extracted from nacre, human dentin or mollusc shells.[120] Furthermore, as the amino acid composition of the soluble matrix of hard and soft shells is nearly identical, ACC is not necessarily in a transient stage, stabilised by specialised proteins. The stabilisation of ACC in hard and soft cuticles does not differ in terms of soluble organic matrix amino acid composition. However, this does not necessarily exclude the presence of different types of proteins. Amorphous calcium carbonate in crab carapace can be assumed to be a stable biogenic phase despite the atypical infrared behaviour. The composition of soluble matrix from the completely dissolved hard shell is given for three identical batches. On the average, this soluble protein matrix with 16.4 mol% acidic and 23.2 mol% polar amino acids (together 39.6 mol%) is less acidic than the fraction obtained after one day of extraction. This observation may hint at a different protein composition in the matrix associated with calcite which had not been dissolved in the one-day extraction.

The organic matrix obtained after five day extraction with ion-exchange resin was investigated by gel electrophoresis in order to separate the different organic macromolecules of the matrix by their weight. Figure 3.3-11 shows the stained mass fractions in the gel. Unfortunately, the proteins accepted the staining reagent so quickly that the staining had to be stopped before the standard protein for mass calibration could be stained. Therefore, the bands visible can not be related to a

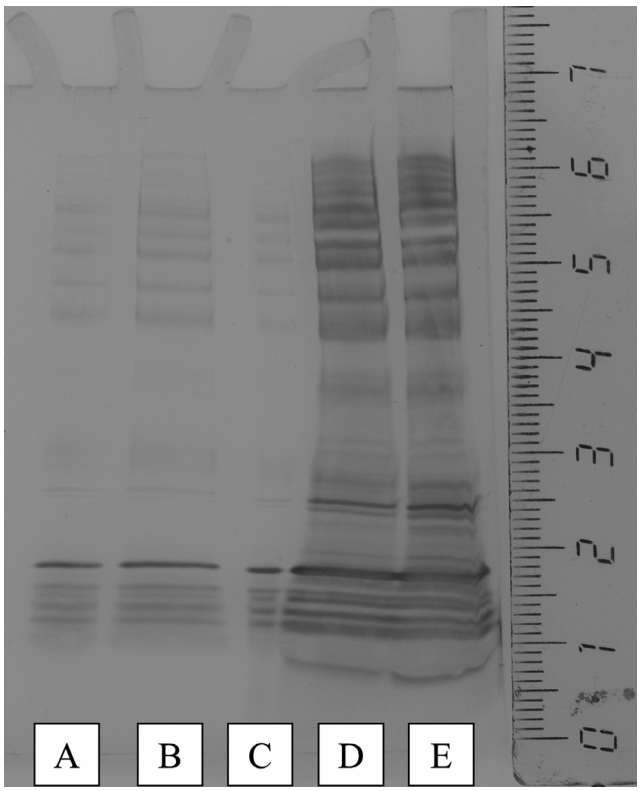

Fig. 3.3-11: Image of the gel electrophoresis of the extracted soluble organic matrix of the carapace in different concentrations (see text for details). All bands are clearly distinguishable.

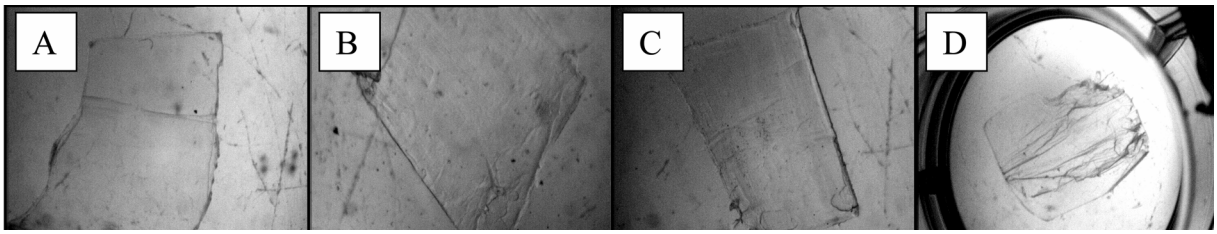

Fig. 3.3-12: Light-microscopic images of substrates after crystallisation experiments. No precipitation occurred in the presence of the extracted soluble matrix proteins. The matrix concentrations were 0.1 mg l^{-1} (A), 1.0 mg l^{-1} (B), and 10.0 mg l^{-1} (C). Image D shows a template with preadsorbed soluble matrix. Even in this setup, no crystallisation occurred.

specific fraction mass. However, the bands are clearly seen and distinguishable, pointing to discrete mass fractions. Amounts of 1 µg (A, B, and C), and 10 µg (D and E) of protein matrix were used. The distinct mass bands in the gel electrophoresis suppose that a separation of the matrix should be possible by future examinations.

Crystallisation experiments with the ammonium carbonate method (see chapter 4.1) were carried out with protein matrix in solution and preadsorbed on a β-chitin and silk substrate as described in literature.[64, 121] No crystallisation of calcium carbonate was induced as it can be seen in Figure 3.3-12. The soluble matrix was used in concentrations of 0.1 mg l^{-1} (A), 1.0 mg l^{-1} (B), and 10.0 mg l^{-1} (C). Image D shows also no crystal growth in the presence of pre-adsorbed protein matrix. In all cases, the inhibitory effect of the matrix was confirmed. Coblentz *et al.* crystallised calcium carbonate in the presence of cuticular proteins extracted from the blue crab *Callinectus sapidus*.[216] They also found that proteins in solution had an inhibitory effect, as the time until beginning crystallisation was delayed. However, they crystallised from an already supersaturated solution whereas here, a slow build-up of the carbonate concentration was achieved. The complete inhibition found here may be due to different experimental conditions.

However, whether the crystalline calcite phase is crystallised on purpose or whether it is a product of a spontaneous crystallisation of the ACC phase, is still under debate. The results obtained indicate that ACC and calcite are precipitated

with purpose by the crab. Other results show that the precipitation of nano-particles is also done by purpose.[217] At present, it is not possible to ascertain the purpose of the magnesium calcite phase.

3.4 Undesired biomineralisation: Atherosclerosis

3.4.1 What is atherosclerosis?

Atherosclerosis is a disease of arterial blood vessels.[218, 219] *Atherom* describes the occurrence of swollen areas of the arterial wall, caused by porridge-like depositions consisting mainly of lipids. *Sklerosis* denotes the increase of collagen fibres. The World Health Organisation (WHO, 1958) defines atherosclerosis as

> *"a variable combination of changes in the intima, consisting of localised depositions of lipids, carbohydrates, blood components, fibrous tissue and mineral".*

Fig. 3.4-1: Schematic representation of the main blood vessels.

Blood vessels consist mainly of smooth muscle cells (myocytes) and endothelial cells. Their structure can be described to consist of three layers: the intima, the media and the adventitia. The innermost layer is the intima, the outermost the adventitia. The endothelial cells of the intima and the muscle cells of the media layer are metabolically coupled. In a normal artery, the muscle cells can contract but not undergo mitosis. Their mitosis is blocked by factors produced by the endothelial cells in the intima. Any damage caused to the endothelium of the arterial wall thus changes the mitosis behaviour of the muscle cells which then proliferate. In a damaged wall, the muscle

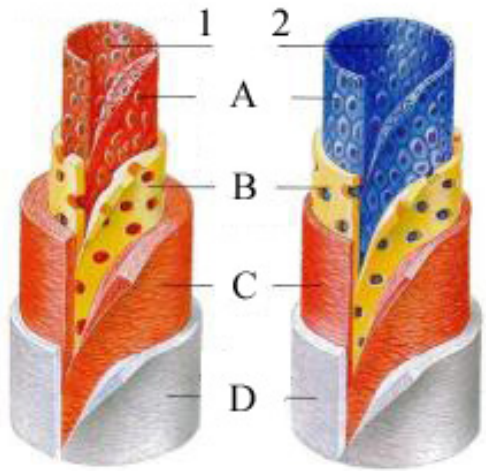

Fig. 3.4-2: Schematic structure of an artery (1) and a vein (2). A: epithelial cells, B: intima layer, C: media layer, D: adventitia layer.

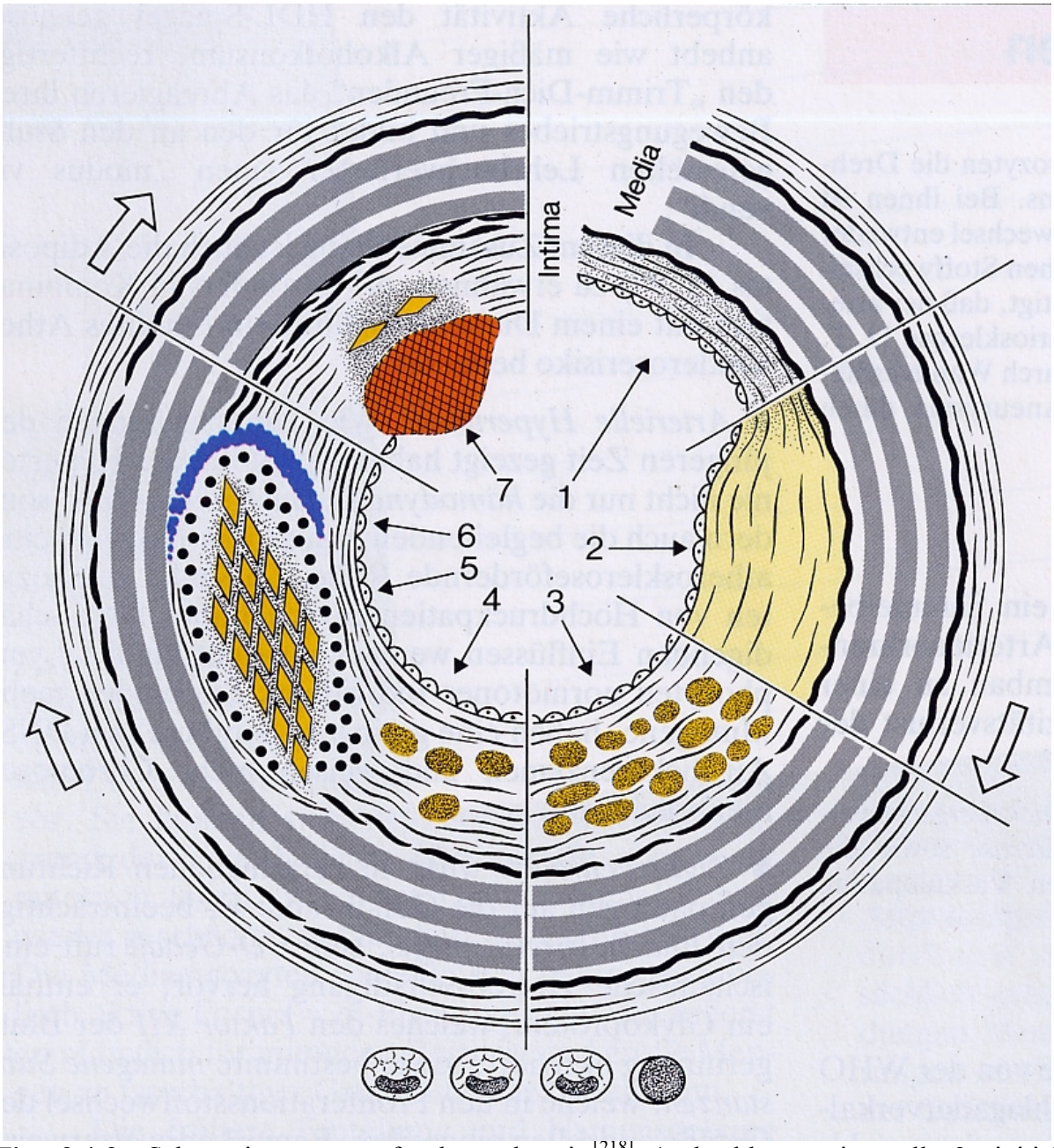

Fig. 3.4-3: Schematic course of atherosclerosis.[218] 1: healthy aortic wall, 2: initial accumulation of lipids, 3: first foamy cells, 4: progressive sclerosis by profilerated myofibroblasts, first media penetration, 5: *atherom* with cholesterol crystals, 6: beginning mineralisation, 7: calcified aortic plaque (*ulcus*).

cells change into an active form which can produce high amounts of fibres. Regardless whether the mitosis suppression mechanism or the general metabolism of the arterial wall cells is disturbed, this leads to a thickening of the wall as in atherosclerosis or a thinning as in aneurysms.

Clinically, the terminus atherosclerosis comprises different diseases of the artery which lead to thickening, hardening, and loss of elasticity of the arterial wall.

These are arteriolosclerosis, Morbus Moenckeberg, and atherosclerosis. Artiolosclerosis shall here simply be described as atherosclerosis in the arteries (arterioles) of organs. Morbus Moenckeberg is calcification of the media layer in arteries in muscle tissue. Mohr *et al*.[220] assume the pathogenesis of this disease to be similar to that of atherosclerosis.

The formal pathogenesis of atherosclerosis can be described in several stages (see Fig. 3.3-4). In a normal arterial wall (1), the endothelial cells of the intima control the mitosis of the muscle cells in the media. An initial damage to the endothelium occurs (2). The causes of these initial changes of the intima are still under debate. The current theory[219] discusses the adhesion of lymphocytes whose cytokines may result in a reduced cell adhesion of the endothelial cells. This allows lipids, proteoglycanes, and other substances from the blood to penetrate the intima. Furthermore, the changed structure of the arterial wall is a trigger signal for thrombocytes whose task is to repair ruptures of blood vessels. The thrombocytes spread interleukins in order to inform the body of the damage. Lymphocytes and thrombocytes create a chronic inflammation of the damaged arterial wall. The lymphocytes and other macrophages try to phagocyte the lipids and other blood materials which do not belong in the intima. This process creates foam cells (lipid storage macrophages, 3). When this process continues, the mitosis behaviour of the muscle cells is affected as described above. Cells which create fibres are expressed (4). At this stage, the process of irreversible hardening of the tissue begins. The media layer also becomes affected and fibrous plaques can be seen when dissected. The next stage of the disease is the formation of an *atherom* (5). The continuing aggregation of lipids and media cell proliferation results in the crystallisation of cholesterol and the beginning crystallisation of calcium phosphate (6). The inflammation process results in a thinning of the endothelium and in cell necrosis. The last stage is the formation of an atherosclerotic ulcus (7). At this stage, the arterial wall is severely

damaged. The blood vessel may close or brake apart. This is the main reason for cardiovascular mortality.

Atherosclerotic lesions are present in all human arteries starting at about the age of thirty years. But not all possible damage sites undergo calcification. Several risk factors have been identified[219]. The most prominent risk factors are diabetes mellitus, hypercholesterolemia, and severe changes in the metabolism, i.e. nephrotic insufficiency and the resulting need of dialysis. But the arterial wall itself also seems to offer structures preferred for lesions[221, 222].

Atherosclerosis is nearly undetectable by established clinical procedures and only identified by the effects it causes. Several methods have been tested to identify lesions in arteries, including ultrasound[223], fluorescence spectroscopy[223, 224] and even Raman spectroscopy[225].

3.4.2 The mechanism of atherosclerotic calcification

For a long time, hypercholesterolemia was thought to be the main reason for atherosclerosis caused in otherwise healthy human beings[226]. Atherosclerosis was regarded as the result of disorders in lipid metabolism. Today, the relationship between blood cholesterol levels and atherosclerosis is no longer in doubt. Concentration on the process of inflammation caused by the lymphocytes and their cytokines began about twenty years ago.[227] It seems, as Steinberg pointed out that "hypercholesterolemia and inflammation [are] partners in crime"[226]. In animal experiments, it could be shown that the monocytes which penetrated the arterial wall undergo a phenotypic modulation. Furthermore, low-density lipids (LDL) from the blood are oxidised in the presence of proteoglycanes. These oxLDL are taken up by the monocytes, resulting in the accumulation of cholesterol. It is still under debate whether these results can be applied to humans. The letter of Virella *et al.*[228] can be seen as an example of that discussion. Nevertheless, there are complex interactions of cytokines, growth factors, and blood constituents in a developing lesion.

The subsequent mineralisation of the lesions has been regarded as a metastatic passive mineralisation process. Doherty *et al.* proposed the mineralisation process to be regulated and directed as common in human bone[229]. This hypothesis opened a new field of atherosclerosis research. Proliferated muscle cells of the intima have been cultured *in vitro* and expressed mineralisation-regulating proteins as known from bone[230]. The cell differentiation of media cells has been shown in mouse experiments to be dependent on matrix-Gla-protein (MGP)[231]. Bovine media muscle cells have been shown to acquire osteoblastic phenotype under certain conditions. Factors produced by macrophages may promote calcification[232]. So far, it is accepted that calcification in atherosclerosis is a regulated process. The current discussion focuses on the question whether atherosclerotic calcification is similar to osteogenesis (bone formation)[233]. Mohr *et al.*[234] studied whether the morphology of different stages of atherosclerotic calcification is similar to osteogenesis. They concluded that the hypothesis of a regulated mineralisation as it occurs in bone cannot be supported for the development of calcified plaques. However, they accept that proteins associated with osteogenesis participate in a transition of calcification to ossification (bone creation). They later concluded[235] that atherosclerotic calcification is biphasic process initiated by the appearance of calcospherites, followed by a secondary calcifying phase in which bone-like apatite is formed.

Next to hypercholesterolemia, disruptions of the calcium or phosphate metabolism can also induce atherosclerotic calcification. Dialysis patients, even those of 20-30 years of age, show severe calcifications and have a higher cardiovascular mortality rate compared to the normal population. Ketteler *et al.*[236] have shown deficiencies of calcium-regulating proteins in dialysis patients and suggested that these deficiencies are linked to the pathogenesis of cardiovascular calcifications. Other studies revealed the α_2-Heremans Schmid glycoprotein (AHSG, fetuin-A) as an inhibitor of calcification[237, 238].

3.4.3 The calcified atherosclerotic lesions[239]

The calcium mineral deposits in atherosclerotic lesions consist of carbonated hydroxyapatite, $Ca_{10}(PO_4/CO_3)_6(OH)_2$, usually with calcium deficiency induced by the incorporation of hydrogen phosphate groups, HPO_4^{2-}. The given formula is not electroneutral and is only given in order to describe the material chemically. The true composition of carbonated apatite is very complex because of nonstoichiometries in all positions (calcium, phosphate, carbonate, and hydroxide). This is the case for all phosphatic biominerals, irrespective of whether they occur in a desired way (like teeth and bone) or in an undesired (pathologic) way as in atherosclerosis. As stated above, it is still under debate whether atherosclerotic calcification imitates osteogenesis. The available literature on atherosclerotic lesions either deals with the medical or the chemical part of the problem[240]. In this work, atherosclerotic plaques of the intima layer of six patients with pathologic results and histology were correlated to the findings on the mineral phase obtained by high-end physicochemical methods.

Case A (S94/02) was a 72 year-old male patient who suffered from a high degree of atherosclerosis, especially of kidneys and heart. He showed no further clinical history. Patient B (S155/02) was a male of 77 years of age who suffered from a high degree of atherosclerosis throughout the whole body. Additionally, he was a dialysis patient with nephrotic insufficiency who had already lost several toes due to blood vessel calcification. Case C (S178/02) was a male of

Tab. 3.4-1: Clinical history of the different samples. Light calcification corresponds to small areas of lipids and small calcified areas, heavy calcification corresponds to large calcified areas and the beginning formation of bone-like structures.

Sample	Patient	Degree of atherosclerosis	Clinical history
A	72 y, male	heavy	none
B	77 y, male	heavy	nephrotic insufficiency, dialysis
C	64 y, male	heavy	nephrotic insufficiency, dialysis; shunts for dialysis
D	71 y, female	heavy (coronar)	nephropathy, dialysis
E	75 y, male	light	lung cancer
F	78 y, male	heavy	only one kidney

64 years of age. He showed a high degree of atherosclerosis and was also a dialysis patient suffering from nephrotic insufficiency. Patient D (S285/02), a female of 71 years of age, showed calcification of the coronary arteries and suffered mainly from a severe complex lung disease. Case E (S287/02) was male and 75 years old. He showed a light atherosclerosis throughout the body and died from lung cancer. Patient F (S301/02) was a male of 78 years of age who showed a very high grade of atherosclerosis throughout the body and died from the rupture of an atherosclerotic aorta aneurysm. He had only one remaining kidney, but was not a dialysis patient. Table 3.4-1 comprises the clinical histories of the samples examined.

All samples were taken from the intima layer of the infested arterial walls and were critically point-dried without fixation or dehydration. Scanning electron microscopy (SEM) and element mapping by energy dispersive X-ray (EDX) analysis, transmission electron microscopy (TEM) and light microscopy were performed by our co-workers from the pathology of the university hospital "Bergmannsheil" in Bochum. Light microscopy showed the differences between the lesions which are soft, fibrous and lipid-rich and the hard mineralised plaques (see Fig. 3.4-4) as described in literature[241]. Scanning electron microscopy allowed to identify the hard atherosclerotic plaques in the arteries (see Fig. 3.4-5a). Song *et al.*[242] conducted an extensive SEM study at atherosclerotic plaques but focused on the luminal surface of the aortas and not the plaques itself. Lee *et al.*[243] did likewise and showed that a large number of microcrystallites and crystal particles of different sizes were embedded in the organic matrix of the plaques. They did not find preferred sites of crystal aggregations within a plaque. Energy dispersive X-ray analysis showed that the plaques consist of calcium and phosphate, equally distributed within in the plaques. (Fig 3.4-5b). The molar ratio of Ca:P was determined to be 1.4:1, pointing to a calcium-deficient hydroxyapatite. Stoichiometric hydroxyapatite $Ca_{10}(PO_4)_6(OH)_4$ has a Ca:P ratio of 1.67:1. Transmission electron microscopy

showed different kinds of mineral depositions together with collagen fibrils (Fig. 3.4-6). Radially structured aggregates with more than one shell were observed in some regions (Fig. 3.4-6c). It was not possible to relate the shape of the crystalline aggregates to the pathologic findings because all samples contained regions with different calcified morphologies. Apparently, the calcification occurred by various mechanisms that do not lead to a distinct morphology. This was also noted by Lee *et al.* and by Tomazic *et al.*[243, 244]. These findings may also support the theory of Mohr *et al.*[235] who proposed a biphasic calcification process in atherosclerotic plaques.

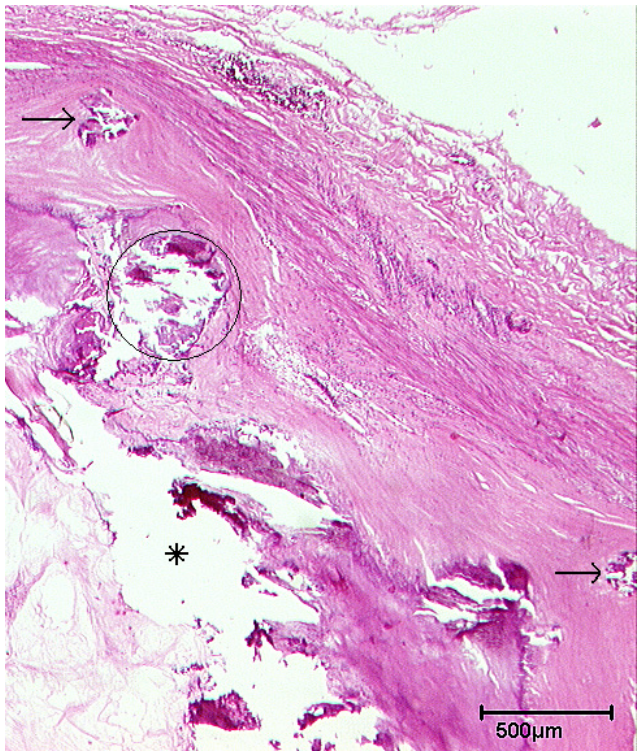

Fig. 3.4-4: Light microscopic image (HE-stain) of a cross section of an atherosclerotic aortic wall. Areas of early calcifications are marked with arrows. The circle indicates a larger calcified area which already penetrates the media layer. The asterisk indicates an artefact created by sample preparation. Image by courtesy of I. Schmitz.

With the aid of thermogravimetric analysis (TGA) the ratio between organic matrix and inorganic material can be quantified[240, 245-247]. In addition, the content of carbonate can be determined from the loss of carbon dioxide. All carbonate is integrated into the apatite phase as ionic substituent[248]. In TGA all samples were heated under dynamic air flow to 900°C. The mass was recorded as function of temperature. All TGA curves are shown in Fig. 3.4-7. Three steps of mass loss can be identified. The first step in the range of up to 200°C can be assigned to the loss of water. The next step is the combustion of organic material

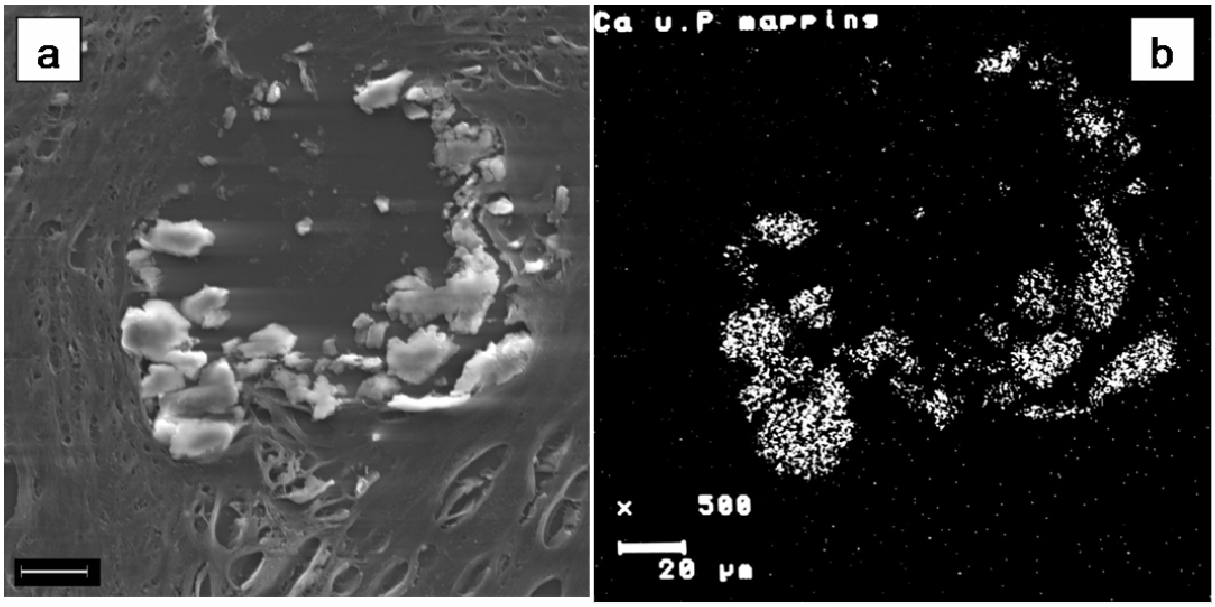

Fig. 3.4-5: Scanning electron micrograph of atherosclerotic lesions (a) in an aorta cross section and energy dispersive X-ray spectrometry of the same area (b, element mapping), showing both calcium and phosphorous (phosphate). Their distribution correlates closely to the morphological results. (case A, scale bar: 20 µm). Pictures by the courtesy of I. Schmitz.

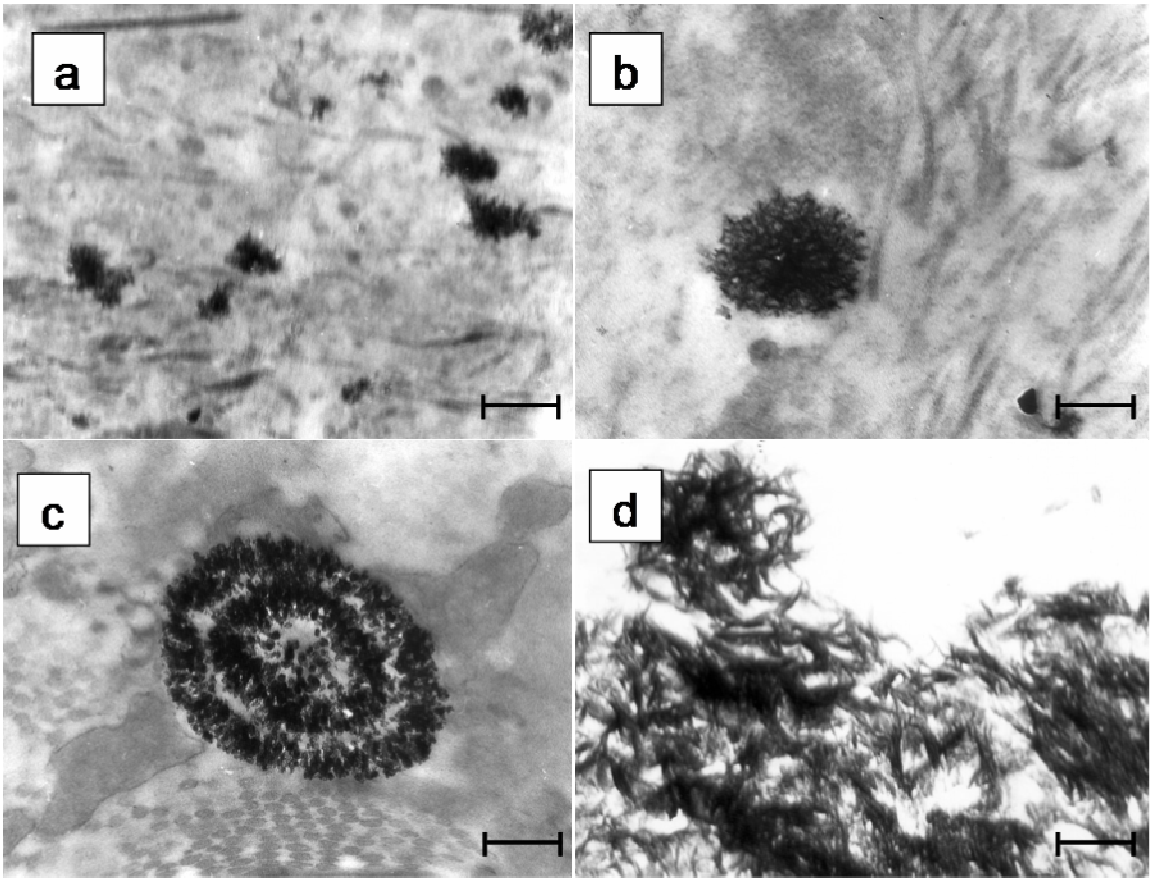

Fig. 3.4-6: Transmission electron microscopy of atherosclerotic plaques. a: collagen fibrils with small electron-dense calcification sites (scale bar: 0.05 µm), b: radially grown aggregate of calcium phosphate bound to a collagen fibre (scale bar: 0.03 µm), c: concentrically grown aggregate of crystals, showing different "layers" of radially grown nanocrystals (scale bar: 0.02 µm), d: typical calcospherites in dense arrangement (scale bar: 0.02 µm). Pictures by courtesy of I. Schmitz.

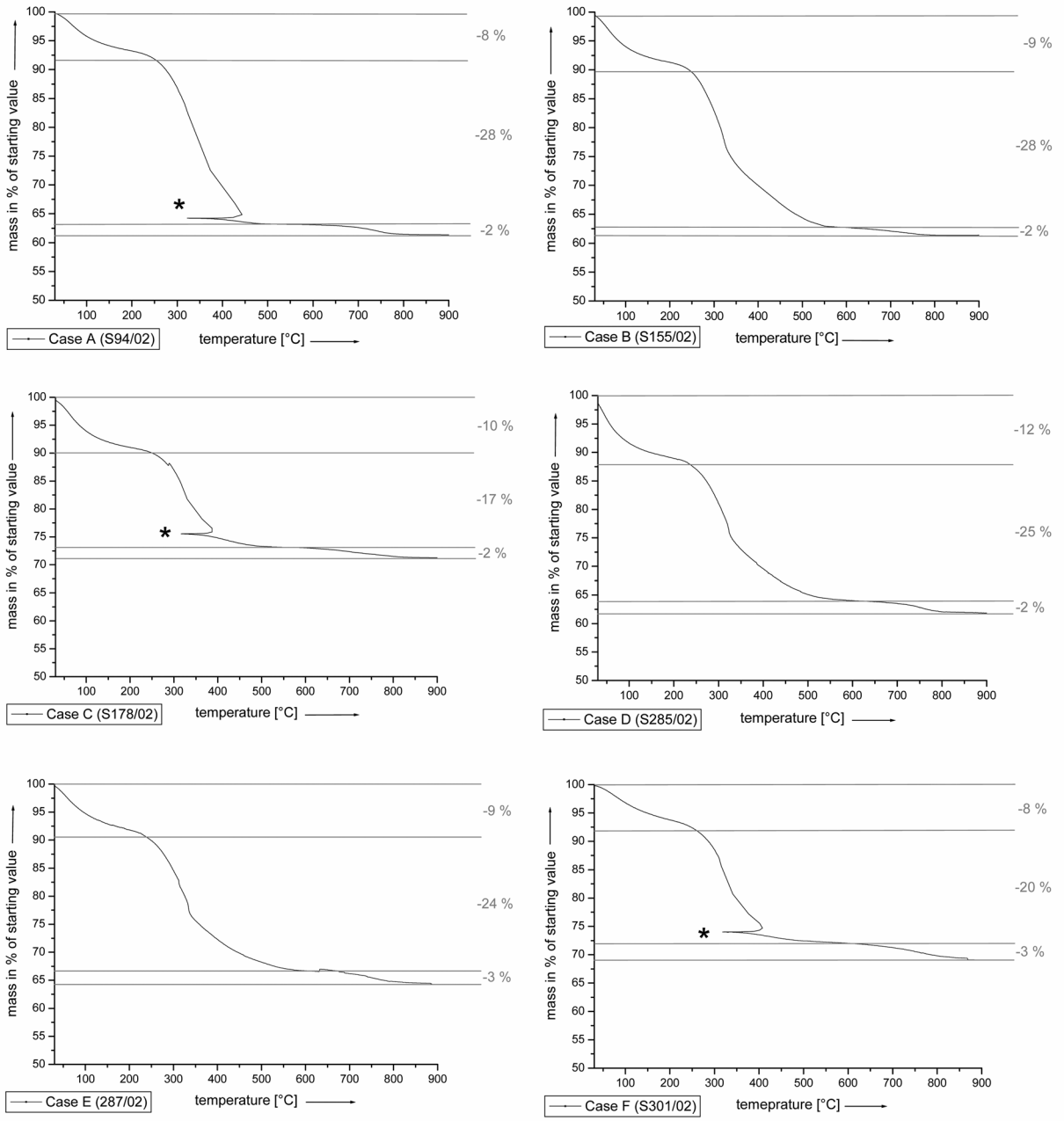

Fig. 3.4-7: Thermogravimetric analysis of the critical-point dried atherosclerotic plaques under air flow. Three different thermal occurrences can be distinguished: the release of water (up to 200°C), the combustion of organic material (up to about 550°C) and the decarboxylation of carbonated apatite. The values are summarised in Table 3.4-2. The distortions marked with an asterisk in cases A, C, and F are measurement artefacts.

which occurs in a temperature range of 200 to 550°C. The decarboxylation of carbonated apatite causes the last step of mass loss, beginning at about 600°C. Because the exact composition of carbonated apatite may vary, the loss of carbon dioxide can be used to calculate a formal content of "$CaCO_3$":

$$m(CaCO_3) = m(CO_2) \cdot \frac{M(CaCO_3)}{M(CO_2)} \qquad \text{(eq. 3.4-1)}$$

with *m* being the mass of the component given in brackets and *M* being the molar mass of the component. The observed mass losses are comprised in Table 3.4-2. For comparison, the values for human bone are given which were determined earlier[247]. However, the bone samples were not subjected to critical point-drying. The examined atherosclerotic plaques contained about 68 wt% mineral. Compared to the bone samples, this is a rather high value. The carbonate content of the plaques' mineral phase is also relatively high compared to bone mineral. Legros *et al.*[245] found 1.8 wt% carbonate in the bone of newborn rats and between 3.4 and 4.7 wt% in the bones of grown-up rats and cows. This corresponds to formal contents of 3.0, 5.3, and 7.8 wt% of "$CaCO_3$". Tomazic *et al.*[244, 249, 250] have found 65 to 85 wt% of inorganic material (weight loss up to 600°C) and on average 11.6 wt% of "$CaCO_3$" in calcified deposits. These values are higher than those determined in this study.

Infrared spectroscopy (IR) was used to identify possible X-ray amorphous or very small amounts of other calcium phosphate phases in the samples. The spectra are shown in Figure 3.4-8. Infrared absorption bands which are typical for calcium phosphate and also for the organic matrix can be identified. The

Tab. 3.4-2: Composition of the atherosclerotic plaques from thermogravimetry.

Case	water / wt%	organic material / wt%	mineral content / wt%	formal content of $CaCO_3$ (in carbonated apatite) / wt%
A	8	28	64	6.7
B	9	28	63	3.8
C	10	14	76	9.3
D	12	25	63	3.5
E	9	24	67	6.0
F	8	18	74	10.8
average	9	23	68	6.7
human bones	5..7	21..68	26..73	0.6..5.2
Tomazic[244,249, 250]	-	65…85	12	-

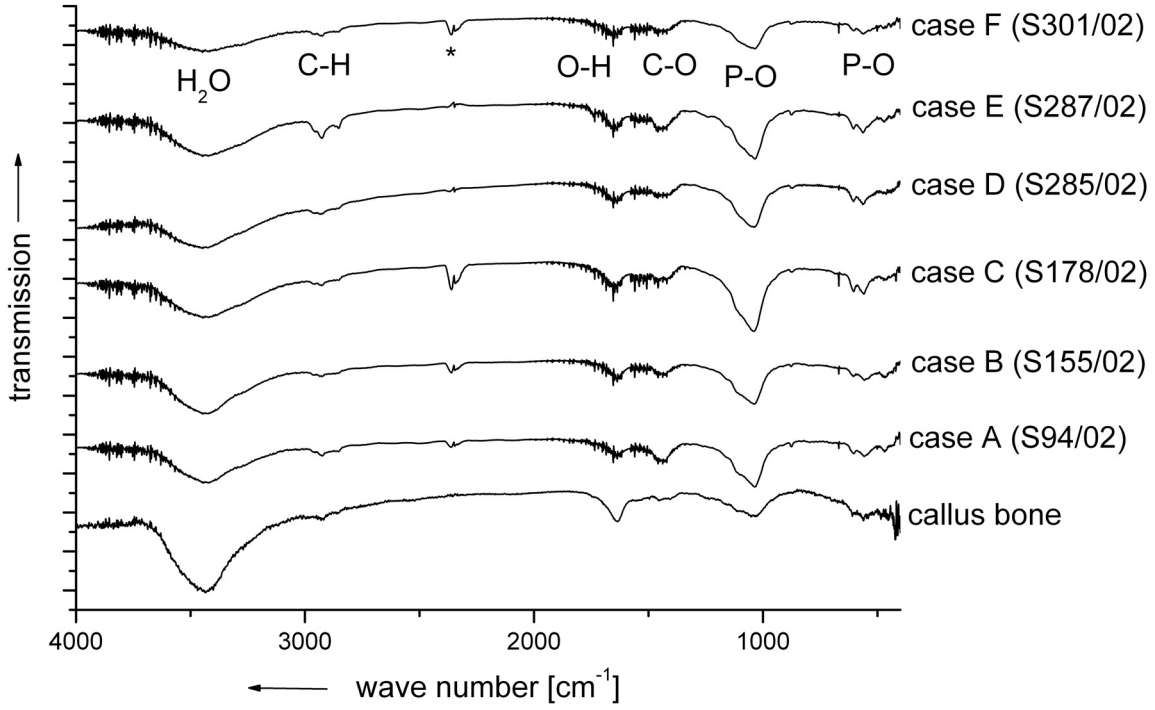

Fig. 3.4-8: Infrared spectra of atherosclerotic plaques in comparison to callus bone.[247] Typical bands of phosphate and organic matrix can be seen.[251] There are no significant differences between the samples, also in comparison to human bone. The asterisk marks artefacts due to absorption by CO_2 in the air.

intensities of the spectra shown are not directly comparable because different masses for each sample were used for pellet preparation. No significant differences in the occurrence of bands can be seen. The spectra are similar to human bone[252]. Similar results were reported by Li *et al.*[253] and Tomazic *et al.*[249]

High-resolution powder X-ray diffraction (XRD) was applied to identify the crystalline phases within the atherosclerotic plaques. The diffractograms of the ground samples are shown in Figure 3.4-9. For comparison, the diffraction patterns of synthetic hydroxyapatite (HAP)[254] and of callus bone[247] are given. The mineral phase of the atherosclerotic plaques can be identified as hydroxyapatite. The broadening of the peaks indicates a small crystal size within the nanometer region. However, the samples show a slightly higher crystallinity than the bone sample, as indicated by slightly better resolved diffraction peaks.

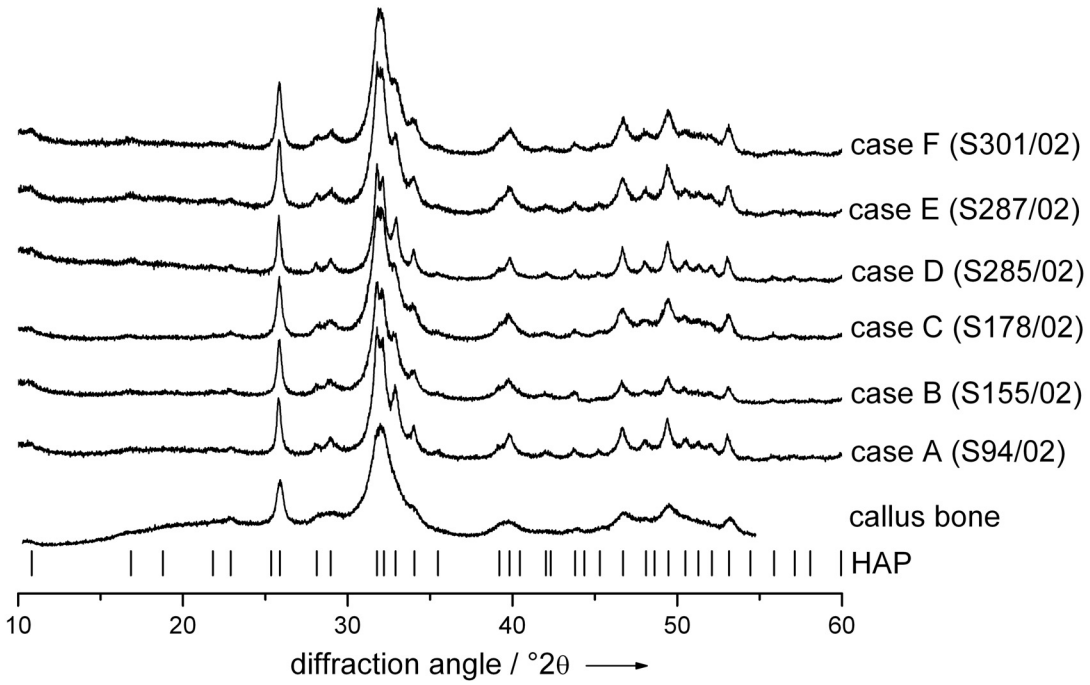

Fig. 3.4-9: High-resolution powder X-ray diffractograms of atherosclerotic plaques in comparison to callus bone and hydroxyapatite. All data were converted to Cu $K\alpha_1$-radiation wavelength (λ=1.54056 Å). All samples consist of nanocrystalline apatite as indicated by the broad diffraction peaks. (HAP=hydroxyapatite)

Despite the different chemical composition of the mineral phases in the plaques as indicated by TGA (table 3.4-2) and the different clinical history of the samples origin (table 3.4-1), no differences in phase or crystallinity can be seen among the atherosclerotic plaques.

The diffraction peak broadening by small crystallites can be semi-quantitatively estimated by the Scherrer equation (see Chapter 5.1.2). The calculated diffraction domain size corresponds roughly to the crystallite size. It should be noted, however, that structural disorder and strain phenomena, e.g. caused by carbonate substitution into the apatite lattice, can also lead to a peak-broadening effect and are not covered by this calculation. The peaks used for calculation are those at 22.9, 25.9, 29.0, 39.8, 43.8, 46.7, and 53.1°2Θ. These peaks correspond to the crystallographic directions (111), (002), (210), (310), (113), (222), (213) and (004), respectively. These peaks were chosen because of the possibility to clearly determine the FWHM necessary for calculation. However, the FWHM at

Tab. 3.4-3: Particle size of calcium phosphate minerals from XRD (estimated by the Scherrer equation) in nm. The positions of the individual reflections are computed for Cu $K\alpha_1$-radiation (λ=1.54056 Å). Standard deviations are given in parentheses.

Reflection (hkl) Position [°2Θ]	**(111) 22.9**	**(002) 25.9**	**(210) 29.0**	**(310) 39.8**	**(113) 43.8**	**(222) 46.7**	**(213) 49.5**	**(004) 53.1**	**Average**
A	26	38	15	16	31	12	22	26	23(8)
B	23	31	12	13	18	25	27	25	22(6)
C	20	23	10	-	25	17	19	20	19(4)
D	22	37	24	18	32	26	27	29	27(6)
E	14	26	14	14	18	20	22	24	19(4)
F	-	24	-	12	18	17	13	24	18(5)
Average	21(4)	30(6)	15(5)	15(2)	24(6)	20(5)	22(5)	25(3)	-
Callus bone[113]	20	21	10	9	24	18	14	22	17

22.9 and 29.0°2Θ was not determinable for sample F (S301/02) due to the low intensity of the peaks. Table 3.4-3 comprises the obtained results. Among the plaque samples, there are no significant differences. The values obtained for the diffraction domain/crystallite size are identical within the experiment uncertainty which we estimate to be about ±20 %. It can be concluded that the apatite phase is nanocrystalline in all cases with average particle sizes of 20-25 nm. An anisotropy of the crystallite size can be determined, depending on the crystallographic direction. The crystal size values obtained for (002) and (004) are higher in all cases, indicating an elongation of the *c*-axis compared to the bone sample. The crystal size values calculated for (210) and (310) indicate a shortening of the *a/b*-axis. This is similar to bone mineral where platelet-like anisotropy of the mineral crystals is well known[255]. However, the anisotropy found here is smaller than in bone mineral.

In order to detect possible amorphous mineral components in the initial tissue as known from biomineralisation (see Chapter 3.3 as an example), the calcined residues of the samples after thermogravimetric analysis were also examined with X-ray powder diffraction. During TGA, all organic material was burned up and potential amorphous or nanocrystalline material crystallised under these conditions. The diffractograms of the calcined samples are shown in Figure

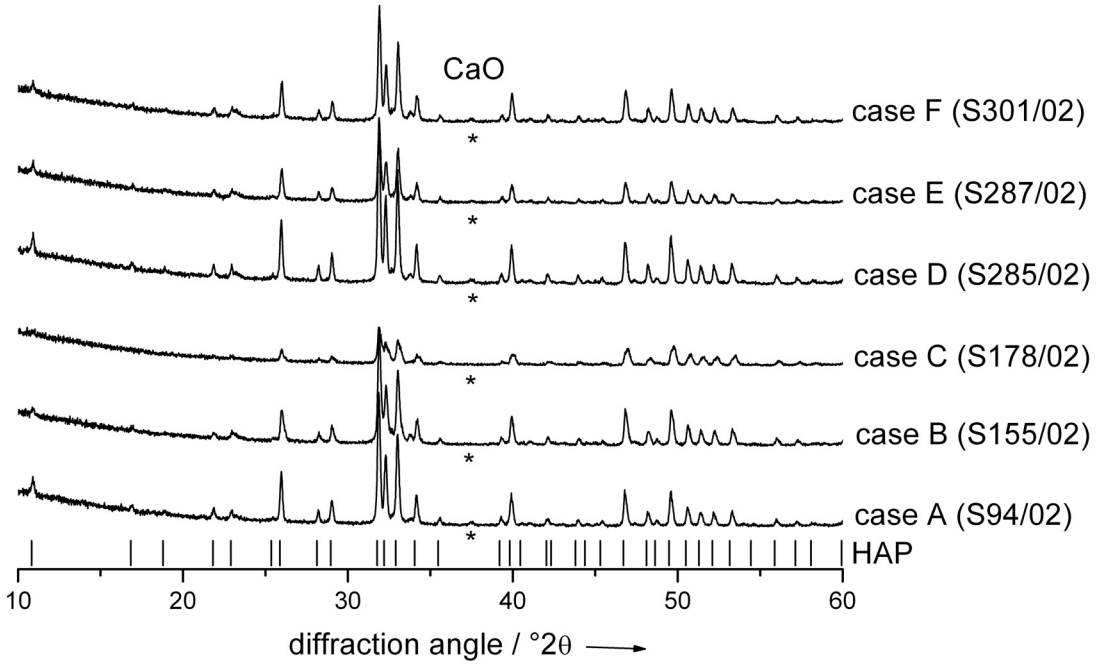

Fig. 3.4-10: X-ray powder diffraction patterns of the calcined residues of the atherosclerotic plaques after heating in TGA to 900°C. All data were converted to Cu $K\alpha_1$-radiation wavelength (λ=1.54056 Å). All samples consist of hydroxyapatite (HAP). Traces of calcium oxide can be identified by its main peak, indicated by an asterisk. Both components originate from the decarboxylation of carbonated apatite.

3.4-10. For comparison, the diffraction patterns of hydroxyapatite (HAP)[254] and the main peak of calcium oxide[256] are indicated. Calcium oxide is formed by decarboxylation of carbonated apatite according the simplified and non-stoichiometric equation[246, 247]:

$$Ca_{10}(PO_4,CO_3)_6(OH)_2 \rightarrow Ca_{10}(PO_4)_6(OH)_2 + CaO + CO_2\uparrow$$

No other phase besides HAP and CaO could be detected which allows the conclusion that only carbonated apatite is present as mineral phase in atherosclerotic plaques. These findings correspond to the results of Tomazic *et al.*[244, 249, 250] However, Bigi *et al.*[257] found hydroxyapatite and some highly crystalline β-tricalcium phosphate β-$Ca_3(PO_4)_2$ (β-TCP). The latter was found in samples from the media layer of the aortic wall. The samples investigated here were of intima origin only.

The results showed that the inorganic phase of the heavily mineralised atherosclerotic plaques consists exclusively of carbonated hydroxyapatite. No major differences between the chemical composition and the ultrastructural appearance of the mineral deposits in the individual patients were found despite the strong differences in the aetiology of each patient. The crystals show a similar anisotropy in crystal dimensions and are of the same size like bone mineral crystals. These results point to similar mechanisms of formation of the vascular calcifications as it is currently under discussion: Bone formation and pathologic calcifications are related to the same "passive" mechanism, i.e. a precipitation from oversaturated body liquids that is controlled by certain inhibitors (like fetuin or matrix GLA protein)[237, 258, 259]. However, the fact that the mineral nanocrystals are of a larger variety in shape and size than bone crystals and show a less distinct anisotropy suggests a smaller degree of shape control in crystallisation compared to bone formation.

4. Simulation of biomineralisation *in vitro*

4.1 Crystallisation under the influence of biomimetic substances

4.1.1 Simulation methods

As explained in chapter 2, the biological precipitation of minerals occurs under controlled conditions. Temperature, ion concentrations, and pH are all kept constant during crystallisation. The reaction rate is controlled by diffusion of ions into the nucleation or growth site and is thus slow compared to chemical precipitation (mixing of ions to form the insoluble precipitate). Organic macromolecules control the phase, morphology and mechanical properties of the forming biocrystal as outlined in chapter 2. In order to crystallise under biomimetic conditions *in vitro*, several experiments have been developed which can be categorised in five methods.

The simplest way of precipitation is mixing of two solutions containing organic macromolecules, similar to chemical crystallisation by slowly adding solution A to solution B.[47] Although, this procedure has nothing in common with biological crystallisation, it allows to examine the general influence of the macromolecules investigated on nucleation and rate of crystal growth.[61] The precipitation rate is either increased or decreased. In the case of calcium carbonate and calcium phosphate, reaction progress is usually determined by monitoring the pH. Carbonate salt solutions react basic in water under the carbonate/hydrogencarbonate equilibrium. When carbonate ions are

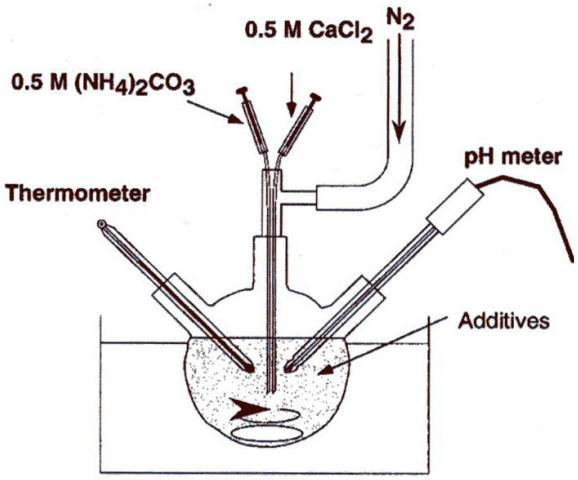

Fig. 4.1-1: Following the precipitation of calcium carbonate by monitoring the solution pH. The precipitate forms under protective atmosphere (N_2).[61]

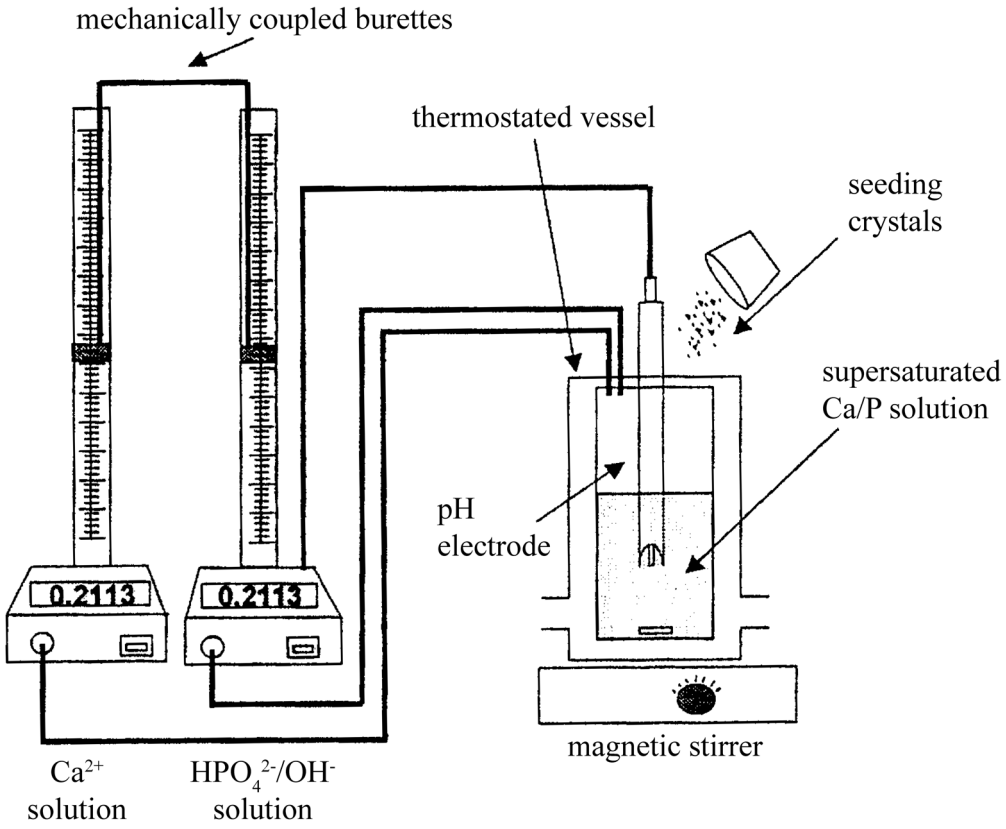

Fig. 4.1-2: Schematic setup of the *C*onstant-*C*omposition-device developed by Nancollas *et al.*[260] By monitoring the pH, the solution concentration is held constant.

removed from the system, hydrogen carbonate dissolves into protons and carbonate ions in order to once more achieve carbonate/hydrogen carbonate equilibrium. The released protons result in a decrease in pH. Figure 4.1-1 shows the experimental setup.

As described above, in biological systems, ion concentrations are kept constant. The constant-composition technique counters the pH decrease and the depletion of ions by adding stock solutions. It was developed by Tomson and Nancollas in 1978 and allows the execution of reproducible experiments at constant concentration conditions.[260] The device consists of a thermostated vessel, containing a supersaturated calcium phosphate solution. Figure 4.1-2 schematically explains the experimental setup. The addition of seeding crystals triggers the crystallisation of hydroxyapatite thus depleting the solution of ions. The pH drops according to:

$$10\ Ca^{2+} + 6\ HPO_4^{2-} + OH^- \rightarrow Ca_{10}(PO_4)_6(OH)_2 + 6\ H_2O$$

During crystallisation, the pH is monitored. Two mechanically coupled burettes containing calcium and phosphate solution, respectively, are triggered if the pH drops beyond a selected threshold. Functionality and reproducibility of the results obtained have been shown in several works.[261-263] The addition of a calcium selective electrode considerably improved the detection method and allowed a better control to hold the ion concentrations constant.[264]

Although the constant-composition method is an approach to biological constant composition mechanisms, crystallisation still occurs much too fast compared to biomineralisation. In biological systems, a controlled diffusion of ions to the nucleation or growth site results in slow crystal growth. A slow crystal growth is achieved with the ammonium carbonate method, first applied for crystallisation experiments by Lia Addadi and Steve Weiner.[33] Small vessels (usually multi-dishes) containing a calcium solution are placed in a desiccator. The drying material is calcium chloride. Additionally, small vessels with ammonium carbonate are placed in the desiccator. To further reduce the diffusion rate, all vessels are covered with thin aluminium foil and only tiny holes allow diffusion. Figure 4.1-3 shows the schematic setup. Ammonium carbonate has a vapour pressure of 69 mbar at 20°C (188 mbar at 30°C) and decomposes slowly over time according to:

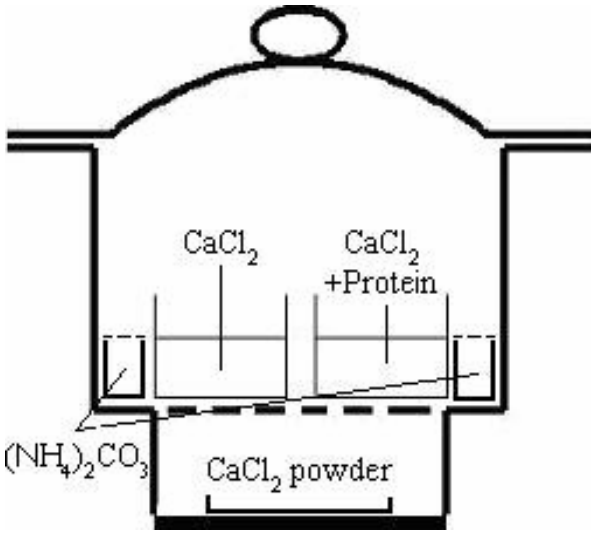

Fig. 4.1-3: Schematic setup of the ammonium carbonate method.

$$(NH_4)_2CO_{3\,(s)} \rightarrow 2\ NH_{3\,(g)} + H_2O_{\,(g)} + CO_{2\,(g)}$$

Water is absorbed by the calcium chloride. Carbon dioxide slowly diffuses into the calcium salt solution, giving a slow crystal growth. The interactions of organic macromolecules can be studied more easily. The major drawback of this method is the incorporation of ammonia into the calcium salt solution, increasing the pH and changing ion activities.

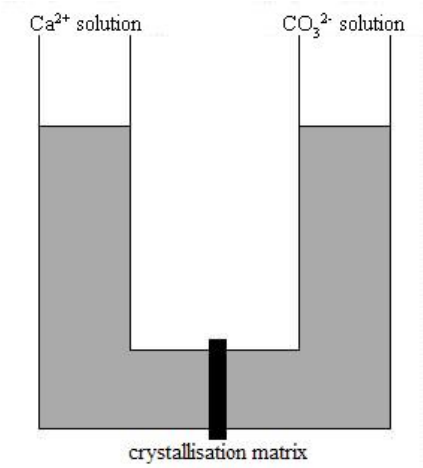

Fig. 3.4-4: Simple double-diffusion setup.

The aim of slow crystallisation controlled by diffusion is achieved by double-diffusion methods. From two vessels separated by a crystallisation matrix, cations and anions diffuse into the matrix where precipitation occurs.[265] Figure 4.1-4 illustrates this simple setup. The method is easy to use and does not involve added ions. However, the concentration of ions decreases and the pH changes during the precipitation. Furthermore, the amount of necessary organic macromolecules is extraordinary, depending on the starting volumes of the stock solutions. A widely used variety of this method is the replacement of the crystallisation

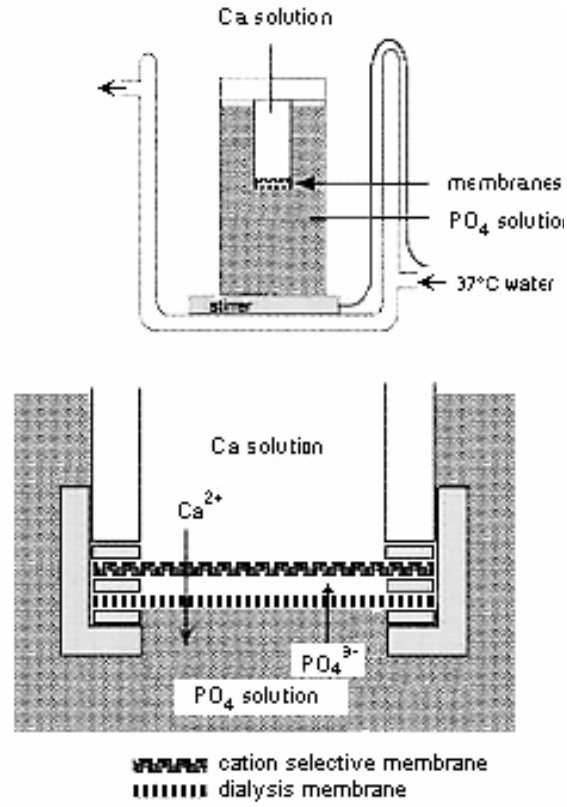

Fig. 3.4-5: *D*ouble-*D*iffusion setup with a crystallisation chamber as developed by Iijima *et al.*[266]

matrix by a crystallisation chamber of small volume as shown in Figure 4.1-5.[266-268] This volume can be used to hold solutions of protein matrices or gels as crystallisation matrix.

Peters and Epple combined the double diffusion method with the constant-composition technique and designed a *constant-composition double-diffusion* device for biomimetic crystallisation of hydroxyapatite and fluoro-hydroxy-apatite.[252] Two vessels containing solutions of calcium and phosphate, respectively, are connected by a crystallisation matrix. When crystallisation in the matrix occurs, the pH decrease is detected. A drop in pH beyond a selected threshold triggers the addition of stock solutions. Ion concentrations, pH value and temperature are held constant during a slow diffusion-controlled crystallisation. So far, this method imitates the biological conditions like no other. However, it is technically rather complex to realise.

4.1.2 Crystallisation of calcium carbonate under the influence of additives

In recent years, biomineralisation has become a popular research area.[60, 269] The influence of organic macromolecules contained in biominerals was already postulated by P.E. Hare in 1963[270] and demonstrated by Y. Kitano and D.W. Hood in 1965.[271] The effect of proteins during crystal growth was proven in many *in vitro* experiments. Wheeler *et al.* extracted the water-soluble organic matrix from oyster shells and dissolved it in solutions with different concentrations of sodium carbonate.[47] The addition of calcium chloride solution yielded calcium carbonate in all cases. However, the inhibiting influence of the additives on nucleation and growth of calcium carbonate was shown. Dissolution of the crystals obtained allowed to relate the quantities of calcium and protein in them.

The organic matrix as structural framework initiates and controls the growth of biominerals.[272, 273] It consists of soluble and insoluble proteins of various kinds.[36, 48] The biological characterisation of extracted soluble matrix proteins

and their effect on morphology or phase of crystals artificially grown in their presence became more important.[48] Soluble organic matrix proteins extracted from mollusc shells are often acidic glycoproteins rich in the amino acid aspartate/aspartic acid. In β-sheet conformation, those proteins were shown to interact specifically with certain crystal faces of calcium dicarboxylates.[33, 274] This was explained by appropriate orientation of the carboxyl-groups of asparagine which create extended structured calcium-interacting domains. When adsorbed on a solid substrate, these proteins are able to induce the growth of calcite from the (001) face.[275] However, poly-aspartic acid was not able to induce oriented calcite formation. The polysaccharides found in the glycoproteins are often sulphated (rich in calcium-attracting sulphate groups). Both components, i.e. proteins and polysaccharides, interact to achieve a specific calcite nucleation.[214, 275, 276]

The ability of soluble matrix constituents to interact with specific crystal faces of the polymorph they were extracted from was shown in different experiments. Soluble matrix proteins were partially purified and calcium carbonate was grown in their presence.[46, 66, 277] Depending on the protein fraction, crystals with different morphologies were obtained. New faces of calcite crystals emerged when specific interactions occurred which blocked the growth of that particular crystal face. Calcium carbonate precipitated on a calcite template in the presence of extracted proteins yielded calcite crystals with an expression of preferred faces like in the biomineral the proteins originated from.[278, 279] The same effect was shown for aragonite precipitated on an aragonitic mollusc shell.[280] Proteins extracted from calcitic and aragonitic layers of nacre were able to induce aragonite prisms and calcite crystals with predominant (104) faces, respectively.[44] Antibodies were shown to recognise specific crystal faces and to absorb on them, leading to a specific change in the morphology of the grown crystal.[52] Unspecific adsorption of macromolecules on crystal surfaces first leads to a change in crystal morphology, then to inhibition of crystal growth and

finally to complete nucleation inhibition, depending on the type of protein or its concentration as shown in various experiments.[281-288] Proteins adsorbed on crystals during growth may stabilise polymorphs usually unstable under ambient conditions like vaterite[289] or even precipitated amorphous calcium carbonate (see chapter 2.2).

For calcite, computer simulation techniques were used to investigate the adsorption of organic molecules to a series of monatomic growth steps.[53] Carboxylic acids and hydroxyl aldehydes (carbohydrates) were found to adsorb strongly, interacting with calcium ions rather than with carbonate ions. Depending on the place of adsorption, either the morphology is changed or the growth rate is reduced. It was calculated that changes of crystal morphology are likely to occur when adsorption occurs on growth steps terminated by either calcium or carbonate ions. In contrast to that, a decrease of general growth rate was found to occur in case of adsorption of the organic molecules on stoichiometric steps. However, the primary structure is not the only essential criterion for successful protein-surface interaction. The backbone of the protein must be flexible enough to allow its unfolding to achieve a maximum interaction.[290] Furthermore, the adsorption of proteins on surfaces does not only depend on polar surfaces. The effect of proteins recognising specific surfaces was also demonstrated for metals[291], metal oxides[292-294], semiconductors[295], and even zeolites.[296] Interactions of biological macromolecules with crystals are chiral as shown by Sugawara *et al.*[297] and Orme *et al.*[298]

The growing agreement that the insoluble organic matrix acts as scaffold for the adsorption of soluble anionic proteins and glycoproteins which then regulate the nucleation and growth of biominerals led to experiments investigating the role of the scaffold.[299, 300] Falini *et al*. showed a necessity of the insoluble organic matrix for adsorbed soluble proteins to exercise control on crystal polymorph formation.[121] The soluble organic matrix extracted from mollusc shells that consisted of aragonite or calcite, respectively, were adsorbed on a mixture of β-

chitin and silk fibroin. The proteins extracted from aragonitic shells induced the formation of aragonite whereas the proteins extracted from calcitic shells induced the formation of calcite. The soluble matrix proteins in solution alone mostly yielded calcite. However, Belcher *et al.* showed the contrary with their crystallisation experiments.[301] They found soluble polyanionic matrix proteins able to induce different calcium carbonate polymorphs, independent from the scaffolds. Similar results were obtained by Feng *et al.*[45] These examples show the complexity and diversity involved when dealing with proteins. As stated before, the terminus protein covers a range of different polymeric molecules and molecular assemblies. It is possible that one type of organic matrix constituents exercises effects only as adsorbates, whereas another type is already active in solution.[269] As highly specialised organic macromolecules, proteins exercise various effects on growing crystals which cannot easily be generalised. A summary of information on the structure of different natural and synthetic proteins and their activity concerning the crystallisation of calcium carbonate is given by Sikes and Wheeler.[287] Treccani *et al.* offer a general overview on proteins involved in biomineralisation processes.[302]

Calcium phosphate[267] and calcium carbonate[268] were precipitated in the presence of gels made of gelatine (denatured collagen from bovine bone) in a double-diffusion setup. Crystals grown in gel showed spherical morphology or were spheres which seemed to be fused. The addition of different additives to calcium carbonate growth showed morphological changes, depending on the additive used and on the composition of the gel.[303-305] Changing from gelatine gel to a polyacrylamide-hydrogel yielded unexpected morphologies of calcite. The particles obtained by Grassmann *et al.* were of pseudo-octahedral morphology. The formation of these pseudo-octahedrons consisting of several individual crystallites was directly connected to the polyacrylamide-hydrogel matrix which was incorporated into the grown crystals. By modifying the polyacrylamide-hydrogel matrix by copolymerisation with acrylic acid, the gel

facilitated the nucleation of small crystallites of vaterite and calcite. Furthermore, the gel stabilised vaterite despite increasing supersaturation. However, after an extended period, a rapid growth of calcite spherules was observed. The authors concluded that the mineralisation mechanism was significantly altered by specific interactions between the matrix network and the forming mineral. Falini *et al.* used a similar setup of gelatine gel and poly-L-aspartate.[306] They obtained oriented crystallites of vaterite by epitaxial crystallisation on a gelatine/polypeptide film. The crystallisation method they employed was ammonium carbonate diffusion and their poly-L-aspartate concentration per gram of gelatine was more than ten times higher than the concentration used by Grassmann *et al*. These results indicate the importance of non-collagenous proteins to exercise control on crystal growth. Tremel *et al.* also showed that acidic peptides acted as growth modifiers of calcite crystals.[307] They designed amphiphilic acididc peptides consisting of alternating hydrophilic aspartic acid residues and of hydrophobic phenylalanine residues. This setup imitates proteins from calcified tissues. Calcite crystals obtained by ammonium carbonate diffusion expressed diamond-like morphology (rhombohedra with faces instead of edges) with 012 and 110-faces. These polar faces were also expressed in crystallisation experiments in the presence of proteins extracted from biominerals.[66, 278]

However, the exact role of additives during crystallisation is still in debate.[269] Immobilised biological macromolecules preadsorbed on surfaces were shown to act as template, alter the nucleation rate or change the morphology of the grown crystals. However, the same additives in solution often inhibited crystal growth completely.[47, 308] Park and Meldrum were able to achieve the precipitation of calcite crystals with non-rhombohedral morphology by external imposition of morphology without the aid of any additives.[265, 309] The first precipitate was amorphous calcium carbonate which later crystallised into calcite. They generated a polymer replicate of a sea urchin skeletal plate in which calcite was

precipitated showing similar morphology like the biomineral. Crystallisation of calcium carbonate by double-diffusion into a β-chitin scaffold yielded the presence of all three water free modifications: calcite, aragonite, and vaterite, depending on the position in the matrix.[310] Therefore, local supersaturation inside the compartmentalised space governs the occurrence of a certain polymorph. This relationship was also noted earlier.[311]

All these experiments show the importance of template and additives of the organic matrix in the formation of biominerals.[269] The local supersaturation and the presence of added ions also have a considerable effect on forming crystals. The most prominent ions present in biomineralisation of calcium carbonate are magnesium cations which are isoelectric to calcium and phosphorous containing anions like phosphate. Magnesium inhibits calcium carbonate crystal growth by incorporation into the crystal lattice.[312] This results in increased mineral solubility and therefore a reduced crystal growth rate. Further, it considerably changes calcite morphology, mostly elongating them along the c-axis.[100, 313, 314]

The presence of phosphate and glycophosphate anions reduces the rate of calcium carbonate nucleation.[315] This was also explained by blockage of crystal growth sites.

Biomimetic experiments are not only carried out in order to investigate biomineralisation processes. Material science is more and more interested in this topic, as biominerals show unique mechanical properties.[57, 60] Artificial additives in the form of diverse block co-polymers yielded hollow spheres of calcite, vaterite discs or *c*-axis oriented needles of calcite.[54] Additives may also increase the nucleation rate[316] or stabilise ACC.[104]

Artificial additives can be used as templates for crystallisation. Epitaxial control is exercised by the template surface when crystallisation occurs on S*elf-*A*ssembled-*M*onolayers* (SAMs). Depending on the template, calcite, aragonite, and vaterite could be precipitated as desired.[38-41, 43, 317, 318] Crystallisation on SAMs offers the opportunity to investigate the interaction between organic layer

and mineral phase.[319] The monolayer packing density was found to be important for polymorph selectivity, whereas monolayer texture differences seemed to define the location of crystal nucleation. Computational model systems for the growth minerals on Langmuir monolayers were employed to demonstrate the various types of nucleating crystal behaviour.[42]

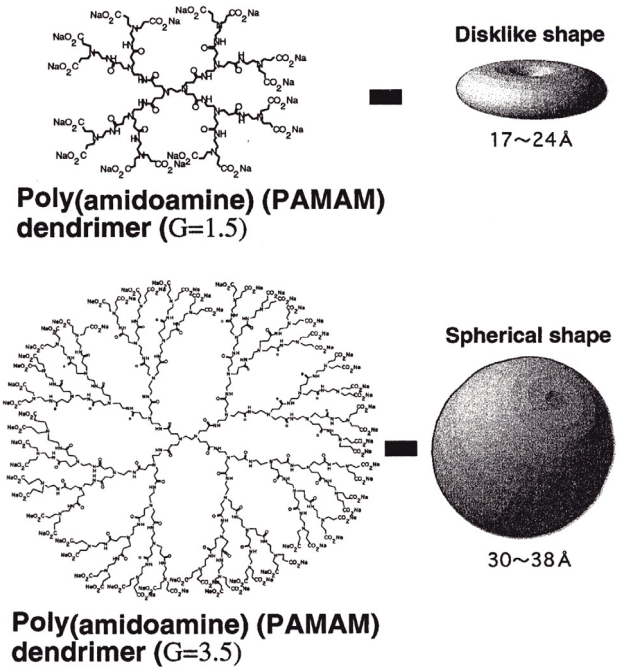

Fig. 4.1-6: Synthetic additives are used to mimic biomineralisation processes by specific adsorption on crystal faces, thus changing morphology.[269]

A relatively new class of organic molecules are dendrimers (see Figure 4.1-6 as an example of this class of molecules).[269] If used as additives, specific polymorphs were precipitated from solution with the aid of dendrimers. Being relatively big molecules, dendrimers were shown to act as nucleation sites.[61, 103, 320] Like with biological macromolecules, dendrimers were shown to stabilise metastable polymorphs. Naka *et al.* were able to stabilise vaterite and ACC with poly(amidoamine) and its sodium salt, respectively, for at least four days.[321]

However, in biology, cells control nucleation site, supersaturation, protein adsorbates, and crystallisation matrix as well as the space and the chronological order of their combination. So far, laboratory experiments were only able to mimic one or two of these parameters together, but never all of them.

4.2 *In-vitro* crystallisation of calcium carbonate in the presence of biological additives

4.2.1 The shell of molluscs[36, 48, 322, 323]

The phylum Mollusca covers animals with a muscular soft body, consisting of the cephalopodium (headfoot) and the visceropallium (gut plus mantle). Most of these animals possess a shell. The best known classes among the Mollusca are Bivalvia, Gastropoda, and Chephalopoda. The class Bivalvia comprises animals which possess shells consisting of two parts like oysters. The Gastropoda comprises snails and slugs whereas the class Chephalopoda comprises animals like squids and octopus. Even more than in terrestrial isopods (see chapter 3.2), the diversity of molluscs impressively demonstrates how a basic body plan can evolve into a variety of different forms adapted to specific environments, e.g. a terrestrial snail and a marine octopus. The simplified phylogenetic relationships of the molluscs are shown in Figure 4.2-1.

Mollusc shells consist of four layers. The outermost layer is the periostracum. Similar to the epicuticle in crustaceans, this layer does not contain any mineral but only proteins and carbohydrates forming a water-proof barrier. It further serves as deposition site for the mineral phase. The next inward layer is the ostracum consisting of calcium carbonate mineral deposits and organic matrix. Prisms of mineral can be arranged in several structures.[323] Very prominent is the cross-lamellar structure, achieving a high structural integrity as shown in

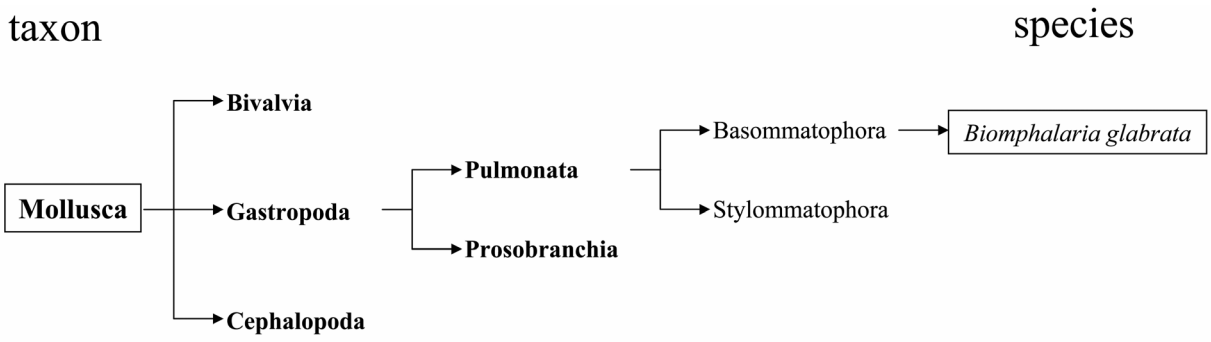

Fig. 4.2-1: The phylogenetic classification of the fresh-water snail *Biomphalaria glabrata*.

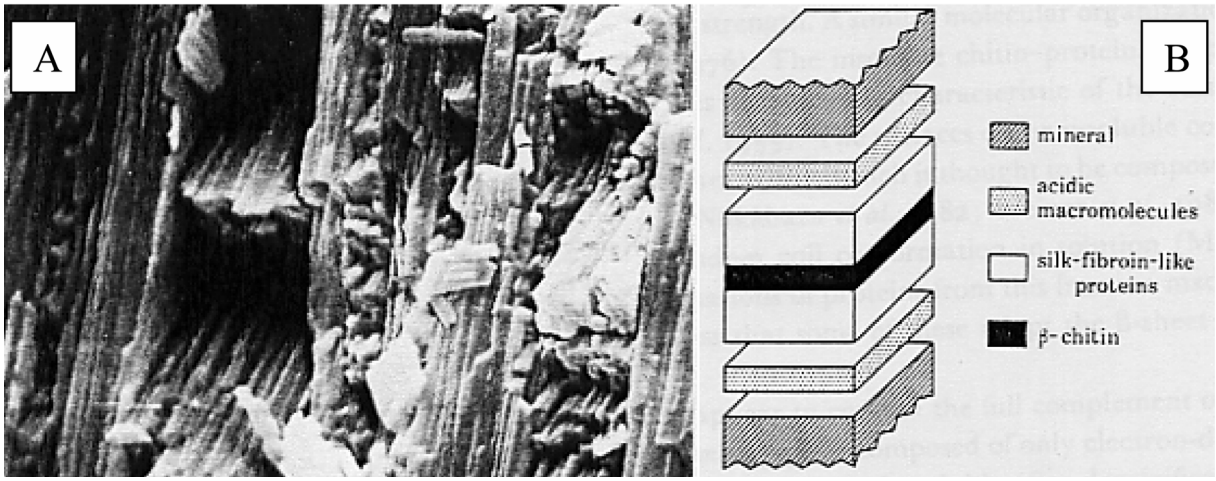

Fig. 4.2-2: SEM image of a cross-lamellar structure of a gastropod shell (A). Image B schematically shows the interactions of mineral and organic matrix. See the text for details.

Figure 4.2-2A. The mineral phase and the organic matrix form a composite material. The insoluble organic matrix consists of β-chitin and silk-fibroin like proteins. Soluble organic matrix proteins are adsorbed on the surface of this framework and connect to the mineral. Figure 4.2-2B shows a schematic representation of this arrangement. It has was shown that the chitin fibres and the protein chains are aligned with the crystallographic *a* and *b*-axes of aragonite, suggesting an epitaxial growth of the mineral on the organic framework.[36]

In the case of the freshwater snail *Biomphalaria glabrata* (Pulmonata, Basommatophora), the embryonic shell formation within the egg begins two days after oviposition.[191] First, the periostracum is formed, and then calcium is accumulated in the extrapallial space between the periostracum and the outer mantle epithelium after about 2.5 days. The shell mineralisation starts with the precipitation of amorphous calcium carbonate as a precursor phase which then crystallises into aragonite. After about three days, the first crystalline aragonite can be detected by XRD.[65] After five days, the embryos are ready to leave the egg.[324] During the life of the animal, shell growth continues, the growth site being located at the mantle edge.[325] Figure 4.2-3 shows a schematic representation of the growth site which can be divided into five growth zones. In

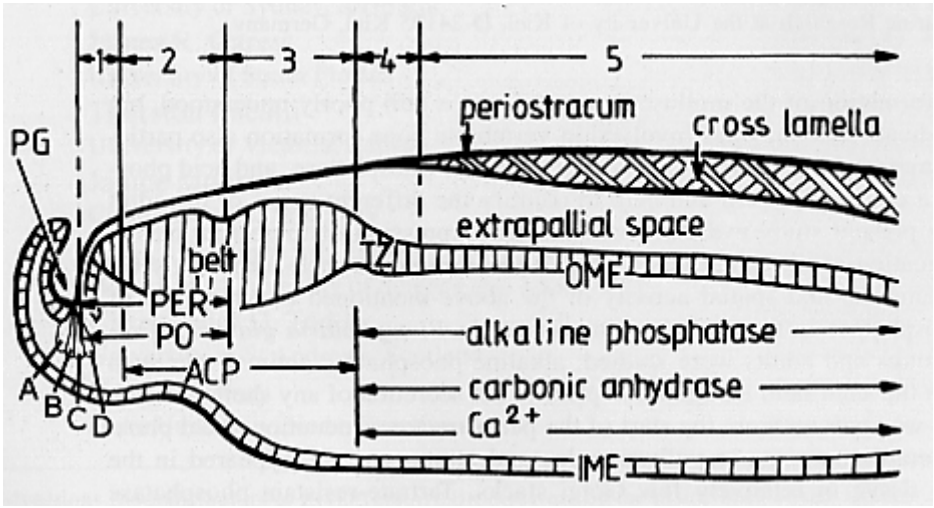

Fig. 4.2-3: Schematic representation of the shell growth zone in *Biomphalaria glabrata*. A-D: specialised cells which form the periostracum. PG: periostracum groove, OME: outer mantle epithelium, IME: inner mantle epithelium, PER, PO, and ACP: zones of presence of specific proteins. Image by courtesy of J. Marxen.

the first distal zone, the periostracum is formed in the periostracum groove (PG) by specialised cells (A, B, C, D). Zones two and three belong to the belt; zone four is a transition zone proximally followed by the outer mantle epithelium (OME). A number of enzymes, e.g. oxidases, carbonic anhydrase, and phophatases were identified in the different regions of the mantle edge, hence the division in the different zones, depending on enzyme occurrence and morphological criteria. Mineral deposition takes place in the extrapallial space between periostracum and OME and is therefore a controlled extracellular precipitation process.[326]

4.2.2 The organic matrix of the shell of the fresh-water snail *Biomphalaria glabrata*

The organic matrix found in the shell of the tropical fresh-water snail *Biomphalaria glabrata* consists of about 1 wt% of the shell's weight of insoluble matrix (IM) and of about 0.03 wt% water-soluble matrix (SM). As stated previously, sulphated carbohydrates together with proteins play a role in biomineralisation (see chapter 4.1). The main components of the SM are proteins (62 wt%), sulphate (7.5 wt%), neutral sugars (8.6 wt%) and amino

sugars (11.9 wt%).[327] Small amounts of uronic acid and phosphate were also found. The SM constituents are proteoglycanes (PGs) or glycosaminoglycanes (GAGs) of high molecular weight and glycoproteins. PGs are glycoproteins containing more polysaccharide than protein. They are polyanionic aggregates consisting of GAGs covalently bound to a core protein and able to bind water in considerable amounts to form gels. A model substance is the easily available mucin, also a PG and GAG mixture found in saliva. GAGs are negatively charged mucopolysaccharides bound in PGs. The only free GAG found is hyaluronic acid. In the SM, the acidic amino acids made up about 23 % whereas 37 % of the amino acids determined were hydrophobic. The sugars present in the SM were glucose, mannose, galactose, N-acetyl-glucosamine and N-acetyl-galactosamine.[328] In gel electrophoresis of the SM, a prominent glycoprotein with a molecular weight of 19.6 kDa and an isoelectrical point of 7.4 was identified. The amino acid sequence of this glycoprotein revealed that it was a member of the dermatopontin familiy which is widespread in mammalin extracellular matrices, including bone and teeth. A unique feature of the 19.6 kDa shell matrix dermatopontin is N-glycosylation with terminal O-methylated mannoses.[329]

By gel electrophoresis and a calcium binding essay, the calcium-binding constituents of IM and SM were determined.[330] The PGs and GAGs were found to be the only calcium binding components. Binding capacity in IM and SM were dependent on solution pH value. At pH 7.4 and in a carbonate environment which resembled the extrapallial fluid, calcium binding capacity was greatest for IM and SM, respectively. Calcium binding by the organic matrix were found to be of low specificity, medium affinity and very dependent on pH value. Therefore, it appears that the prominent 19.6 kDa glycoprotein is not necessarily related to calcium binding but to organic matrix framework integrity.

4.2.3 Comparison of the ammonium carbonate method to double-diffusion techniques[283]

In cooperation with Dr. Julia Marxen and Prof. Dr. Wilhelm Becker from the University of Hamburg, fractions of the soluble organic matrix shell of the freshwater snail *Biomphalaria glabrata* were investigated regarding their influence on calcium carbonate precipitation. As described before, biomineralisation occurs under strict control of nucleation conditions by providing a nucleation template. If the first steps of biomineralisation, i.e. the processes of nucleation and preferential adsorption on specific crystal faces are considered, it turns out that a suitable crystallisation method is required for studying effects of biological macromolecules during precipitation. The *C*onstant-*C*omposition-*D*ouble-*D*iffusion technique developed by Peters and Epple for precipitation of calcium phosphate was adapted for the crystallisation of calcium carbonate.[331] Figure 4.2-4 shows a scheme of the modified setup.

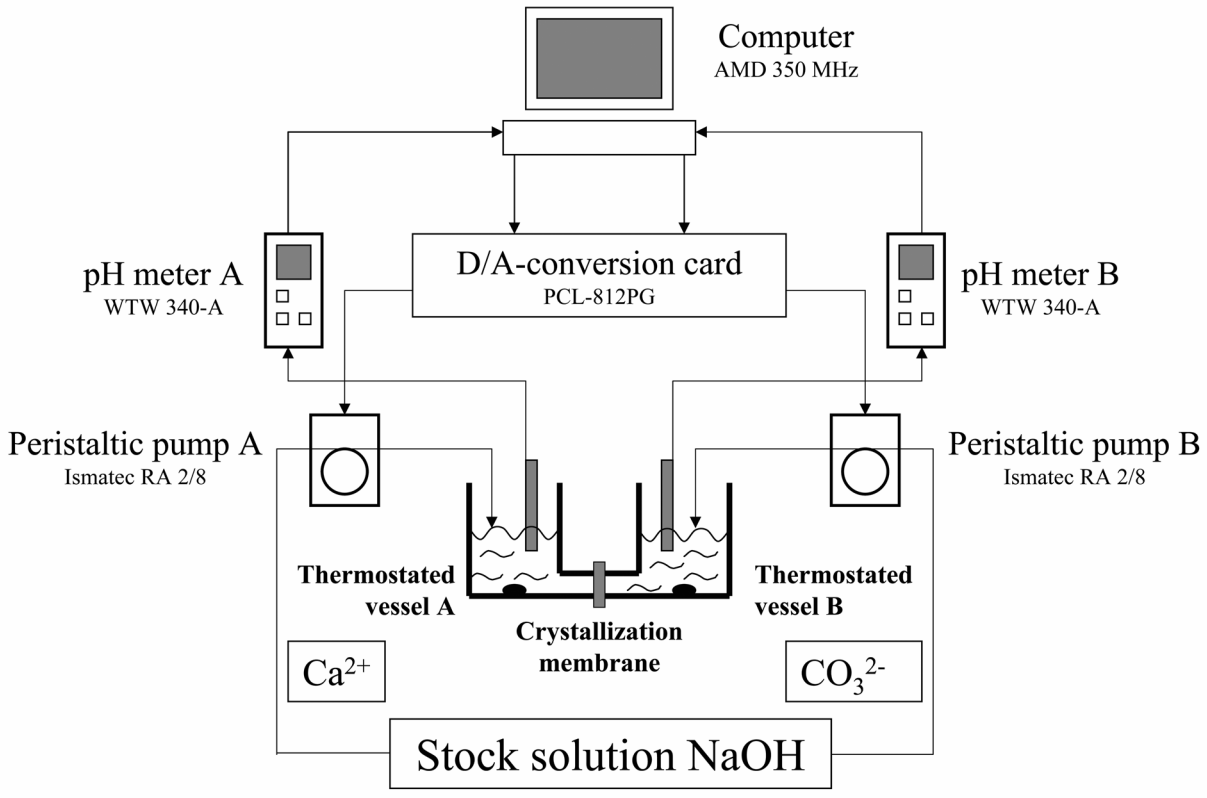

Fig. 4.2-4: Setup of the CCDD-device. The pH in each thermostated reaction vessel is monitored. If the value drops below a threshold, NaOH is added to keep the pH constant.

The device consists of two temperature-controlled vessels. Vessel A contains a calcium nitrate solution of 5 mmol l^{-1} and vessel B contains a sodium carbonate solution with the same concentration. Both vessels are separated by a permeable crystallisation membrane which was a filter paper. With the double-diffusion technique, the two components of a precipitate like Ca^{2+} and CO_3^{2-} diffuse into the membrane where crystallisation occurs. This setup has the advantage of permitting a very slow crystallisation, depending on the type and thickness of the membrane used. During crystallisation, the pH in the vessels decreases according to:

$$Ca^{2+}{}_{(aq)} + HCO_3^-{}_{(aq)} \rightarrow CaCO_{3\,(s)} + H^+{}_{(aq)}$$

Figure 4.2-5A shows the pH value monitored during a crystallisation experiment without pH control. The values decrease from the starting values of 9.39 at the calcium side and 9.52 at the carbonate side. However, the drop at the carbonate side is lower due to the buffering effect of the carbonate solution. After about two days, the pH at the calcium side rises slowly. This is due to the end of the precipitation and the equilibration of pH between both vessels. Although the pH of both solutions was equal before filling them into the apparatus, there was always a small offset between the pH monitored (9.39 and 9.52) and adjusted in both vessels (9.44 and 9.45, respectively). It is suspected that this is due to an electrostatic potential of the membrane influencing the pH electrodes. The offset leads always to a lower value at the calcium side and to a higher value at the carbonate side. Figure 4.2-5B shows the pH value monitored during a crystallisation experiment in which the pH in both compartments was controlled. If the pH-value dropped below a threshold, the computer activated peristaltic pumps that added a solution of sodium hydroxide to the vessel whose pH-value had dropped below the threshold. Each vessel was served by its own peristaltic

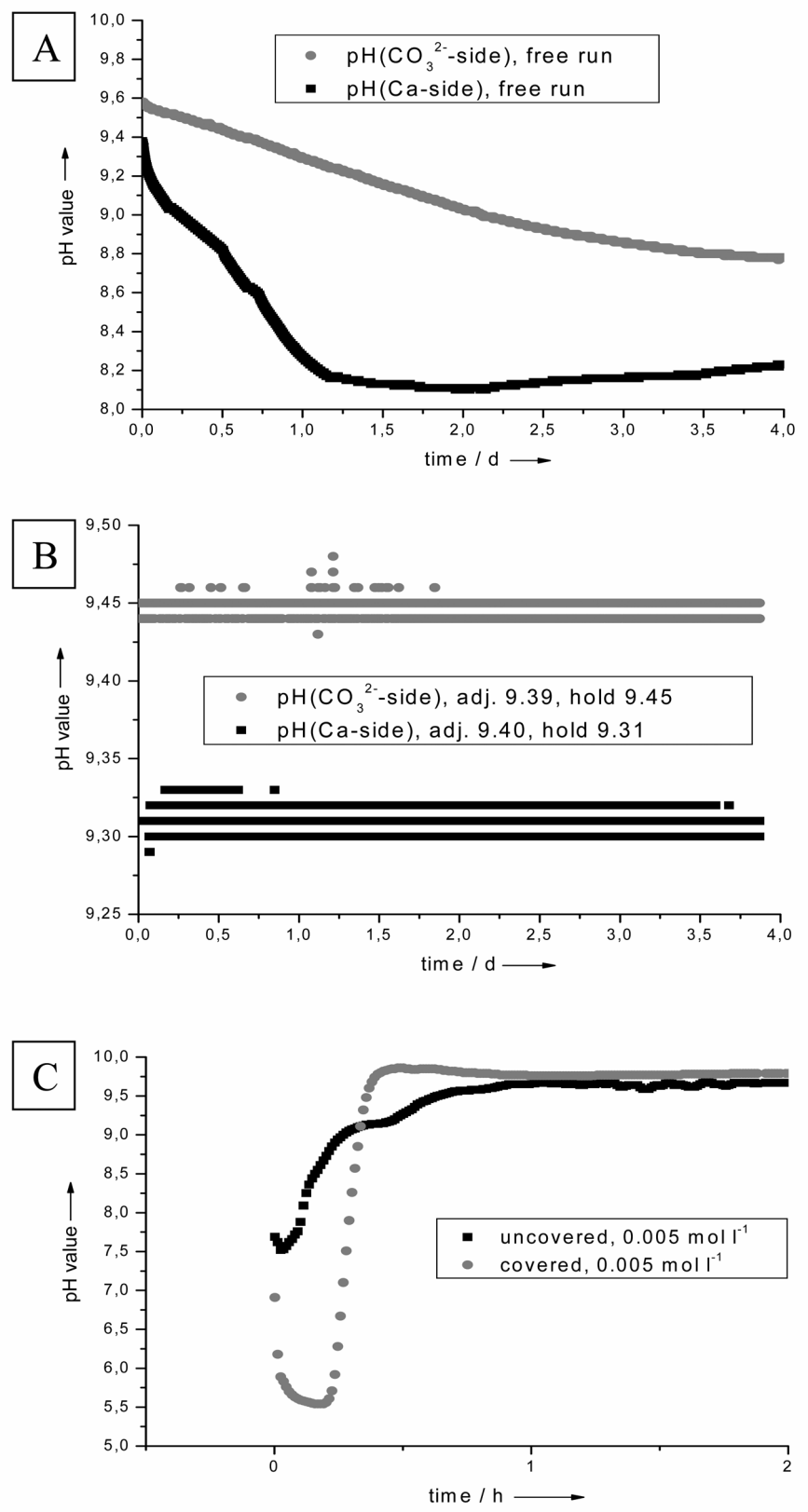

Fig. 4.2-5: pH curves over three days in both reaction vessels without regulation (A), at constant conditions in the CCDD-device (B), and in the calcium solution in the ammonium carbonate method (C).

pump. Therefore, the pH was kept constant in both vessels within about ±0.02 units. As threshold value for each vessel the first values shown by the pH meters were used. In this experiment, these were pH 9.31 at the calcium side and pH 9.45 at the carbonate site. The adjusted values were pH 9.40 and 9.39, respectively.

The decreasing solubility of carbon dioxide in aqueous solutions restricted the possible pH range. From computations of the equilibrium between hydrogen carbonate and carbon dioxide and from practical experience, it was found that it is not possible to set a pH to be held constant of less than 8.0 on the carbonate side of the apparatus. Therefore, a pH of 9.4 was adjusted, at which the regulation turned out to be stable during the experiments.

The major drawback of the CCDD technique is the constantly changing supersaturation as both solutions are depleted on ions during crystallisation. The same drawback applies to the ammonium carbonate diffusion technique which was chosen as the method of comparison. Diffusion of carbon dioxide into the solution leads to a slow crystallisation of calcium carbonate in a calcium solution. Two types of experiment were executed. The beaker containing the calcium nitrate solution was either covered with a hole-dotted aluminium foil or left open so that there was free access of the ammonium carbonate “vapour”. The pH value was monitored in both cases (Figure 4.2-5C). After a drop in pH during the first half hour, the pH had increased to about 9.7 in both cases. Later, the pH dropped constantly to values of about 9.0 in uncovered beakers and about 9.2 in covered beakers after 24 hours (data not shown). The pH increase was due to ammonia diffusion into the solution. Covering the beaker with aluminium foil - intended to slow down the diffusion - led to an even more drastic pH variation. It should be emphasised that this experiment was repeated several times, and also with concentrations of calcium between 5 and 20 mmol l^{-1}. Weighing the formed calcium carbonate showed that almost all material had precipitated after

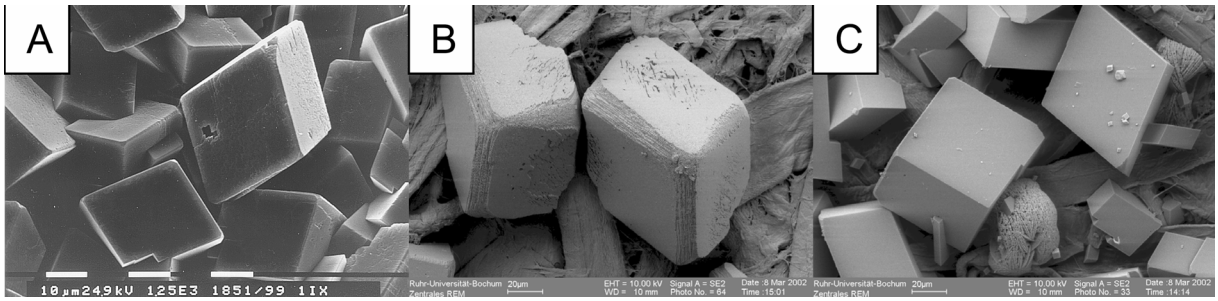

Fig. 4.2-6: Calcite crystals obtained in experiments without any additives in the ammonium carbonate method (A), in an unregulated CCDD-experiment (B), and in a regulated CCDD-experiment (C). The rombohedra in C are far better expressed as in A and B.

about 20 h. Therefore, the variation of pH occurred during the precipitation of calcium carbonate. The pH is not constant during the crystallisation with this method and changes considerably during the first nucleation and growth steps.

Crystallisation of calcium carbonate was carried out in the CCDD device both regulated and unregulated and with the ammonium carbonate method. 25 ml of solutions of calcium nitrate and sodium carbonate with a concentration of 5 mmol l^{-1} were used in each experiment. The solution pH was adjusted to 9.40±0.05 in each case with HNO_3 and NaOH before pouring into the device vessels or the desiccator. The stock solution of NaOH had a concentration of 10 mmol l^{-1}. All experiments were performed at 22±2°C for about four days in the case of CCDD experiments and one day in the case of the ammonium carbonate method. Ashless 589(3) filter paper (blue ribbon, Schleicher & Schuell, No. 300210) with an approximate thickness of 140 µm was used as crystallisation membrane in the CCDD device. The ammonium carbonate diffusion experiments were performed in a desiccator with a volume of about 5 l. The calcium nitrate solution was poured into a beaker with a surface of about 25 cm^2. Figure 4.2-6 shows the resulting calcium carbonate crystals obtained in experiments without any additives with ammonium carbonate diffusion (A), unregulated CCDD (B), and regulated CCDD (C). Calcite was obtained in all cases, except for solitary aragonite crystals. The ammonium carbonate method gives well-shaped calcite rhombohedra. For the double-diffusion experiments, the calcite crystals are significantly better developed under controlled

conditions, i.e. the edges are sharper. In case of the CCDD experiments, crystallisation occurred mostly at the carbonate side of the membrane, indicating a faster diffusion of calcium through the filter.

Before testing the not easily available soluble organic matrix of *Biomphalaria glabrata*, bovine serum albumin (BSA) was applied to the experiments as a model substance. Concentrations of 0.01 mg l^{-1}, 0.10 mg l^{-1}, and 1.00 mg l^{-1} of additive in 5 mmol l^{-1} calcium nitrate and sodium carbonate solution were used, respectively. The protein was added after adjusting the pH to 9.40±0.05. The volumes were 100 ml in the regulated CCDD device and 25 ml in the ammonium carbonate method. The proteins were fully dissolved in the solution before the experiment. All glass surfaces which came in contact with protein were silanised before with 10 % $(CH_3)_3SiCl$ in chloroform. Figure 4.2-7 shows the crystals obtained with the ammonium carbonate method (A series) and the regulated CCDD device (B series). In case of the ammonium carbonate method, the BSA concentrations were 0 mg l^{-1} (1), 0.01 mg l^{-1} (2), 0.10 mg l^{-1} (3), and 1.00 mg l^{-1} (4). In the case of the CCDD device, the BSA concentrations were 0 mg l^{-1} (1), 0.1 mg l^{-1} (2), 1.0 mg l^{-1} (3), and 10.0 mg l^{-1} (4). The precipitation of calcium carbonate by the ammonium carbonate method showed that there was almost no influence of the BSA concentration on the crystal shape. In all cases calcite rhombohedra and solitary aragonite spherules were obtained. Crystal sizes were of the same order of magnitude which was verified by X-ray diffractometry (Figure 4.2-8A). Only traces of aragonite were detected, all calcite was well crystalline. In the CCDD device, there was a clear effect of increasing BSA concentration on precipitation. The amount of precipitate decreased with increasing concentration of protein. This was attributed to an inhibiting effect of the albumin. It is also obvious that there was always more than one polymorph present: calcite rhombohedra were mixed with aragonite spherules as in other similar experiments reported in the

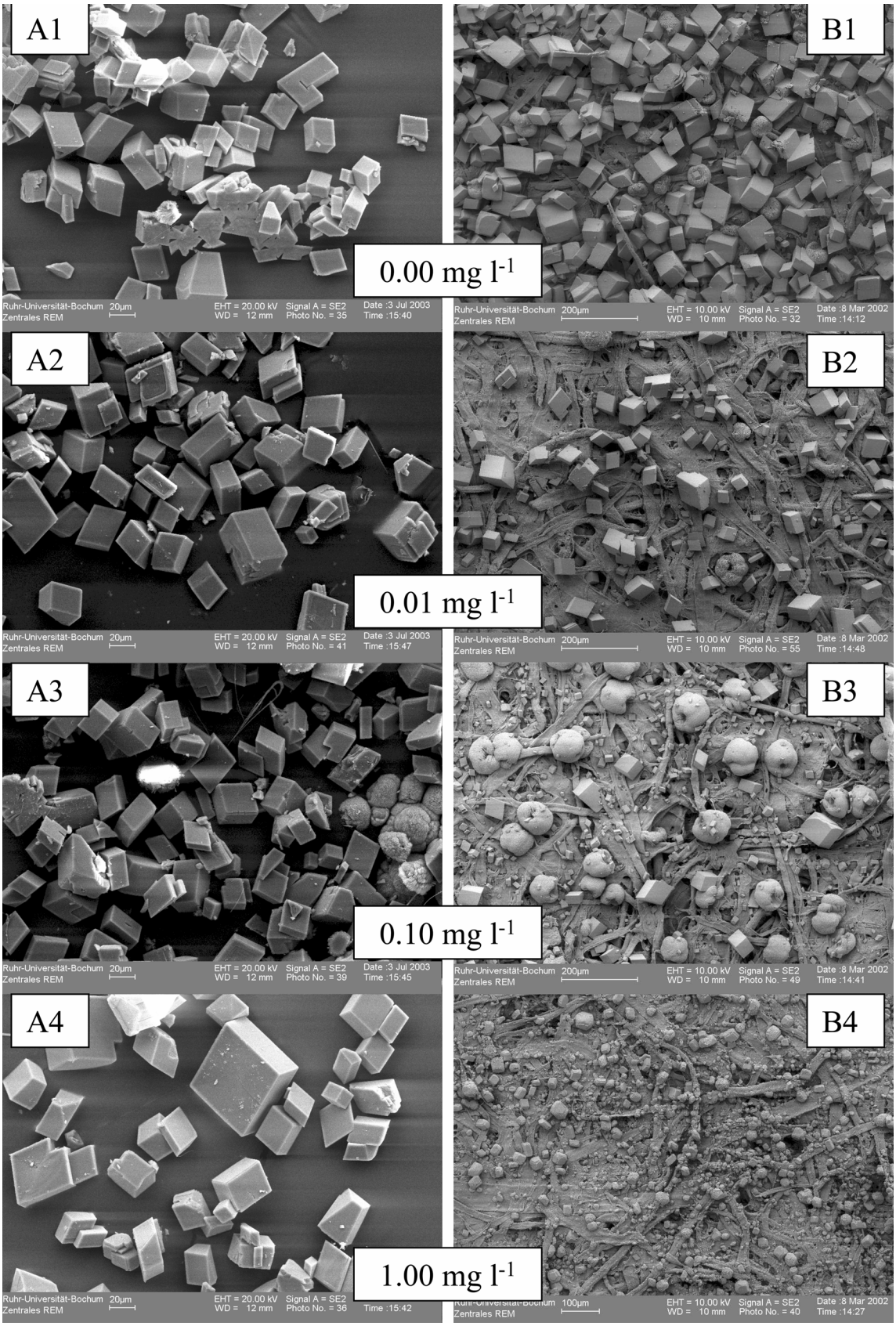

Fig. 4.2-7: SEM images of crystals obtained in experiments with BSA as a control additive in the ammonium carbonate method (series A) and in the CCDD-device (series B). The concentrations of BSA are indicated in the picture. The influence of the additive on growing crystals is clearly and only seen in the CCDD-experiments.

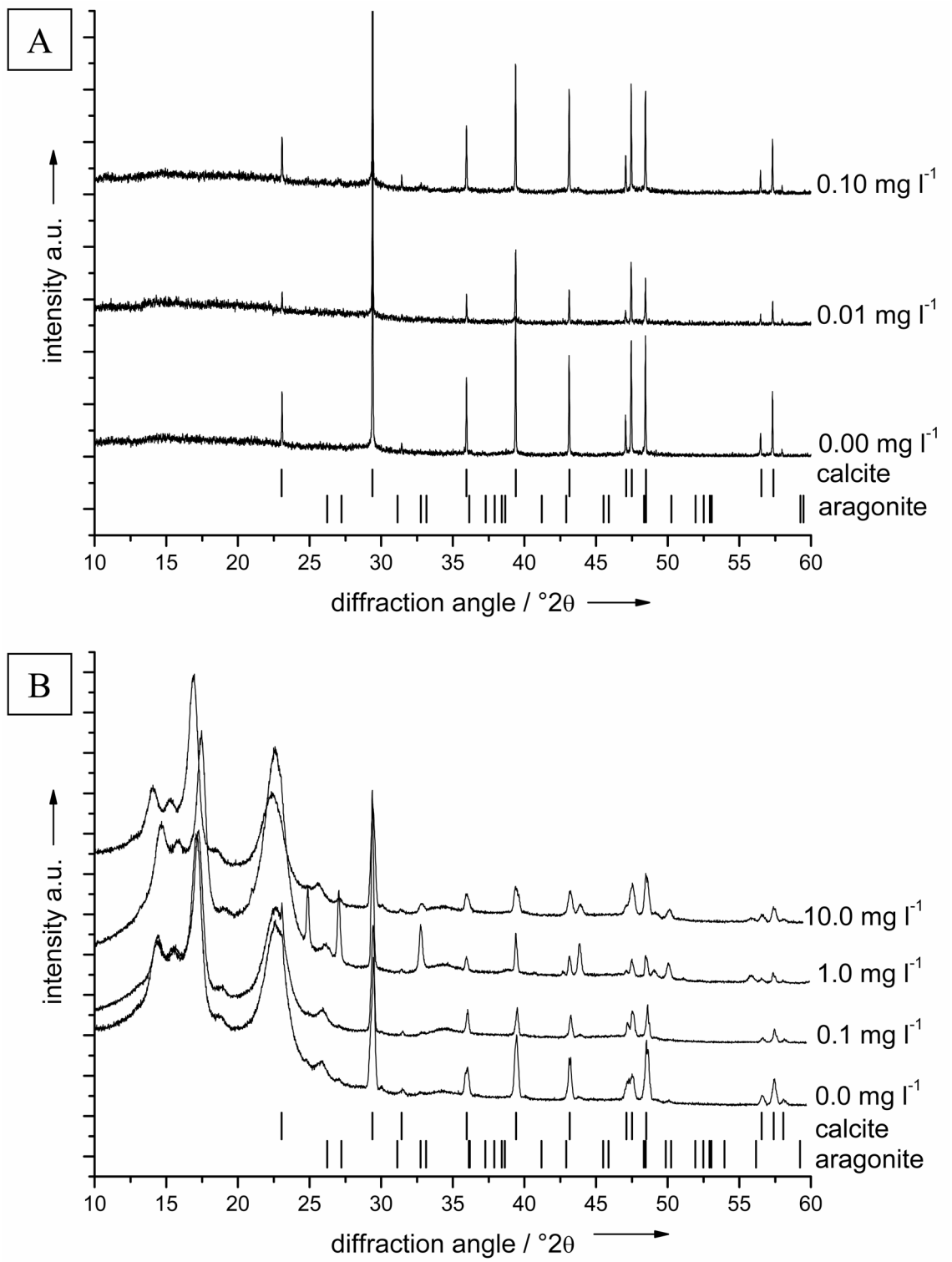

Fig. 4.2-8: Powder X-ray diffractograms of the crystals obtained in the ammonium carbonate method (A) and in the CCDD-device (B). In picture B, the big broad peaks below 25°2Θ result from the cellulose of the filter paper on which the crystals were precipitated.

literature.[40, 121, 306, 310, 332] There was a trend from calcite rhombohedra to aragonite spheres with increasing BSA concentration. In X-ray diffractometry, diffraction peaks of both polymorphs were found in all four cases (Figure 4.2-

8B). However, the preferred orientation of the obtained crystals and the influence of the cellulose crystallisation membrane made a quantitative analysis very difficult. Diffraction peaks of vaterite or monohydrocalcite, $CaCO_3 \cdot H_2O$, were not detected. Unfortunately, not all papers published using the ammonium carbonate method report X-ray diffractometric analysis of the precipitated crystals, i.e. sometimes conclusions are drawn only from the morphology.

In the ammonium carbonate diffusion setup, calcium and BSA were in solution. The forming nuclei of calcium carbonate were coordinated by BSA by means of hydrogen bonds and electrostatic attraction.[333] There are strong interactions in the non-stoichiometric complexes. The formation of soluble BSA-calcium carbonate complexes increased the relative solubility of calcium carbonate. The relative undisturbed growth of the calcite crystals in all cases may be explained by BSA being in solution and saturated with calcium ions, thus non-interacting with the growing crystals. The effective concentration of free BSA may have been too small for a visible interaction between growing calcite crystals and the protein. Fan *et al.* also obtained calcite with this method in the presence of fetal BSA, preadsorbed on mica.[288] They also observed a preferred orientation of the calcite crystals and explained this finding by their BSA being adsorbed, acting as a template, whereas the BSA in the experiments executed here was in solution. In the CCDD setup, the crystallisation matrix played an important role i.e. it may act as crystallisation template. Cellulose powder was found to be a substrate favouring the deposition of calcite crystals.[334] Therefore, the visible influence of BSA to promote the precipitation of aragonite is probably not an artefact created by the crystallisation membrane. The size of the crystallites decreased with increasing protein concentration. From SEM pictures, the following numbers for the maximum crystal diameter were obtained for the albumin concentrations of 0, 0.1, 1, and 10 mg l^{-1}: Calcite rhombohedra: 52(10), 41(12), 33(12), 15(5) µm; aragonite spherulae: 50(15), 80(20), 72(14), 11(2) µm (by averaging over about 30-50 crystallites; standard deviation given in

parentheses). Yang *et al.* who also used a kind of a diffusion-controlled method found a strong direction towards vaterite induced by the presence of BSA.[335] However, they did not insert a membrane but let two solutions diffuse into each other, therefore this discrepancy can be attributed to different experimental conditions. This underscores how the crystallisation method may change the effect of additives on crystal shape and polymorphic phase. Jin *et al.* reported a general inhibiting effect of different protein hydrolysates on the crystal growth of calcium carbonate.[285] However, no information on the polymorphic phase was reported.

In both setups, the soluble organic matrix of the shell of the freshwater snail *Biomphalaria glabrata* was investigated regarding its effect on calcium carbonate precipitation. The experimental conditions used were identical to those described above; the concentration of matrix was 1.00 mg l^{-1}. Figure 4.2-9A shows the crystals obtained by the ammonium carbonate method. There was no discernible effect of the additive on the crystal size or morphology, also in comparison to the other figures, Figure 4.2-9B shows the complete inhibition exercised by the matrix in the CCDD setup. There was no mineral deposition (also at higher magnification), i.e. no crystals were found on either side of the membrane or within. A possible explanation could be a very strong interaction

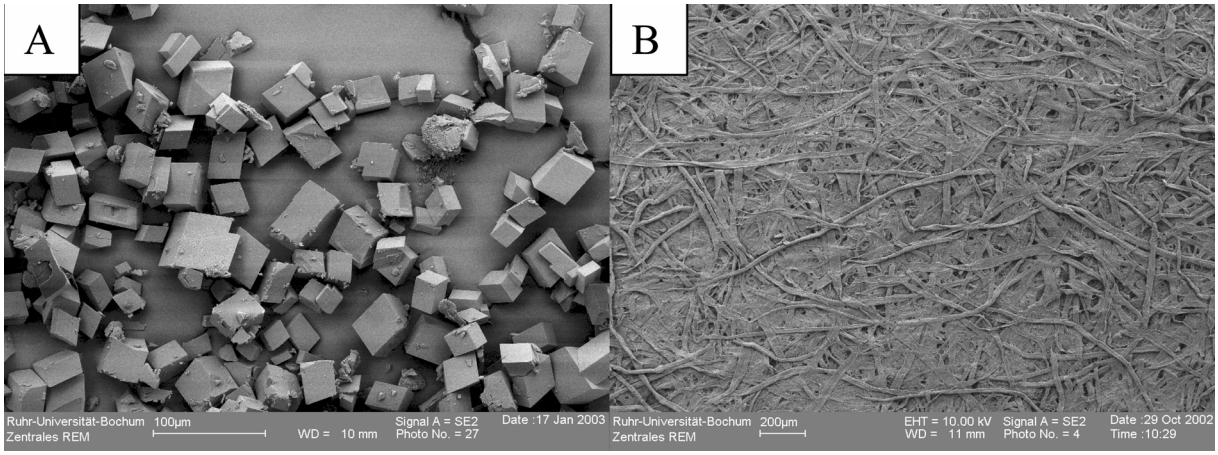

Fig. 4.2-9: SEM images of crystals obtained in the ammonium carbonate method in the presence of 1 mg l^{-1} extracted soluble matrix proteins (A). In the CCDD-device, the same concentration of soluble matrix sample led to complete inhibition of crystal growth (B).

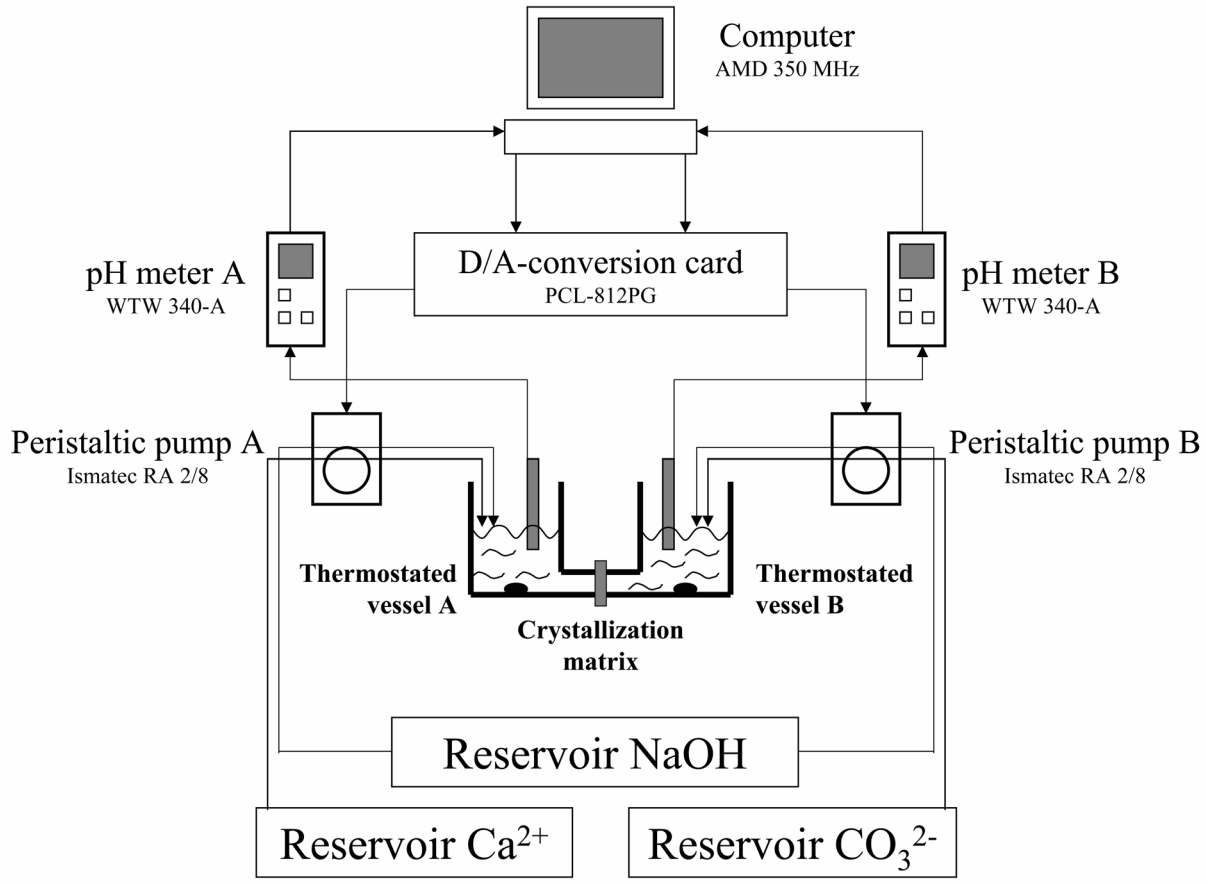

Fig. 4.2-10: Scheme of the modified setup of the CCDD-device. When NaOH is added, a double concentrated ion solution is pumped at the same time, thus countering the dilution effect caused by the addition of pure base.

of the shell matrix with growing crystals so that nucleation and growth were both inhibited. A strong inhibition of crystal growth by soluble shell matrix proteins was also reported by Wheeler *et al.* in fast precipitation experiments.[47] For further studies, the CCDD device setup was changed. By adding base, the volume increases and the ion concentration decreases. This is important because at the end of the experiments, the volume had nearly doubled. In order to counter this effect, a second pumping channel was added to each pump. If base was pumped into a vessel due to a drop in pH below the threshold, the corresponding ion solution was also added. This ion stock solution was of double concentration (10 mmol l^{-1}), modified by a factor resulting from pump channel calibration. This ensured that the total added volume was of starting

concentration (5 mmol l^{-1}). This improved setup, now allowing true constant-composition experiments, is shown in Figure 4.2-10. However, as now double volume is added, the reaction time had to be reduced to three days in order to prevent the vessels from running over. Experiments with the soluble organic matrix in concentrations similar to BSA (0.01 to 1.00 mg l^{-1}) were performed in the regulated CCDD device and with the ammonium carbonate method. Figure 4.2-11 shows the crystals obtained with the ammonium carbonate method (A series) and the regulated CCDD device (B series). Concentrations of soluble matrix were 0 mg l^{-1} (1), 0.01 mg l^{-1} (2), 0.10 mg l^{-1} (3), and 1.00 mg l^{-1} (4). In the case of the ammonium carbonate method, nearly no influence of the soluble matrix on crystal phase or morphology is visible. All pictures in Figure 4.2-11 are similar to those shown in the other figures and show calcite rhombohedra. However, at the concentration of 0.01 mg l^{-1} (A2), a relatively high amount of aragonite spherules can be seen. In the CCDD device, the inhibiting influence of the soluble matrix is easily seen and related to protein concentration.

A number of groups have studied the influence of proteins using the ammonium carbonate diffusion method. In general, it has been observed that the nucleating template plays a significant role. Mollusc shell macromolecules that were adsorbed on β-chitin and silk fibroin were able to direct the crystallisation towards the biologically favoured polymorph (i.e. the one present in the corresponding mollusc).[121] Soluble matrix from calcitic biominerals yielded calcite crystals, whereas soluble matrix from aragonitic biominerals yielded aragonite crystals. Falini *et al.* found the crystallisation on collagenous matrices in the presence of acidic polypeptides yielded vaterite, depending on the deformation of the collagen matrix membrane.[306] Tremel *et al.* used self-assembled monolayers as templates for calcium carbonate deposition.[40] The effect of adsorbing biomacromolecules on the morphology of calcite crystals was clearly demonstrated by Addadi, Aizenberg, Albeck and Weiner.[276, 278] In

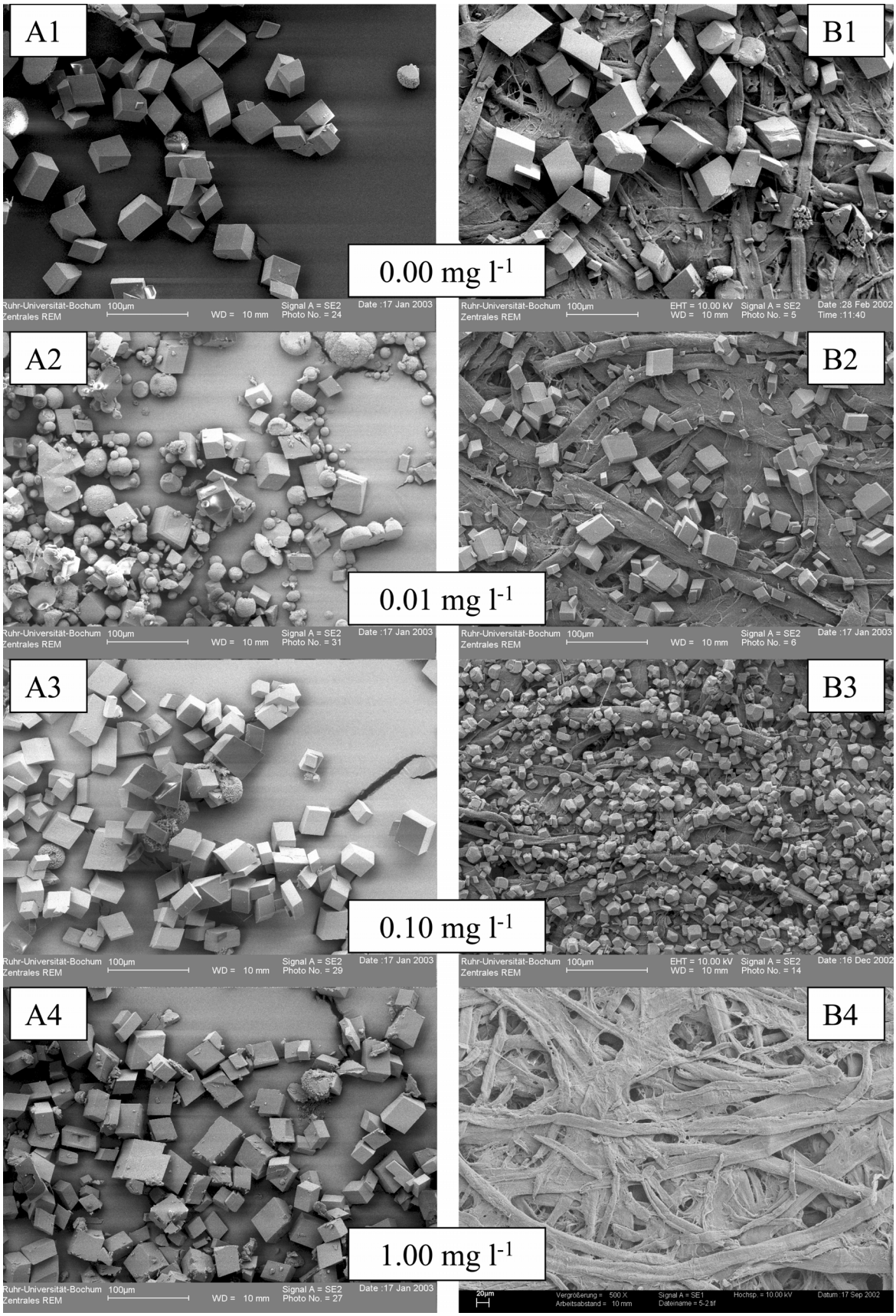

Fig. 4.2-11: SEM images of crystals obtained with the ammonium carbonate method (series A) and the regulated CCDD-device (series B) in the presence of extracted soluble matrix proteins. Additive concentrations are indicated in the picture.

those experiments, crystals grown by the ammonium carbonate method showed variation in morphology or phase depending on the template on which the crystals were grown. Here, with the proteins in solution, there was no effect on morphology or phase on calcium carbonate precipitated in the presence of extracted soluble matrix.

Double diffusion techniques were applied less frequently to the precipitation of calcium carbonate. Meldrum *et al.* have crystallised single-crystalline calcite in complex morphology within sea-urchin skeletal plates by a double diffusion method during about 16 h.[265] They have reported pH changes from 5.8 to about 8 on the $CaCl_2$ side and a more or less constant pH of 11 on the Na_2CO_3 side. Falini *et al.* crystallised calcium carbonate into a membrane of β-chitin from squid pens.[310] They measured a pH of 6.8 at the calcium side and 9.6 at the carbonate side. Usually, all three polymorphs were observed, but magnesium had a strong influence towards aragonite formation.

As seen in the studies above, the crystallisation method played a significant role during crystallisation. The effect of biological additives was more clearly seen with the CCDD technique than with the ammonium carbonate technique. This could be demonstrated for the model protein BSA as well as for the soluble matrix of the shell of the freshwater snail *Biomphalaria glabrata*. Compared to the ammonium carbonate method, the double diffusion approach has the advantage of avoiding the simultaneous crystallisation of ammonium carbonate and the presence of large amounts of ammonium ions which might influence the crystallisation and which have to be removed by washing the precipitate with water. If the double diffusion is carried out in a pH-regulated way, the crystallisation conditions are better defined and more stable.

4.3 Development of a multi-CCDD device

4.3.1 Concept and design

The conventional CCDD device consists of two thermostated vessels, connected with each other through a membrane where crystallisation occurs. During the precipitation of calcium carbonate, the pH value drops, triggering the addition of base and ion solution to hold the concentrations constant. Reaction solutions of 25 ml and stock solutions of 25 ml with double concentration are necessary. This setup has two major disadvantages: the first is the high amount of protein necessary for conducting an experiment; 50 ml of reaction solutions and 50 ml of stock solutions with double concentration, and the second is the long time necessary to test a series of different additive concentrations, with one experiment taking at least three days.

To improve the time-consuming single-experiment setup, a multi-experiment setup was developed. The only combination of volume reduction and multiple experiments possible was the design of crystallisation compartments similar to the system developed by Iijima *et al.*[336] They developed a dual-membrane system for the precipitation of calcium phosphate, creating a crystallisation chamber. In a double-diffusion setup, the ions travelled into the chamber containing biological macromolecules. The membrane on the calcium side was cation selective, whereas on the anion side a dialysis bag was used. However, they did not hold ion concentrations constant and the vessels depleted on ions.

The conventional CCDD-device was explained in the previous chapter. The constant-composition of the solutions was achieved by adding base and double concentrated ion solution simultaneously if the pH dropped below a selected threshold. Even by countering the dilution effects by adding double-concentrated ion solution while adding base in the conventional CCDD-device, the solutions deplete on ions due to precipitation of calcium carbonate. The addition of base counters the drop of pH, not the drop in the amount of ions in solution. The whole problem of ion depletion can be countered by always

allowing fresh solutions to be in contact with the crystallisation membrane. As this setup would increase the necessary amount of protein, a crystallisation chamber had to be applied instead of a single membrane. The crystallisation chamber contains a protein solution into which the ions from the stock solutions diffuse through inert membranes forming the borders of the chamber. The principal idea is shown in Figure 4.3-1.[337] The described setup is used for determining diffusion coefficients of ions and consists of a dual-membrane chamber. The feeding solutions are pumped constantly to achieve a constant concentration in the chambers before the membranes.

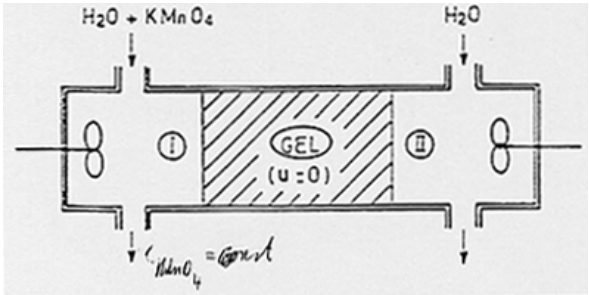

Fig. 4.3-1: Setup of a diffusion chamber used to determine diffusion coefficients which gave rise to the multi-CCDD-device design.

The basic idea of a new CCDD device was the construction of a crystallisation chamber of defined volume in which the precipitation in the presence of biological additives would occur. This would drastically reduce the amount of additive needed to execute an experiment. Constant composition would be achieved by constantly pumping fresh solution along the membranes of the chamber. The pH of these solutions would be held constant to a value set by the operator.

Figure 4.3-2 summarises the setup in a scheme. The pH value in two reservoir vessels with calcium nitrate and sodium carbonate solution, respectively, is adjusted and held constant by the addition of base and double concentrated ion solution if the pH drops below the threshold like in the conventional CCDD-device. Unlike in the conventional CCDD setup, the solutions are not in contact with each other, therefore they do not deplete on ions because of precipitation. Both solutions are pumped at a fixed rate to either side of several crystallisation chambers. So, every chamber is constantly served by ion solutions with constant

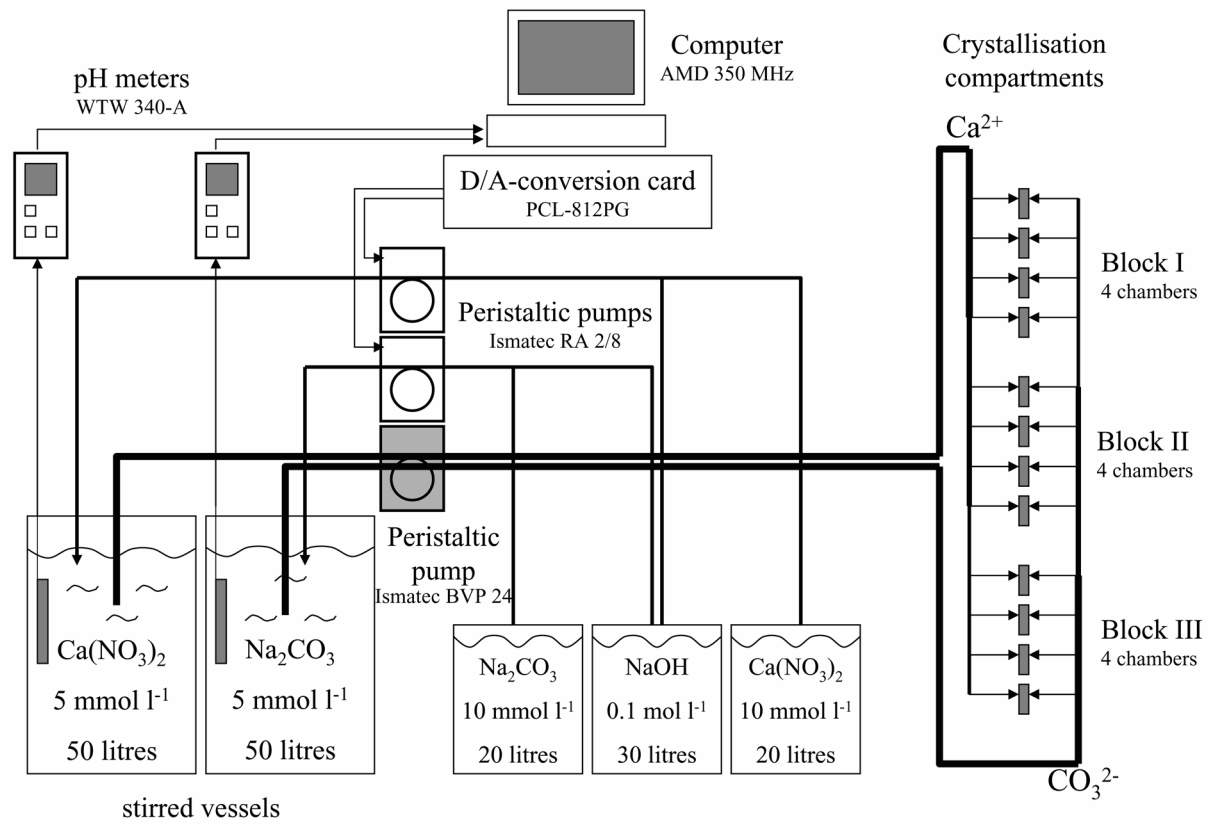

Fig. 4.3-2: Schematic representation of the multi-CCDD-device setup. About 50 l of reservoir solutions of calcium and carbonate, respectively, are held at constant composition. If the pH in a vessel drops below a threshold, NaOH and double-concentrated stock solutions (in 25 l containers) are added. The reservoir solutions are constantly pumped to the crystallisation chambers (three blocks of four chambers each) where they pass by.

composition. The solutions pass along the membranes and then into a waste container. The device was planned for three racks of compartments with four compartments each, allowing the execution of experiments with four different additive concentrations, instantly repeated three times in exactly the same conditions. A picture of the device is given in the appendix.

The crystallisation chamber is illustrated in Figure 4.3-3. It consists of a central core holding a shaft for filling and two rings (A). The cylindrical volume has a diameter of 15.9 mm and a size of 5 mm, forming a volume of 993 mm^3. The excess volume is to stand in the filling shaft. The left and right borders of the core are formed by membranes made of dialysis bags. These membranes are stuck between the core piece and the rings (B). Rings and core are connected via screws.

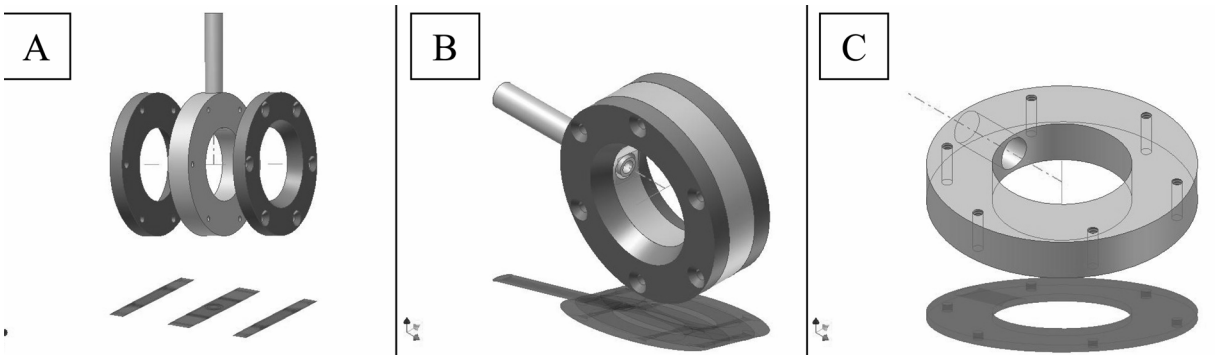

Fig. 4.3-3: The crystallisation chamber (A) is formed by the main body (with filling shaft) and two rings. Between rings and the main body, the membranes are positioned. Image B shows the assembled chamber. Image C shows the main body (without filling shaft) which holds six screws for fastening the rings.

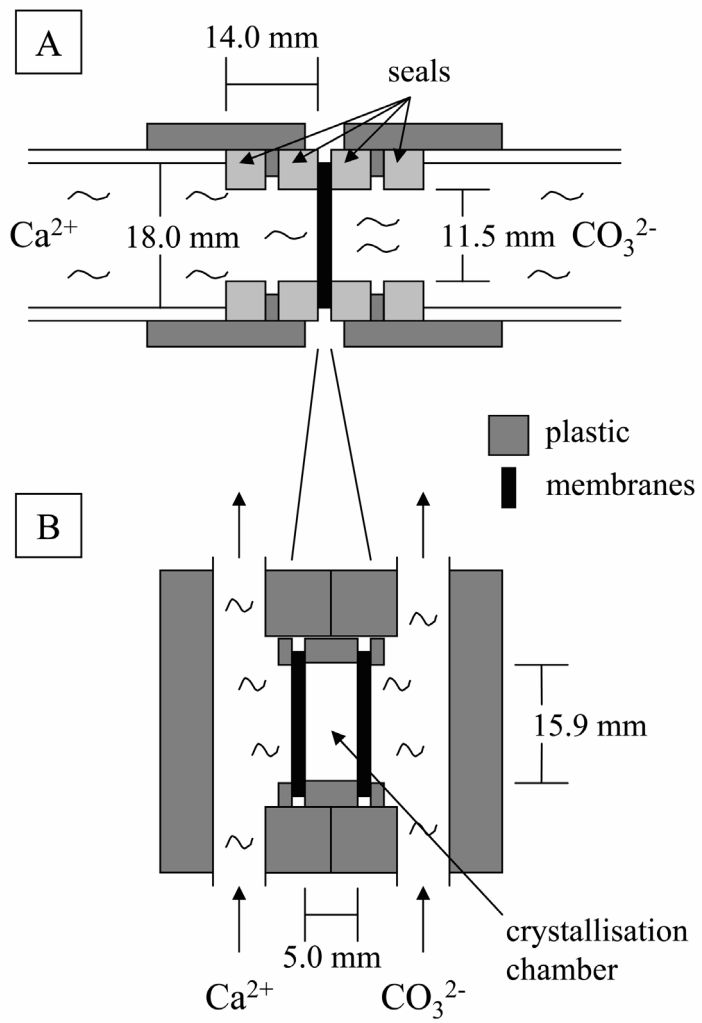

Fig. 3.4-4: A: cross-section of the crystallisation membrane of the conventional CCDD-device. B: cross-section of a crystallisation chamber of the multi-CCDD-setup.

The change from the use of a crystallisation membrane to a crystallisation compartment is the deployment of a new concept and needs to be considered in detail. Figure 4.3-4 shows cross-sections of the conventional CCDD-setup (A) and of a crystallisation compartment (B). In the classical setup, both solutions met directly through a crystallisation membrane. Crystallisation occurs almost exclusively at the carbonate side, indicating a faster diffusion of calcium through the membrane. As soon as the calcium ions reached the carbonate solution, the precipitate was formed. Therefore, precipitation usually occurs in carbonate-rich environment. In the crystallisation chamber, however, a concentration profile develops depending on diffusion of the ions. Diffusion is a microscopic transport of mass which occurs to balance differences in concentration or density. The difference in concentration Δc over distance l is the driving force:

$$\frac{(c_1 - c_2)}{l} = \frac{\Delta c}{l} = \frac{\mathrm{d}c}{\mathrm{d}x} \qquad \text{(eq. 4.3-1)}$$

c_i = concentration at point i, l = distance, $\mathrm{d}c/\mathrm{d}x$ = differential expression (non-linear case)

The flow of amount of substance I_n can be expressed as:

$$I_n = \frac{\mathrm{d}n}{\mathrm{d}t} = A * D * \frac{\Delta c}{l} = A * D * \frac{\mathrm{d}c}{\mathrm{d}x} \qquad \text{(eq. 4.3-2)}$$

n = amount of substance, t = time, A = surface through which flow occurs, D = diffusion coefficient

The density of substance flow j_n is described as (Fick's first law):

$$j_n = \frac{\mathrm{d}I_n}{\mathrm{d}A} = -D * \frac{\mathrm{d}c}{\mathrm{d}x} = -D\frac{\Delta c}{l} \qquad \text{(eq. 4.3-3)}$$

For the present conditions, the flow of amount of substance I_n and the density of substance flow j_n was calculated. The concentration difference is calculated from the concentration outside the chamber (5 mmol l^{-1}) and the calcite solubility product (resulting in a concentration of 0.057 mmol l^{-1}). The distance l is the width of the crystallisation chamber (0.5 cm). The surface A is determined by the diameter of the chamber (1.59 cm). The diffusion coefficient of calcium in water is $7.9*10^{-6}$ cm^2 s^{-1} and that of carbon dioxide in water is $1.9*10^{-5}$ cm^2 s-^{1}.[338] Table 4.3-1 summarises all calculated values. The flow of amount of calcium ions is I_{Ca} is $1.4*10^{-8}$ mmol s^{-1}. The flow of amount of carbonate ions is I_{Carb} is $1.4*10^{-8}$ mmol s^{-1}.

However, the substance flow does not depend on the diffusion coefficient only. The limiting step is the diffusion of calcium and carbonate ions through the dialysis bag membranes. Dialysis bags are semi-permeable membranes, allowing the transport of small molecules while prohibiting larger ones. They consist of regenerated cellulose which is hydrophilic and allows the diffusion of inorganic ions. Regenerated cellulose denotes chemically precipitated cellulose fibres from viscose. Viscose is an industrial product of natural cellulose solved in base and treated with carbon disulfide. The addition of base to viscose yields regenerated cellulose. Despite their hydrophilic properties, dialysis bags

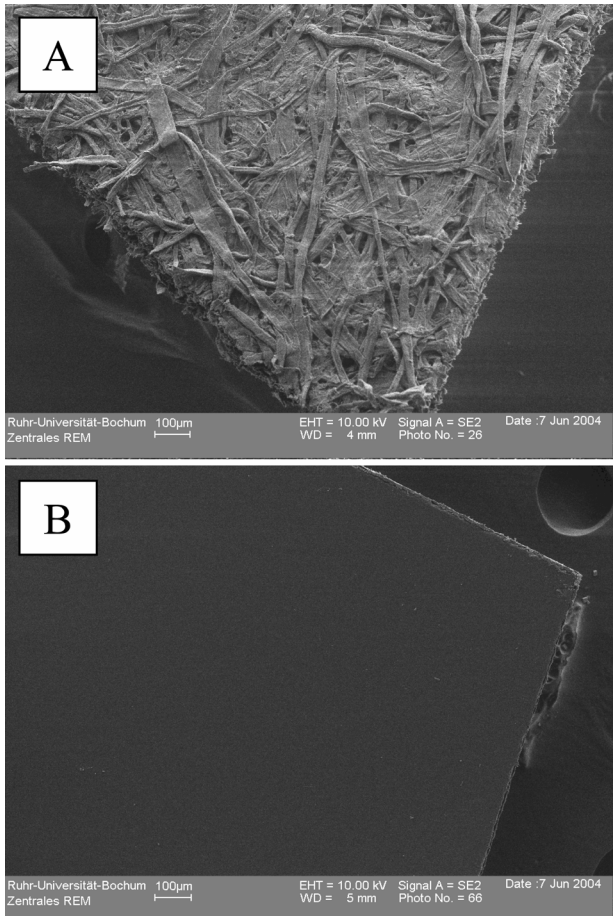

Fig. 4.3-5: The surface of untreated crystallisation membranes. A: filter paper, B: dialysis bag.

Tab. 4.3-1: Consideration of diffusion of calcium and carbonate ions.

Value	Unit	Calcium ions	Carbonate ions
c_1	mmol l^{-1}	0.5	0.5
c_2	mmol l^{-1}	0.057	0.057
$\Delta\mathbf{c}$	mmol l^{-1}	0.443	0.443
Δc	mmol cm^{-3}	$0.443*10^{-3}$	$0.443*10^{-3}$
l	cm	0.5	0.5
A (d=1.59 cm)	cm^2	1.986	1.986
D	cm^2 s^{-1}	$7.9*10^{-6}$	$1.9*10^{-5}$
I_n	mmol s^{-1}	$1.4*10^{-8}$	$3.4*10^{-8}$
j_n	mmol s^{-1} cm^{-2}	$0.7*10^{-8}$	$1.7*10^{-8}$

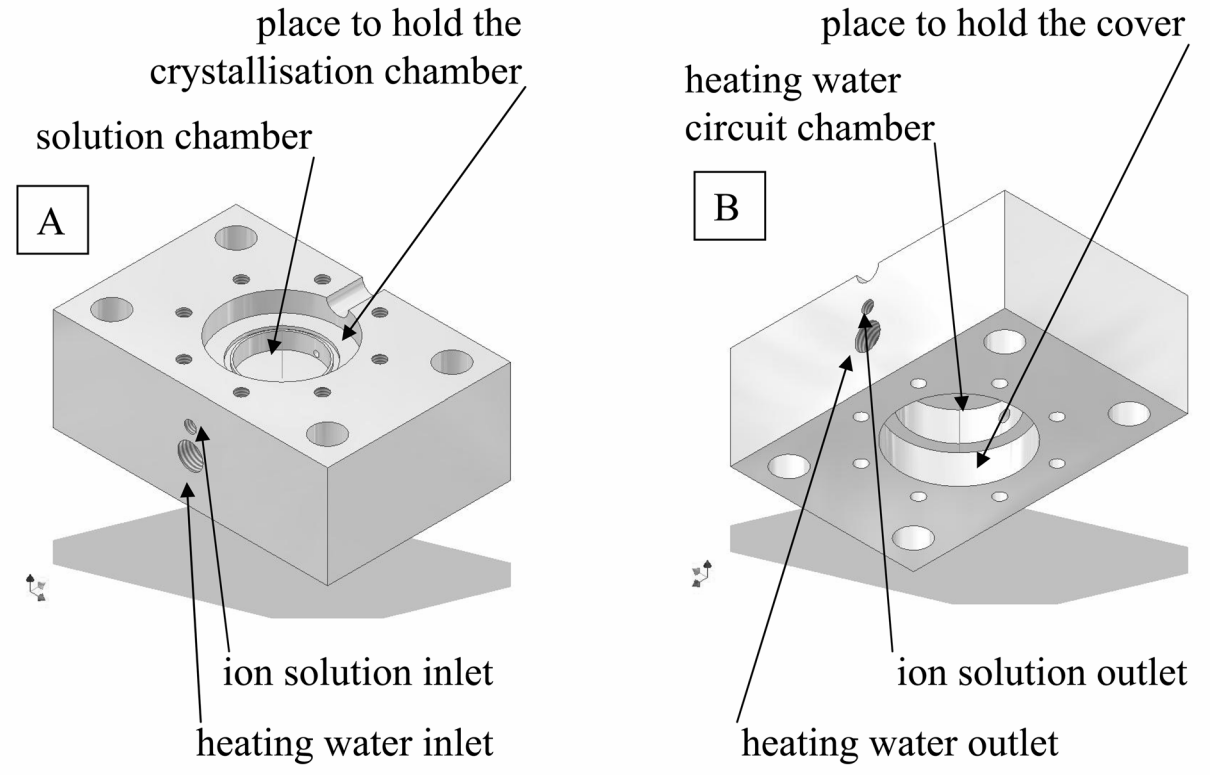

Fig. 4.3-6: One half of a box holding the crystallisation chamber (A: inwards, B: outwards). The box part contains a volume for the ion solution to come into contact with the membrane of the crystallisation chamber and a volume for heating conduits.

show a small protein adsorption, making dialysis bags ideal inert membranes. Equally important, the surface of dialysis bags in comparison to the filter papers used in the conventional CCDD-device is well defined. Figure 4.3-5 shows the differences in surface topography between a filter paper (A) and a dialysis bag (B).

The crystallisation chamber is held by a two-part compartment box as shown in Figure 4.3-6. An assembled compartment holds the crystallisation chamber and is then put on racks. As seen in the picture, a compartment box part has two major deepenings on each side. The deepening at the inside holds the crystallisation chamber. The in diameter smaller deepening below it holds the ion solution as shown in the scheme in Figure 8.3-4. At the outside, the deepenings are to hold water of a heating circuit and the corresponding cover. This feature was included for future experiments at constant temperature. Solution compartment and heating water compartment are fed from the bottom and release the leaving flow at the top of the compartment. The volume to hold the ion solution on each side of the crystallisation chamber has a diameter of 19 mm and a size of 3 mm. To this 850 mm^3, a volume formed by the ring of the chamber holding the membrane between itself and the chamber core has to be added (see Figure 4.3-3B). The compartment holding box dimensions are outlaid in Figure 4.3-7. Neglecting the 50° edge, this volume has a diameter of 15.9 mm^3 and a size of 3 mm. These 596 mm^3 and the volume of the deepening form a volume of 1446 mm^3 filled with ion solution in front of the membrane. The solution flow was set to 0.5 ml min^{-1}. The hydrodynamic residence time is defined as:

$$\tau = \frac{V}{\dot{V}} \qquad \text{(eq. 4.3-4)}$$

with τ being the hydrodynamic residence time [min], V the volume [mm^3] and $\dot{V}$ the flow [mm^3 min^{-1}]. The residence time for the ion solution in this volume in front of the membrane therefore is 2.9 min.

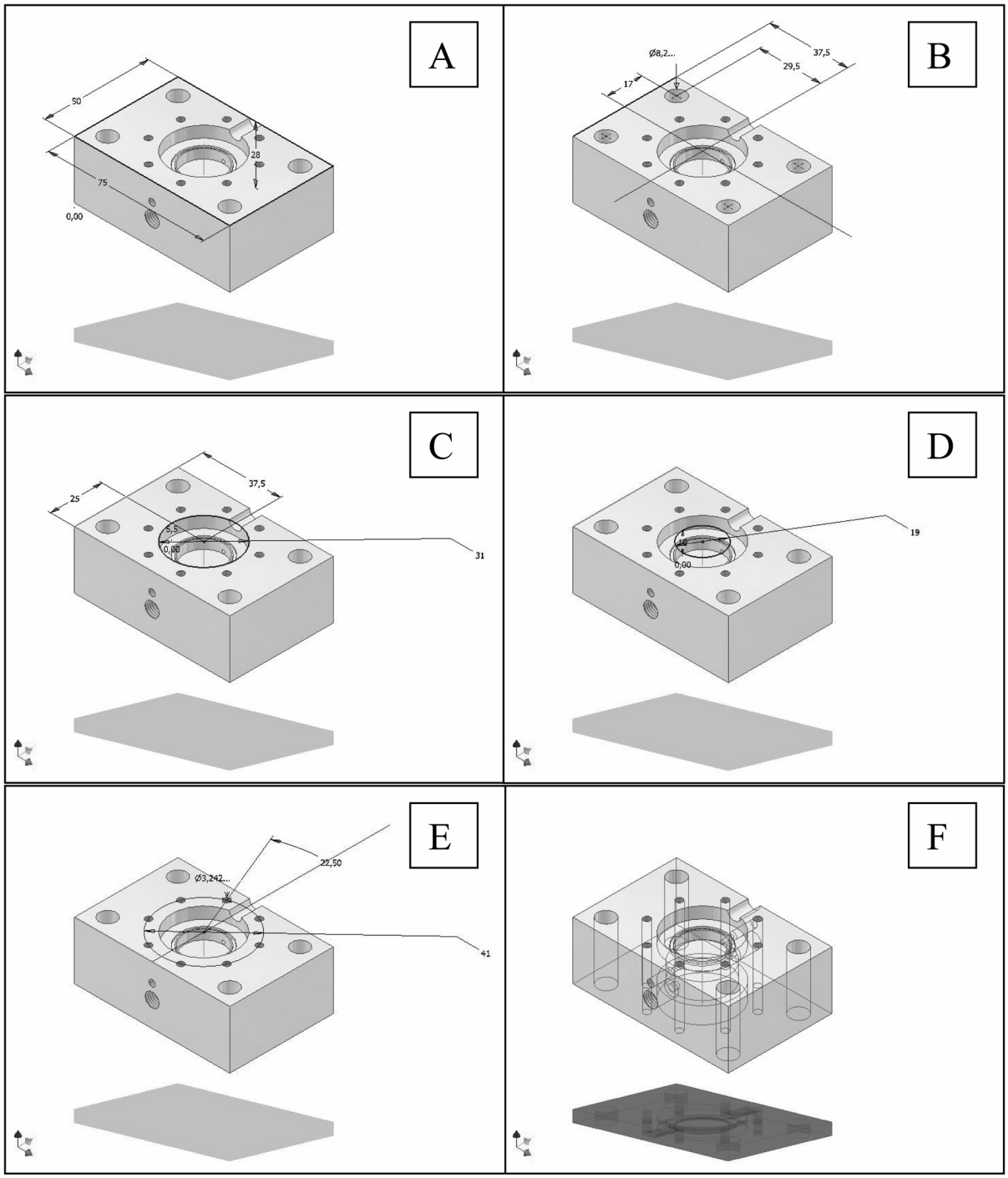

Fig. 4.3-7: Holding box dimensions as designed by the author and A. Lindner in isometric 3D representation. A: base dimensions, B: drilling definitions, C: main space definitions, D: solution volume definition, E: screw scaffold definition, F: hidden lines (not shown in the other images for clarity).

4.3.2 Technical specifications

The multi-CCDD-device consists of three racks with four crystallisation compartments each. Two 50 l vessels contain a calcium nitrate solution and a sodium carbonate solution which are constantly pumped to the crystallisation compartments (feeding solutions). The pH in these vessels is held constant by

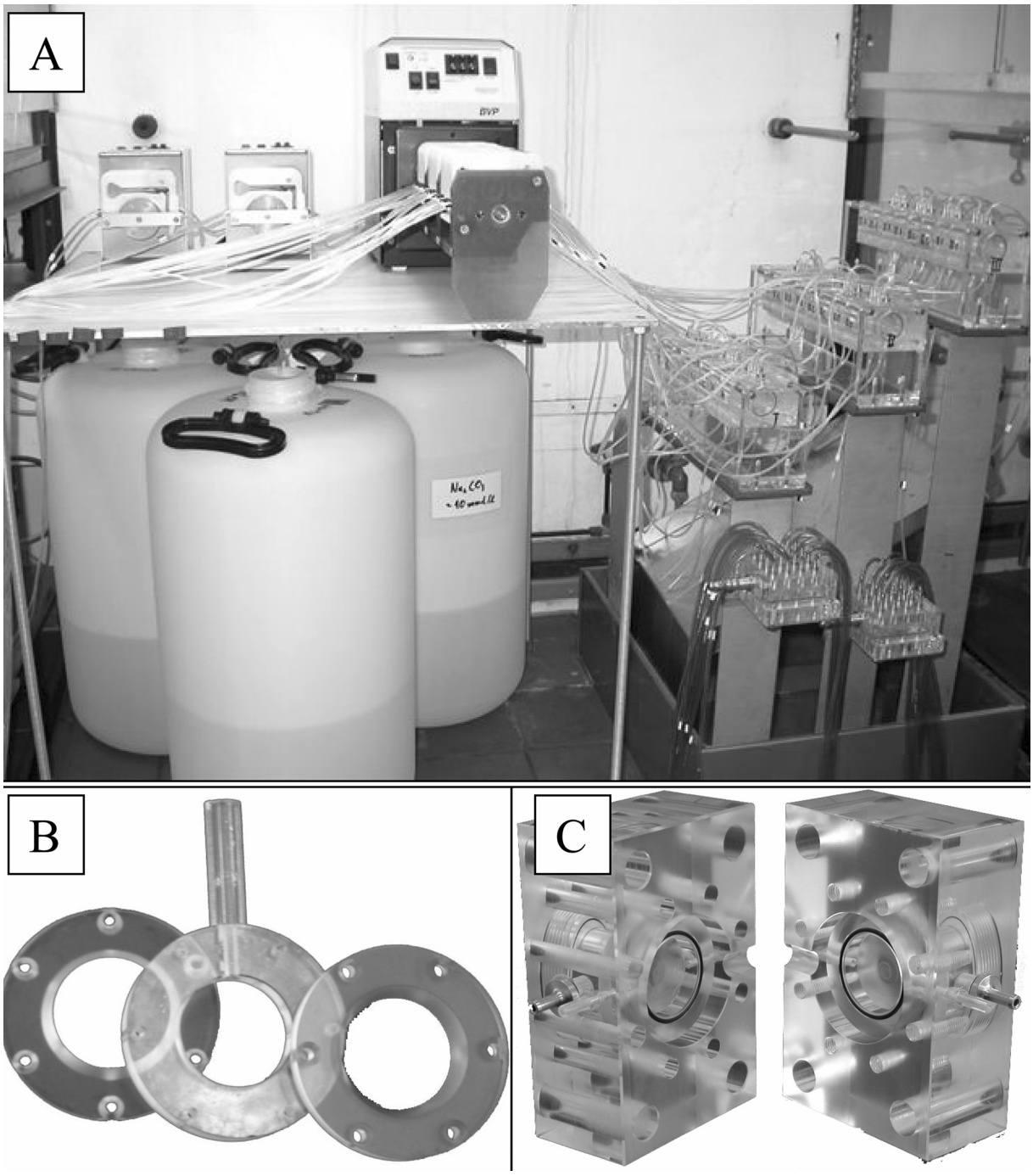

Fig. 4.3-8: A: the real multi-CCDD-device (the 50 l-reservoir solution vessels are not shown). B: crystallisation chamber parts (main body and rings), C: two-part holding box.

adding base. When base is added due to pH drop, double concentrated calcium and carbonate solution are pumped simultaneously to counter the dilution effect (stock solutions). Figure 4.3-8 shows the multi-CCDD device. Figure A shows the pumps and stock solutions as well as the racks holding the crystallisation compartments. The 50 l vessels containing the feeding solutions are not seen. A crystallisation compartment consists of a crystallisation chamber (B) held by a compartment box consisting of two parts (C). The crystallisation chamber has a volume of 1 ml and holds a solution of additives in whose presence precipitation of calcium carbonate occurs. The rate of precipitation is controlled by diffusion, slowing down nucleation and growth considerably. Three racks hold four compartments each, allowing the execution of twelve experiments simultaneously. This setup allows the variation of additive concentrations over a wide range. Potentially, the solution in the chambers can also be exchanged by a gel in which precipitation occurs.

For constant composition, a computer monitors the pH value of the feeding solutions and controls pumps to add base to keep the pH constant. The pH-meters are connected to the computer via the RS-232 interfaces (COM1 and COM2). For communication with the analogously controlled peristaltic pumps, a digital/analogous conversion card is necessary. Here, an Advantech PCL-812PG ISA card was employed. This card offers 16 digital and 16 analogous input channels, 16 digital and two analogous output channels. The analogous output channels offer a maximum voltage of 5 V and are used to control the pumps. A screwboard ACLD-9188 is used to translate the computer

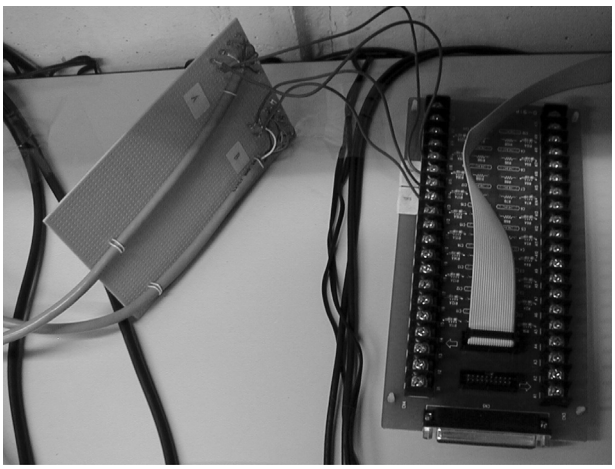

Fig. 4.3-9: ACLD-9188 screwboard to connect the computer bus exiting the A/D conversion card and the pump controls.

Table 4.3-2: Technical details and communication parameters of the pH-meters.

technical details		**communication parameters**		**string commands**	
type:	WTW 340-A	baud rate:	4800	value request:	K.7^M
electrode:	SenTIX 41	data bits:	8	device check:	K.18^M
range:	0.00–14.00 pH	parity:	none	(de)activate:	K.9^M
	0.0–80°C	stop bits:	1		
error:	± 0.02 pH	idle time:	500 ms		
	± 0.1°C	wait time:	50 ms		

bus into accessible ports (Figure 4.3-9). The computer program "VisiDAQ Genie 3.11" is used for device communication and control. VisiDAQ and the user developed programs are explained in the appendix.

For constantly monitoring the pH and the temperature in the feeding vessels, two WTW 340-A pH-meters are employed. Measuring was carried out with WTW SenTIX 41 electrodes. The hand controls of the devices are deactivated when connected to a computer. The functions of the buttons are replaced by string commands sent by the computer depending on the conditions. For reliable communication, the communication parameters had to be adjusted. Technical details, communication parameters and string commands are listed in Table 4.3-2. The communication parameters *wait time* and *idle time* arise from the control program VisiDAQ, whereas all other values are defined in the interface communication protocol. The *idle time* defines the time for which the program waits for a response from the pH-meter. The *waiting time* after the *idle time* has passed without response defines the time before trying another communication attempt. However, these values were determined empirically and must be adjusted for every new control problem.

In case the pH in one of the feeding vessels drops below the selected threshold, NaOH is added to counter the pH drop. As the changes are small and relatively small amounts of volume have to be added, ISMATEC Reglo Analog 4/6 peristaltic pumps are employed, allowing the simultaneous addition of up to four different solutions (see Table 4.3-3). Here, two channels were used at each pump; one for base, the other for double-concentrated ion solution. The pump remote control is established over a 15-pin analogous interface (see Figure 4.3-

10). Remote control is activated by connecting PIN2 and PIN3 with PIN1. Speed control is achieved over PIN5 and PIN1 which are connected to the screwboard ACLD-9188. The voltage applied by the computer (0–5 V) is directly correlated to pump speed.

Table 4.3-3: Technical und experimental parameters of the peristaltic pumps.

model:	ISMATEC Reglo Analog MS 4/6
tension range:	0-5 V *Remote-Control*
speed:	2-100 rpm
tubes:	Tygon®, d_i=0.95 mm
range of flow:	0.13-6.4 ml min^{-1}

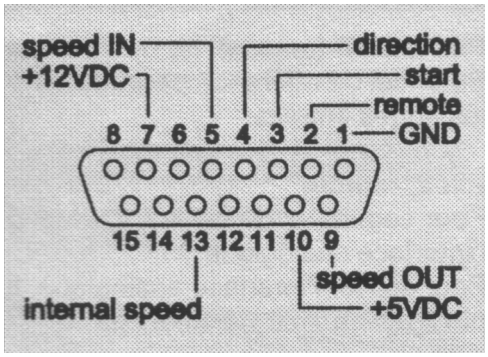

Figure 4.3-10: PIN occupation of the interface.

In all experiments, Tygon® tubes with an internal diameter of 0.95 mm were employed. The material of these tubes is PVC. Thus the tube walls are hydrophobic and withstand base. Two pump channels are used. Each channel is calibrated separately as to how much water is pumped per volt. The resulting calibration factors f_i are divided to yield a concentration factor F:

$$F = \frac{f_2}{f_1} \qquad \text{(eq. 4.3-5)}$$

The concentration of the double-concentrated ion stock solution has to be multiplied with factor F to assure that the volume added (base + ion solution) is of the same concentration like the solution in the feeding vessel.

4.3.3 Testing the multi-CCDD device

Experiments with the multi-CCDD device were carried out as described in the appendix. Calcium nitrate and sodium carbonate solution of 5 mmol l^{-1} were pumped with 0.5 ml min^{-1} alongside the membranes of the crystallisation chambers made of dialysis bags. The pH value in both vessels was kept constant at 9.45 and the experiment was run for three days. Figure 4.3-11 shows the pH

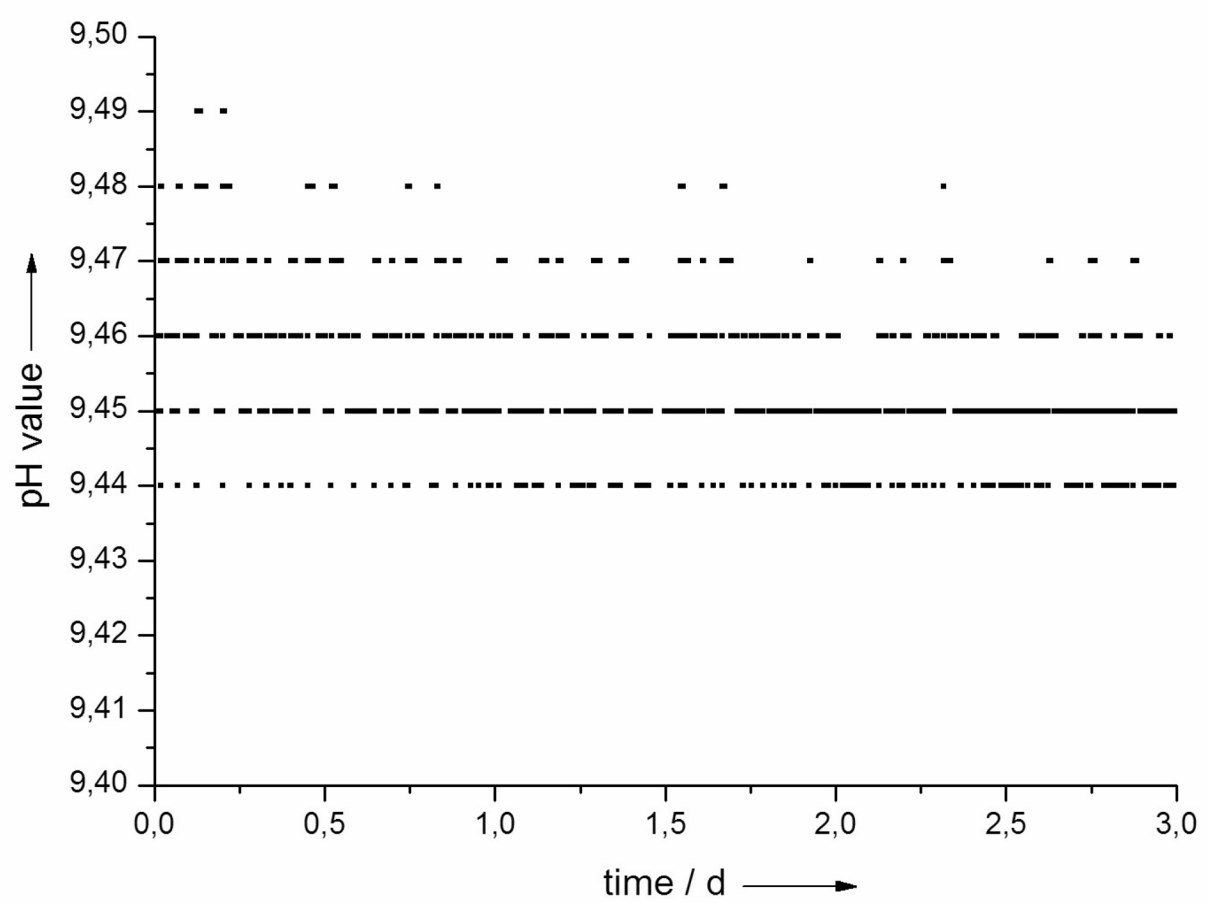

Fig. 4.3-11: pH-control exercised by the programmed control. The value is held constant at ±0.03 units. For clarity, only the curve of the calcium solution is shown.

value in the calcium vessel during the experiment. The curve for carbonate is similar but not shown as the values are identical and the curves would not be distinguishable. During the experiment, all calcium and carbonate solutions leaving the compartment boxes were pooled and tested for pH. No deviation except within the device's error range was found. Therefore, the solutions passing along the crystallisation chamber membranes kept the adjusted pH. The additive tested was poly-L-aspartic acid (pAsp) which is known to inhibit crystal growth. Additionally, aspartic acid is the main component of acidic amino acids of soluble organic matrices extracted from biominerals (see chapter 4.1). The concentration of the additive in the crystallisation chamber was 10, 100, and 1000 mg l^{-1}. Additionally, in every rack a chamber without any additive was run for control.

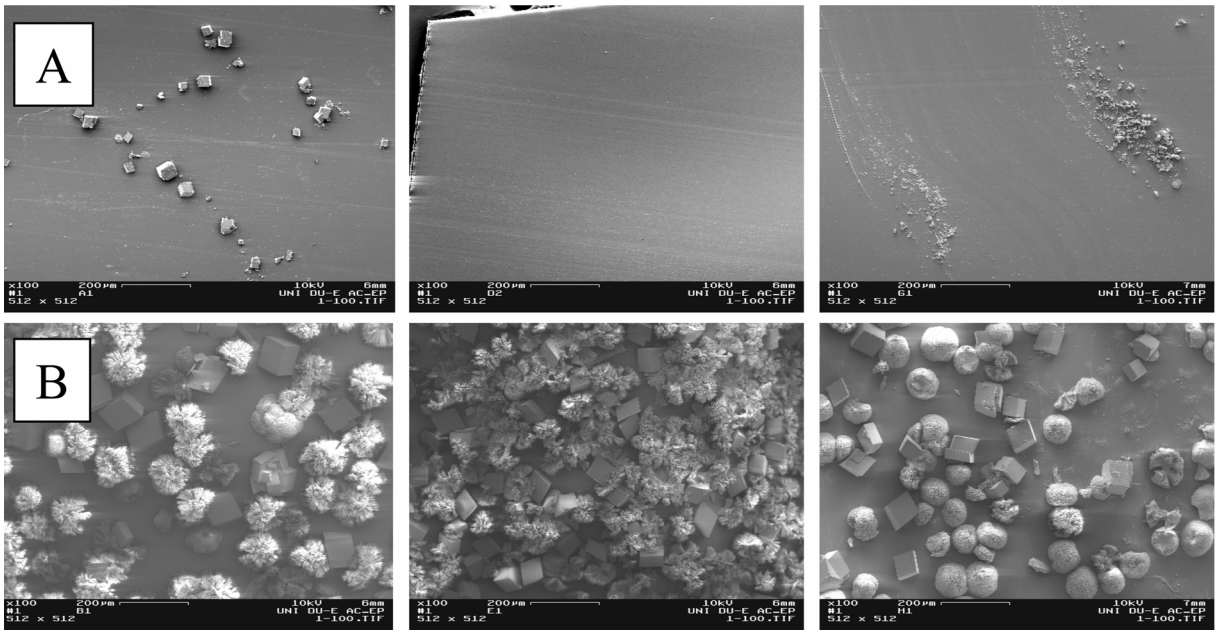

Fig. 4.3-12: SEM images of the inside of the membranes of the crystallisation chamber without any additive. From left to right: rack I, rack II, and rack III. Series A shows the calcium side where nearly no precipitation occurred. Series B shows the inside of the membrane at the carbonate solution. Calcite crystals and aragonite spherules can be identified in all cases.

Control experiments without any additive are shown in Figure 4.3-12. Series A shows SEM images of the membranes inside the crystallisation chamber on the calcium side. Hardly any precipitation occurred in rack I whereas in racks II and III no crystals can be seen. The formations seen in image A3 are artefacts from sample preparation. In higher magnification, no crystals can be identified. For comparison, all images seen in this figure are of the same magnification (100x). Series B shows the membrane inside the crystallisation chamber on the carbonate side. Here, precipitation of calcium carbonate occurred. Calcite and aragonite formations can be identified. No preferred orientation of the crystals grown is visible. It shall be noted that no crystallisation ever occurred at the walls of the crystallisation chamber. Precipitates were found only at the membranes. Precipitation mainly occurred on the carbonate side of the conventional CCDD-device. Therefore, the precipitate was formed in carbonate rich environment, only. This observation is in contrast to the theoretical calculations of the chapter before. The cellulose membranes seem to reduce carbonate ion diffusion.

In the presence of poly-aspartic acid, no crystallisation occurred at all. Precipitation was inhibited completely at the calcium side of the crystallisation chamber as shown in Figure 4.3-13 as well as at the carbonate side of the chamber as shown in Figure 4.3-14. However, textures of the membranes can be seen in the images of Figure 4.3-14. These derive from crystals formed outside of the chamber in the carbonate feeding solution passing the membrane. The crystals below form the textures of the inside surface of the membrane. Great care was taken that the sides of the membranes were not mixed. Table 4.3-4 shows the concentration of calcium ions in each crystallisation chamber as determined by atom absorption spectroscopy. The concentrations of about 2 to 3 mmol l^{-1} are far above supersaturation levels for calcium carbonate precipitation (0.63 mmol l^{-1} in the case of ACC). Because the additive prevented crystallisation within the chamber, calcium ions diffused through the membrane on the carbonate side to form a precipitate in the carbonate feeding solution.

The observation of poly-aspartic acid inhibiting precipitation is in accordance with the literature. Njegic *et al*. found poly-L-aspartic acid to inhibit crystal formation in overgrowth experiments at a comparable pH of 9.3.[339] They found that pAsp inhibited more strongly than poly-L-glutamic acid (pGlu) or poly-L-lysine (pLys). This finding is possibly correlated to the secondary structure of these macromolecules. pAsp adopts predominant a β-sheet conformation, pGlu adopts partially β-sheet conformation whereas pLys adopts a random coil conformation. Even industry considers the use of pAsp as inhibitor.[340, 341]

The multi-CCDD device is a reasonable development of the conventional CCDD setup which offers a higher yield of directly comparable results with a lower amount of protein necessary for experiment execution. The use of a crystallisation chamber offers the flexible exchange of the medium in which precipitation occurs, i.e. gel or solution. The multi-CCDD device yields results comparable with literature.

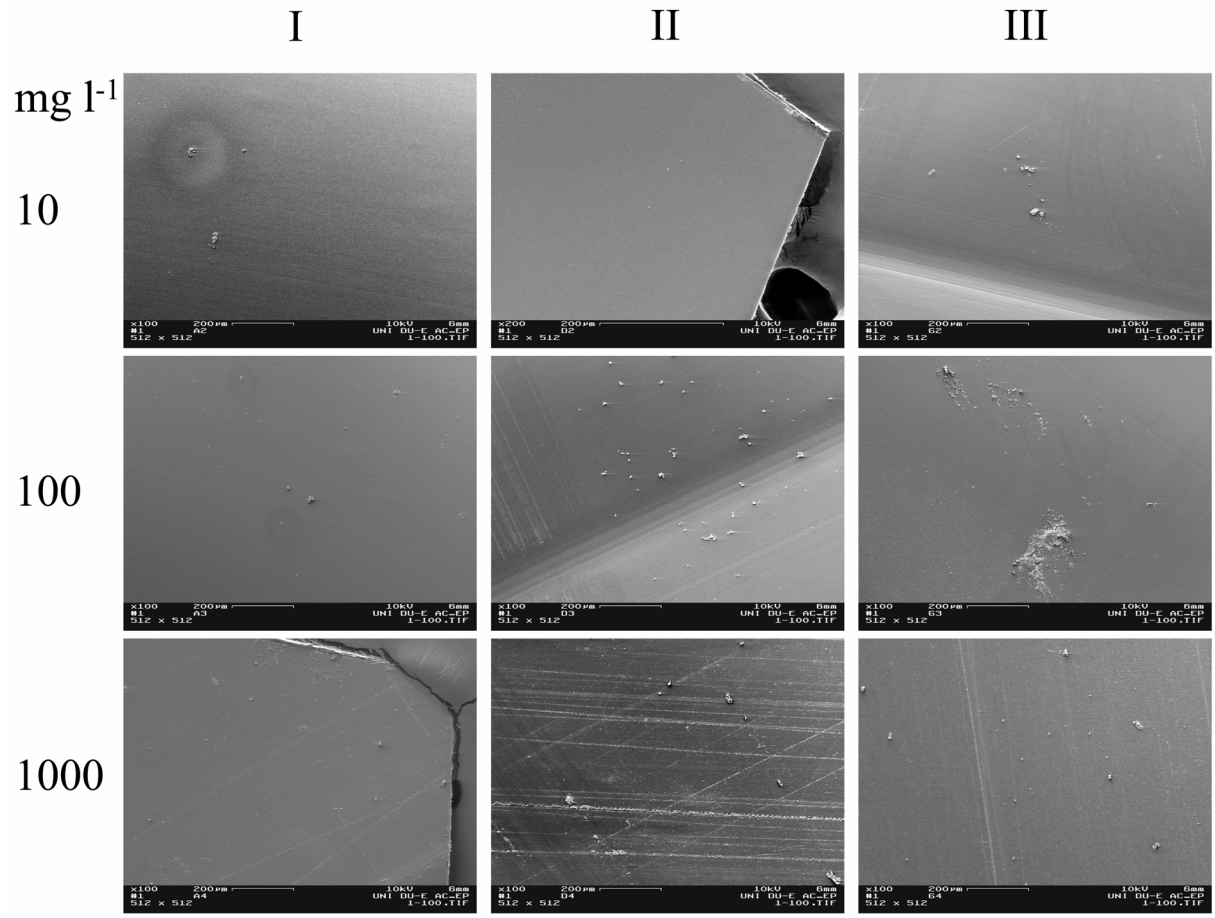

Fig. 4.3-13: SEM images of the inside of membranes at the calcium side of the crystallisation chamber. No precipitation occurred at any concentration of poly-Asp.

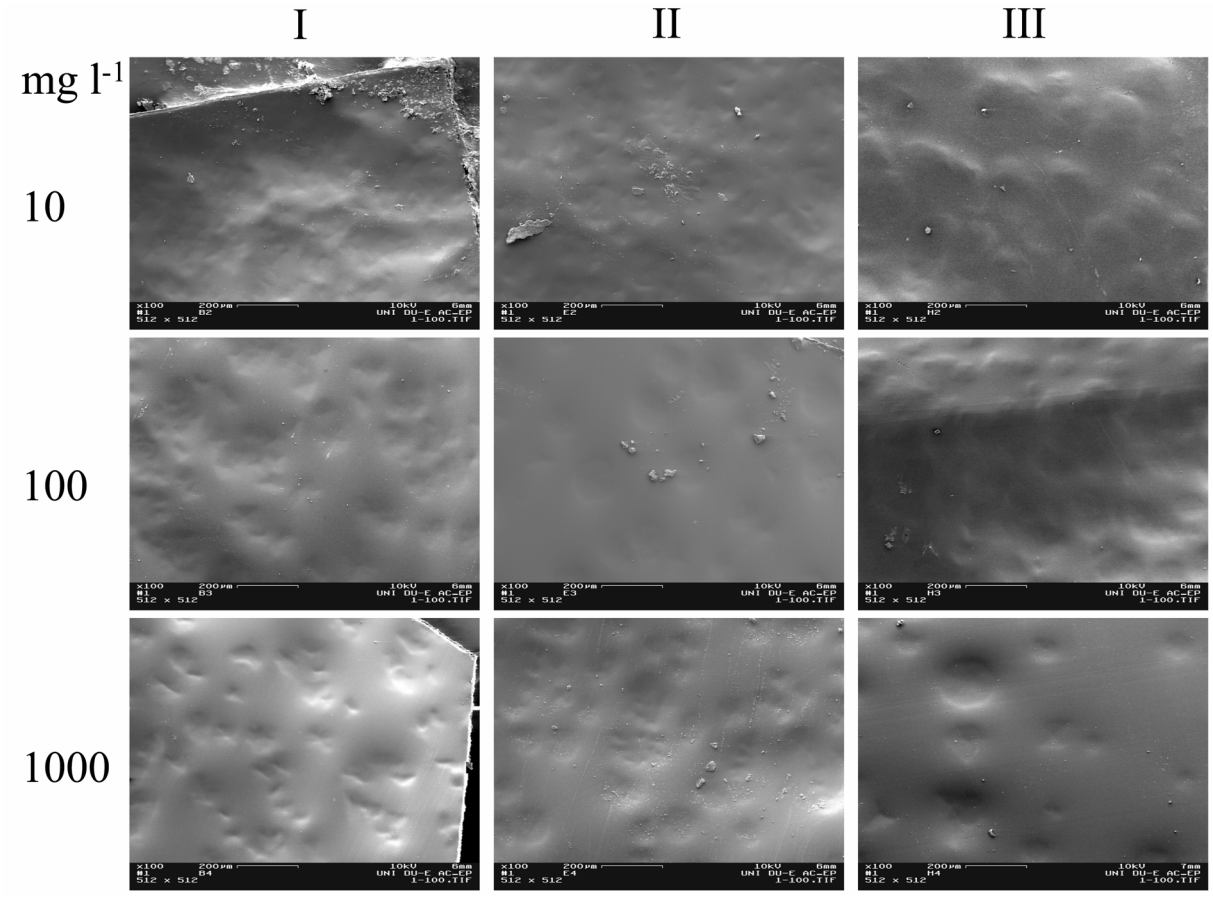

Fig. 4.3-14: SEM images of the inside of the membranes at the carbonate side of the crystallisation chamber. No precipitation occurred at any concentration of poly-Asp. The textures seen arise from crystals of calcium carbonate formed at the outside of the membrane in the carbonate feeding solution. The additive prevented crystallisation and therefore, the calcium ions also passed the carbonate-side membrane into the carbonate feeding solution.

5. Methods

5.1 X-ray powder diffractometry (XRD)

5.1.1 Machinery

The diffraction of a bundle of X-rays by the lattice planes of a crystalline substance allows the identification, and in the case of mixtures of crystalline materials, the quantification of crystalline phases present. While quantification involves the use of the Rietveld method, the mere presence of diffraction peaks can be used to identify a crystal phase. The occurrence of peaks depends on constructive interference of the diffracted X-rays and is described by the Bragg-equation[342]

$$n \cdot \lambda = 2 \cdot d_{hkl} \cdot \sin(\Theta) \qquad \text{(eq. 5-1)}$$

with n being an integer value, λ the wavelength in Å, d_{hkl} the distance between the lattice planes hkl in Å and Θ the diffraction angle.

Two experiment geometries were used for measurement. The Bragg-Brentano-Geometry was used at laboratory diffractometers and the transmission-geometry at the synchrotron. Because of the nature of the samples, the use of capillaries was not possible. All measurements were done with flat sample holders. Samples were rotated with about 2 Hz.

At the University of Bochum, a Bruker D8 Advance diffractometer was used with a Cu X-ray tube, primary Göbel mirror and 8° PSD (Position Sensitive Detector). Cu-Kβ radiation was filtered out with a primary Ni filter. At the University of Duisburg-Essen, a STOE IP-PSD diffractometer with primary Ge(111) monochromator and half circle PSD was employed. At the Weizmann Institute of Science, a Rigaku Rotoflex-RU 200 B was used with a rotating anode, primary and secondary Soller aperture. Synchrotron measurements were carried out at beamline B2 at HASYLAB (Hamburger

Synchrotronstrahlungslabor) at DESY (Deutsches Elektronensynchrotron) with a half circle PSD. The accelerator ring was operated with a positron energy of 4.5 GeV and currents of 70 to 150 mA. The wavelength used varied between 1.1 and 1.3 Å, depending on the individual experiment. For comparison reasons all diffractograms shown in this work were converted to Cu $K\alpha_1$-radiation (λ=1.54056 Å).

5.1.2 Interpretation of X-ray powder diffractograms

As stated above, the position of observed diffraction peaks indicates the crystal phase of the materials present in the sample examined. The International Centre for Diffraction Data (ICDD) database entries were used for reference. If no peaks could be observed, the substance examined was X-ray amorphous.

The full width at half maximum (FWHM) of a peak is an indicator for the size of the diffraction domain which is often correlated with the crystallite size. The diffraction domain size can be estimated with the Scherrer-Equation[342, 343]

$$D = \frac{K \cdot \lambda \cdot 57.3}{\beta_{1/2} \cdot \cos(\Theta)} \qquad \text{(eq. 5-2)}$$

with D being the average domain size in Å, $\beta_{1/2}$ the full peak width at half peak maximum in °2Θ, K a constant (set to 1), λ the wavelength in Å and Θ the diffraction angle of the corresponding peak. This equation gives an estimate of the crystallite size. It should be noted, however, that structural disorder and strain phenomena, e.g. caused by added atoms in the lattice, can also lead to a peak-broadening effect. Formally, the model from which this correlation is derived is only valid for spherical particles.

Quantitative analysis of a powder diffractogram is possible with the Rietveld method[132, 344-346]. With known space group and cell dimensions of the phases present, the observed diffraction pattern can be fitted according to Le Bail *et al.*[347]. A hypothetical diffractogram is calculated and the calculated intensities

of the peaks are fitted to the observed intensities by variation of the peaks' profile parameters. For calculating the peaks, Gauß, Lorentz, or Pseudo-Voigt functions are used. Pseudo-Voigt functions are mathematical mixtures of Gauß and Lorentz functions, the mixture parameter η is also open for refinement. The profile parameters are defined by the full width at half maximum (FWHM). For Gauß type functions the FWHM is given by

$$\beta_{1/2,G} = \sqrt{U \cdot \tan^2(\Theta) + V \cdot \tan(\Theta) + W + \frac{Z}{\cos^2(\Theta)}} \qquad \text{(eq. 5-3)}$$

for Lorentz type functions the FWHM is given by

$$\beta_{1/2,L} = X \cdot \tan(\Theta) + \frac{Y}{\cos(\Theta)} \qquad \text{(eq. 5-4)}$$

with U, V, W, X and Y the profile parameters to be refined and Θ the diffraction angle. For Pseudo-Voigt functions both values are correlated by η whose exact definition depends on the Gauß and Lorentz functions used. After refinement of the profile, a structural model derived from the database is applied in the Rietveld method. Originally developed for crystal structure refinement from powder diffractograms, this method also allows the calculation of a phase mixture in wt% without an external standard substance[348]. After refinement of the structural model (atom positions, temperature factors), the Rietveld computer programs are able to quantify the phase mass ratio in wt% by the following correlation

$$W_P = \frac{S_P(ZMV)}{\sum_i S_i(ZMV)} \qquad \text{(eq. 5-5)}$$

with W_P being the mass proportion of phase P in wt%, S_P the scale factor of phase P depending on the number of formula units in the elementary cell (Z), the molar mass of a formula unit (M) and the volume of the elementary cell (V).

For a highly crystalline material, the Rietveld method is very accurate[193]. The accuracy of this method decreases with decreasing signal to noise ratio. A general problem while applying the Rietveld method for this work lay in the biological origin of samples examined. Biominerals tend to have preferred orientation and/or be very small. Unfortunately, the preferred orientation in biominerals is often not a simple variation of orientation along the crystallographic main axis, e.g. plates or needles, but complex orientations, e.g. agglomeration of crystallites around a central area or structure distortion by incorporated biological macromolecules. As these phenomena are not incorporated in the Rietveld theory, refinement of biological samples often yields inaccurate results which increases inaccuracy of the quantitative phase analysis.

For determination of the content of X-ray amorphous material in a sample, 50:50 or 90:10 weight mixtures of sample and silicon dioxide (quartz) were examined by XRD and the Rietveld method applied. For Rietveld calculations, the program FULLPROF of the WinPLOTR software[349] was used.

5.2 X-ray single crystal diffractometry

All measurements were carried out at the beamline F1 at HASYLAB at DESY. The accelerator ring conditions were similar to those described above. The wavelength used was always λ=0.5 Å with an exposure time of 15 s/frame and a step width $\Delta\omega$=0.2°. Samples were fixed at the sample holder (glass capillary or carbon fibre) with commercial available glue and thus sealed from the environment, preventing the escape or intake of water from the air.

The obtained data sets were normalised and corrected. The orientation matrix was determined at HASYLAB. The resulting data files were analysed and the structures were solved and refined with the SHELXTL program.[350]

5.3 Infrared spectroscopy (IR)

Infrared radiation (wavelength 760 nm up to 500 μm[7]) does not trigger electronic excitation in substances but vibrational and/or rotational excitation. To be infrared active, a molecule must possess a dipole moment or must generate a dipole moment by vibration. The main modes of vibration are:

- valence bond vibration: The atoms vibrate along a bond axis. In the case of more atoms bond to a central atom, this vibration can be symmetric (all "away" or "towards" the central atom) or asymmetric.
- deformation vibration: In molecules with at least three atoms, the angle between the two bonds is changed by vibration either in the plane of the bonds as bending or rocking vibrations or out of the plane of the bonds as twist (up and down) or wagging (up/up or down/down) vibration.

The energy in infrared spectra is usually given in wave numbers. The use of wave numbers offers the advantage of being directly proportional to the frequency of the absorbed radiation and thus the energy absorbed:

$$\Delta E = \mathrm{h} \cdot \mathrm{c} \cdot \tilde{\upsilon} \qquad \text{(eq. 5-6)}$$

with ΔE the absorbed energy in J, h=6.626·10^{-34} J s Plank's constant, c=3·10^{10} cm s^{-1} speed of light and $\ddot{v}$ the wave number in cm^{-1}.

The rate of absorption of infrared energy mainly depends on the mass of the atoms to vibrate. As certain groups in molecules always consist of the same atoms (e.g. -COOH or -NH_2) general rules can be applied. If absorption of a certain energy occurs, a certain group must be present in the substance examined. Lists of groups and their typical absorption wave numbers is given in the literature[251].

All samples examined were mixed with an about 200 fold excess of potassium bromide and pressed into pellets at 10 tons for 15 minutes. At the University of Bochum, measurements were carried out with a Perkin-Elmer 1720X instrument in transmission mode (resolution 2 cm^{-1}, averaging of 10 scans). At the University of Duisburg-Essen, samples were analysed in a Bruker Vertex 70 FT-IR spectrometer (resolution 2 cm^{-1}, averaging of 20 scans). At the Weizmann Institute of Science, the pellets were analysed with a Midac M2000 portable FT-IR spectrometer (resolution 4 cm^{-1}, averaging of 15 scans).

5.4 Scanning electron microscopy (SEM)

Classical microscopes are limited in resolution to the magnitude of visible light (400-750 nm[7]). With scanning electron microscopes, much smaller objects can be observed and resoluted as high energy electrons are used for image creation. Electrons have wave character and their wavelength depends on their acceleration in a magnetic field:

$$\lambda = \frac{1{,}226}{\sqrt{U \cdot 10^{-9}}} \qquad \text{(eq. 5-7)}$$

with λ the wavelength in m and U the voltage.

The accelerated electrons are focussed by magnetic field lenses into a tight and narrow beam which scans an area of the sample. The diameter of the beam defines the maximum resolution of the instrument. The actual image observed is created by the secondary electron emissions of the scanned sample area. As electron emission from the surface is easier and more intense than from the inside of a sample, a contrast-rich 3D-image is created.

The samples must be electrically conducting. Isolating samples must be coated with a thin film of gold by sputtering. Sputtering exposes the samples to seven minutes of vacuum and an electric field. Not fully conductive areas result in partial charging of the sample and are seen as white areas in the black/white SEM image.

For SEM observation a LEO model 1530 microscope at the University of Bochum was used. Additionally, an X-ray detector for energy dispersive X-ray analysis (EDX) permitted the detection of elements present in the sample. At the Weizmann Institute of Science, a FEI (Philips) XL30 ESEM-FEG microscope without EDX option was used.

5.5 Thermogravimetric analysis (TGA)

In a thermobalance, the weight of a sample is measured as a function of temperature. As long as no reaction occurs, the weight remains constant. With increasing temperature, incorporated solvent molecules may leave a sample or it may decompose or react with oxygen, thus changing the weight of the sample.

At the University of Bochum, thermogravimetric analyses were carried out with a TG/DTA-S II, Seiko Exstar 6000 instrument. At the University of Duisburg-Essen, samples were heated in a Netzsch STA 409PC thermobalance. The sample mass was typically 5-15 mg. The samples were heated from 30 to 1000°C at 10 K min^{-1} under dynamic oxygen atmosphere (50-300 ml min^{-1}) in Al_2O_3 crucibles.

5.6 Extended X-ray absorption fine structure spectroscopy (EXAFS)

Depending on the energy of an X-ray beam which is applied to a sample, the main beam loses intensity. This may be due to classical Rayleigh diffraction (XRD), ionisation of the sample due to absorption, Compton-scattering or particle/antiparticle pair generation (at very high energies). The exact effect at certain energy depends on the elements present in the sample.[7] For absorption, the energy loss can be described with the Lambert-Beer-Law:

$$\mu(\mathrm{E}) \cdot d = \ln\left(\frac{I_0}{I_1}\right) \qquad \text{(eq. 5-8)}$$

with I_0 and I_1 the intensities before and after the sample, d the sample thickness and μ(E) the linear absorption coefficient of the sample.

Information about the coordination sphere of an element in a sample can be obtained by monitoring the absorbed energy during excitation of a core electron. The electron leaving the atom interacts with the electron shells of the surrounding neighbour atoms. As electrons can be perceived as waves and rays, the outgoing electron is considered being scattered back from the neighbour atoms of the coordination sphere. Outgoing and backscattering photon waves can positively and negatively interfere with each other, resulting in periodic oscillations of the absorption coefficient and thus the obtained spectrum. These oscillations contain information about kind, number, distance and geometry of the neighbouring atoms.[351] Figure 5.6-1 shows an EXAFS spectrum of a sample of amorphous calcium carbonate from the sternal deposits of *Porcellio scaber* (see chapter 3.3).

In the case of the samples analysed here, EXAFS spectroscopy was performed at beamline E4 at HASYLAB at DESY. Monochromatisation of the white beam

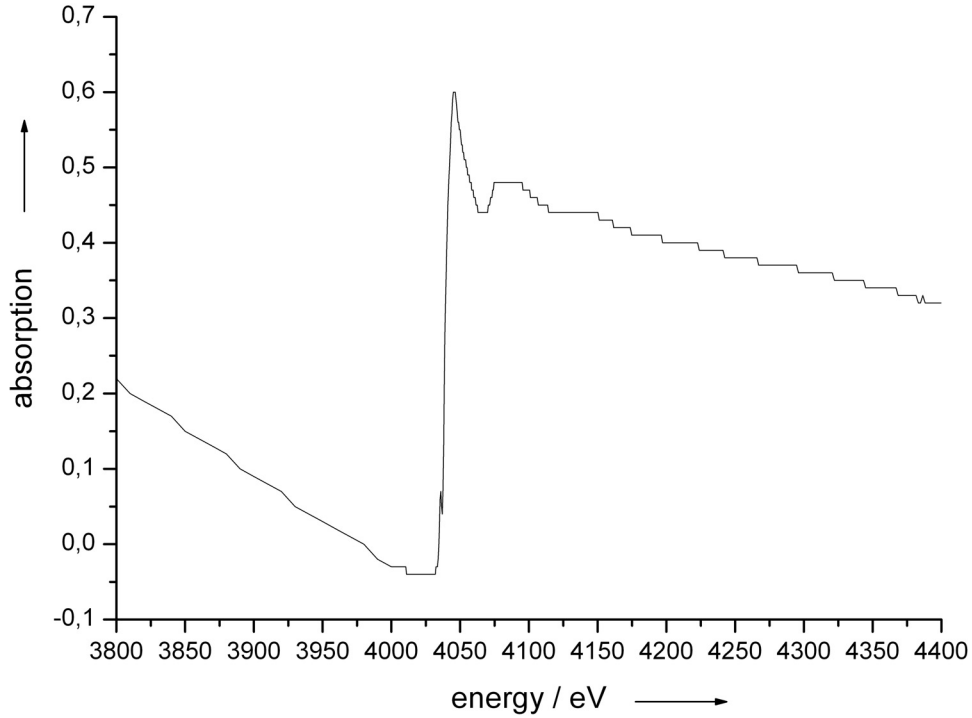

Fig. 5.6-1: Absorption of energy at the K-edge of calcium.

was done with a Si(111) double crystal monochromator. The ring was operated under the conditions described above. The energy scan was performed in transmission mode at liquid nitrogen temperature (-195.8°C) near the Ca K-edge energy of 4038.5 eV. The exact region scanned was 3800 to 4400 eV. The samples were slightly ground and fixed between two layers of adhesive tape.

For quantitative data evaluation, the programs SPLINE and XFit were used.[352] Theoretical standards were computed with the program FEFF 6.01a.[353] All fits were carried out with k^3-weighted data in *R*-space. The amplitude reduction factor S_0^2 was fixed to 0.60. For the reference compounds calcite, aragonite and vaterite, the coordination numbers were kept to the values derived from the crystal structure. For the ACC samples, the coordination numbers were allowed to vary. The error in this variable coordination number is about ±30 % because there is a strong mathematical correlation with the Debye-Waller factor σ^2. The typical error margin of EXAFS experiments for the first shell distance is about ±0.02 Å. These estimated errors are significantly higher for the second, third and fourth shells which are less well defined.

5.7 Experimental procedures

5.7.1 Animals

Animal samples for experiements were generally prepared and provided by cooperation partners. The crabs at the Weizmann Institute of Science were caught at Palmachim beach in the morning at low tide. They were held for about 4 hours in an aquarium with sea water taken during the hunt. Specimens were sacrificed by immersion into liquid nitrogen and dissected while frozen. Carapace pieces were stored at -80°C and ground when needed. Powders were also stored in thoroughly closed Eppendorf tubes at -80°C.

5.7.2 Procedures with protein

All organic substances of biological origin were stored in a freezer at -20°C. All glass surfaces which came in contact with protein were silanised beforehand with 10 % $(CH_3)_3SiCl$ in chloroform. Stock solutions were made by dissolving a discrete mass of protein in double-distilled water. Aliquots of 750 µl were taken and frozen separately. Solutions were thawed by transfer into a fridge at 4°C for 4 hours and then leaving them at room temperature for about the same time. Protein solutions were added to salt solutions after adjusting pH value. At the Weizmann Institute of Science, proteins extracted were stored at -80°C, but otherwise treated as described.

5.7.3 Crystallisation experiments

a) General procedures

After use, all glass surfaces were washed first with diluted HCl, then washed thoroughly with cleaner and finally rinsed with double-distilled water and allowed to dry. Surfaces which came in contact with protein were silanised before use with 10 % $(CH_3)_3SiCl$ in chloroform. After each experiment, the tubes were washed with concentrated HCl and double-distilled water. Before use, the medium to pump was used to clean the tubes.

All computer-monitored experiments were controlled by an AMD K6-II 450 MHz or an Intel Pentium-II 200 MHz computer under Windows95 equipped with a PCL-812PG D/A-conversion card. For pH and temperature measurements, WTW 340-A pH-meters with SenTix 41 electrodes were used. Two ISMATEC RA 2/8 peristaltic pumps were used to add the base and ion stock solutions in CCDD experiments; in multi-CCDD experiments, ISMATEC RA 4/8 peristaltic pumps were used. The computer control was programmed with the software VisiDAQ. The regulation quality was about ±0.04 pH.
The membranes covered with crystals were rinsed with 98 % ethanol and then air dried. After one day, a quarter of the membrane was cut out to be prepared for SEM analysis at side A; another quarter was cut out as SEM sample for side B. The rest of the membrane was subject to X-ray diffraction.

b) Ammonium carbonate method

The ammonium carbonate diffusion experiments were performed according to procedures described in literature[275, 276, 278] in a desiccator with a volume of about 5 l for 24 hours at 22±2°C. 25 ml calcium nitrate solution was put into a beaker with a surface of about 25 cm^2. The experiments were carried out with a calcium nitrate concentration of 5 mmol l^{-1}. The beaker was covered with a hole-dotted aluminium foil to slow down diffusion rate. The pH was continuously recorded by a pH-meter connected to a computer.

c) CCDD experiments

In the CCDD device, volumes of 100 ml or 25 ml on each side for precipitation were used. Solutions of 5 mmol l^{-1} of calcium nitrate and sodium carbonate, respectively, were used. The stock solution of NaOH had a concentration of 10 mmol l^{-1}. Ion stock solutions were of double concentration multiplied by a factor determined by the pump channel calibration to ensure that the overall added volume (base+stock solution) had a concentration of 5 mmol l^{-1}. The pH of both

reaction solutions was adjusted to 9.40±0.05 and the protein additives were fully dissolved in the solution before filling the solutions into the device. The stock solution pH were left unadjusted. The pH to hold constant by the computer was the first value shown on the pH-meters after filling the solutions into the device. Unless otherwise noted, all experiments were performed at a temperature of 29±0.5°C for typically three days. Ashless 589(3) filter paper (blue ribbon, Schleicher & Schuell, No. 300210) with an approximate thickness of 140 µm was used as crystallisation membrane. Additionally, SERVA Membra-Cel dialysis tubing MWCO 3500 (No. 44311, LOT 16335) dialysis membranes were used.

d) Multi-CCDD experiments

The reservoir vessels were filled with 50 l of solutions of calcium nitrate and sodium carbonate of 5 mmol l^{-1}, respectively. The pH of both solutions was adjusted to 9.40±0.05 with HNO_3 and NaOH. The adjusted value was held constant. Stock solutions of 30 l of 0.1 mol l^{-1} NaOH, 20 l of 10 mmol l^{-1} times the pump channel calibration factor of calcium nitrate and sodium carbonate, respectively, were used. Protein solutions to be filled into the crystallisation chamber were prepared from stock solutions using double-distilled water. The pH of these solutions was not controlled. Unless otherwise noted, all experiments were performed at 22±2°C for about three days. As crystallisation membrane, SERVA Membra-Cel dialysis tubing MWCO 3500 (No. 44311, LOT 16335) dialysis bags were used.

6. Summary

Biomineralisation is the precipitation of minerals by organisms. It is a highly regulated process controlling crystal nucleation and growth. The resulting biominerals are composite materials consisting of a very small amount of organic macromolecules (typically about 1 wt%) and the inorganic phase. The organic matrix consists of a water-soluble fraction and a water-insoluble fraction.

The biological nucleation is regulated by the insoluble matrix being a template for crystallisation and thus regulating the polymorphic phase of the precipitated mineral. Sometimes, acidic amino acid groups of proteins are arranged in a way similar to cation distances in mineral phases, thus forming a template for the precipitation of a certain phase. Nucleation may occur within a cell or a compartment formed by a group of specialised cells. These regulate the ion flow into the crystallisation zone, thereby controlling pH and ion concentrations, important parameters in crystallisation processes.

Under normal conditions, a crystal would grow according to its equilibrium form, i.e. calcite would form rhombohedra. The morphology of a growing biomineral is regulated by soluble macromolecules which adsorb to certain crystal faces and are incorporated into the growing crystal or inhibit further growth of certain crystal faces. The resulting composite material shows unusual properties which neither the mineral nor the biological macromolecules alone possess e.g. a snail house shows the hardness of steel.

The present work contains results from six different projects. The first part deals with the analysis of several biominerals. Solid state analytical methods like X-ray diffractometry, thermogravimetry, and infrared spectroscopy were applied to analyse biominerals of different origin. The second part deals with different crystallisation methods in order to simulate biomineralisation processes. The interaction of biological macromolecules and growing crystals may give hints to the function of these molecules *in vivo*.

Analysing biominerals sometimes yields astonishing results contradicting usual expectations. One of these unexpected findings was the presence of calcium sulphate hemihydrate in the gravity sensors of jellyfish, a water-deficient phase precipitated by an organism consisting mostly of water. Several species of jellyfish were analysed with respect to the mineral of their gravity sensors. X-ray powder diffractometry and single crystal diffractometry showed that the use of hemihydrate is spread over several phylogenetic groups of jellyfish. This finding may lead to a reconsideration of the current phylogenetic relationships of groups and families.

In the last years, amorphous calcium carbonate (ACC) became prominent as a biomineral precipitated on purpose by several organisms. Crustaceans which possess a mineralised cuticle make extensive use of ACC. This cuticle has to be shed regularly to accommodate animal growth. Water-based crustaceans can easily replace calcium carbonate lost with the shed cuticle because these ions are abundant in sea water. Land-based crustaceans, however, cannot replace calcium and carbonate necessary for replacement of the lost substance by their usual diet. Therefore, during evolution, they developed a mechanism for dissolving calcium carbonate from the cuticle before moult. The mineral is stored in the form of ACC in special deposits. These deposits were analysed more closely in the isopod *Porcellio scaber*. The mineral is stored in spherules packed in the sternal region of the animal. It is X-ray amorphous but shows a near range packing order of ions similar to either vaterite or monohydrocalcite. The precipitation of the thermodynamically most unstable ACC as storage phase allows a fast dissolution of the mineral due to the phase's high solubility (about 33 times higher than vaterite).

However, hints to the presence of ACC in the cuticles of terrestrial isopods which were not at all in the moulting phase were found in infrared spectra. The cuticles of several species of terrestrial isopods were therefore analysed with respect to the mineral phases present. X-ray powder diffraction and Rietveld

refinement gave the presence of magnesium calcite. The overall content of calcium and magnesium was determined by atom absorption spectroscopy. Thermogravimetric analysis gave the content of organic components and carbonate due to the release of carbon dioxide. Analysis of these results allowed the quantitative determination of contents in the cuticles in intermoult stage. Magnesium calcite, amorphous calcium carbonate and amorphous calcium phosphate were the mineral phases detected in the cuticles. The relative proportions of these compounds and organic matrix corresponded well with the predation defence strategies of the species examined. The mineral phases in different stages of moult of *P. scaber* were analysed, but these investigations have to be repeated before drawing final conclusions.

Magnesium calcite is found in land-based as well as water-based crustaceans. The carapace of a Mediterranean crab in different moult stages was analysed. The general structure of the carapace was determined by SEM analysis in mineralised and demineralised samples. The mineral phase consisted of magnesium calcite and amorphous calcium carbonate. It could be shown that the presence of magnesium calcite is no artefact from sample preparation. This finding was correlated with the composition of extracted soluble organic matrix. The fraction associated with fast dissolving ACC is different from the fraction associated with the later dissolving magnesium calcite, suggesting a precipitation of this phase on purpose by the organism.

The examples above illustrate the degree of control over mineralisation processes that biology has developed since the first traces of biomineralisation about 3.5 billion years ago. However, the more complex biological systems become the more they are prone to failures. The body of today's mammals is one of the most complex biological systems so far. In blood which is supersaturated with respect to calcium phosphate, proteins prevent the precipitation of this mineral. However, this protection mechanism fails in humans over the age of about sometimes thirty. In arteries, plaques consisting of

calcium phosphate and organic components are formed, resulting in damaged arteries. This disease, atherosclerosis, develops during ageing and is the major cause of death in the industrialised nations. Atherosclerotic plaques were examined with respect to their mineral phase consisting of nanocrystalline carbonated hydroxyapatite. No correlation between the mineralised particles and the clinical history of the patients was found. The crystals in the plaques were similar to bone crystals but showed a larger variety of size and shape and a less distinct anisotropy, pointing to a smaller degree of shape control during precipitation in contrast to bone formation.

The second part of this work deals with the simulation of biomineralisation *in vitro*. The constant-composition-double-diffusion technique developed by Peters and Epple for the precipitation of calcium phosphate was converted to the precipitation of calcium carbonate. Calcium carbonate was precipitated in the CCDD-device and with the ammonium carbonate method in the presence of biological additives. Bovine serum albumin (BSA) and the soluble matrix of the shell of the freshwater snail *Biomphalara glabrata* were used as additives. The crystals obtained in the CCDD device showed a clear influence of BSA on morphology and number of crystals precipitated. The soluble matrix of the snail shell led to a complete inhibition and no crystals were observed. However, in the ammonium carbonate method, all experiments gave calcite and some aragonite despite the presence of different concentrations of BSA or the soluble shell matrix. The CCDD device simulates biomineralisation conditions better than the ammonium carbonate method, because the influence of biological additives on forming crystals was more obvious. However, the CCDD setup has the disadvantage of producing only one result in three days with a substantial amount of protein necessary. The device was reconsidered and transformed into a multi-CCDD setup. Twelve simultaneous experiments are now possible in the revised setup. The amount of protein additive is reduced considerably, because the crystallisation no longer occurs in or on a single membrane like in the

conventional setup, but in a specially designed crystallisation chamber. In experiments with the additive poly-aspartic acid, the inhibiting influence of the additive reported in literature could be repeated at different concentrations.

7. Literature

[1] H. A. Lowenstam, S. Weiner, *On biomineralization*, Oxford University Press, New York, **1989**.
[2] H. Tiemann, I. Sötje, G. Jarms, C. Paulmann, M. Epple, B. Hasse, *J. Chem. Soc., Dalton Trans.* **2002**, 1266.
[3] H. C. Lichtenegger, T. Schöberl, M. H. Bartl, H. Waite, G. D. Stucky, *Science* **2002**, *298*, 389.
[4] H. Elderfield, *Science* **2002**, *296*, 1618.
[5] D. W. Rogers, R. Chase, *Behav. Ecol. Sociobiol.* **2001**, *50*, 122.
[6] L. Addadi, S. Weiner, *Angew. Chem.* **1992**, *104*, 159.
[7] Römpp, CD-ROM ed., Georg Thieme Verlag, Stuttgart, **1995**.
[8] W. Kleber, H. J. Bautsch, J. Bohm, *Einführung in die Kristallographie*, 17. ed., Verlag Technik Berlin, München, **1990**.
[9] M. Volmer, *Kinetik der Phasenbildung*, Theodor Steinkopff Verlag, Dresden, **1939**.
[10] W. K. Burton, N. Cabrera, F. C. Frank, *Phil. Trans. R. Soc. Lond. A* **1951**, *234*, 299.
[11] J. Nyvlt, J. Ulrich, *Admixtures in Crystallisation*, VCH Weinheim, New York, **1995**.
[12] M. H. Salimi, J. C. Heughebaert, G. H. Nancollas, *Langmuir* **1985**, *1*.
[13] G. H. Nancollas, N. Purdie, *Quart. Rev. Biol.* **1964**, *18*, 1.
[14] F. Peters, Universität Hamburg (Hamburg), **2001**.
[15] C. A. Mitchell, L. Yu, M. D. Ward, *J. Am. Chem. Soc.* **2001**, *123*, 10830.
[16] W. Ostwald, *Z. Phys. Chem.* **1897**, *22*, 289.
[17] A. Gutjahr, University of Bonn (Bonn), **1993**.
[18] S. Suzuki, M. Ohgaki, *J. Mat. Sci. Lett.* **1998**, *17*, 381.
[19] S. J. Zawacki, P. Koutsoukos, M. H. Salimi, G. H. Nancollas, *ACS Symposium* **1986**, *322*.
[20] S. Sugio, A. Kashima, S. Mochizuki, M. Noda, K. Kobayashi, *Protein Eng.* **1999**, *12*, 439.
[21] I. Sarashina, K. Endo, *Am. Mineral.* **1998**, *83*, 1510.
[22] S. Mann, *Biomimetic materials chemistry*, VCH Weinheim, New York, Cambridge, **1996**.
[23] S. Weiner, L. Addadi, *J. Mater. Chem.* **1997**, *7*, 689.
[24] J. L. Kirschvink, D. S. Jones, B. J. McFadden, Plenum, New York, **1985**.
[25] H. A. Lowenstam, *Bull. Geol. Soc. Amer.* **1962**, *73*, 435.
[26] M. F. Glaessner, *The dawn of animal life*, Cambride University Press, Cambridge, **1985**.
[27] M. Magaritz, W. T. Holser, J. L. Kirschvink, *Nature* **1986**, *320*, 258.
[28] B. Pokroy, E. Zolotoyabko, *J. Mater. Chem.* **2003**, *13*, 682.
[29] H. Tong, J. Hu, W. Ma, G. Zhong, S. SYao, N. Cao, *Biomaterials* **2001**, *23*, 2593.
[30] J. M. Rensberger, M. Watabe, *Nature* **2000**, *406*, 619.
[31] P. Ball, *Nature* **2001**, *409*, 413.
[32] S. Weiner, L. Addadi, *Trends Biochem. Sci.* **1991**, *16*, 252.
[33] L. Addadi, S. Weiner, *Proc. Natl. Acad. Sci. U.S.A.* **1985**, *82*, 4110.
[34] D. Volkmer, *Chem. unserer Zeit* **1999**, *1*, 6.
[35] I. S. Johnston, *Scanning Electron Microsc.* **1979**, *11*, 421.
[36] S. Weiner, W. Traub, *Phil. Trans. R. Soc. Lond. B* **1984**, *304*, 425.
[37] S. Mann, *J. Mater. Chem.* **1995**, *5*, 935.
[38] P. Buijnsters, J. Donners, S. Hill, B. Heywood, R. Nolte, B. Zwanenburg, N. Sommerdijk, *Langmuir* **2001**, *17*, 3623.
[39] D. Volkmer, M. Fricke, D. Vollhardt, S. Siegel, *J. Chem. Soc., Dalton Trans.* **2002**, 1.

[40] J. Küther, G. Nelles, R. Seshadri, M. Schaub, H. J. Butt, W. Tremel, *Chem. Eur. J.* **1998**, *4*, 1834.
[41] I. Lee, S. Han, S. Lee, H. J. Choi, K. Kim, *Adv. Mater.* **2002**, *14*, 1640.
[42] D. M. Duffy, J. H. Harding, *J. Mater. Chem.* **2002**, *12*, 3419.
[43] M. Travaille, J. Donners, J. Gerritsen, N. Sommerdijk, R. Nolte, H. van Kempen, *Adv. Mater.* **2002**, *14*, 492.
[44] Q. L. Feng, F. Z. Cui, G. Pu, R. Z. Wang, H. D. Li, *Mat. Sci. Eng.* **2000**, *11C*, 19.
[45] Q. L. Feng, G. Pu, Y. Pei, F. Z. Cui, H. D. Li, T. N. Kim, *J. Cryst. Growth* **2000**, *216*, 459.
[46] J. Aizenberg, J. Hanson, M. Ilan, L. Leiserowitz, T. F. Koetzle, L. Addadi, S. Weiner, *FASEB J.* **1995**, *9*, 262.
[47] A. P. Wheeler, J. W. George, C. A. Evans, *Science* **1981**, *212*, 1397.
[48] A. P. Wheeler, K. W. Rusenko, C. S. Sikes, in *Chemical Aspects of Regulation of Mineralization* (Eds.: C. S. Sikes, A. P. Wheeler), University of South Alabama Publication Services, Mobile, **1988**, pp. 9.
[49] S. Mann, *J. Chem. Soc., Dalton Trans.* **1997**, *21*, 3953.
[50] A. S. Mount, A. P. Wheeler, R. P. Paradkar, D. Snider, *Science* **2004**, *304*, 297.
[51] N. Bouropoulos, S. Weiner, L. Addadi, *Chem. Eur. J.* **2001**, *7*, 1881.
[52] N. Kessler, D. Perl-Treves, L. Addadi, M. Eisenstein, *Proteins* **1999**, *34*, 383.
[53] N. H. de Leeuw, T. G. Cooper, *Cryst. Growth Des.* **2004**, *4*, 123.
[54] L. Qi, J. Li, J. Ma, *Adv. Mater.* **2002**, *14*, 300.
[55] L. Qi, H. Cölfen, M. Antonietti, M. Li, J. D. Hopwood, A. J. Ashley, S. Mann, *Chem. Eur. J.* **2001**, *7*, 3526.
[56] A. Sugawara, T. Ishii, T. Kato, *Angew. Chem.* **2003**, *115*, 5457.
[57] T. Kato, A. Sugawara, N. Hosoda, *Adv. Mater.* **2002**, *14*, 869.
[58] C. Söllner, M. Burghammer, E. Busch-Nentwich, J. Berger, H. Schwarz, C. Riekel, T. Nicolson, *Science* **2003**, *302*, 282.
[59] L. Addadi, S. Weiner, *Nature* **1997**, *389*, 912.
[60] K. M. McGrath, *Adv. Mater.* **2001**, *12*, 989.
[61] K. Naka, Y. Chujo, *Chem. Mater.* **2001**, *13*, 3245.
[62] S. Mann, J. Webb, J. P. Williams, *Biomineralisation - Chemical and Biochemical Perspectives*, VCH Verlagsgesellschaft, Weinheim, **1989**.
[63] Y. Levi-Kalisman, G. Falini, L. Addadi, S. Weiner, *J. Struct. Biol.* **2001**, *135*, 8.
[64] Y. Levi, Weizmann Institute of Science (Rehovot), **1996**.
[65] B. Hasse, H. Ehrenberg, J. C. Marxen, W. Becker, M. Epple, *Chem. Eur. J.* **2000**, *6*, 3679.
[66] J. Aizenberg, J. Hanson, T. F. Koetzle, S. Weiner, L. Addadi, *J. Amer. Chem. Soc.* **1997**, *119*, 881.
[67] T. Loerting, M. H. Moore, R. K. Khanna, *Spectrochim. Acta A* **1991**, *47*, 255.
[68] A. F. Holleman, E. Wiberg, *Lehrbuch der Anorganischen Chemie*, 101 ed., Walter de Gruyter, Berlin, **1995**.
[69] K. Sawada, *Pure Appl. Chem.* **1997**, *69*, 921.
[70] E. N. Maslen, V. A. Streltsov, N. R. Streltsova, *Acta Crystallogr.* **1993**, *B 49*, 636.
[71] B. Dickens, J. S. Boewen, *J. Res. Natl. Bur. Stand.* **1971**, *A 75*, 27.
[72] S. R. Kamhi, *Acta Crystallogr.* **1963**, *16*, 770.
[73] H. Effenberger, *Monatsh. Chem.* **1981**, *112*, 899.
[74] K. F. Hesse, H. Kueppers, E. Suess, *Z. Kristallogr.* **1983**, *163*, 227.
[75] O. S. Pokorovskii, *Lithol. Min. Res.* **1996**, *31*, 474.
[76] E. D. Glover, R. F. Sippel, *Geochim. Cosmochim. Acta* **1967**, *31*, 603.
[77] A. Mucci, J. W. Morse, *Geochim. Cosmochim. Acta* **1983**, *47*, 217.
[78] R. A. Berner, *Geochim. Cosmochim. Acta* **1975**, *39*, 489.

[79] Y. Dauphin, *Appl. Spectrosc.* **1999**, *53*, 184.
[80] J. R. Goldsmith, D. L. Graf, *Am. Mineral.* **1958**, *43*, 84.
[81] G. Wolf, C. Günther, *J. Therm. Anal. Cal.* **2001**, *65*, 687.
[82] Y. Dauphin, *Appl. Spectrosc.* **1997**, *51*, 253.
[83] B. Hasse, Ruhr-Universität Bochum (Bochum), **2001**.
[84] G. Wolf, E. Königsberger, H. G. Schmidt, L. C. Königsberger, H. Gamsjäger, *J. Therm. Anal. Cal.* **2000**, *60*, 463.
[85] K. M. Wilbur, N. Watabe, *Ann. N. Y. Acad. Sci.* **1963**, *109*, 82.
[86] D. Carlström, *Biol. Bull.* **1963**, *125*, 441.
[87] H. C. W. Skinner, G. W. Osbaldiston, A. N. Wilner, *Am. Mineral.* **1977**, *62*, 273.
[88] K. Kamiya, S. Sakka, K. Terada, *Mater. Res. Bull.* **1977**, *12*, 1095.
[89] Y. Kojima, A. Kawanobe, T. Yasue, Y. Arai, *J. Ceram. Soc. Jpn. Int. Edn.* **1994**, *102*, 1131.
[90] A. Mikkelsen, A. B. Andersen, S. B. Engelsen, H. C. B. Hansen, O. Larsen, L. H. Skibsted, *J. Agric. Food Chem.* **1999**, *47*, 911.
[91] J. Johnston, H. E. Merwin, E. D. Williamson, *Amer. J. Sci.* **1916**, *41*, 473.
[92] L. Brecevic, *J. Cryst. Growth* **1989**, *98*, 504.
[93] J. R. Clarkson, T. J. Price, C. J. Adams, *J. Chem. Soc., Faraday Trans.* **1992**, *88*, 243.
[94] L. N. Plummer, E. Busenberg, *Geochim. Cosmochim. Acta* **1982**, *46*, 1011.
[95] G. Dorfmüller, *Deutsch. Zuckerind.* **1938**, *51*, 1217.
[96] N. Koga, Y. Nakagoe, H. Tanaka, *Thermochim. Acta* **1998**, *318*, 239.
[97] I. Matsushita, Y. Hamada, T. Moriga, T. Ashida, I. Nakabayashi, *J. Ceram. Soc. Jpn.* **1996**, *104*, 1081.
[98] M. Faatz, F. Gröhn, G. Wegner, *Adv. Mater.* **2004**, *16*, 996.
[99] E. Loste, F. C. Meldrum, *Chem. Commun.* **2001**, 901.
[100] E. Loste, R. M. Wilson, R. Seshadri, F. C. Meldrum, *J. Cryst. Growth* **2003**, *254*, 206.
[101] S. Raz, S. Weiner, L. Addadi, *Adv. Mater.* **2000**, *12*, 38.
[102] M. M. Reddy, G. H. Nancollas, *J. Cryst. Growth* **1976**, *35*, 33.
[103] J. Donners, B. Heywood, E. W. Meijer, R. Nolte, N. Sommerdijk, *Chem. Eur. J.* **2002**, *8*, 2561.
[104] J. J. M. Donners, B. R. Heywood, E. W. Meijer, R. J. M. Nolte, C. Roman, A. Schenning, N. Sommerdijk, *Chem. Commun.* **2000**, *19*, 1937.
[105] J. J. M. Donners, E. W. Meijer, R. J. M. Nolte, N. Sommerdijk, *Polym. Mat. Sci. Eng.* **2001**, *84*, 1039.
[106] H. Cölfen, L. Qi, *Chem. Eur. J.* **2001**, *7*, 106.
[107] P. Kjellin, K. Holmberg, M. Nyden, *Colloids Surf. A* **2001**, *194*, 49.
[108] J. Y. Gal, J. C. Bollinger, H. Tolosa, N. Gache, *Talanta* **1996**, *43*, 1497.
[109] E. Beniash, J. Aizenberg, L. Addadi, S. Weiner, *Proc. R. Soc. Lond.* **1997**, *264*, 461.
[110] S. Raz, P. C. Hamilton, F. H. Wilt, S. Weiner, L. Addadi, *Adv. Funct. Mater.* **2003**, *13*, 480.
[111] I. M. Weiss, N. Tuross, L. Addadi, S. Weiner, *J. Exp. Zool.* **2002**, *293*, 478.
[112] A. Becker, U. Bismayer, M. Epple, H. Fabritius, B. Hasse, J. Shi, A. Ziegler, *J. Chem. Soc., Dalton Trans.* **2003**, 551.
[113] M. G. Taylor, K. Simkiss, G. N. Greaves, M. Okazaki, S. Mann, *Proc. R. Soc. Lond.* **1993**, *252B*, 75.
[114] Y. Levi-Kalisman, S. Raz, S. Weiner, L. Addadi, I. Sagi, *Adv. Funct. Mater.* **2002**, *12*, 43.
[115] G. F. Xu, N. Yao, I. A. Aksay, J. T. Groves, *J. Amer. Chem. Soc.* **1998**, *120*, 977.
[116] J. Aizenberg, D. A. Muller, J. L. Grazul, D. R. Hamann, *Science* **2003**, *299*, 1205.
[117] J. Aizenberg, S. Weiner, L. Addadi, *Conn. Tiss. Res.* **2003**, *44*, 20.
[118] J. Aizenberg, G. Lambert, S. Weiner, L. Addadi, *J. Amer. Chem. Soc.* **2002**, *124*, 32.

[119] J. Aizenberg, G. Lambert, L. Addadi, S. Weiner, *Adv. Mater.* **1996**, *8*, 222.
[120] B. A. Gotliv, S. Weiner, L. Addadi, *ChemBioChem* **2003**, *4*, 522.
[121] G. Falini, S. Albeck, S. Weiner, L. Addadi, *Science* **1996**, *271*, 67.
[122] L. Addadi, S. Raz, S. Weiner, *Adv. Mater.* **2003**, *15*, 959.
[123] J. C. Elliot, P. E. Mackie, R. A. Young, *Science* **1973**, *180*, 1055.
[124] T. Ikoma, A. Yamazaki, S. Nakamura, M. Akao, *J. Sol. St. Chem.* **1999**, *144*, 272.
[125] P. Koutsoukos, G. H. Nancollas, *J. Cryst. Growth* **1981**, *53*, 10.
[126] J. D. Termine, R. A. Peckauskas, A. S. Posner, *Arch. Biochem. Biophys.* **1970**, *140*, 318.
[127] A. Becker, A. Ziegler, M. Epple, *J. Chem. Soc., Dalton Trans.* **2004**, *accepted*.
[128] H. A. Lowenstam, S. Weiner, *Science* **1985**, *227*, 51.
[129] J. Puech, J. C. Heughebaert, G. Montel, *J. Cryst. Growth* **1982**, *56*, 20.
[130] D. Skrtic, in *Dental Materials: V - Polymer Materials-Chemistry Program*, American Dental Association Foundation, Hawaii Convention Center Exhibit Hall 1-2, **2004**.
[131] B. F. Pedersen, D. Semmingsen, *Acta Crystallogr.* **1982**, *38B*, 1074.
[132] W. Abriel, R. Nesper, *Z. Kristallogr.* **1993**, *205*, 99.
[133] C. Bezou, A. Nonat, K. Mutin, *J. Sol. St. Chem.* **1995**, *117*, 165.
[134] A. Kirfel, G. Will, *Acta Crystallogr.* **1980**, *B36*, 2881.
[135] F. Hanic, *Br. Ceram. Trans. J.* **1985**, *84*, 22.
[136] D. Freyer, Technische Universität Bergakademie Freiberg (Freiberg), **2000**.
[137] M. Oetzel, Rheinisch-Westfälische Technische Hochschule Aachen (Aachen), **1999**.
[138] W. Kraus, G. Nolze, 2.3 ed., Federal Institute for Materials Research and Testing, Berlin, **1999**.
[139] B. Werner, in *Lehrbuch der speziellen Zoologie, Band 1: Wirbellose Tiere, 2. Teil* (Ed.: H. E. Gruner), Fischer, **1984**, pp. 11.
[140] G. Jarms, U. Bamstedt, H. Tiemann, M. B. Martinussen, J. H. Fossa, *Sarsia* **1999**, *84*, 55.
[141] P. Ax, *Das System der Metazoa I - Ein Lehrbuch der phylogenetischen Systematik*, Fischer Verlag, Stuttgart, **1995**.
[142] P. Schuchert, *Z. Zool. Syst. Evolut. Forsch.* **1993**, *31*, 161.
[143] Y. A. Vinnikov, M. Z. Aronove, T. A. Kharkeevich, T. P. Tsirulis, E. A. Lavrova, Y. V. Natochin, *Z. Mikrosk. Anat. Forsch.* **1981**, *95*, 127.
[144] J. F. Gerrath, *Progr. Phycol. Res.* **1993**, *9*, 79.
[145] O. Kopetzky-Rechtperg, *Beihefte zum Botanischen Centralblatt* **1930**, *XLVI*, 291.
[146] A. J. Brook, A. Fortheringham, J. Bradly, A. Jenkins, *Br. phycol. J.* **1980**, *15*, 261.
[147] G. Jarms, H. Tiemann, U. Bamstedt, *Mar. Biol.* **2002**, *141*, 647.
[148] C. L. Singla, *Cell Tissue Res.* **1975**, *158*, 391.
[149] D. Chapman, *J. Mar. Biol. Ass. U.K.* **1985**, *65*, 617.
[150] D. Pollmanns, M. Hündgen, *Zool. Jb. Anat.* **1981**, *105*, 508.
[151] D. Spangenberg, C. W. Beck, *Trans. Amer. Microsc. Soc.* **1968**, *87*, 329.
[152] S. Ueno, C. Imai, A. Mitsutani, *J. Plankton Res.* **1995**, *17*, 1381.
[153] S. Ueno, C. Imai, A. Mitsutani, *Proc. 6th Int. Conf. Coelenterate Biology* **1997**, 491.
[154] A. Becker, I. Sötje, C. Paulmann, F. Beckmann, T. Donath, R. Boese, O. Prymak, H. Tiemann, M. Epple, *J. Chem. Soc., Dalton Trans.* **2004**, submitted.
[155] G. Ramel, *Internet* **1995**, www.eartlife.net.
[156] N. F. Hadley, in *Sci. Am., Vol. 7*, **1986**, pp. 98.
[157] A. Ziegler, T. Grospietsch, T. H. Carefoot, J. P. Danko, M. Zimmer, I. Zerbst-Boroffka, S. C. Pennings, *J. Comp. Physiol.* **2000**, *170B*, 329.
[158] B. Messner, *Crustaceana* **1965**, *9*, 285.
[159] D. S. Neufeld, J. N. Cameron, *J. Exp. Biol.* **1993**, *184*, 1.

[160] L. M. Passano, in *The physiology of Crustacea* (Ed.: T. H. Watermann), Academic Press, New York, **1960**, pp. 473.
[161] A. Ziegler, F. H. E. Scholz, *J. Comp. Physiol.* **1997**, *167B*, 536.
[162] C. G. H. Steel, *Can. J. Zool.* **1993**, *71*, 4.
[163] A. Ziegler, *Cell Tiss. Res.* **1996**, *284*, 459.
[164] A. Ziegler, *Cell Tiss. Res.* **1997**, *29*, 63.
[165] W. Herold, *Zoologisches Jahrbuch für Anatomie und Ontogenie der Tiere* **1913**, *35*, 457.
[166] K. W. Verhoeff, *Zeitschrift für Morphologie und Ökologie der Tiere* **1940**, *37*, 126.
[167] C. G. H. Steel, *Can. J. Zool.* **1982**, *60*, 429.
[168] A. Ziegler, E. Merz, *J. Struct. Biol.* **1999**, *127*, 263.
[169] J. Glötzner, A. Ziegler, *Anthropod Structure& Development* **2000**, *29*, 241.
[170] M. Hagedorn, A. Ziegler, *J. Exp. Biol.* **2002**, *205*, 1935.
[171] A. Ziegler, *J. Histochem. Cytochem.* **1997**, *45*, 437.
[172] A. Ziegler, *Cell Calcium* **2002**, *31*, 307.
[173] M. Hagedorn, D. Weihrauch, D. W. Towle, A. Ziegler, *J. Exp. Biol.* **2003**, *206*, 2167.
[174] A. Ziegler, D. Weihrauch, D. W. Towle, M. Hagedorn, *Cell Calcium* **2002**, *32*, 131.
[175] A. Ziegler, D. Weihrauch, M. Hagedorn, D. W. Towle, R. Bleher, *J. Exp. Biol.* **2004**, *207*, 1749.
[176] D. Drobne, J. Strus, *Env. Toxicol. Chem.* **1996**, *15*, 126.
[177] P. Greenaway, *Biol. Rev.* **1985**, *60*, 425.
[178] S. Sparks, P. Greenaway, *J. Exp. Biol.* **1984**, *113*, 43.
[179] F. Graf, J. C. Meyran, *J. Morphol.* **1983**, 1.
[180] F. Graf, *Arch. Zool. Exp. Gen.* **1978**, *119*, 143.
[181] A. Ziegler, B. Miller, *Zoomorphology* **1997**, *117*, 181.
[182] H. Fabritius, A. Ziegler, *J. Struct. Biol.* **2003**, *142*, 281.
[183] A. Ziegler, *J. Struct. Biol.* **1994**, *112*, 110.
[184] W. B. White, in *The infrared spectra of minerals* (Ed.: V. C. Farmer), Mineralogical Society, London, **1974**, pp. 227.
[185] U. Bismayer, *Rev. Mineral. Geochem.* **2000**, *39*, 265.
[186] Y. Levi-Kalisman, S. Raz, S. Weiner, L. Addadi, I. Sagi, *J. Chem. Soc., Dalton Trans.* **2000**, 3977.
[187] Y. Levi-Kalisman, S. Raz, S. Weiner, L. Addadi, I. Sagi, *Adv. Funct. Mater.* **2002**, *12*, 43.
[188] M. G. Taylor, K. Simkiss, G. N. Greaves, M. Okazaki, S. Mann, *Proc. R. Soc. Lond. B* **1993**, *252*, 75.
[189] Y. Levi-Kalisman, S. Raz, S. Weiner, L. Addadi, I. Sagi, *J. Chem. Soc. Dalton Trans.* **2000**, 3977–3982.
[190] B. Hasse, H. Ehrenberg, J. C. Marxen, W. Becker, M. Epple, *Chem. Eur. J.* **2000**, *6*, 3679.
[191] J. C. Marxen, W. Becker, D. Finke, B. Hasse, M. Epple, *J. Mollus. Stud.* **2003**, *69*, 113.
[192] S. R. Wood, J. D. Russel, *Crustaceana* **1987**, *53*, 49.
[193] A. Gualtieri, *J. Appl. Crystallogr.* **2000**, *33*, 267.
[194] S. V. Dorozhkin, M. Epple, *Angew. Chem. Int. Ed.* **2002**, *41*, 3130.
[195] S. Bhagavantam, T. Venkatarayudu, *Proc. Ind. Acad. Sci.* **1939**, *A9*, 224.
[196] G. Herzberg, *Molecular spectra and molecular structure. II. Infrared and Raman spectra of polyatomic molecules*, van Nostrand, New York, **1945**.
[197] Y. Dauphin, *Appl. Spectrosc.* **1999**, *53*, 184.
[198] R. Chester, H. Elderfield, *Sedimentology* **1967**, *9*, 5.

[199] A. Becker, U. Bismayer, M. Epple, H. Fabritius, B. Hasse, J. Shi, A. Ziegler, *J. Chem. Soc. Dalton Trans.* **2003**, 551.
[200] J. C. Marxen, W. Becker, D. Finke, B. Hasse, M. Epple, *J. Molluscan Studies* **2003**, *69*, 113.
[201] H. Schmalfuss, *Symp. Zool. Soc. Lond.* **1984**, *53*, 49.
[202] P. Greenaway, *Biol. Rev.* **1985**, *60*, 425.
[203] P. Compère, G. Goffinet, *Tissue & Cell* **1987**, *19*, 839.
[204] K. K. Vijayan, A. D. Diwan, *Comp. Biochem. Physiol.* **1996**, *114A*, 91.
[205] E. E. Williams, M. J. Anderson, T. J. Miller, S. D. Smith, *Comp. Biochem. Physiol. B* **2004**, *137*, 235.
[206] L. Brecevic, A. E. Nielson, *J. Cryst. Growth* **1989**, *98*, 504.
[207] J. Strus, A. Beljec, in *Isopod systhematics and evolution* (Eds.: B. Censley, R. C. Brusca), A. A. Balkemer, Brookfield, **2001**.
[208] S. Cannini, J. Paula, M. Vannini, *Mar. Biol.* **1999**, *133*, 429.
[209] G. Guerao, P. Abelló, J. P. Cuesta, *Zoosystema* **1997**, *19*, 439.
[210] J. P. Cuesta, A. Rodríguez, *Hydrobiologia* **2000**, *436*, 119.
[211] T. Tscheulin, *Projektberichte des Institute oceanographique Laboratoire Arago* **1998**, *20*, 20.
[212] S. Cannicci, M. Gomei, B. Boddi, M. Vannini, *Estuarine, Costal and Shelf Science* **2002**, *54*, 983.
[213] B. K. Filshie, in *Insect Ultrastructure, Vol. 1* (Ed.: K. a. Akai), **1982**, pp. 281.
[214] S. Albeck, S. Weiner, L. Addadi, *Chem. Eur. J.* **1996**, *2*, 278.
[215] L. Addadi, S. Weiner, *personal communication* **2004**.
[216] F. E. Coblentz, T. H. Shafer, R. D. Roer, *Com. Biochem. Physiol. B* **1998**, *121*, 349.
[217] R. Tang, L. Wang, C. A. Orme, T. Bonstein, P. J. Bush, G. H. Nancollas, *Angew. Chem.* **2004**, *116*, 2751.
[218] U. N. Riede, H. E. Schaefer, 3. ed., Georg Thieme Verlag Stuttgart, New York, **1993**, p. 1184.
[219] K. J. Bühling, J. Lepenies, K. Witt, *Intensivkurs allgemeine und spezielle Pathologie*, 2. ed., Urban&Fischer München, Jena, **2000**.
[220] W. Mohr, E. Görz, *Z. Kardiol.* **2002**, *91*, 557.
[221] A. Tanimura, T. Cho, Y. Saito, T. Nakashima, *Acta Pathol. Jap.* **1986**, *36*, 35.
[222] A. M. Vikhert, N. H. Sternby, A. M. Livshits, J. Duskova, *Atherosclerosis* **1994**, *106*, 129.
[223] S. Warren, K. Pope, Y. Yazdi, A. J. Welch, S. Thomson, A. L. Johnston, M. J. Davis, R. Richards-Kortum, *Trans. Biomed. Eng.* **1995**, *42*, 121.
[224] A. Christov, E. Dai, M. Drangova, L. Liu, G. S. Abela, P. Nash, G. McFadden, A. Lucas, *Photochem. Photobiol.* **2000**, *72*, 242.
[225] P. J. M. Brands, S. W. E. van de Poll, J. A. Quaedackers, P. H. A. Mutsaers, G. J. Puppels, A. van der Laarse, M. J. A. de Voigt, *Nuc. Instr. Meth. Phys. Res.* **2001**, *181*, 454.
[226] D. Steinberg, *Nat. Med.* **2002**, *8*, 1211.
[227] R. Ross, *Nature* **1993**, *362*, 801.
[228] G. Virella, M. F. Lopes-Virella, *Nat. Med.* **2003**, *9*, 243.
[229] T. M. Doherty, R. C. Detrano, *Calcif. Tissue Int.* **1994**, *54*, 224.
[230] C. M. Shanahan, D. Proudfoot, K. L. Tyson, N. R. B. Cary, P. L. Weissberg, *Z. Kardiol.* **2000**, *89*, II/63.
[231] K. I. Boström, *Z. Kardiol.* **2000**, *89*, II/69.
[232] A. Shiori, K. Mori, S. Jono, T. Wakikawa, Y. Hiura, H. Koyama, Y. Okuno, Y. Nishizawa, H. Morii, *Z. Kardiol.* **2000**, *89*, II/75.

[233] F. Parhami, Y. Tintut, J. K. Patel, N. Mody, A. Hemmat, L. L. Demer, *Z. Kardiol.* **2001**, *90*, III/27.
[234] W. Mohr, E. Görz, *Z. Kardiol.* **2002**, *91*, 212.
[235] W. Mohr, E. Görz, *Z. Kardiol.* **2003**, *92*, 60.
[236] M. Ketteler, C. Wanner, T. Metzger, P. Bongartz, R. Westenfeld, U. Gladzwia, L. J. Schurgers, C. Vermeer, W. Jahnen-Dechent, J. Floege, *Kidney Int.* **2003**, *63*, S84.
[237] W. Jahnen-Dechent, C. Schäfer, A. Heiss, J. Grötzinger, *Z. Kardiol.* **2001**, *90*, III/47.
[238] M. Ketteler, P. Bongartz, R. Westenfeld, J. E. Wildberger, A. H. Mahnken, R. Böhm, T. Metzger, C. Wanner, W. Jahnen-Dechent, J. Floege, *Lancet* **2003**, *361*, 827.
[239] A. Becker, M. Epple, K. M. Müller, I. Schmitz, *J. Inorg. Biochem.* **2004**, *98*, 2032.
[240] M. Epple, P. Lanzer, *Z. Kardiol.* **2001**, *90*, III/2.
[241] A. Tanimura, D. H. McGregor, H. C. Anderson, *J. Exp. Path.* **1986**, *2*, 261.
[242] S. H. Song, M. R. Roach, *Yonsei Med. J.* **1998**, *39*, 430.
[243] Y. S. Lee, H. C. Chen, S. M. Lai, *Proc. Natl. Sci. Counc. B* **1993**, *16*, 169.
[244] B. B. Tomazic, *Z. Kardiol.* **2001**, *90*, III/68.
[245] R. Legros, N. Balmain, G. Bonel, *Calcif. Tissue Int.* **1987**, *41*, 137.
[246] D. Tadic, M. Epple, *Biomaterials* **2004**, *25*, 987.
[247] F. Peters, K. Schwarz, M. Epple, *Thermochim. Acta* **2000**, *361*, 131.
[248] R. Z. Legeros, *Nature* **1965**, *206*, 403.
[249] B. B. Tomazic, W. E. Brown, L. A. Queral, M. Sadovnik, *Atherosclerosis* **1988**, *69*, 5.
[250] B. B. Tomazic, in *Hydroxyapatite and related materials* (Eds.: P. W. Brown, B. Constantz), CRC Press, Boca Raton, **1994**, pp. 93.
[251] M. Hesse, H. Meier, B. Zeeh, *Spektroskopische Methoden in der organischen Chemie*, 5. ed., Georg Thieme Verlag, Stuttgart, **1995**.
[252] F. Peters, M. Epple, *J. Chem. Soc., Dalton Trans.* **2001**, 3585.
[253] C. Li, D. Ebenstein, C. Xu, J. Chapman, D. Saloner, J. Rapp, L. Pruitt, *J. Biomed. Mater. Res.* **2003**, *64A*, 197.
[254] P. de Wolff, *Technisch Physische Dienst, Delft, The Netherlands*.
[255] S. Weiner, H. D. Wagner, *Annu. Rev. Mater. Sci.* **1998**, *28*, 271.
[256] H. McMurdie, *Powder Diff.* **1986**, *1*, 266.
[257] A. Bigi, E. Foresti, A. Incerti, A. Ripamonti, N. Roveri, *Inorg. Chim. Acta* **1980**, *55*, 81.
[258] T. Schinke, M. D. McKnee, G. Karsenty, *Nat. Genet.* **1999**, *21*, 150.
[259] W. Jahnen-Dechent, T. Schinke, A. Trindl, W. Muller-Esterl, F. Sablitzky, S. Kaiser, M. Blessing, *J. Biol. Chem.* **1997**, *272*, 31496.
[260] M. B. Tomson, G. H. Nancollas, *Science* **1978**, *200*, 1059.
[261] M. Iijima, H. Kamemizu, N. Wakamatsu, *J. Cryst. Growth* **1998**, *193*, 182.
[262] G. H. Nancollas, S. J. Zawacki, in *Industrial Crystallization* (Eds.: S. J. Jancic, E. J. de Jong), Elsevier, Amsterdam, **1984**, pp. 51.
[263] T. Umegaki, G. H. Nancollas, T. Kanzawa, *Memoirs of Faculty of Tech. Tokyo Metropolitan University* **1989**, *39*, 151.
[264] H. Gilman, D. W. L. Hukins, *J. Inorg. Biochem.* **1994**, *55*, 21.
[265] R. J. Park, F. C. Meldrum, *Adv. Mater.* **2002**, *14*, 1167.
[266] M. Iijima, Y. Moriwacki, R. Yamaguchi, Y. Kuboki, *Conn. Tiss. Res.* **1997**, *36*, 73.
[267] S. Busch, U. Schwarz, R. Kniep, *Chem. Mater.* **2001**, *13*, 260.
[268] O. Grassmann, G. Müller, P. Löbmann, *Chem. Mater.* **2002**, *14*, 4530.
[269] F. C. Meldrum, *Int. Mater. Rev.* **2003**, *48*, 187.
[270] P. E. Hare, *Science* **1963**, *139*, 216.
[271] Y. Kitano, D. W. Hood, *Geochim. Cosmochim. Acta* **1965**, *29*, 29.
[272] H. A. Lowenstam, *Science* **1981**, *211*, 1126.

[273] L. Addadi, J. Aizenberg, S. Albeck, G. Falini, S. Weiner, in *Supramolecular Stereochemistry* (Ed.: J. S. Siegel), Kluwer Academic Publishers, **1995**, pp. 127.
[274] L. Addadi, S. Weiner, *Mol. Cryst. Liq. Cryst.* **1986**, *134*, 305.
[275] L. Addadi, J. Moradian-Oldak, E. Shay, N. G. Maroudas, S. Weiner, *Proc. Natl. Acad. Sci. U.S.A.* **1987**, *84*, 2732.
[276] S. Albeck, L. Addadi, S. Weiner, *Conn. Tiss. Res.* **1996**, *35*, 365.
[277] S. Albeck, J. Aizenberg, L. Addadi, S. Weiner, *J. Amer. Chem. Soc.* **1993**, *115*, 11691.
[278] J. Aizenberg, S. Albeck, S. Weiner, L. Addadi, *J. Cryst. Growth* **1994**, *142*, 156.
[279] J. Aizenberg, M. Ilan, S. Weiner, L. Addadi, *Conn. Tiss. Res.* **1996**, *34*, 255.
[280] F. Manoli, E. Dalas, *J. Cryst. Growth* **2000**, *217*, 422.
[281] F. H. Shen, Q. L. Feng, C. M. Wang, *J. Cryst. Growth* **2002**, *242*, 239.
[282] S. Boggavarapu, J. Chang, P. Calvert, *Mat. Sci. Eng.* **2000**, *11C*, 47.
[283] A. Becker, W. Becker, J. C. Marxen, M. Epple, *Z. allg. anorg. Chem.* **2003**, *629*, 2305.
[284] F. Manoli, E. Dalas, *J. Cryst. Growth* **2000**, *217*, 416.
[285] D. H. Jin, Y. Zhang, Y. Suzuki, T. Nagunuma, T. Ogawa, E. Hatakeyama, K. Muramoto, *J. Agric. Food Chem.* **2000**, *48*, 5450.
[286] A. R. Hoch, M. M. Reddy, G. R. Aiken, *Geochim. Cosmochim. Acta* **2000**, *64*, 61.
[287] C. S. Sikes, M. L. Yeung, A. P. Wheeler, in *Surface Reactive Peptides and Polymers: Discovery and Commerzialisation* (Eds.: C. S. Sikes, A. P. Wheeler), American Chemical Society, **1991**, pp. 50.
[288] Y. W. Fan, F. Z. Cui, J. Ge, *Single Mol.* **2001**, *2*, 121.
[289] J. Kanakis, E. Dalas, *J. Cryst. Growth* **2000**, *219*, 277.
[290] V. Gerbaud, D. Pignol, E. Loret, J. A. Bertrand, Y. Berland, J. C. Fontecilla-Camps, J. P. Canselier, N. Gabas, J. M. Verdier, *J. Biol. Chem.* **2000**, *275*, 1057.
[291] S. Brown, *Nat. Biotechnol.* **1997**, *15*, 269.
[292] S. Brown, *Proc. Natl. Acad. Sci. U.S.A.* **1992**, *89*, 8651.
[293] C. F. Barbas, J. S. Rosenblum, R. A. Lerner, *Proc. Natl. Acad. Sci. U.S.A.* **1993**, *90*, 6385.
[294] K. Kjaergard, J. K. Sorensen, M. A. Schembri, P. Klemm, *Appl. Environ. Microbiol.* **2000**, *66*, 10.
[295] S. R. Whaley, D. S. English, E. L. Hu, P. F. Barbara, A. M. Belcher, *Nature* **2000**, *405*, 665.
[296] S. Nygaard, R. Wendelbo, S. Brown, *Adv. Mater.* **2002**, *14*, 1853.
[297] T. Sugawara, Y. Suwa, K. Ohkawa, H. Yamamoto, *Macromol. Rapid Commun.* **2003**, *24*, 847.
[298] C. A. Orme, A. Noy, A. Wierzbicki, M. T. McBride, M. Grantham, H. H. Teng, P. M. Dove, J. J. DeYoreo, *Nature* **2001**, *411*, 775.
[299] S. Mann, *Nature* **1988**, *132*, 119.
[300] S. Weiner, *Crit. Rev. Biochem. Mol. Biol.* **1986**, *20*, 365.
[301] A. M. Belcher, X. H. Wu, R. J. Christensen, P. K. Hansma, G. D. Stucky, D. E. Morse, *Nature* **1996**, *381*, 56.
[302] L. Treccani, S. Khoshnavaz, S. Blank, K. von Roden, U. Schulz, I. M. Weiss, K. Mann, M. Radmacher, M. Fritz, in *Biopolymers* (Ed.: A. Steinbüchl), Wiley VCH, Berlin, **2002**, pp. 289.
[303] O. Grassmann, P. Löbmann, *Biomaterials* **2003**, *25*, 277.
[304] O. Grassmann, P. Löbmann, *Chem. Eur. J.* **2003**, *9*, 1310.
[305] O. Grassmann, R. B. Neder, A. Putnis, P. Löbmann, *Am. Mineral.* **2003**, *88*, 647.
[306] G. Falini, S. Fermani, M. Gazzano, A. Ripamonti, *Chem. Eur. J.* **1998**, *4*, 1048.
[307] D. Volkmer, M. Fricke, T. Huber, N. Sewald, *Chem. Commun.* **2004**, 1872.
[308] A. P. Wheeler, C. S. Sikes, *Amer. Zool.* **1984**, *24*, 933.

[309] R. J. Park, F. C. Meldrum, *J. Mater. Chem.* **2004**, *14*, 2291.
[310] G. Falini, S. Fermani, A. Ripamonti, *J. Inorg. Biochem.* **2002**, *91*, 475.
[311] G. Falini, S. Fermani, M. Gazzano, A. Ripamonti, *J. Chem. Soc., Dalton Trans.* **2000**, 3983.
[312] K. J. Davis, P. M. Dove, J. J. DeYoreo, *Science* **2000**, *290*, 1134.
[313] D. M. Devery, A. J. Ehlmann, *Am. Mineral.* **1981**, *66*, 592.
[314] D. Kralj, J. Kontrec, L. Brecoeevic, G. Falini, V. Nöthig-Laslo, *Chem. Eur. J.* **2004**, *10*, 1647.
[315] M. M. Reddy, *J. Cryst. Growth* **1977**, *41*, 287.
[316] R. K. Pai, S. Hild, A. Ziegler, O. Marti, *Langmuir* **2004**, *20*, 3123.
[317] K. Ichikawa, N. Shimomura, M. Yamada, N. Ohkubo, *Chem. Eur. J.* **2003**, *9*, 3235.
[318] Y. Han, J. Aizenberg, *Angew. Chem.* **2003**, *115*, 3796.
[319] A. L. Litvin, L. A. Samuelson, D. H. Charynch, W. Spevak, D. L. Kaplan, *J. Phys. Chem.* **1995**, *99*, 492.
[320] J. Küther, R. Seshadri, W. Tremel, *Angew. Chem.* **1998**, *110*, 3196.
[321] K. Naka, Y. Tanaka, Y. Chujo, Y. Ito, *Chem. Commun.* **1999**, 1931.
[322] J. C. Marxen, Unversität Hamburg (Hamburg), **1995**.
[323] K. Bandel, in *Biomineralisation - Forschungsberichte, Vol. 10*, Akademie der Wissenschaften und der Literatur, Mainz, **1979**, p. 38.
[324] U. Bielefeld, W. Becker, *Int. J. Dev. Biol.* **1991**, *35*, 121.
[325] J. C. Marxen, P. E. Witten, D. Finke, O. Reelsen, M. Rezgaoui, W. Becker, *Invertebrate Biology* **2003**, *122*, 313.
[326] U. Bielefeld, K. Ziergold, K. H. Körtje, W. Becker, *Histochemical J.* **1992**, *24*, 927.
[327] J. C. Marxen, W. Becker, *Comp. Biochem. Physiol.* **1997**, *118B*, 23.
[328] J. C. Marxen, M. Hammer, T. Gehrke, W. Becker, *Biol. Bull.* **1998**, *194*, 231.
[329] J. C. Marxen, M. Nimtz, W. Becker, K. H. Mann, *Biochim. Biophys. Acta* **2003**, *1650*, 92.
[330] J. C. Marxen, W. Becker, *Comp. Biochem. Physiol.* **2000**, *127B*, 235.
[331] A. Becker, Diploma Thesis thesis, Ruhr-Universität Bochum (Bochum), **2002**.
[332] G. Falini, S. Fermani, M. Gazzano, A. Ripamonti, *Chem. Eur. J.* **1997**, *3*, 1807.
[333] Y. H. Shen, A. J. Xie, *J. Southeast University* **1998**, *28*, 182.
[334] E. Dalas, P. G. Klepetsanis, G. Koutsoukos, *J. Coll. Interf. Sci.* **2000**, *224*, 56.
[335] L. Yang, X. M. Ma, X. Y. Zhang, Y. M. Tang, K. Jang, J. M. Guo, *J. Chin. Chem.* **2002**, *49*, 45.
[336] M. Iijima, Y. Moriwacki, H. B. Wen, A. G. Fincham, J. Moradian-Oldak, *J. Dent. Res.* **2002**, *81*, 69.
[337] C. Vidal, G. Dewel, P. Borckhans, *Au delà de l'équilibre*, **1994**.
[338] E. Cussler, *Diffusion, Mass Transfer in Fluid Systems*, 2nd ed., Cambridge University Press, Cambridge, **1997**.
[339] B. Njegic, D. Kralj, G. Falini, L. Brecevic, in *Emerging Microscopy for Advanced Materials Development - Imaging and Spectroscopy on Atomic Scale*, Berlin, **2004**, p. conference abstract.
[340] K. C. Low, A. P. Wheeler, L. P. Koskan, in *Hydrophilic polymers: performance with enverionmental acceptance* (Ed.: J. E. Glass), ACS, Washington D.C., **1996**, pp. 99.
[341] W. Hater, in *Henkel Technologies - water treatment*, Düsseldorf, **2002**, pp. 1.
[342] H. P. Klug, L. E. Alexander, *X-ray diffraction procedures for polycrystalline and amorphous materials*, Wiley-Interscience, New York, **1974**.
[343] P. Scherrer, *Nachr. Ges. Wiss. Göttingen* **1918**, *2*, 98.
[344] H. M. Rietveld, *J. Appl. Crystallogr.* **1969**, *2*, 65.
[345] H. M. Rietveld, *Acta Crystallogr.* **1967**, *22*, 151.

[346] L. B. McCusker, R. B. von Dreele, D. E. Cox, D. Louer, P. Scardi, *J. Appl. Crystallogr.* **1999**, *32*, 36.
[347] A. Le Bail, H. Duroy, J. L. Fourquet, *Mater. Res. Bull.* **1988**, *23*, 447.
[348] R. J. Hill, C. J. Howard, *J. Appl. Crystallogr.* **1987**, *20*, 467.
[349] J. Rodriguez-Carvajal, *Abstracts of the Satellite Meeting on Powder Diffraction of the XV Congress of the IUCr, Toulouse, France* **1990**, 127.
[350] W. S. Sheldrick, 6.12 ed., Bruker ASX Inc., Madison, WI, USA, **2001**.
[351] S. Ebbinghaus, University of Hamburg (Hamburg), **1998**.
[352] P. J. Ellis, H. C. Freeman, *J. Synchrotron Rad.* **1995**, *2*, 190.
[353] S. I. Zabinsky, J. J. Rehr, A. Ankudinov, R. C. Albers, M. J. Eller, *Phys. Rev. B* **1995**, *52*, 2995.

8. Appendix

8.1 List of abbreviations

ACC	amorphous calcium carbonate
ACP	amorphous calcium phosphate
ASE	anterior sternal epithelium
ATP	adenosine-triphosphate
BSA	bovine serum albumin
CAP	carbonated apatite
DDW	double-distilled water
DESY	Deutsches Elektronen Synchrotron
dsl	distal spherular layer
EDTA	ethylenediaminetetraacetate
EDX	energy dispersive X-ray analysis
EXAFS	Extended X-ray Absorption Fine Structure
FWHM	Full Width at Half Maximum
GAG	glycosaminoglycane
HAP	hydroxyapatite
HASYLAB	Hamburger Synchrotron Laboratory
hl	homogeneous layer
ICDD	International Centre for Diffraction Data
IM	insoluble matrix
IN	interstitial network
LDL	low density lipids
MGP	matrix-Gla-protein
MWCO	molecular weight cut-off
pAsp	poly-L-aspartic acid
PG	proteoglycane
pGlu	poly-L-glutamic acid
pLys	poly-L-lysine
psl	proximal spherular layer
SEM	scanning electron microscopy
SM	soluble matrix
TEM	transmission electron microsocopy
TCP	tricalcium phosphate
TGA	thermogravimetric analysis
XRD	(powder) X-ray diffractometry

8.2 Determination of magnesium in calcite by analysis of the cell parameters according to Goldsmith *et al.*[80]

Goldsmith *et al.* correlated the length of the elementary cell's axes of calcite with the content of magnesium in the mineral. As outlined in chapter 2.2, calcite crystallises in the rhombohedral space group $R\,\bar{3}c$ (No. 167) with a=b=4.9896 Å, c=17.061 Å, α=β=90°, and γ=120°.[73] The values for a and c decrease with increasing content in magnesium, expressed as "magnesium carbonate" [mol%]. Goldsmith *et al.* determined the cell constants with three different methods on four samples of different magnesium carbonate content, determined by AAS:

$MgCO_3$ mol%	***a*-axis Å**				***c*-axis Å**			
	1	**2**	**3**	**aver.**	**1**	**2**	**3**	**aver.**
0.00	-	-	-	4.9899	-	-	-	17.0640
4.94	4.9676	4.9679	4.9679	4.9678	16.9510	16.9520	16.9500	16.9510
9.89	4.9428	4.9448	4.9435	4.9437	16.8520	16.8450	16.8500	16.8490
14.83	4.9216	4.9213	4.9219	4.9216	16.7350	16.7360	16.7350	16.7353
19.78	4.9022	-	-	4.9022	16.6360	-	-	16.6360

The average of the values determined for each magnesium content and the database entry for calcite as zero point allow a linear regression and the determination of formulae to calculate magnesium contents from cell constants (see figure 8.2-1). The relation of a_0 to magnesium content can be expressed as

$$y = -222.86 \cdot x + 1112 \quad (R^2=0.9987) \qquad \text{(eq. 9.2-1)}$$

with y being the content of magnesium carbonate [mol%] and x the length of the a-axis of magnesium calcite [Å]. The relation of c_0 to the magnesium content follows the formula

$$y = -46.112 \cdot x + 786.9 \quad (R^2=0.9995) \qquad \text{(eq. 9.2-2)}$$

with *y* being again the content of magnesium carbonate [mol%] and *x* the length of the *c*-axis of magnesium calcite [Å].

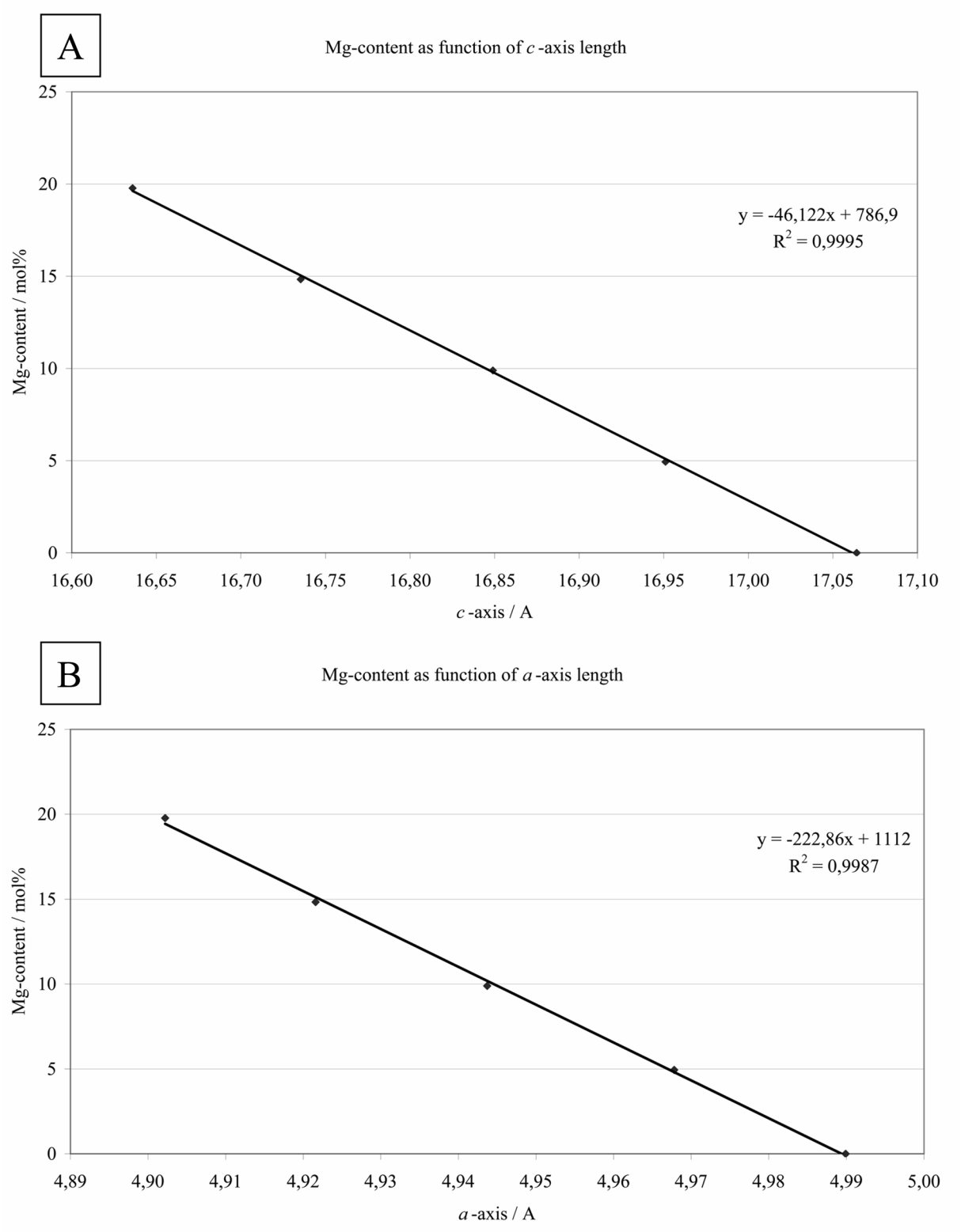

Fig. 8.2-1: The relation of the cell constants of calcite (above a_0, below c_0) and the content of magnesium according to Goldsmith *et al.* A clear linear correlation can be seen.

8.3 List of data obtained from single crystal structure refinement of a statolith of *Aurelia aurita*

Table 8.3-1: Crystal data and structure refinement for the statolith of *Aurelia aurita* obtained with the SHELXTL program.

Identification code	au2all	Crystal system	monoclinic
Empirical formula	Ca $O_{4.67}$ S	Space group	*C* 2
Formula weight	146.81 Da	Unit cell dimensions	*a*=12.1229(8) Å
Density (calculated)	2.698 g cm^{-3}		*b*=6.9928(8) Å
F(000)	440		*c*=6.3959(4) Å
Temperature	297 K		*α*=90°
Crystal size	20 x 8 x 8 µm		*β*=90.032(3)°
Crystal color	clear		*γ*=90°
Crystal description	block	Volume	542.20(8) $Å^3$
Wavelength	0.50000 Å	Z	6

Table 8.3-2: Experimental conditions

Diffractometer control software	HASYLAB Runtime, Bruker AXS SMART Version 5.054
Diffractometer measurement device	HASYLAB Beamline F1
Diffractometer measurement method	Fullsphere data collection in omega at 0.3° scan width two runs with 720 frames, phi = 0°, 270° and two runs with 436 frames, phi = 88°, 180°
Diffractometer measurement method	Data collection in omega at 0.3° scan width one run with 740 frames, phi = 0°, chi = 0°
Theta range for data collection	2.24° to 33.16°
Completeness to theta	= 33.16° 94.1 %
Index ranges	-25<=*h*<=25, -14<=*k*<=14, -8<=*l*<=13
Computing data reduction	Bruker AXS SAINT program Vers. 6.02A
Absorption coefficient	1.111 mm^{-1}
Computing absorption correction	Bruker AXS SADABS program multiscan V2.03
Absorption correction details	R.H. Blessing, Acta Cryst. (1995) A51 33-38
Computing structure solution	Bruker AXS SHELXTL Vers. 6.12
Computing structure refinement	Bruker AXS SHELXTL Vers. 6.12
Refinement method	Full-matrix least-squares on F^2
Reflections collected	11466
Independent reflections	5082 [*R*(int) = 0.0609]

Data / restraints / parameters	2963 / 1 / 101
Goodness-of-fit on F^2	1.028
Weighting details	w = 1/[σ^2 (F_0^2)+ (0.0400*P)^2+2.0000*P], where P = (F_0^2+2Fc^2)/3
Final R indices [I>2σ(I)]	R1 = 0.0717, wR2 = 0.1633
R indices (all data)	R1 = 0.1306, wR2 = 0.1937
Absolute structure parameter	0.19(13)
Absolute structure details	Flack H.D., Acta Cryst. A39 (1983) 876-881
Largest diffraction peak and hole	1.358 and -1.563 eÅ^{-3}

Table 8.2-3: Atomic coordinates (x 10^4) and equivalent isotropic displacement parameters (Å^2 x 10^3) for the project. U(eq) is defined as one third of the trace of the orthogonalised U_{ij} tensor.

Atom	x	y	z	U(eq)
Ca(1)	0	3691(2)	0	23(1)
Ca(2)	2727(1)	5511(1)	3334(1)	24(1)
O(1W)	48(12)	7308(17)	9434(15)	59(3)
O(2W)	483(6)	8728(13)	6650(20)	74(4)
S(1)	2251(1)	10489(1)	1669(1)	12(1)
S(2)	0	3733(2)	5000	12(1)
O(1)	3166(3)	10121(5)	220(4)	31(1)
O(2)	2520(3)	12046(5)	3124(4)	31(1)
O(3)	2018(2)	8796(5)	2979(5)	33(1)
O(4)	1291(3)	10980(5)	360(5)	34(1)
O(5)	644(2)	2540(6)	6447(4)	31(1)
O(6)	732(3)	4932(5)	3694(5)	33(1)

Table 8.3-4: Bond lengths [Å] and angles [°] determined.

Ca(1)-O(1)#1	2.442(3)	O(1)#1-Ca(1)-O(5)#6	117.56(9)
Ca(1)-O(1)#2	2.442(3)	O(1)#2-Ca(1)-O(5)#6	78.32(10)
Ca(1)-O(4)#3	2.469(4)	O(4)#3-Ca(1)-O(5)#6	69.15(11)
Ca(1)-O(4)#4	2.469(4)	O(4)#4-Ca(1)-O(5)#6	82.41(12)
Ca(1)-O(5)#5	2.535(3)	O(5)#5-Ca(1)-O(5)#6	142.95(19)
Ca(1)-O(5)#6	2.535(3)	O(1)#1-Ca(1)-O(1W)#6	67.9(3)
Ca(1)-O(1W)#6	2.555(12)	O(1)#2-Ca(1)-O(1W)#6	64.3(3)
Ca(1)-O(1W)#5	2.555(12)	O(4)#3-Ca(1)-O(1W)#6	139.4(3)
Ca(1)-O(6)	2.669(4)	O(4)#4-Ca(1)-O(1W)#6	139.6(3)
Ca(1)-O(6)#7	2.669(4)	O(5)#5-Ca(1)-O(1W)#6	116.6(2)
Ca(1)-S(2)	3.1981(2)	O(5)#6-Ca(1)-O(1W)#6	100.4(2)
Ca(1)-S(2)#5	3.1981(2)	O(1)#1-Ca(1)-O(1W)#5	64.3(3)
Ca(2)-O(5)#8	2.435(3)	O(1)#2-Ca(1)-O(1W)#5	67.9(3)
Ca(2)-O(2)#4	2.439(4)	O(4)#3-Ca(1)-O(1W)#5	139.6(3)
Ca(2)-O(6)	2.463(3)	O(4)#4-Ca(1)-O(1W)#5	139.4(3)
Ca(2)-O(3)	2.463(4)	O(5)#5-Ca(1)-O(1W)#5	100.4(2)
Ca(2)-O(2W)#9	2.503(8)	O(5)#6-Ca(1)-O(1W)#5	116.6(2)
Ca(2)-O(2)#9	2.525(3)	O(1W)#6-Ca(1)-O(1W)#5	16.5(4)
Ca(2)-O(1)#1	2.532(3)	O(1)#1-Ca(1)-O(6)	67.38(9)
Ca(2)-O(3)#9	2.664(4)	O(1)#2-Ca(1)-O(6)	96.79(11)
Ca(2)-O(4)#1	2.667(4)	O(4)#3-Ca(1)-O(6)	122.88(11)
Ca(2)-S(1)#9	3.1966(10)	O(4)#4-Ca(1)-O(6)	87.52(10)
Ca(2)-S(1)#1	3.1996(10)	O(5)#5-Ca(1)-O(6)	142.62(9)
Ca(2)-Ca(2)#8	4.1317(8)	O(5)#6-Ca(1)-O(6)	53.99(9)
O(1W)-O(1W)#10	0.733(19)	O(1W)#6-Ca(1)-O(6)	63.9(3)
O(1W)-Ca(1)#11	2.555(12)	O(1W)#5-Ca(1)-O(6)	78.2(3)
O(2W)-Ca(2)#8	2.503(8)	O(1)#1-Ca(1)-O(6)#7	96.79(11)
S(1)-O(1)	1.469(3)	O(1)#2-Ca(1)-O(6)#7	67.38(9)
S(1)-O(2)	1.469(3)	O(4)#3-Ca(1)-O(6)#7	87.52(10)
S(1)-O(4)	1.474(3)	O(4)#4-Ca(1)-O(6)#7	122.88(11)
S(1)-O(3)	1.477(3)	O(5)#5-Ca(1)-O(6)#7	53.99(9)
S(1)-Ca(2)#8	3.1966(10)	O(5)#6-Ca(1)-O(6)#7	142.62(9)
S(1)-Ca(2)#12	3.1996(10)	O(1W)#6-Ca(1)-O(6)#7	78.2(3)
S(2)-O(5)#6	1.470(3)	O(1W)#5-Ca(1)-O(6)#7	63.9(3)
S(2)-O(5)	1.470(3)	O(6)-Ca(1)-O(6)#7	142.04(16)
S(2)-O(6)#6	1.480(3)	O(1)#1-Ca(1)-S(2)	93.11(6)
S(2)-O(6)	1.480(3)	O(1)#2-Ca(1)-S(2)	86.45(6)
S(2)-Ca(1)#11	3.1981(2)	O(4)#3-Ca(1)-S(2)	95.74(9)
O(1)-Ca(1)#13	2.442(3)	O(4)#4-Ca(1)-S(2)	85.08(9)
O(1)-Ca(2)#12	2.532(3)	O(5)#5-Ca(1)-S(2)	154.11(8)
O(2)-Ca(2)#14	2.439(4)	O(5)#6-Ca(1)-S(2)	26.65(7)
O(2)-Ca(2)#8	2.525(3)	O(1W)#6-Ca(1)-S(2)	81.3(2)
O(3)-Ca(2)#8	2.664(4)	O(1W)#5-Ca(1)-S(2)	97.6(2)
O(4)-Ca(1)#14	2.469(4)	O(6)-Ca(1)-S(2)	27.36(6)
O(4)-Ca(2)#12	2.667(4)	O(6)#7-Ca(1)-S(2)	151.90(7)
O(5)-Ca(2)#9	2.435(3)	O(1)#1-Ca(1)-S(2)#5	86.45(6)
O(5)-Ca(1)#11	2.535(3)	O(1)#2-Ca(1)-S(2)#5	93.11(6)
		O(4)#3-Ca(1)-S(2)#5	85.08(9)
O(1)#1-Ca(1)-O(1)#2	131.7(2)	O(4)#4-Ca(1)-S(2)#5	95.74(9)
O(1)#1-Ca(1)-O(4)#3	152.39(13)	O(5)#5-Ca(1)-S(2)#5	26.65(7)
O(1)#2-Ca(1)-O(4)#3	75.10(12)	O(5)#6-Ca(1)-S(2)#5	154.11(8)
O(1)#1-Ca(1)-O(4)#4	75.10(12)	O(1W)#6-Ca(1)-S(2)#5	97.6(2)
O(1)#2-Ca(1)-O(4)#4	152.39(13)	O(1W)#5-Ca(1)-S(2)#5	81.3(2)
O(4)#3-Ca(1)-O(4)#4	79.67(16)	O(6)-Ca(1)-S(2)#5	151.90(7)
O(1)#1-Ca(1)-O(5)#5	78.32(10)	O(6)#7-Ca(1)-S(2)#5	27.36(6)
O(1)#2-Ca(1)-O(5)#5	117.56(9)	S(2)-Ca(1)-S(2)#5	178.94(7)
O(4)#3-Ca(1)-O(5)#5	82.41(12)	O(5)#8-Ca(2)-O(2)#4	131.69(14)
O(4)#4-Ca(1)-O(5)#5	69.15(11)	O(5)#8-Ca(2)-O(6)	152.44(14)

O(2)#4-Ca(2)-O(6)	74.98(12)
O(5)#8-Ca(2)-O(3)	75.22(13)
O(2)#4-Ca(2)-O(3)	152.29(12)
O(6)-Ca(2)-O(3)	79.59(11)
O(5)#8-Ca(2)-O(2W)#9	65.6(2)
O(2)#4-Ca(2)-O(2W)#9	66.1(2)
O(6)-Ca(2)-O(2W)#9	140.28(19)
O(3)-Ca(2)-O(2W)#9	140.13(19)
O(5)#8-Ca(2)-O(2)#9	78.30(11)
O(2)#4-Ca(2)-O(2)#9	117.35(10)
O(6)-Ca(2)-O(2)#9	82.48(12)
O(3)-Ca(2)-O(2)#9	69.19(11)
O(2W)#9-Ca(2)-O(2)#9	108.1(3)
O(5)#8-Ca(2)-O(1)#1	117.43(10)
O(2)#4-Ca(2)-O(1)#1	78.44(11)
O(6)-Ca(2)-O(1)#1	69.32(10)
O(3)-Ca(2)-O(1)#1	82.45(12)
O(2W)#9-Ca(2)-O(1)#1	108.7(3)
O(2)#9-Ca(2)-O(1)#1	143.17(13)
O(5)#8-Ca(2)-O(3)#9	96.76(11)
O(2)#4-Ca(2)-O(3)#9	67.27(10)
O(6)-Ca(2)-O(3)#9	87.51(10)
O(3)-Ca(2)-O(3)#9	122.80(10)
O(2W)#9-Ca(2)-O(3)#9	70.8(3)
O(2)#9-Ca(2)-O(3)#9	53.89(9)
O(1)#1-Ca(2)-O(3)#9	142.73(11)
O(5)#8-Ca(2)-O(4)#1	67.47(9)
O(2)#4-Ca(2)-O(4)#1	96.86(11)
O(6)-Ca(2)-O(4)#1	122.83(10)
O(3)-Ca(2)-O(4)#1	87.68(11)
O(2W)#9-Ca(2)-O(4)#1	71.2(3)
O(2)#9-Ca(2)-O(4)#1	142.73(11)
O(1)#1-Ca(2)-O(4)#1	53.76(8)
O(3)#9-Ca(2)-O(4)#1	142.02(11)
O(5)#8-Ca(2)-S(1)#9	86.50(7)
O(2)#4-Ca(2)-S(1)#9	92.92(7)
O(6)-Ca(2)-S(1)#9	85.03(8)
O(3)-Ca(2)-S(1)#9	95.71(8)
O(2W)#9-Ca(2)-S(1)#9	89.2(3)
O(2)#9-Ca(2)-S(1)#9	26.59(7)
O(1)#1-Ca(2)-S(1)#9	154.23(7)
O(3)#9-Ca(2)-S(1)#9	27.31(7)
O(4)#1-Ca(2)-S(1)#9	152.01(7)
O(5)#8-Ca(2)-S(1)#1	93.04(7)
O(2)#4-Ca(2)-S(1)#1	86.62(7)
O(6)-Ca(2)-S(1)#1	95.83(8)
O(3)-Ca(2)-S(1)#1	85.15(8)
O(2W)#9-Ca(2)-S(1)#1	89.7(3)
O(2)#9-Ca(2)-S(1)#1	154.20(8)
O(1)#1-Ca(2)-S(1)#1	26.57(6)
O(3)#9-Ca(2)-S(1)#1	151.91(8)
O(4)#1-Ca(2)-S(1)#1	27.21(6)
S(1)#9-Ca(2)-S(1)#1	178.89(5)
O(5)#8-Ca(2)-Ca(2)#8	65.52(9)
O(2)#4-Ca(2)-Ca(2)#8	148.77(9)
O(6)-Ca(2)-Ca(2)#8	87.69(9)
O(3)-Ca(2)-Ca(2)#8	37.98(8)
O(2W)#9-Ca(2)-Ca(2)#8	122.3(3)
O(2)#9-Ca(2)-Ca(2)#8	33.02(8)
O(1)#1-Ca(2)-Ca(2)#8	119.81(10)
O(3)#9-Ca(2)-Ca(2)#8	86.54(8)
O(4)#1-Ca(2)-Ca(2)#8	114.36(8)
S(1)#9-Ca(2)-Ca(2)#8	59.29(3)
S(1)#1-Ca(2)-Ca(2)#8	121.41(3)
O(1W)#10-O(1W)-Ca(1)#11	81.8(2)
O(1)-S(1)-O(2)	111.2(2)
O(1)-S(1)-O(4)	106.2(2)
O(2)-S(1)-O(4)	111.2(2)
O(1)-S(1)-O(3)	111.2(2)
O(2)-S(1)-O(3)	106.1(2)
O(4)-S(1)-O(3)	110.98(18)
O(1)-S(1)-Ca(2)#8	128.74(14)
O(2)-S(1)-Ca(2)#8	50.29(14)
O(4)-S(1)-Ca(2)#8	124.95(16)
O(3)-S(1)-Ca(2)#8	55.82(15)
O(1)-S(1)-Ca(2)#12	50.45(13)
O(2)-S(1)-Ca(2)#12	128.90(14)
O(4)-S(1)-Ca(2)#12	55.82(16)
O(3)-S(1)-Ca(2)#12	124.95(16)
Ca(2)#8-S(1)-Ca(2)#12	178.89(5)
O(5)#6-S(2)-O(5)	110.8(3)
O(5)#6-S(2)-O(6)#6	111.01(19)
O(5)-S(2)-O(6)#6	106.6(2)
O(5)#6-S(2)-O(6)	106.6(2)
O(5)-S(2)-O(6)	111.01(19)
O(6)#6-S(2)-O(6)	111.0(3)
O(5)#6-S(2)-Ca(1)#11	128.60(14)
O(5)-S(2)-Ca(1)#11	50.63(13)
O(6)#6-S(2)-Ca(1)#11	55.98(15)
O(6)-S(2)-Ca(1)#11	124.75(15)
O(5)#6-S(2)-Ca(1)	50.63(13)
O(5)-S(2)-Ca(1)	128.60(14)
O(6)#6-S(2)-Ca(1)	124.75(15)
O(6)-S(2)-Ca(1)	55.98(15)
Ca(1)#11-S(2)-Ca(1)	178.94(7)
S(1)-O(1)-Ca(1)#13	142.77(18)
S(1)-O(1)-Ca(2)#12	102.98(16)
Ca(1)#13-O(1)-Ca(2)#12	112.42(9)
S(1)-O(2)-Ca(2)#14	142.55(19)
S(1)-O(2)-Ca(2)#8	103.12(19)
Ca(2)#14-O(2)-Ca(2)#8	112.65(11)
S(1)-O(3)-Ca(2)	137.1(2)
S(1)-O(3)-Ca(2)#8	96.87(19)
Ca(2)-O(3)-Ca(2)#8	107.33(10)
S(1)-O(4)-Ca(1)#14	137.1(2)
S(1)-O(4)-Ca(2)#12	96.98(18)
Ca(1)#14-O(4)-Ca(2)#12	107.17(11)
S(2)-O(5)-Ca(2)#9	142.86(17)
S(2)-O(5)-Ca(1)#11	102.72(18)
Ca(2)#9-O(5)-Ca(1)#11	112.56(10)
S(2)-O(6)-Ca(2)	137.3(2)
S(2)-O(6)-Ca(1)	96.66(18)
Ca(2)-O(6)-Ca(1)	107.27(9)

Table 8.3-5: Symmetry transformations used to generate equivalent atoms

#1 -x+1/2,y-1/2,-z	#2 x-1/2,y-1/2,z	#3 -x,y-1,-z	#4 x,y-1,z
#5 x,y,z-1	#6 -x,y,-z+1	#7 -x,y,-z	#8 -x+1/2,y+1/2,-z+1
#9 -x+1/2,y-1/2,-z+1	#10 -x,y,-z+2	#11 x,y,z+1	#12 -x+1/2,y+1/2,-z
#13 x+1/2,y+1/2,z	#14 x,y+1,z		

Table 8.3-6: Anisotropic displacement parameters ($Å^2 x\ 10^3$) for au2all. The anisotropic displacement factor exponent takes the form: $-2\sigma^2 [h^2 a^{*2} U11 + ... + 2 h k a^* b^* U12]$

atom	**U_{11}**	**U_{22}**	**U_{33}**	**U_{23}**	**U_{13}**	**U_{12}**
Ca(1)	17(1)	41(1)	10(1)	0	0(1)	0
Ca(2)	37(1)	23(1)	10(1)	0(1)	0(1)	-11(1)
O(1W)	54(5)	60(5)	63(8)	7(5)	-4(7)	-8(6)
O(2W)	20(3)	18(3)	184(11)	-28(5)	15(4)	3(2)
S(1)	16(1)	13(1)	8(1)	3(1)	-1(1)	2(1)
S(2)	13(1)	16(1)	8(1)	0	4(1)	0
O(1)	40(2)	38(2)	14(1)	5(1)	12(1)	20(1)
O(2)	54(2)	24(1)	14(1)	-9(1)	-9(1)	12(1)
O(3)	31(1)	36(2)	33(1)	26(1)	-6(1)	-8(1)
O(4)	28(1)	39(2)	34(2)	19(1)	-19(1)	-6(1)
O(5)	21(1)	58(2)	15(1)	15(1)	-1(1)	8(1)
O(6)	40(2)	25(1)	33(1)	7(1)	26(1)	-1(1)

8.4 The multi-CCDD device

8.4.1 Construction plans

The construction of the multi-CCDD device was done in cooperation with Armin Lindner (University of Bochum). The device consists of over 300 movable parts, excluding tubes, pumps, and vessels. Figure 8.4-1A shows those parts before unpacking whereas Figure 8.4-1B shows the device installed with all tubes. Table 8.4-1 lists all parts of the device. Figures 8.4-2 to 8.4-6 show the detailed construction plan of the crystallisation compartment and the two-part box holding and feeding the crystallisation compartment with ion solutions. Technical drawings were made with the CAD program "Autodesk Inventor 7.0" and follow the German DIN regulations.

Table 8.4-1: Detailed list of integral parts of the multi-CCDD device. Not included are materials for temperature control or inert atmosphere.

Part	type	number	part	type	number
compartments	constructed item	12	tubes, 0.2 m	Tygon 0.95 mm	24
compartment rings	constructed item	24	tubes, 0.6 m	Tygon 0.95 mm	24
compartment boxes	constructed item	24	tubes, 2.0 m	Tygon 0.95 mm	32
Gaskets	d_i=20mm, d=1mm	24	tubes, pumping	Tygon 0.95 mm	32
screws, large	M4x40, A2 / 912	72	tubes, 0.02 m	Tygon 1.20 mm	104
screws, small	M1.6x5, A2 / 963	144	peristaltic pumps	Ismatec RA 4/8	2
Racks	constructed item	3	peristaltic pump	Ismatec BVP 24	1
rack supports	constructed item	6	stirrers	IKA-Werk RW20	2

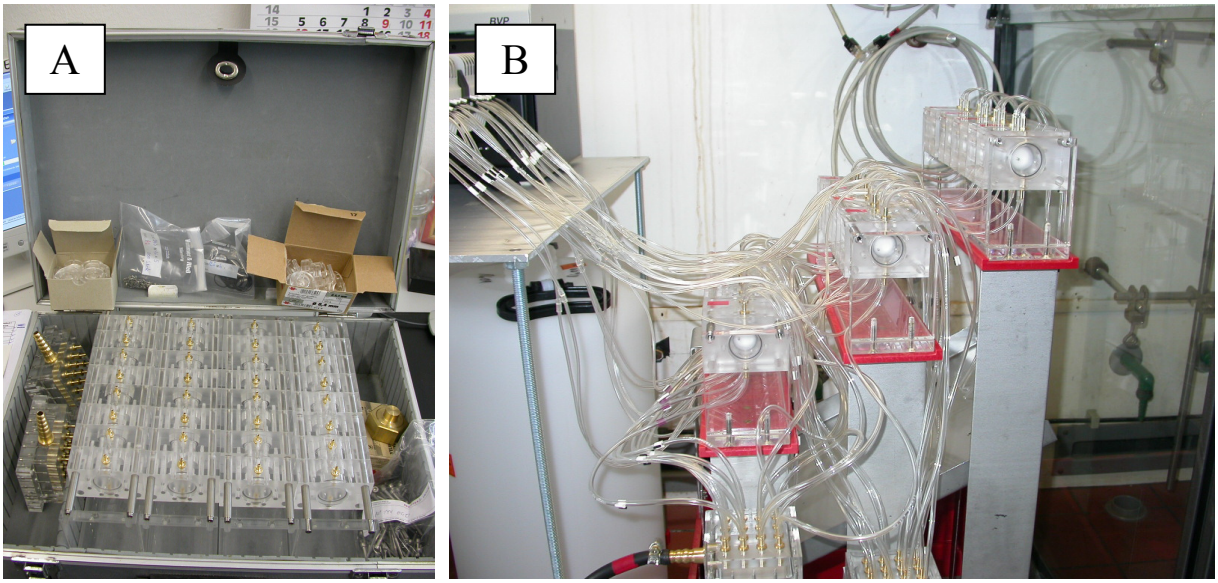

Figure 8.4-1: A: all movable parts of the device before unpacking and installing. B: the installed device with all three racks holding four compartment boxes each.

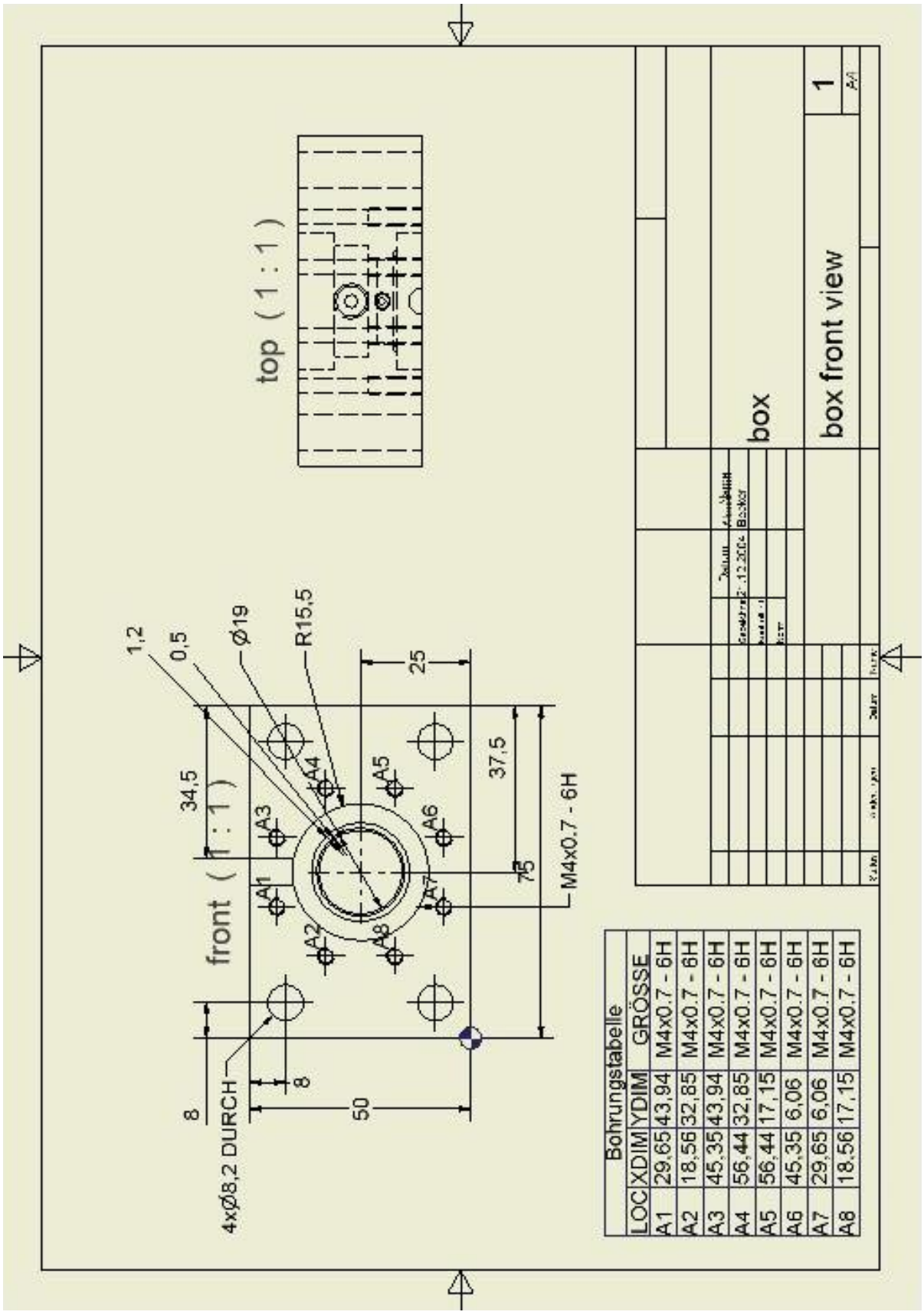

Figure 8.4-2: The compartment-holding box from the inside. The central deepenings are to hold the crystallisation compartment. In the front view, hidden lines are not shown, in the top view measurements are not shown for clarity. All values are given in millimetres. The scale of drawings is 1:1 on a full A4 page.

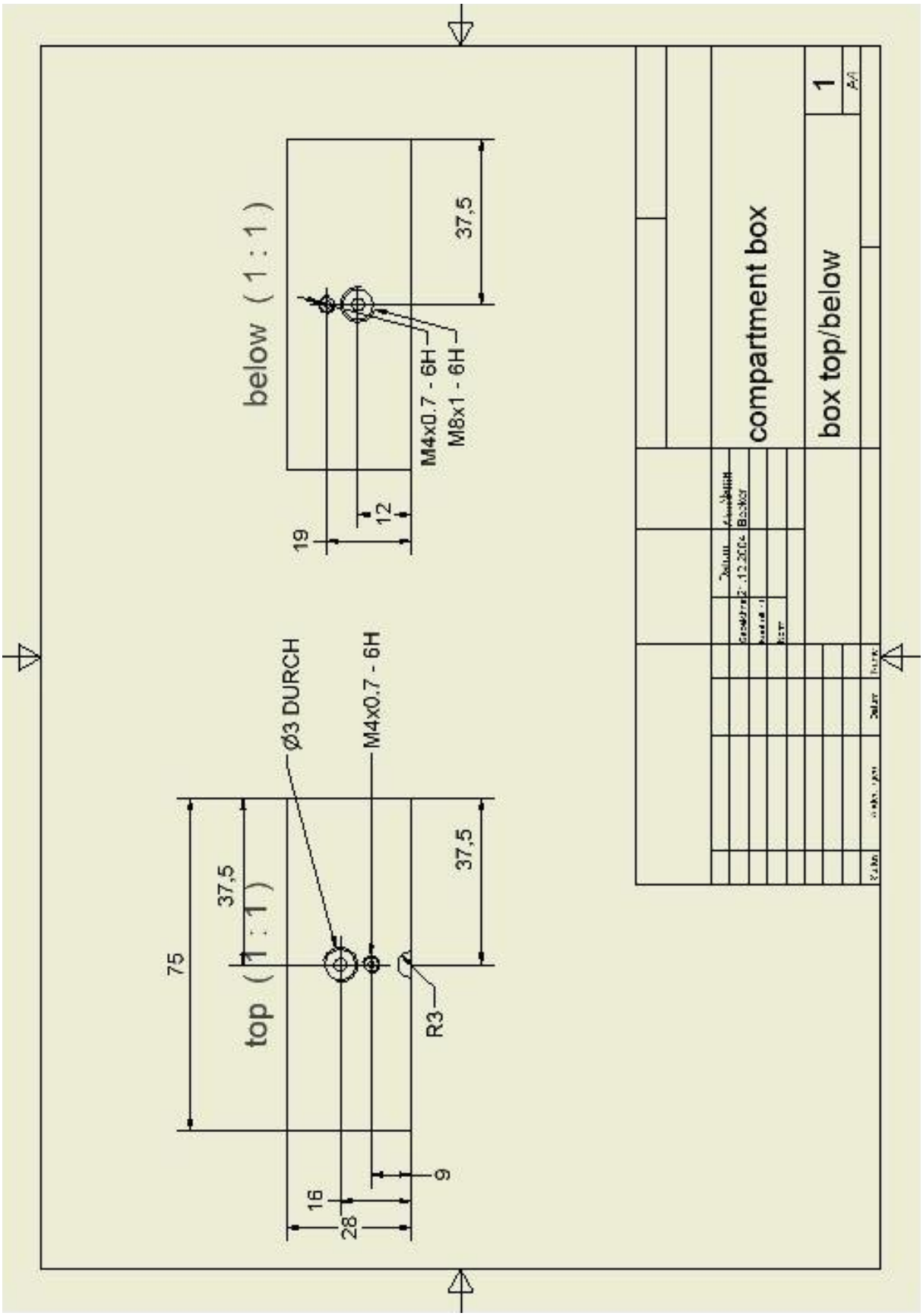

Figure 8.4-3: View of the compartment box from top and below without hidden lines. All values are given in millimetres. The scale of drawings is 1:1 on a full A4 page.

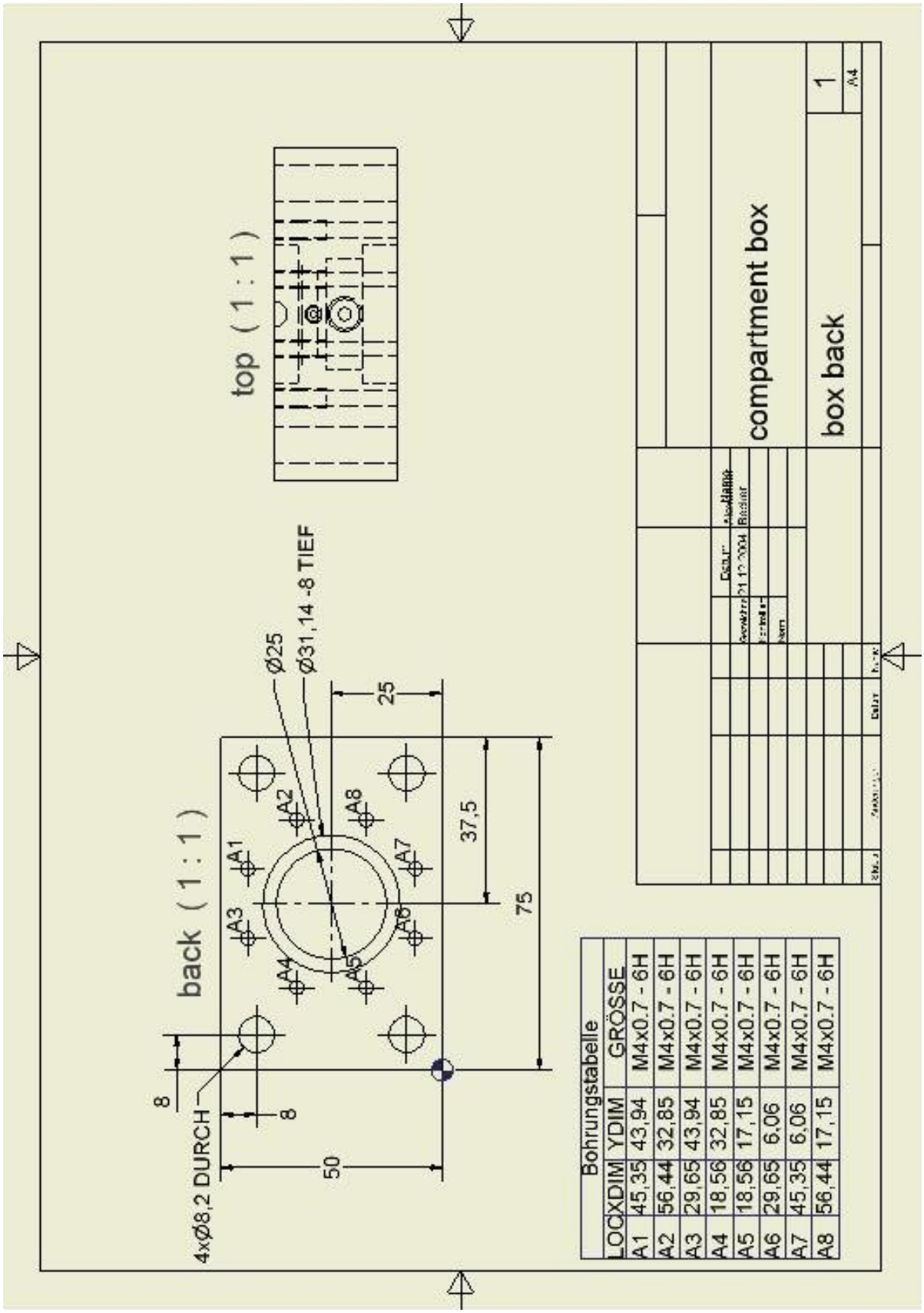

Figure 8.4-4: The compartment holding box from the outside. The central deepenings here are for holding heating water. In the front view, hidden lines are not shown, in the top view measurements are not shown for clarity. All values are given in millimetres. The scale of drawings is 1:1 on a full A4 page.

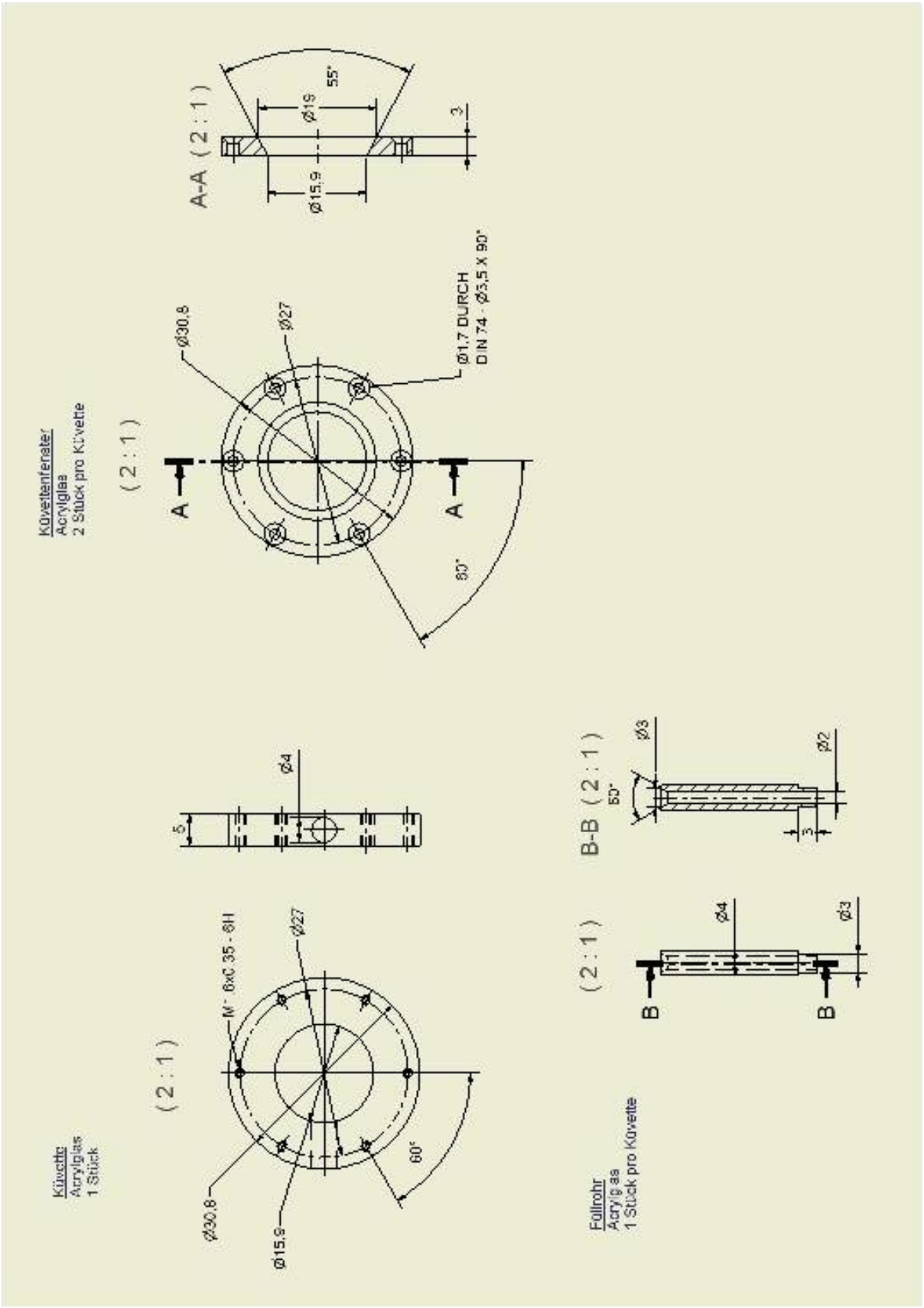

Figure 8.4-5: The crystallisation compartment consisting of the central core with short rifle for filling and two rings. Between core and ring at each side, the membranes are held. All values are given in millimetres. The scale of drawings is 2:1 on a full A4 page. Drawing by A. Lindner.

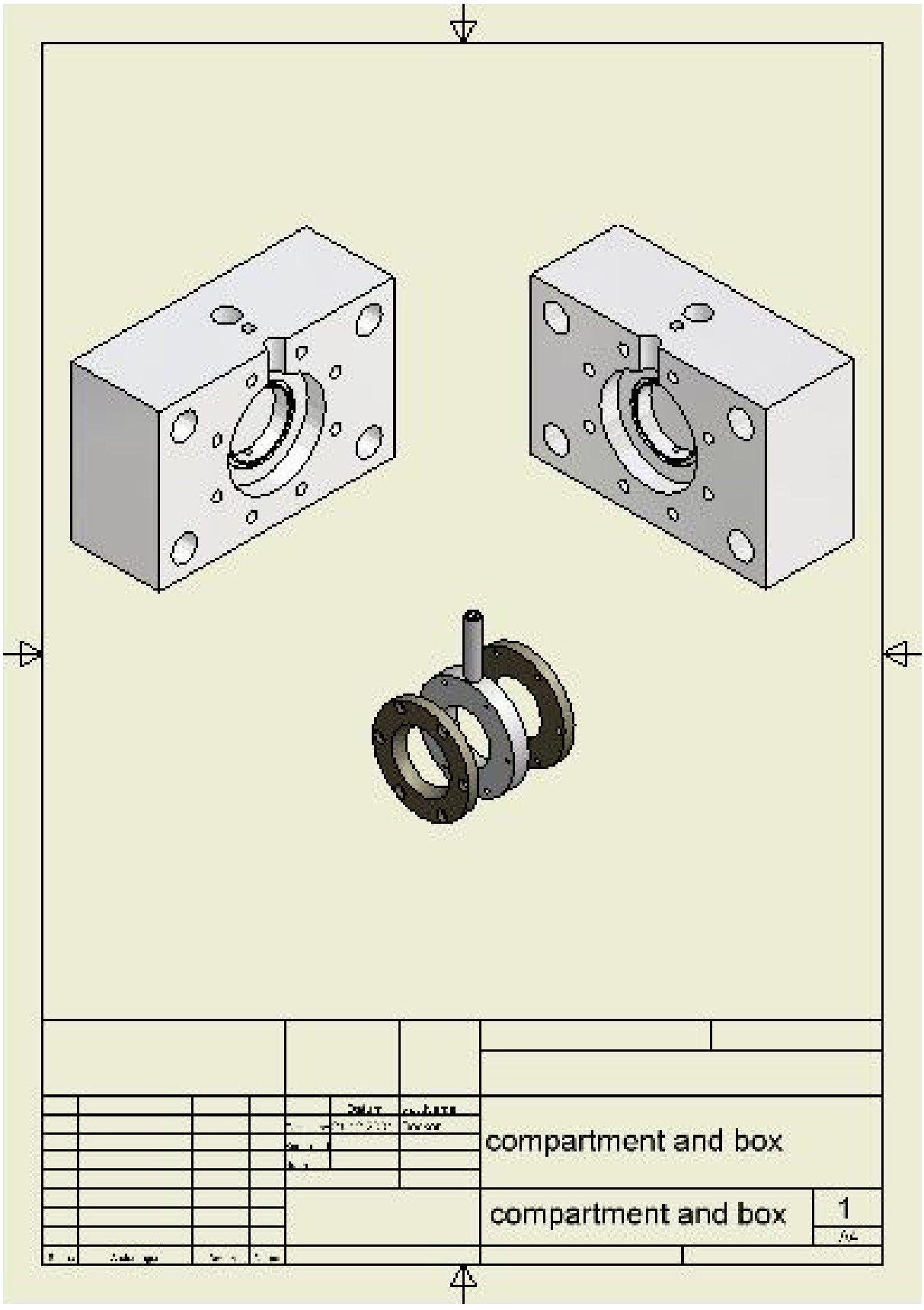

Figure 8.4-6: Isometric view on a holding box consisting of two parts and the crystallisation compartment consisting of three parts to be held in the box. The scale of drawings is 1:1 on a full A4 page.

8.4.2 Achieving computer control

Constant composition is achieved by computer control. The pH values of the feeding solutions are monitored and base and double-concentrated ion solution are added if the value drops below a threshold. Computer control was programmed with the program “VisiDAQ Genie 3.11”. It allows direct communication with interfaces and peripheral devices such as digital/analogous-interpreter cards and pH meters.

VisiDAQ programs are called *strategies* and are divided into *tasks* which constitute the actual programs created by the programmer and *displays* which are screen images with input and output modules also designed by the programmer. A strategy can contain several tasks and displays. If a strategy is run, the first task will run while the first display is shown. From the main task, other subroutines (tasks) can be evoked and stopped. Each task is executed repeatedly until stopped by script command or the user. The program is executed and repeated a certain time later again. This *scan period time* can be defined by the user.

Programming in tasks depends on icons called blocks representing routines executed by the VisiDAQ program. It assigns protocols and programs necessary for communication with hardware and operating system without the involvement of the user. E.g. the block responsible for communication with a peripheral device attached to the serial port handles all actual system communication between VisiDAQ, operating system and device. The values obtained by this communication can be used for processing in a task of a strategy. Program blocks can be programmed by the user in C++ or Visual Basic for processing.

The VisiDAQ strategy controlling the multi-CCDD device was simply called “multi”. It consists of five tasks and three displays. Except for the main task (task-1) and the calibration value loading task (task-2), all tasks are inactive when running the strategy and activated by script command depending on user

action. The task names, task jobs and scan period times are listed in Table 8.4-2. The ideal scan period time for the actual control task was found to be two seconds, because the pH-meters do not react faster in communication attempts.

Table 8.4-2: List of the tasks, the task jobs and the scan period times of the CCDD control strategy „multi".

task #	task job	scan period
task 1	main control, value definition	0.5 s
task 2	loading calibration values	1.0 s
task 3	actual CC program	2.0 s
task 4	activation of pumps for tube filling	0.5 s
task 5	stop of pumping	0.5 s

Figure 8.4-7 shows the main displays of the strategy "multi". It shows the main display (A) where the user defines the filling volume of the reservoir vessels, the flow of the feeding solutions, and the pH values in each vessel to be held constant. This display shows the calibration values loaded for processing. It also offers the possibility to activate the peristaltic pumps outside the CC program in order to fill the tubes for preparation. The control menu allows a change to other displays. The actual CC program display is shown in Figure B. It shows the

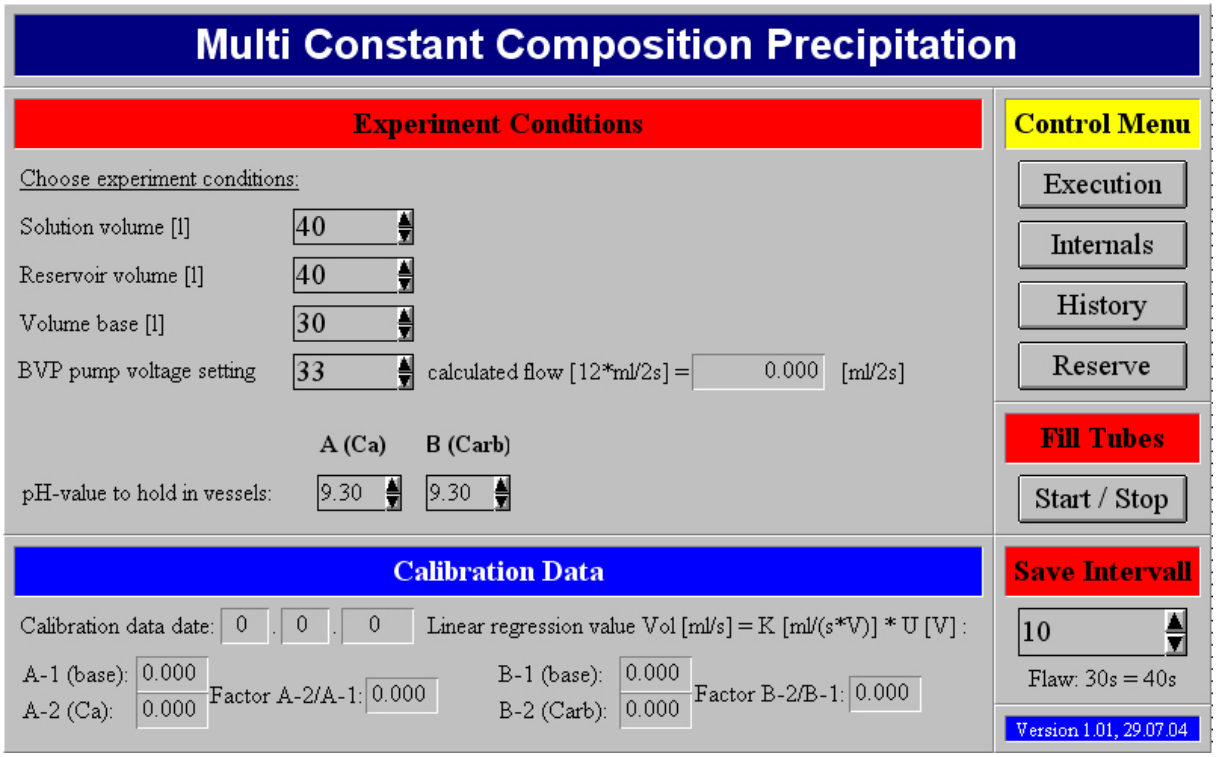

Fig. 8.4-7: Main display of the VisiDAQ-strategy "multi". Here, the user defines the start values of volumes and the pH to hold.

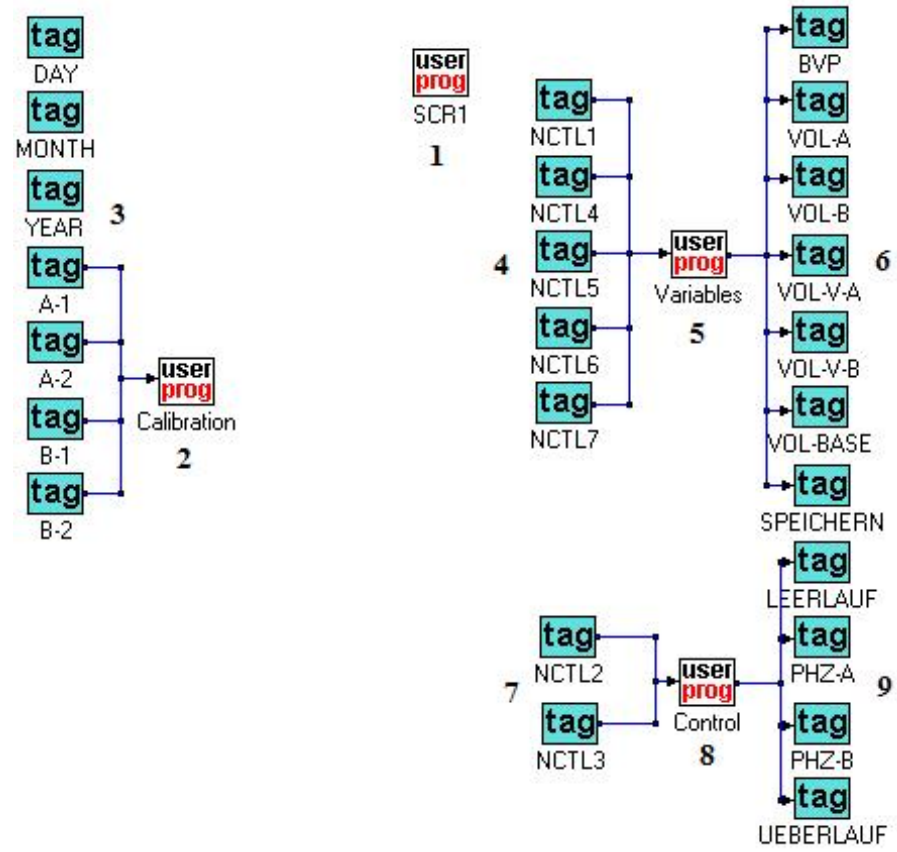

Fig. 8.4-8: The main task icon arrangement of VisiDAQ-strategy "multi". Block 1 controls the (de)activation of tasks. In block 2 the calibration factors for the pumps are defined. The blocks indicated with 3 are values loaded from a file. The blocks labelled with 4 represent the values defined by the user in the main task window. They are processed in block 5 and given to the permanent memory in the blocks labelled 6. The same happens with the pH values set by the user to hold constant in blocks 7, 8 and 9. See text for details.

device setup schematically with two big containers representing the vessels which feed the crystallisation compartments and three small containers representing the reservoir vessels containing base and double concentrated ion solutions. All containers indicate their filling level. The big containers also show the pH to hold, the actual pH, temperature, actually added volume, and the volume added to the respective vessel so far. The display further holds the buttons to start and end a CC experiment.

The main task icon arrangement is shown in Figure 8.4-8. The program block SCR1 (1) contains the script control in Visual Basic, starting and ending tasks. When the strategy is started, task-2 loads calibrated values and hands them over to *virtual tags* which represent a permanent memory accessible to all tasks.

These values are loaded from this memory, represented by blocks called *tags* (2) and handed over to a user programmed block called “Calibration” (3). This block assigns variables to the tag values and allows them to be shown on the main display. All values defined by the user in the main display are represented by tags (4 and 7). The user programmed blocks “Variables” (5) and “Control” (8) assign them to variables and hand them over to the permanent memory represented by tags (6 and 9). This is necessary because the permanent memory is not directly accessible. Values to be stored in permanent memory have to be defined in variables whose values can then be handed over to the permanent memory.

Task-2 is shown in Figure 8.4-9. It loads values from a text file, assigns them to variables in the corresponding user program block and hands them over to the permanent memory. These are the values loaded in (2) in the main task.

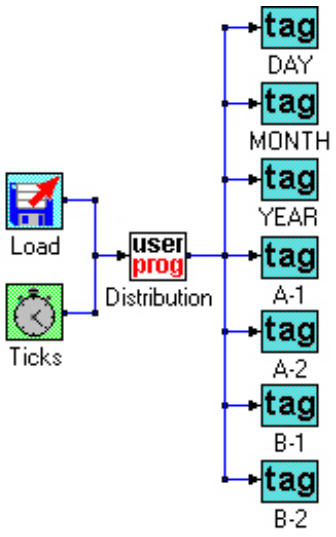

Fig. 8.4-9: Task-2 icon arrangement. This task loads the calibration values.

The actual CC program is found in task-3. The icon arrangement is shown in Figure 8.4-10. For processing, time is very important. Unfortunately, VisiDAQ as a 16-bit program does not process values greater than 65536 and sometimes does not count correctly every two seconds. Therefore, an explicit time control had to be established (1) consisting of a task timer block “Task time” for showing in the program display and two time blocks counting in seconds the “Real time” elapsed and a “Cycle time”. The real time in seconds is saved whereas the cycle time is used for control. The cycle time prevents the variable for time used in processing to become greater than 65536. The values in the permanent memory are loaded and translated into variables in (2) and (3). The user program block “Filling level” also defines a control variable for

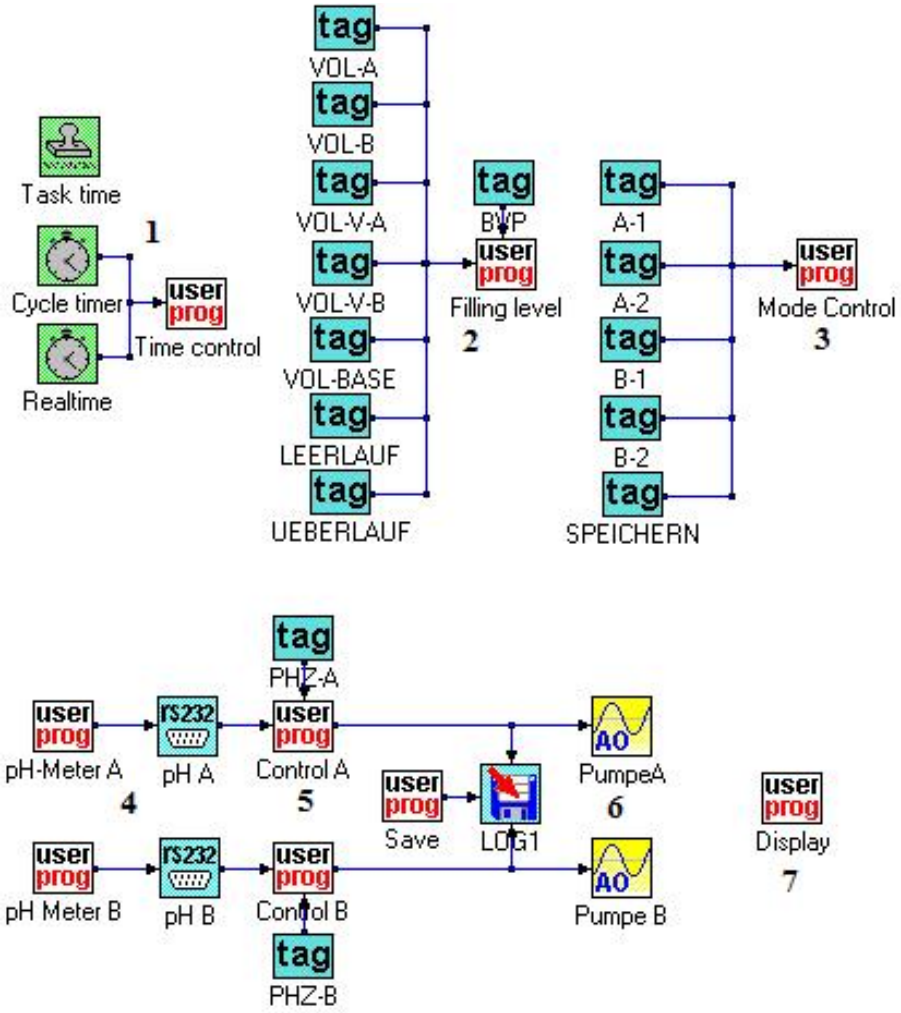

Fig. 8.4-10: Icon arrangement of task-3 which represents the actual CC-control programm. The blocks labelled 1 control the time cycles, the tags in block 2 load values from the permanent memory. The blocks indicated with 3 control the filling status of the vessels, depending on starting value and volume pumped. The blocks in 4 send commands to the pH-meters. Their responses are interpreted in 5. In 6, the pumps are controlled. Block 7 shows a response on the display window.

stopping the program if a reservoir vessel runs low or feeding vessel runs full. The communication with the pH meters is regulated in the user programs “pH-meter” and the communication blocks “pH”. A prompt string is send to the pH-meters which send a response string which are handed over to the user programs “Control” (5) which contain the actual CC programming. Depending on the pH value, the pumps are activated (6). Every ten seconds, time, temperature and pH of each feeding vessel are saved. The actual condition is translated into variables for showing on the display (7), i.e. if a pump is activated the connecting tubes will change colour.

8.4.3 User programs

The start and end of tasks are controlled in the main task and programmed in Visual Basic. VisiDAQ assigns values for each task status i.e. idle is 0, active is 1, stopped is 3. These values are obtained from VisiDAQ and handed over for observation. Task control is achieved by comparing a start button's condition (BBTN, 1=active, 0=inactive) and issuing appropriate start orders:

```
Sub Start()
        Dim MyTask As ScanTask                          //dimension of value
        Dim MyTask1 As ScanTask                         //dimension of value
        Dim MyTask2 As ScanTask                         //dimension of value
        Dim MyTask3 As ScanTask                         //dimension of value
        Dim MyTask4 As ScanTask                         //dimension of value
        Dim MyTag As Tag                                //dimension of value
        Dim p1 As Integer                               //dimension of value
        Dim p2 As Integer                               //dimension of value
        Dim p3 As Integer                               //dimension of value

        'Status of tasks                                //determination of status values
        Set MyTask1=GetScanTask("Task2")
        MyStatus1=MyTask1.GetStatus
        Set MyTask2=GetScanTask("Task3")
        MyStatus2=MyTask2.GetStatus
        Set MyTask3=GetScanTask("Task4")
        MyStatus3=MyTask3.GetStatus
        Set MyTask4=GetScanTask("Task5")
        MyStatus4=MyTask4.GetStatus

        'Filling-Start button's status and control      //comparison and execution
        Set MyTag=GetTag("Disp1","BBTN1")
        p1=MyTag.value
        If p1=1 Then
                Set MyTask=GetScanTask("Task4")
                MyTask.start
        End If
        If p1=0 Then
                Set MyTask=GetScanTask("Task4")
                MyTask.stop
        End If
        If (p1=0 And MyStatus1=0 And MyStatus2=0 And MyStatus3=0) Then
                Set MyTask=GetScanTask("Task5")
                MyTask.start
        End If

        'Start button's status and control              //comparison and execution
        Set MyTag=GetTag("Disp2","BBTN8")
        p2=MyTag.value
        If p2=1 Then
                Set MyTask=GetScanTask("Task3")
                MyTask.start
        End If

        'Stop button's status and control               //comparison and execution
        Set MyTag=GetTag("Disp2","BBTN5")
```

```
        p3=MyTag.value
        If p3=1 Then
                Set MyTask=GetScanTask("Task3")
                MyTask.stop
        End If
        If (p3=1 And MyStatus1=0 And MyStatus2=0 And MyStatus3=0) Then
                Set MyTask=GetScanTask("Task5")
                MyTask.start
        End If

        outputi 0,MyStatus1                          //output of status values
        outputi 1,MyStatus2
        outputi 2,MyStatus3
        outputi 3,MyStatus4
End Sub
```

The main task contains three user program blocks (Figure 9.4-8). These are not used for actual calculation but definition of variables. The values of the variables are handed over to the permanent memory:

a) "Calibration"

```
b1=TAG11*0.001;          //calibration value of channel 1 of pump A [l V-1 s-1]
b2=TAG12*0.001;          //calibration value of channel 2 of pump A [l V-1 s-1]
b3=TAG13*0.001;          //calibration value of channel 1 of pump B [l V-1 s-1]
b4=TAG14*0.001;          //calibration value of channel 2 of pump B [l V-1 s-1]

b5=b2/b1;                //factor for multiplying with double calcium concentration
b6=b4/b3;                //factor for multiplying with double carbonate concentration

output (#0,b5);          //value output for display
output (#1,b6);          //value output for display
```

b) "Control"

```
b7=TAG24;                //pH value to hold in calcium feeding vessel
b8=TAG25;                //pH value to hold in carbonate feeding vessel
b=2;                     //minimum filling level in reservoir vessels [l]
b9=50;                   //maximum filling level in feeding vessels [l]

output(#0,b7);           //value output for permanent memory
output(#1,b8);
output(#2,b);
output(#3,b9);
```

c) "Variables"

```
c1=TAG26;                //volume of calcium feeding vessel [l]
c2=TAG26;                //volume of calcium feeding vessel [l]
c3=TAG42;                //volume of calcium reservoir vessel [l]
c4=TAG42;                //volume of calcium reservoir vessel [l]
c5=TAG43;                //volume of base [l]
c6=TAG16;                //BVP pump velocity in Ismatec arbitrary units
c7=TAG23;                //save interval [s]

c8=(c6/999)*0.25*2*12*0.001;  //BVP flow in 12 channels [l 2s-1]
```

```
if (c7==10) {c9=0.1;}          //reciprocal definition of save interval selected
if (c7==20) {c9=0.05;}
if (c7==30) {c9=0.025;}
if (c7==40) {c9=0.025;}
if (c7==50) {c9=0.02;}

output (#1,c1);                //output of values for permanent memory
output (#2,c2);
output (#3,c3);
output (#4,c4);
output (#5,c5);
output (#6,c8);
output (#7,c9);
output (#0,c7);
```

In task-2, calibration values are loaded from a text file and assigned to a variable. The values of these variables are handed over to permanent memory:

```
a=ET1;                         //time [s]
a1=INF1;                       //value read from file

if (a == 0) {a2=a1;}           //first value assigned day
if (a == 1) {a3=a1;}           //second value assigned month
if (a == 2) {a4=a1;}           //third value assigned year
if (a == 3) {a5=a1;}           //fourth value assigned calibration value pump A, channel 1
if (a == 4) {a6=a1;}           //fifth value assigned calibration value pump A, channel 2
if (a == 5) {a7=a1;}           //sixth value assigned calibration value pump B, channel 1
if (a == 6) {a8=a1;}           //seventh value assigned calibration value pump B, channel 2

output (#0,a2);                //output of values for permanent memory
output (#1,a3);
output (#2,a4);
output (#3,a5);
output (#4,a6);
output (#5,a7);
output (#6,a8);
```

Task-3 is the actual CC control program. It contains several user program blocks (Figure 8.4-10.)

a) “Time control”

```
d=ET3;                                  //real time of system [s]
d1=ET2;                                 //time cycle of an hour [s]

d2=d1;                                  //correction of cycle time to even values [s]
if (d2*0.5 != int(d2*0.5)) {d2=d2+1;}

d3=d1-2;                                //correction of pH-meter reactivation time [s]
if (d3*0.5 != int(d3*0.5)) {d3=d3+1;}

d4=d1-8;                                //correction of save time [s]
if (d4*0.5 != int(d4*0.5)) {d4=d4+1;}

output (#0,d);                          //value output for other blocks
```

```
output (#1,d1);
output (#2,d2);
output (#3,d3);
output (#4,d4);
```

b) „Filling level“

```
e=TAG39;                                  //BVP flow with 12 channels [l 2s-1]
e1=TAG31;                                 //volume of calcium feeding vessel [l]
e2=TAG32;                                 //volume of carbonate feeding vessel [l]
e3=TAG33;                                 //volume of calcium reservoir vessel[l]
e4=TAG34;                                 //volume of carbonate reservoir vessel [l]
e5=TAG35;                                 //volume of base [l]
e6=TAG49;                                 //maximum filling level of feeding vessels [l]
e7=TAG37;                                 //minimum filling level of reservoir vessels [l]

e8=e8+e;                                  //volume removed by BVP pump so far [l]
n1=e1+k-e;                                //actual volume of calcium feeding vessel [l]
n2=e2+l-e;                                //actual volume of carbonate feeding vessel [l]
n3=e3-k2;                                 //actual volume of calcium reservoir vessel [l]
n4=e4-l2;                                 //actual volume of carbonate reservoir vessel [l]
n5=e5-k1-l1;                              //actual volume of base [l]

if (n1>=e6 || n2>=e6)  {o1=1;}            //comparison and definition of control variable
else {o1=0;}
if (n3<=e7 || n4<=e7)  {o2=1;}
else {o2=0;}
if (n5<=e7)  {o3=1;}
else {o3=0;}

if (o1==1 || o2==1 || o3==1) {o4=1;}      //comparison and definition of stop variable
else {o4=0;}

output (#0,n1);                           //value output for other blocks or display
output (#1,n2);
output (#2,n3);
output (#3,n4);
output (#4,n5);
output (#5,o4);
output (#6,e8);
```

c) “Mode control”

```
h=TAG38;                          //reciprocal save interval
h3=TAG27;                         //calibration value of channel 1 of pump A [l V-1 s-1]
h4=TAG29;                         //calibration value of channel 2 of pump A [l V-1 s-1]
h5=TAG28;                         //calibration value of channel 1 of pump B [l V-1 s-1]
h6=TAG30;                         //calibration value of channel 2 of pump B [l V-1 s-1]

output (#0,h);                    //value output for other blocks
output (#2,h3);
output (#2,h4);
output (#4,h5);
output (#5,h6);
```

d) “pH-meter A” (B, respectively)

```
g1="K.7";                         //usual command string requesting pH value
//all 100 s command string requesting internal check; if no response, activation string
```

```
if (d2*0.1==int(d2*0.1) && d2*0.002!=int(d2*0.002) && i1!=0)
 {g1="K.18";}
if (d2*0.1==int(d2*0.1) && d2*0.002!=int(d2*0.002) && i1==0 && d != 0)
 {g1="K.9";}

//all 500 s command string deactivation; one cycle later, command string activation
if (d2*0.002==int(d2*0.002) && d2 != 0)
 {g1="K.9";}
if (d3*0.002==int(d3*0.002) && d3 != 0)
 {g1="K.9";}

sprintf (g2,"%s\r",g1);          //inserting command string into send string (g2="K.n^M")

output (#0,g2);                  //output of send string to pH-meter communication block
```

e) "Control A" (B, respectively)

```
i1=FLOAT(SER1[1]);               //pH value in calcium feeding vessel, conversion string/value
i2=FLOAT(SER1[2]);               //temperature in calcium feeding vessel, conversion string/value
i3=SER1[0];                      //status response string
i4=TAG15;                        //pH value to hold

if (i3=="K.7*" && i1!=0 && o4==0)      //functioning pH meter and not stopped due to filling
 {
 if (i1<i4)                            //pH below threshold
  {
  i5=i4-i1;                            //delta pH for calculation
  i6=i5*i5*exp(-0.5*i5-0.3)+0.3*i5;    //calculation of tension to apply
  if (i6<0.05) {i6=0.05;}              //minimum tension for pump to function
  i7=i7+2;                             //time pumps run so far [s]
  i8=2*h3*i6;                          //adding volume of base [l]
  i9=2*h5*i6;                          //adding volume of calcium reservoir solution [l]
  i=i9+i8;                             //overall volume adding [l]
  k=k+i;                               //overall volume added so far [l]
  k1=k1+i8;                            //volume of base added so far [l]
  k2=k2+i9;                            //volume of calcium stock solution so far [l]
  k3=i;                                //display volume adding [l]
  k4=1;                                //activate tubes in display
  }
 else {i6=0; k3=0; k4=0;}
 }
else {i6=0; k3=0; k4=0;}

output (#0,i6);                  //output of values calculated for other blocks and display
output (#1,k1);
output (#2,k2);
output (#3,k);
output (#4,i1);
output (#5,i2);
output (#6,i3);
output (#7,k3)
```

e) "Save"

```
//all save interval seconds Log-file on; increase number of saved values
if (d4*h==int(d4*h)) {m=1; m1=m1+1;}
if (d4*h!=int(d4*h)) {m=0;}

output (#0,m);                   //output values for other blocks or display
output (#1,m1);
```

```
output (#2,d);                    //save real time to disk
```

f) “Display”

```
//Displaykontrolle

if (m==1) {m2=6;}                          //display „saving“ or
if (m==0)
  {
  if (o1==1 || o2==1 || o3==1) {m2=7;}     //display “stopped” or
  else
      {
      if (i3=="K.7*" && j3=="K.7*")        //pH-meters functioning
          {
          if (i6!=0 && j6==0) {m2=2;}      //display “pumping calcium”
          if (i6==0 && j6!=0) {m2=3;}      //display “pumping carbonate”
          if (i6!=0 && j6!=0) {m2=4;}      //display “pumping both”
          if (i6==0 && j6==0) {m2=1;}      //display “measuring”
          }
      else {m2=5;}                         //display “pH-meter check”
      }
  }


//graphics control

if (k4==0 && l4==0) {m3=0; m4=0; m5=1;}      //BVP pump
if (k4==1 && l4==0) {m3=1; m4=0; m5=1;}      //BVP pump, calcium pump
if (k4==0 && l4==1) {m3=0; m4=1; m5=1;}      //BVP pump, carbonate pump
if (k4==1 && l4==1) {m3=1; m4=1; m5=1;}      //all pumps

output (#0,m2);                   //output values for display
output (#1,m3);
output (#2,m4);
output (#3,m5);
```

8.5 Safety and disposal

The following list contains all chemical compounds which were used in experiments for this work. The column “symbol” lists the international hazard symbols appropriate for the specific compound. “R-Sätze” and “S-Sätze” are listings of dangers and safety precautions demanded by German law.

compound	symbol	R-Sätze	S-Sätze	disposal
acetone	F	11	9-16-23-33	1a
ammonium carbonate	Xn	22	-	2
bovine serum albumin	-	-	-	2
calcium carbonate	-	-	-	2
calcium nitrate	O, Xi	8-36	-	3
calcium sulphate	-	-	-	2
chloroform	Xn	22-38-40-48/20/22	2-36/37-46	1b
ethanol	F	11	7-16	1a
hydrochloric acid	C	34-37	26-36/37/39-45	4
poly-L-aspartic acid	-	-	-	2
nitric acid	C, O	35	32.2-26-36/37/39-45	4
sodium hydroxide	C	35	26-37/39-45	3
sodium chloride	-	-	-	2
silicon dioxide (quartz)	-	-	-	2
trimethylchlorsilane	X	26-36-52/53	(1/2-)24-27-45-61	3

Disposal:

1: organic solvents were disposed in the organic solvents disposal container for (a): non-halogenated solvents and (b): halogenated solvents

2: solids were disposed in the container for solid waste

3: inorganic compounds were dissolved in water, made acidic and transferred to the container for acidic heavy metal solutions

4: acids were transferred to the container for heavy metal solutions

8.6 Publications

a) Publications in scientific journals

1: A. Becker, W. Becker, M. Epple, J.C. Marxen, *In-vitro Crystallisation of Calcium Carbonate in the Presence of Biological Additives – Comparison of the Ammonium Carbonate Method with Double-Diffusion Techniques*, **Z**eitschrift für **anorg**anische und **allg**emeine **Chem**ie **628** (2002) 2184-2211.

2: A. Becker, U. Bismayer, M. Epple, B. Hasse, H. Fabritius, J. Shi, A. Ziegler, *Structural Characterisation of X-ray amorphous calcium carbonate (ACC) in sternal deposits of the crustacea Porcellio scaber*, **J**ournal of the Royal **Chem**ical **Soc**iety, Dalton **Trans**actions (2003) 551-555.

3: A. Becker, M. Epple, I. Schmitz, *A combined study of clinically well characterised human atherosclerotic plaques with histological, chemical, and ultrastructural methods*, **J**ournal of **Inorg**anic **Biochem**istry **98** (2004) 2032-2038.

4: A. Becker, M. Epple, A. Ziegler, *The mineral phase in the cuticles of two species of Crustacea consists of magnesium calcite, amorphous calcium carbonate, and amorphous calcium phosphate*, **J**ournal of the Royal **Chem**ical **Soc**iety, **Dalton Trans**actions in press.

5: A. Becker, I. Sötje, C. Paulmann, F. Beckmann, T. Donath, R. Boese, O. Prymak, H. Tiemann, M. Epple, *Calcium sulphate hemihydrate is the inorganic mineral in statoliths of scyphozoan medusae (Cnidaria)*, **J**ournal of the Royal **Chem**ical **Soc**iety, **Dalton Trans**actions in press.

6: C. Günther, A. Becker, G. Wolf, M. Epple, In vitro *synthesis and characterisation of amorphous calcium carbonate*, **Z**eitschrift für **anorg**anische und **allg**emeine **Chem**ie in press.

b) Further publications

1: A. Becker, A. Ziegler, H. Fabritius, M. Epple, *Structural characterisation of amorphous calcium carbonate in sternal deposits of crustaceans*, HASYLAB Annual Report (2002).

2: T. Welzel, A. Becker, W. Meyer-Zaika, M. Epple, *Characterisation of calcium phosphate nanoparticles*, HASYLAB Annual Report (2003).

3: A. Becker, C. Paulmann, I. Sötje, H. Tiemann, M. Epple, *Crystallographic phase determination of calcium sulphate microcrystals from deep-sea medusae*, HASYLAB Annual Report (2003).

4: A. Becker, I. Schmitz, A. Ziegler, M. Epple, *Biomineral phases as a result of regulated (Crustacea cuticles) and unregulated (atherosclerosis) processes*, HASYLAB Annual Report (2004).

5: A. Becker, I. Sötje, H. Tiemann, R. Boese, M. Epple, *Calcium sulphate hemihydrate is the inorganic material in medusae gravity sensors*, HASYLAB Annual Report (2004).

c) Conference presentations

1: A. Becker, M. Epple, W. Becker, J.C. Marxen, *Simulation von Biomineralisation – Kontrollierte Fällung von Calciumcarbonat*, Jahrestagung der Deutschen Gesellschaft für Kristallographie, Kiel, 2002.

2: A. Becker, M. Epple, W. Becker, J.C. Marxen, *Crystallisation of calcium carbonate in the presence of biological additives*, Workshop des DFG Schwerpunktprogramms Biomineralisation, Mainz, 2004.

3: A. Becker, F. Boßelmann, M. Epple, W. Becker, J.C. Marxen, *Crystallisation of calcium carbonate in the presence of biological additives*, Berichtskolloquium des Schwerpunktprogramms Biomineralisation, Bonn, 2004.

4: A. Becker, M. Epple, A. Ziegler, *The mineral phase in the cuticles of Crustacea consists of magnesium calcite, amorphous calcium carbonate, and amorphous calcium phosphate*, Berichtskolloquium des Schwerpunktprogramms Biomineralisation, Bonn, 2004.

8.7 Curriculum vitae

29.07.1976	Birth in Hagen
1983 – 1987	Grundschule „Friedenstal“ in Ennepetal
1987 – 1993	Städtische Realschule Ennepetal
1993 – 1996	Märkisches Gymnasium Schwelm
1995 – 2003	Civil service with the Volunteer Fire-fighters
07/1996 – 10/1996	Traineeship at the Siegfried Jacob Metallwerke GmbH in Ennepetal
10/1996 – 09/1998	Grundstudium at the Ruhr-University of Bochum
09.10.1998	Diplom-Vorprüfung
10/1998 – 06/1999	Studies at the Ecole Européenne de Chimie, Polymères et Matériaux in Strasbourg (F)
07/1999 – 09/1999	Traineeship at the company SICPA in Annemasse (F)
10/1999 – 09/2001	Hauptstudium at the Ruhr-University of Bochum
10/2001 – 03/2002	Diploma thesis in the group of Prof. Dr. M. Epple in Bochum, “*Kristallisation von Calciumcarbonat unter dem Einfluss biomimetischer Fremdstoffe“*
26.03.2002	Diplom-Hauptprüfung
04/2002 – 04/2005	Doctoral thesis in the group of Prof. Dr. M. Epple. Subject: “*Structural Characterisation of Biominerals and Biomimetic Crystallisation of Calcium Carbonate”*
04/2002 – 09/2003	Scientific Asisstant in the group of solid state chemistry at the Ruhr-University of Bochum.
10/2003 – 05/2005	Scientific Asisstant at the institute of ionorganic chemistry at the University of Duisburg-Essen.
11/2003 – 02/2004	Cooperation work with Prof. Dr. Lia Addadi and Prof. Dr. Steve Weiner at the Weizmann Institute of Science in Rehovot (ISR)

Danksagung

Bedanken möchte ich mich ganz herzlich bei Prof. Dr. Matthias Epple für die Gelegenheit bei ihm promovieren zu können, für die hervorragende auch nicht-wissenschaftliche Betreuung und die steten „fünf Minuten“ auch unter Zeitdruck, sowie etliche Mitnahmekilometer und die Gelegenheit, meine „Computerwut“ ausleben zu dürfen.

Bei meinen Kooperationspartnern Dr. J. Marxen, Dr. I. Sötje und Dr. H. Tiemann (Hamburg), Dr. I. Schmitz (Bochum) und Dr. A. Ziegler (Ulm) für die stets exzellente Zusammenarbeit und das sehr gute Verhältnis, das sehr oft sehr über Kollegialität hinaus ging.

Für die direkte Hilfe bei der Erstellung dieser Arbeit und der Lösung vieler kleiner und großer Probleme möchte ich den folgenden Personen danken:
Dr. R Neuser (Bochum) und Dipl.-Ing. S. Boukercha (Essen) für die Hilfestellung am Rasterelektronenmikroskop während der Stunden vor diesem faszinierenden Gerät.
Frau S. Grumm (Bochum) für Messungen an der Thermowaage.
Frau K. Brauner und V. Hiltenkamp (Essen) für AAS-Messungen.
Dr. C. Bähtz, Dr. B. Hasse, Dr. M. Knapp und Dr. C. Paulmann (Hamburg) für ihre Hilfe am HASYLAB.
Herrn A. Lindner (Bochum) für die Hilfe bei der Konstruktion und den Bau der Teile der Multi-CCDD-Anlage.
Prof. Dr. R. Boese (Essen) für die Hilfe bei der Auswertung der Einkristalldiffraktomtriedaten, für sein stetes Interesse am Fortgang der Arbeit und sein persönliches Engagement.
Dr. C. Schiller für viele Diskussionen, das Beantworten komplexerer Fragen und den geistigen Beistand.
Allen weiteren Mitgliedern des Arbeitskreises für Diskussionen, Tipps und ihre Geduld. Inzwischen sind sie zu zahlreich, um sie namentlich zu nennen.

Mein besonderer Dank gilt Cand.-Chem. M. Matthes für seine Ausdauer, Freundschaft und die Hilfe bei der Einrichtung und Administration unseres Netzwerks sowie Dipl.-Biol. F. Bosselmann für ihre Freundschaft und die moralische und tatkräftige Unterstützung.

Für die gute Aufnahme in bestehende Strukturen, die sehr gute Kollegialität, die stete Hilfsbereitschaft und die geistige Verbundenheit möchte ich mich bei den „neuen“ Kollegen aus Essen bedanken, insbesondere bei Frau B. Nota, Frau U. Giebel und Herrn W. Scholz.

Für die sehr gute Aufnahme, viel Zeit und einen besonderen Einblick möchte ich mich ganz herzlich bei Prof. Dr. L. Addadi und Prof. Dr. S. Weiner (Rehovot, ISR) bedanken. Gleiches gilt für die sehr freundschaftliche Aufnahme durch ihre Arbeitsgruppe. Bei Ron Littman, M. Sc. möchte ich mich sehr für seine Freundschaft, seine Unterrichtsstunden in Hebräisch und die vielen wertvollen wissenschaftlichen und nichtwissenschaftlichen Diskussionen bedanken.

Ich möchte mich sehr bei Ron Littman, M. Sc., Rev. Major C. M. Artley, M. A. und seiner Frau S. M. Artley, M. A., B. Ed. für ihre Hilfe und Korrektur dieser Arbeit in englischer Sprache bedanken.

Für die Unterstützung während der gesamten Zeit der Promotion und davor möchte ich mich bedanken bei:
Herrn P. Hein für das andauernde Interesse und die Bereitschaft, mich immer mit Lesestoff zu versorgen.
Dr. Dörner von den Siegfried Jacob Metallwerken dafür, dass er mich davon überzeugt hat, den Studiengang Chemie zu wählen und nach Frankreich zu gehen.
Herrn A. Graef. Dipl.-Chem. E. Mark, Frau U. Fischer, Dipl.-Chem. G. Thie und meiner Rollenspieltruppe für ihre treue Freundschaft.

Ohne die finanzielle und moralische Unterstützung meiner Eltern, meiner Schwester Tanja und meines Schwagers Jörg wären das Studium und diese Arbeit nicht möglich gewesen.

Alle, die hier ungenannt bleiben, bitte ich um Nachsicht. Diese Liste erhebt keinen Anspruch auf Vollständigkeit.

Eidesstattliche Erklärung

Hiermit versichere ich, dass ich die vorliegende Arbeit mit dem Titel

„Structural Characterisation of Biominerals and Biomimetic Crystallisation of Calcium Carbonate"

selbst verfasst und keine außer den angegebenen Hilfsmitteln und Quellen benutzt habe und dass die Arbeit in dieser oder ähnlicher Form noch bei keiner anderen Fakultät eingereicht worden ist.

Essen, im April 2005

Alexander Becker